INVESTIGATIONS OF A PRINTED CIRCUIT HEAT EXCHANGER FOR SUPERCRITICAL CO2 AND WATER

by

HOSEOK SONG

B.S., Inha University, South Korea, 2004

A THESIS

submitted in partial fulfillment of the requirements for the degree

MASTER OF SCIENCE

Department of Mechanical and Nuclear Engineering
College of Engineering

KANSAS STATE UNIVERSITY
Manhattan, Kansas

2007

Approved by:

Major Professor
Dr. Akira T. Tokuhiro

Abstract

In the STAR-LM (Secure Transportable Autonomous Reactor-Liquid Metal) reactor concept developed at Argonne National Laboratory (ANL), a supercritical CO_2 (S-CO_2) Brayton cycle is used as the power conversion system because it features advantages such as a higher efficiency due to less compressive work, and competitive cost due to a reduced complexity and size. From the components of the cycle, high performance of both the recuperator and precooler has a large influence on the overall cycle efficiency and plant economy. One attractive option for optimizing the performance of the cycle is to use an high efficiency heat exchanger such as the Printed Circuit Heat Exchanger (PCHE) manufactured by Heatric. The PCHE is a compact heat exchanger with high effectiveness, wide operating range, enhanced safety, and low cost. PCHEs are used in various industrial applications, but are relatively new to the nuclear industry.

In this study, performance testing of a PCHE using supercritical CO_2 and water as heat transfer media were performed at ANL. The heat transfer characteristics of the PCHE under operating conditions of the STAR_LM precooler were investigated. The S-CO_2 , defined the "hot-side", had its outlet condition near the pseudocritical point at 7.5MPa (~31°-32°C). We found that of all the thermophysical properties undergoing rapid change near the critical point, heat transfer for S-CO_2 is strongly correlated with the specific heat of CO_2. Additional experiments performed with different bulk temperatures and pressures on the hot side also supported this conclusion. We proposed plotting the heat transfer results, $(Nu^2 + Pr^{2/3})$ versus $(RePr^{4/3})$, based on an order-of-magnitude analysis, to reveal the close proximity of the outlet to pseudocritical conditions.

In order to check the experimental results, a nodal model of a segmented PCHE using a traditional log-mean temperature difference method was developed. This approach provided the temperature distribution along the heat exchanger. Additionally a CFD simulation (FLUENT) of a 4-layer, zig-zag channeled PCHE was developed. Comparison of the simulation and LMTD nodal model revealed that indeed specific heat strongly influenced the heat transfer.

Table of Contents

List of Figures

List of Tables

NOMENCLATURE

Symbols	Description
A	area, m^2
A_c	cross-sectional area, m^2
C_f	friction coefficient
c_p	specific heat at constant pressure, J/kg·K
D	diameter, m
D_h	hydraulic diameter, m
f	friction factor
G	mass velocity, kg/m^2s
Gr	Grashof number
h	convection heat transfer coefficient, W/m^2
i	enthalpy, J/g
j_H	Colburn j factor for heat transfer
k	thermal conductivity, W/m·K
L	metal wall thickness, m
$\dot{m}$	mass flow rate, kg/s
Nu	Nusselt number
P	perimeter, m
p	pressure, N/m^2
Pr	Prandtl number
Q	volumetric flow rate, gpm or m^3/s
q	heat transfer rate, W
R_t	thermal resistance, K/W
Re	Reynolds number
r	radius, m
S	supercritical fluid

St	Stanton number
T	temperature, K
U	overall heat transfer coefficient, $W/m^2 \cdot K$
u, v, w	mass average fluid velocity components, m/s
V	volume, m^3; fluid velocity, m/s

Greek Letters

α	Thermal diffusivity, m^2/s
Δp	pressure drop, N/m^2
ΔT_{lm}	log mean temperature difference
μ	viscosity, $Kg/s \cdot m$
ν	kinematic viscosity, m^2/s
ρ	mass density, kg/m^3
τ	shear stress, N/m^2

Subscripts

ANL	Argonne National Laboratory
b, bulk	bulk fluid
c	cross-sectional; cold side
CO_2	carbon dioxide
D	diameter
h	hydrodynamic; hot side
H_2O	water
in	inlet
out	outlet
t	thermal
total	total
w, wall	wall

Acknowledgements

I would like to thank Dr. Akira Tokuhiro for his guidance and for the opportunity to study at Kansas State University.

I would also like to thank Dr. Dae H. Cho and Steve Lomperski for helping me on the experiment at Argonne National Laboratory.

I would also like to express my thanks to the members of my committee for devoting their time so that this project could be successfully completed.

I would like to thank to my family and J. H. Yoo for their support.

CHAPTER 1 - Introduction

1.1 Research background

The world's population is predicted to increase up to about 10 billion by 2050. As the world population is increasing, the consumption of energy is also growing. So the shortage of energy has become a major issue these days due to the rapid growth of population. In considering global electricity consumption, the International Energy Agency projects a doubling of world electricity demand by 2030, creating the need for 740GWe of new generating capacity in the next quarter century. In 2005 the global generating capacity is 367GWe. The reasons why nuclear power is mainly considered are due to its environmental and economic competition. First, nuclear energy is promising as shown in Figure 1.1. If coal power plant is replaced with nuclear power plant, every 22tonnes of uranium used for electricity would save the emission of about one million tonnes of carbon dioxide, relative to coal [2].

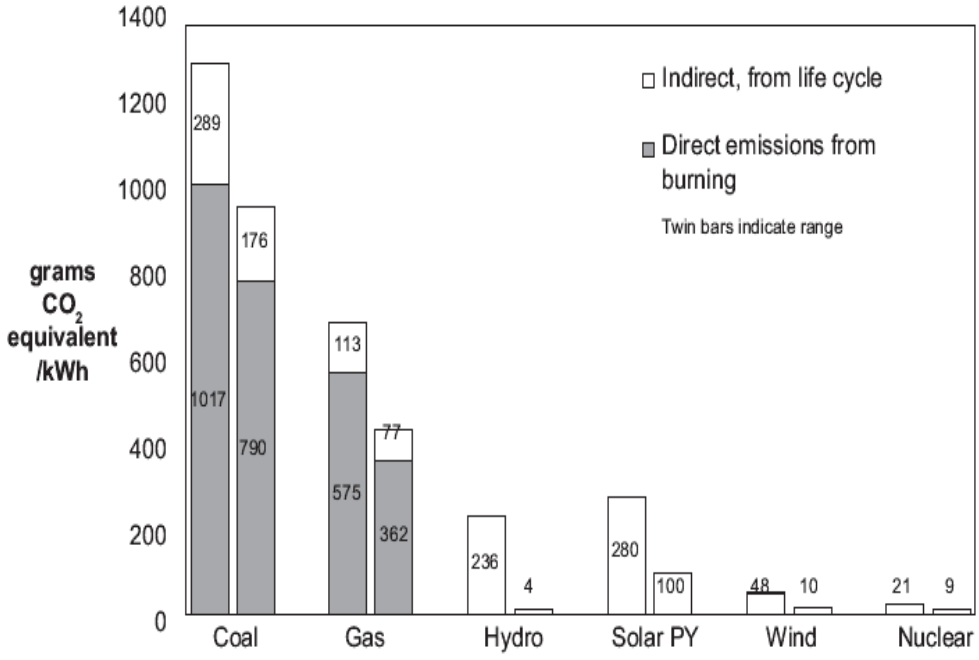

Figure 1.1Greenhouse Gas Emission from Electrical production [2]

Secondly, nuclear energy is competitive in generating costs compared with other energy sources. As Figure 1.2 shows, a nuclear power plant provides electricity at the most competitive price.

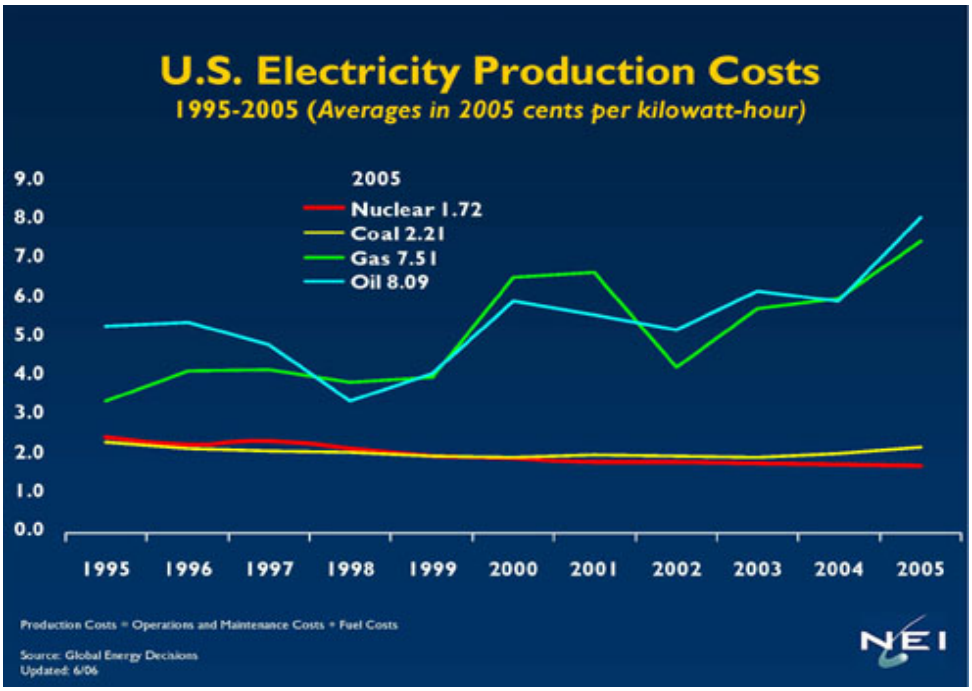

Figure 1.2 Comparison of electricity production costs [22]

The electricity production cost with each energy source is evaluated based on fuel cost, operation cost and maintenance cost. As shown in Figure 1.2, the gas production cost is 4 times more than that of nuclear. However, nuclear plants have relatively high capital costs. The competitiveness of nuclear energy depends on the capital cost of the plant, and reduction of capital can be expected by reduced construction time. For this reason, the Secure Transportable Autonomic Reactor (STAR) was designed by Argonne National Laboratory (ANL) to meet the goals of economics, proliferation resistance, sustainability, and the possibility of long-term operation (15-20 years) without refueling [20]. The STAR-LM system employs closed cycle gas turbines because compared to a steam cycle, the closed cycle gas turbines are simple, compact, and less expensive, and have shorter construction periods, thus reducing the capital costs [20].

The STAR-LM cycle uses lead (Pb) as reactor coolant and the supercritical CO_2 (S-CO_2) as the working fluid. As Figure 1.3 shows, the STAR-LM cycle consists of STAR reactor, turbine, high temperature recuperator, low temperature recuperator, pre-cooler, and compressors.

CO_2 has unique characteristics near its critical point. Figure 1.4 and Figure 1.5 show the density and specific heat with critical point and the outlet temperature of the precooler in the STAR-LM system.

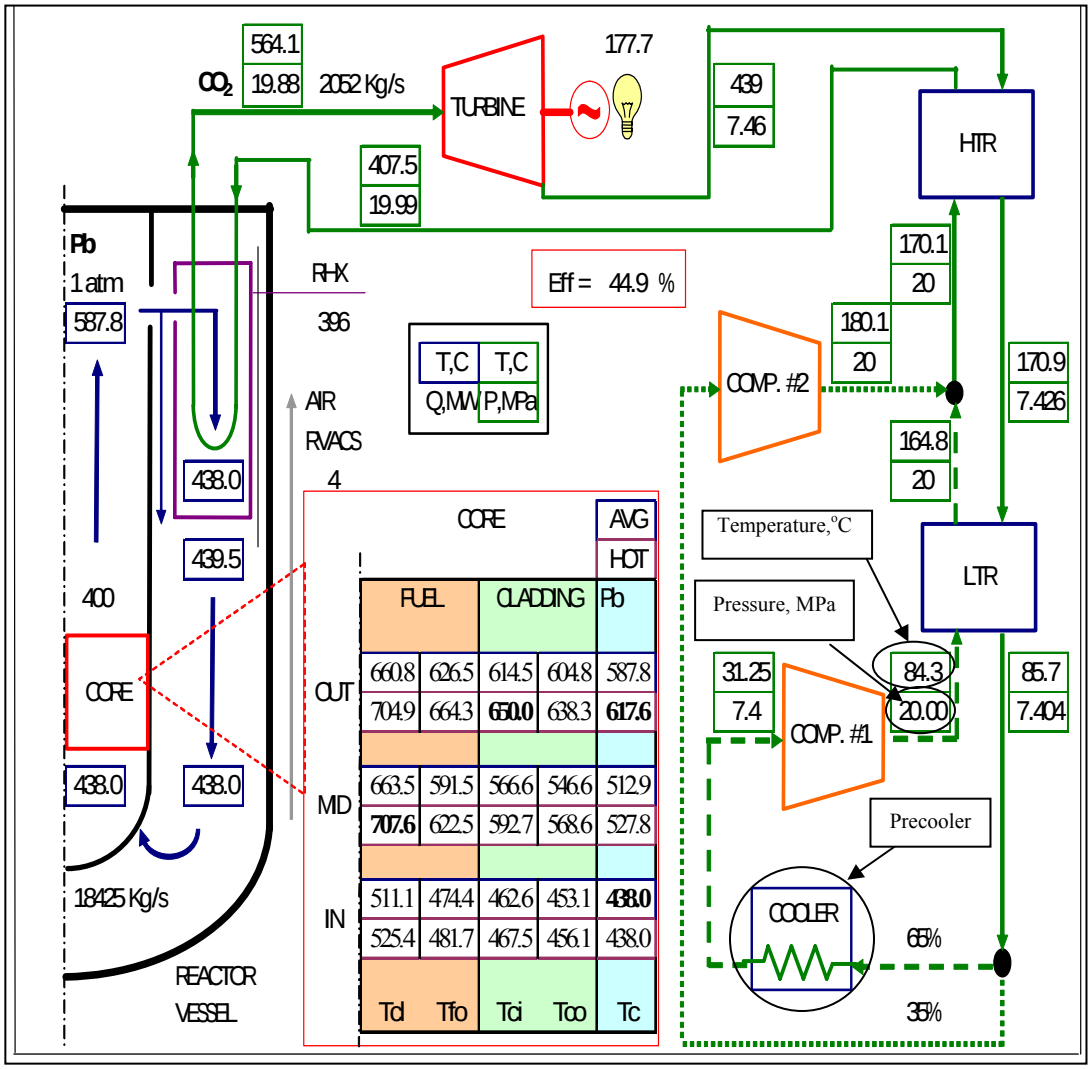

Figure 1.3. Process diagram for the STAR-LM reactor [20]

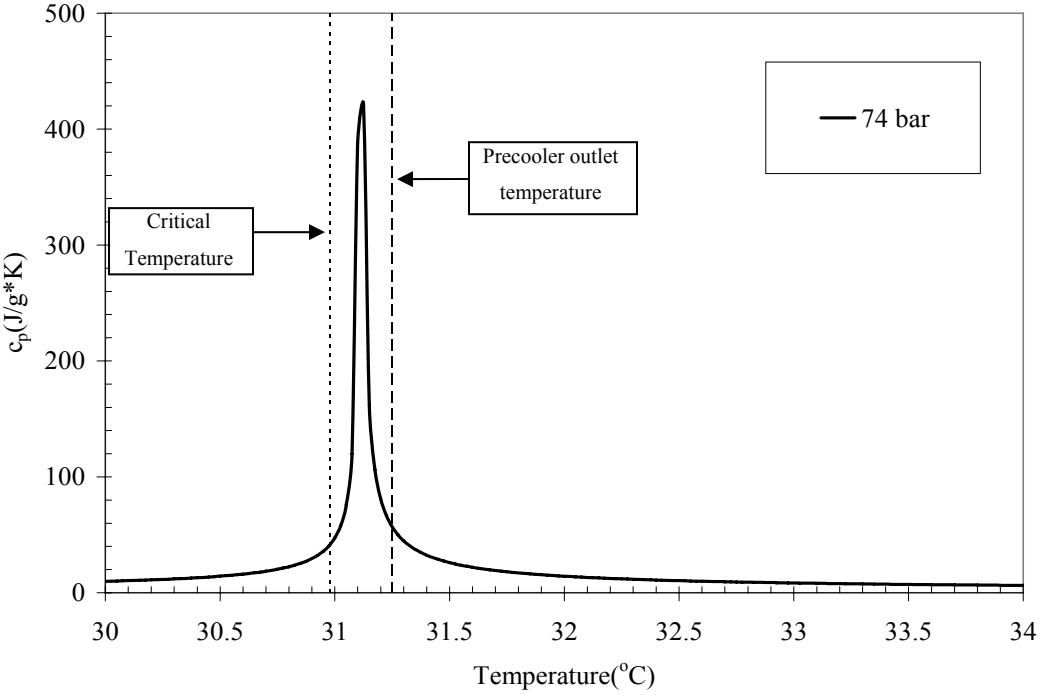

Figure 1.4 Specific heat of CO_2 at 7.4 MPa

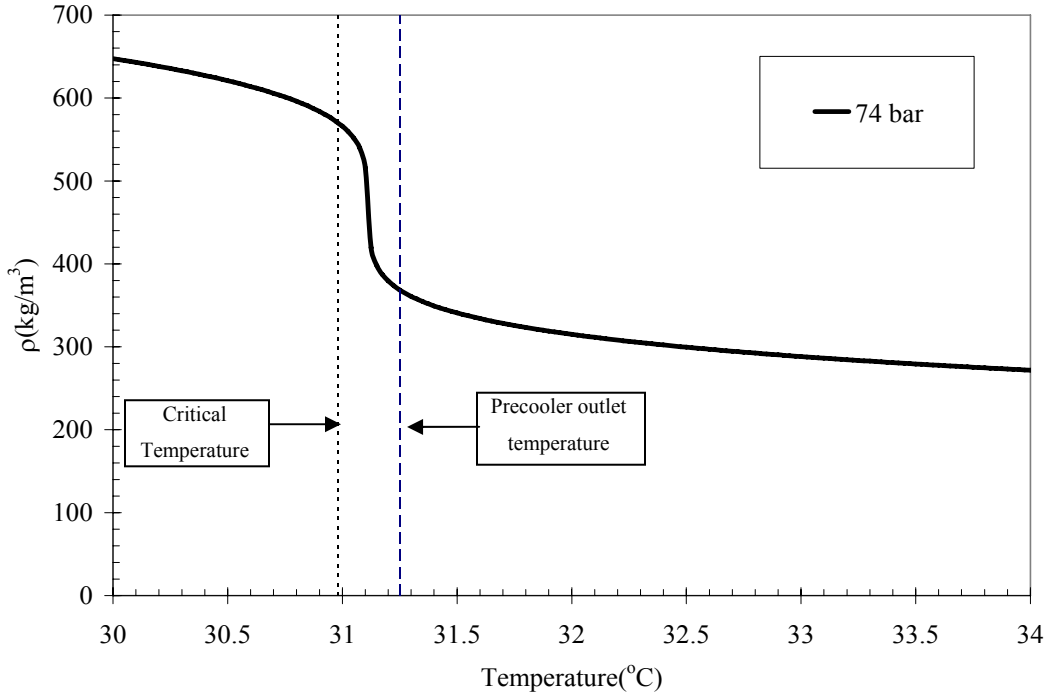

Figure 1.5 Density profile at 7.4 MPa

The critical temperature is 30.98°C. The precooler outlet temperature is 31.25°C in the STAR-LM system. The specific heat reaches a maximum value at the supercritical point as shown in Figure 1.4. We thus can realize high efficiency if we operate the heat exchanger in this thermophysical regime.

The density decreases near the critical temperature as shown in Figure 1.5. This characteristic reduces the required compressor work done on CO_2 as it is compressed just before the density decreases rapidly near the critical point in the compressor.

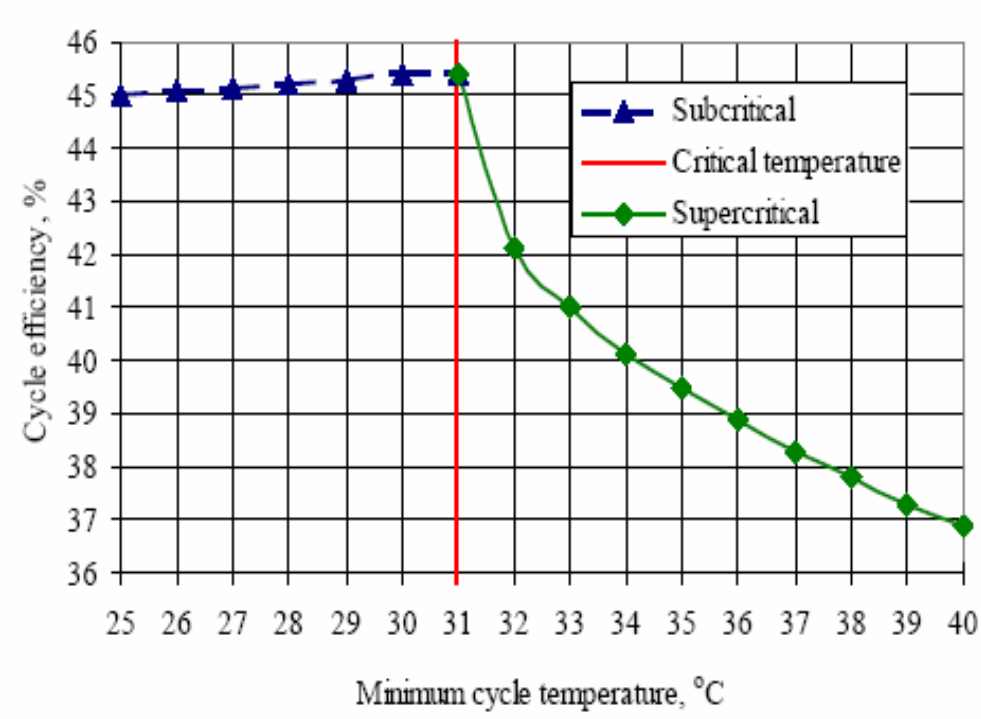

Figure 1.6 Minimum temperature optimization [20]

Figure 1.6 shows the cycle efficiency versus minimum temperature in the STAR-LM system. The minimum temperature is the outlet temperature of the precooler in the STAR-LM system. The highest efficiency is achieved at the critical point as shown. However, the STAR-LM system has a slightly higher temperature on the outlet of the precooler. It is 31.25°C. With this temperature, the calculated system efficiency is 43.8% [20].

There are several reasons to have a higher temperature than the critical temperature (30.98°C). If the precooler outlet temperature is 31°C, the length of the

precooler is estimated as 26.5m [20] as shown in Table 1. As the outlet temperature of the precooler increases slightly to 31.25^{o}C, the length of the precooler decreases down to 12.1m [20]. Thus, although an increase in outlet temperature requires more compressor work, the relative decrease in length is more than 50% relative to 26.5m. Additionally, for compressor durability, it is necessary to avoid two phase flow in the compressor [20]. 31.0^{o}C is too close to the critical point, 30.98^{o}C. In order to keep CO_2 in a supercritical state, one must have a margin of safety; 31.25^{o}C was deemed practical and achievable. For the reasons discussed above, the outlet temperature of the precooler is set slightly higher than the critical point.

Table 1.1. Cycle efficiency according to the outlet temperature of the precooler [20]

Precooler outlet temp.	31.00^{o}C	31.25^{o}C
Heat exchanger length	26.5m	12.1m
Compressor #1 work	27.6MW	40.0MW
Cycle efficiency	45.8%	43.8%

In this study, we focus on the PCHE as the precooler of the STAR-LM system due to its importance as discussed above based on the operating condition as shown in Figure 1.3. In addition, more experiments are conducted with changing the temperature and pressure with supercritical CO_2.

1.2 Objectives

The present work reports on the performance of a Printed Circuit Heat Exchanger (PCHE) as a key component in the power conversion system of a Generation IV advanced nuclear system (STAR-LM). The PCHE is being considered as a precooler and the recuperators (2) in the STAR-LM system.

The Heatric PCHE of a proprietary design was performance tested at Argonne National Laboratory using water and supercritical CO_2 as heat transfer media. We followed the following objectives based on the scope-of-work agreed upon with support from DOE.

First, the PCHE heat transfer lengths were verified based on limited information provided by Heatric. As complete, detailed specifications were not provided, we estimated the basic dimensions of the PCHE such as zigzag channel angle and channel diameter. From this, we estimated the size of the interior hot and cold channels.

Second, the flow characteristics of the PCHE were investigated experimentally. From this, the hydraulic characteristics, similarities and differences, of both the hot and cold side were noted.

Third, heat transfer characteristics of the PCHE with water on both the hot and cold sides were studied experimentally. The convective heat transfer coefficient with water was determined. These measurements were carried out prior to measurement of the heat transfer coefficients with CO_2.

Fourth, heat transfer characteristics of the PCHE with CO_2 were investigated experimentally. This was the primary goal of this study. Operating experience with the CO_2 loop, near the critical point, was also gained.

Fifth, analytical methods to predict and verify the experimental results were developed. In particular, we sought to estimate the temperature distribution in the PCHE. The analysis was based on the measured overall heat transfer coefficient in CO_2/water test, the thermophysical properties of CO_2 (about the critical point) and water, and a modified heat exchanger analysis. Finally, a simplified computational fluid dynamics model of the PCHE was developed to further support our analytical approach.

CHAPTER 2 - Literature Review

2.1. STAR-LM system

The Generation IV Advanced Reactor systems are expected to achieve significant reductions in capital and operating costs by taking advantage of the benefits of modular construction, up-to-date manufacturing practices, design simplifications, design innovations, and advanced technologies. Significant realistic reductions in plant costs, size, and complexity combined with a significant increase in plant efficiency may potentially be realized through the use of an advanced power conversion technology consisting of a gas turbine Brayton cycle utilizing S-CO_2 as the working fluid. S-CO_2 has significantly higher density (relative to helium), which reduces the need for compressive work in the bottom part of a Brayton cycle; thus increasing the overall cycle efficiency.

S-CO_2 Brayton cycle has been considered as the power conversion system for the Secure Transportable Autonomous Reactor (STAR) project at Argonne National Laboratory. The STAR-LM (Liquid Metal) version is a high temperature, fast flux reactor driven by natural circulation. It employs molten lead (or lead-bismuth eutectic) as the primary coolant and uses an indirect Brayton cycle for the generation of electricity. The plant is designed to operate with a turbine inlet temperature of ~550^{o}C and is expected to have a cycle efficiency of about 45 percent. [32]

One of the key components for the S-CO_2 power system is the regenerative heat exchanger, known as the "recuperator". This is where heat exchange between two flowing streams of S-CO_2 takes place. While the benefits of the S-CO_2 Brayton cycle are attributed to the unique thermophysical properties of S-CO_2 (e.g. density and specific heat), these same properties also present technical challenges to the recuperator design.

The high and low temperature recuperators, HTR and LTR, respectively, each operate with S-CO_2 on both sides of the heat exchanger. The precooler, on the other hand, uses S-CO_2 on the hot side and H_2O from the ultimate heat sink on the cold side. In particular, cycle efficiency is sensitive to the effectiveness of both the recuperators and

precooler [20]. The hydraulic characteristics of the heat exchangers are also of interest because pressure drops must be considered in the task of detailed cycle optimization [28].

As S-CO_2 is a working fluid in the STAR-LM system, past studies on supercritical fluids have been studied. In the next section, supercritical fluids such as S-CO_2 and water will be discussed.

2.2. Supercritical Fluid

The critical point of a fluid is defined as a point where the difference between the vapor and liquid disappears [11]. The region above the critical point is called a supercritical phase as shown in Figure 2.1. The upper right region defines the supercritical state. The critical point of CO_2 is at 30.98^{o}C and 7.38MPa.

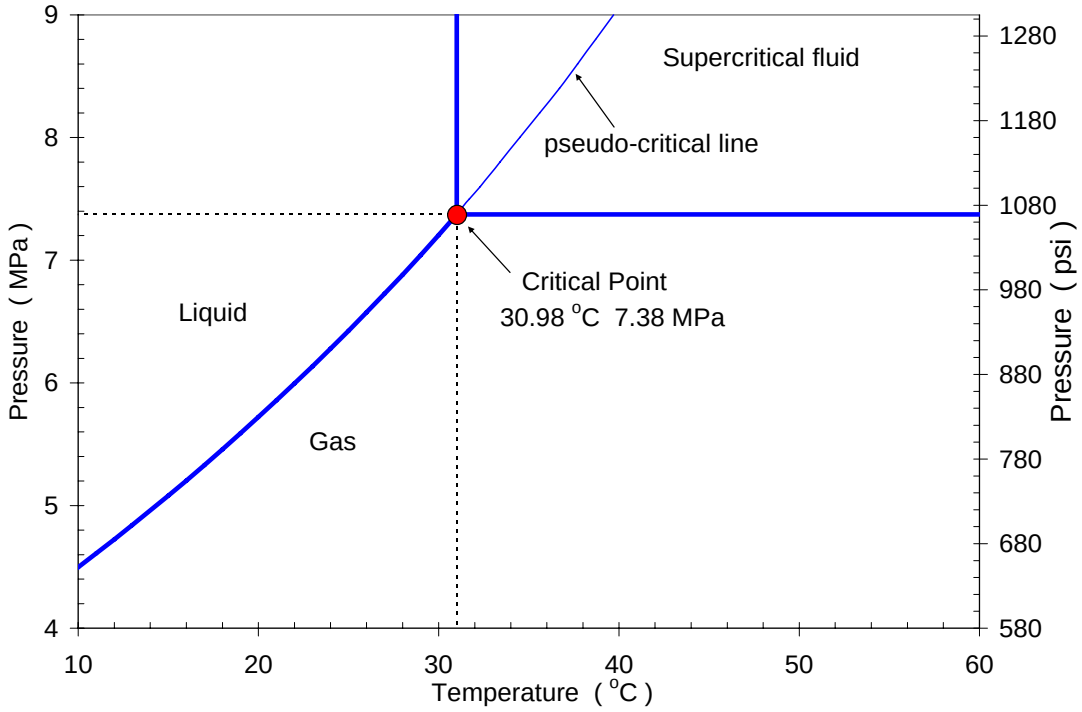

Figure 2.1 P-T diagram of CO_2

In supercritical phase, the fluid cannot be defined to be in a liquid state or gas state. In supercritical region, the pseudocritical temperature is the most interesting factor because thermophysical properties change dramatically. In the optimization of the STAR-LM system by Moisseytsev, these properties were considered to achieve the highest efficiency. For each supercritical pressure, the value of temperature at which the specific heat capacity reaches a peak value is called the pseudocritical temperature. Supercritical fluids have unique changes in thermoproperties near the pseudocritical temperature. When bulk temperature decreases below the pseudocritical temperature, the supercritical fluid changes from a gas-like state to a liquid-like state. As such, heat transfer studies in the supercritical region have been carried out, both experimentally and theoretically by a number of investigators. Although there are a number of heat transfer studies with pure substances and refrigerants, we will primarily concentrate on CO_2 unless other fluids contribute to the purpose of this work.

Sabersky et al. [30] investigated forced convection heat transfer of CO_2 at near the critical point with an electrically heated flat plate. They showed that the forced convection heat transfer coefficient of CO_2 near the critical point became large as the fluid temperature approached the pseudocritical point. Huai [6], J. Pettersen [28], and Wood et al. [34] showed that for horizontal convection flow, the heat transfer also changes with specific heat change. In other words, the heat transfer begins increasing below the pseudocritical point; reaches a peak value at, and then decreases beyond the pseudocritical point at the given pressure as the temperature increases.

A number of correlations for heat transfer of supercritical fluids have been established theoretically and experimentally. Bringer et al. [3] proposed a correlation for supercritical water up to 34.5MPa and also for a CO_2:

$$Nu_x = C\,\mathrm{Re}^{0.77}\,\mathrm{Pr}_w^{0.55}$$

where subscript w means wall, C=0.0266 for water and C=0.0375 for CO_2.

McAdams [19] proposed use of the much quoted Dittus and Boelter equation for forced convective heat transfer in turbulent flows and at supercritical pressures:

$$Nu_b = 0.0243\,\mathrm{Re}_b^{0.8}\,\mathrm{Pr}_b^{0.4}$$

where subscript b means “bulk”.

Swenson et al. [33] studied heat transfer to supercritical water in smooth-bore tubes. They showed that the conventional correlations did not work well because of rapid changes in themophysical properties of supercritical water near the pseudocritical point.

Liao et al. [14, 15] investigated heat transfer from S-CO_2 in horizontal micro circular tubes cooled to a constant temperature. Stainless steel tubes having diameters of 0.70, 1.40, and 2.16mm were used at pressures from 74 to 120bar, temperatures from 20°C to 110°C, and mass flow rates from $\dot{m}$ = 0.02 to 0.2kg/min, and Reynolds numbers from Re=10^4 to 2×10^5. They presented a correlation for horizontal flow for the circular tubes of d=0.70, 1.40, and 2.16mm as follows.

$$Nu_b = 0.124\,\mathrm{Re}_b^{0.8}\,\mathrm{Pr}_b^{0.4}\left(\frac{Gr}{\mathrm{Re}_b^2}\right)^{0.203}\left(\frac{\rho_w}{\rho_b}\right)^{0.842}\left(\frac{\overline{c_p}}{c_{p,b}}\right)^{0.384}$$

The maximum relative error between the above correlation and the experimental data is about 21.8%. The experiment result shows that the previous conventional correlation for normal size tubes cannot predict the heat transfer coefficient in microchannels.

Pettersen et al. [29] investigated heat transfer and pressure drop characteristics of S-CO_2 in 0.79 mm microchannel tubes at pressures of 81, 91, and 101bar under cooling conditions. The results showed that the closer temperature is to the pseudocritical point, the higher the peak heat transfer coefficient. The heat transfer coefficient changed along with specific heat at each pressure. The heat transfer coefficient increases as the pressure approaches the critical pressure of CO_2 (73.8bar).

2.3. Micro and zigzag channels

Plate heat exchangers with wavy or zigzag channels provide excellent heat transfer performance as evaporators and condensers in small refrigeration system [13]. For compactness, a printed circuit heat exchanger also employs zigzag microchannels where the hydraulic channel sizes between 0.1 mm and 2mm are defined as microchannels [10]. Zigzag microchannels elongate the heat exchange length within heat exchangers to facilitate heat transfer. Past investigations have shown different trends in heat transfer and flow regimes between traditional and microchannel based heat exchangers. For example, Peng, X. F. et al. [25] studied flow characteristics in a rectangular microchannel with the hydraulic diameters of D_h= 0.133~0.367 mm. They found that the transition from laminar flow occurs at about Re=300 and the transition to the fully turbulent flow regime at about Re=1000. They showed that the heat transfer and flow characteristics were affected by the geometric parameters experimentally. They found that there was an optimum channel size when the width to height ratio is 1/2 or 2.

Wang and Peng et al. [27] studied forced convection of water and methanol in rectangular channels. They claimed that the heat transfer could be predicted by a modification of the Dittus-Boelter equation by modifying the experimental constant from 0.023 to 0.00805:

$$Nu = 0.00805\,\mathrm{Re}^{4/5}\,\mathrm{Pr}^{1/3}$$

In their experiment, liquid temperature, velocity and microchannel size changed the transition and laminar heat transfer behavior in microchannels. It was shown that at a given liquid temperature and velocity, transition to turbulent heat transfer occurs at lower Re, as the channel size becomes smaller. The transition is initiated at about Re=1000~1500, which is small compared with the conventional size channels.

Similar experiments using microchannels were conducted by Adams et al [1]. They investigated single-phase forced convection in circular microchannels with diameters, D= 0.76 and D=1.09 mm. They calculated heat transfer coefficients and Nusselt numbers for water. The results were compared with predicted values calculated using a correlation for traditional channels. The correlation is the following:

$$Nu = \frac{(f/8)(\mathrm{Re}-1000)\,\mathrm{Pr}}{K + 12.7(f/8)^{1/2}(\mathrm{Pr}^{2/3}-1)}$$

where $K = 1.07 + (900/\mathrm{Re}) - [0.63/(1+10\,\mathrm{Pr})]$, and $f = (1.82\log(\mathrm{Re}) - 1.64)^{-2}$.

Adam's experimental results were larger than the predicted values because the Gnielinski's correlation could not explain the enhancement in heat transfer by the decrease of the microchannel size. They showed that enhancement in heat transfer increased as the channel diameter decreased.

Peiyi et al. [24] investigated the flow friction and heat transfer of gases flowing through microchannels and observed that the convective flow heat transfer characteristics departed from conventional channels. They showed that the friction factors were above those obtained from the traditional Moody chart and that the transition from laminar to turbulent flow occurred much earlier, at Reynolds numbers of about 400~900 due to the roughness of channels.

The published literatures also contain several studies on zigzag channels and wavy channels. These channel configurations have been used for compactness and to generally increase the heat transfer path length. O'Brien et al. [23] investigated forced convection heat transfer coefficients and friction factors for flow in a corrugated duct with corrugation angle of 30 degrees, width of 5.08 cm, and height of 0.508 cm. The Reynolds number ranged from 1500 to 25000. They showed, through flow visualization, a highly complex flow pattern including a strong forward flow and recirculating flow. Their study showed heat transfer enhancement with the corrugated duct flow relative to a conventional parallel-plate heat exchanger.

Y. S. Lee et al. [13] studied heat transfer in wavy channels. They showed that the laminar and the turbulent flow regimes in the corrugated channels are not distinguished as in circular pipes. That is, laminar flow for a circular straight channel may not be laminar in a wavy channel. In fact, they showed that the heat transfer does not change in both laminar and turbulent regimes for channel width less than 30 mm, while the distinction is more apparent in wider channels.

Jiao et al. [9] studied the flow resistance and heat transfer in a zigzag duct. They showed that the critical Reynolds number laminar flow to turbulent flow transition is

about 100 to 150. Also, heat transfer experiments for various zigzag ducts and plate heat exchangers evidently revealed no generalized dimensionless correlation for zigzag channels. They proposed correlations based on experimentally measured Reynolds and Prandtl numbers.

2.4. Printed Circuit Heat Exchanger

One type of compact heat exchanger that is under consideration to serve as a recuperator and precooler is a PCHE [17]. A PCHE consists of stacked plates with each plate chemically-etched with microchannels; the plates are then diffusion bonded.

In fact, Moisseytsev [20] showed a comparison of 9 heat exchanger designs for the STAR-LM LFR concept: 1) stacked U-tubes heat exchanger, 2) U-tubes heat exchanger, 3) concentric tubes heat exchanger, 4) straight tubes heat exchanger, 5) straight annuli heat exchanger, 6) helical coil heat exchanger, 7) plate type heat exchanger with U-turn, 8) counter flow plate type heat exchanger, and 9) printed circuit heat exchanger. A compact heat exchanger design such as a PCHE was indeed much smaller than traditional heat exchanger types. However, basic heat transfer data to evaluate the PCHE's performance, under reactor-relevant conditions, are lacking. Further its performance level in an actual power plant is uncertain.

The only other published work using the PCHE with S-CO_2 are works by Ishizuka et al. [8]. Their PCHE unit was rated at 3kW as compared to our 17.5kW.

Ishizuka et al. [8] conducted thermal hydraulic tests with a 3kW Heatric heat exchanger using CO_2. The hot and cold side pressures ranged between 2~4MPa (20~40bar) and 6~11MPa (60~110bar), respectively, with fluid temperatures between 110^{o}C and 280^{o}C. The CO_2 on the cold side was in many cases supercritical (critical point at 7.38MPa, 30.98^{o}C) though all tests were carried out far from the pseudocritical region where there are sharp changes in fluid properties with temperature. The effectiveness (η) of the heat exchanger was found to be very high, ~99%, for all test cases. Pressure loss and heat transfer coefficients correlated well with Reynolds number and there were no notable differences between subcritical and supercritical conditions. The average heat transfer coefficient increased with the CO_2 pressure.

CHAPTER 3 - Test Loop

Figure 3.1 and 3.2 are schematics of the present experimental loop. The loop is located at ANL. The test apparatus consists of a closed CO_2 loop and a water line in an open loop. The CO_2 loop consists of a pump, a flow meter, an electrically heated pipe section (1m), two pressure meters, the Printed Circuit Heat Exchanger rated at 17.5kW, a pressurizer, 9 K-type thermocouples, two platinum RTDs (Resistance Temperature Detectors) an accuracy of $\pm 0.1^{o}C$, a CO_2 reservoir tank, a helium reservoir tank. For this study, the helium reservoir tank was not used. The water line consists of a flow meter, pressure meter, and two platinum RTDs.

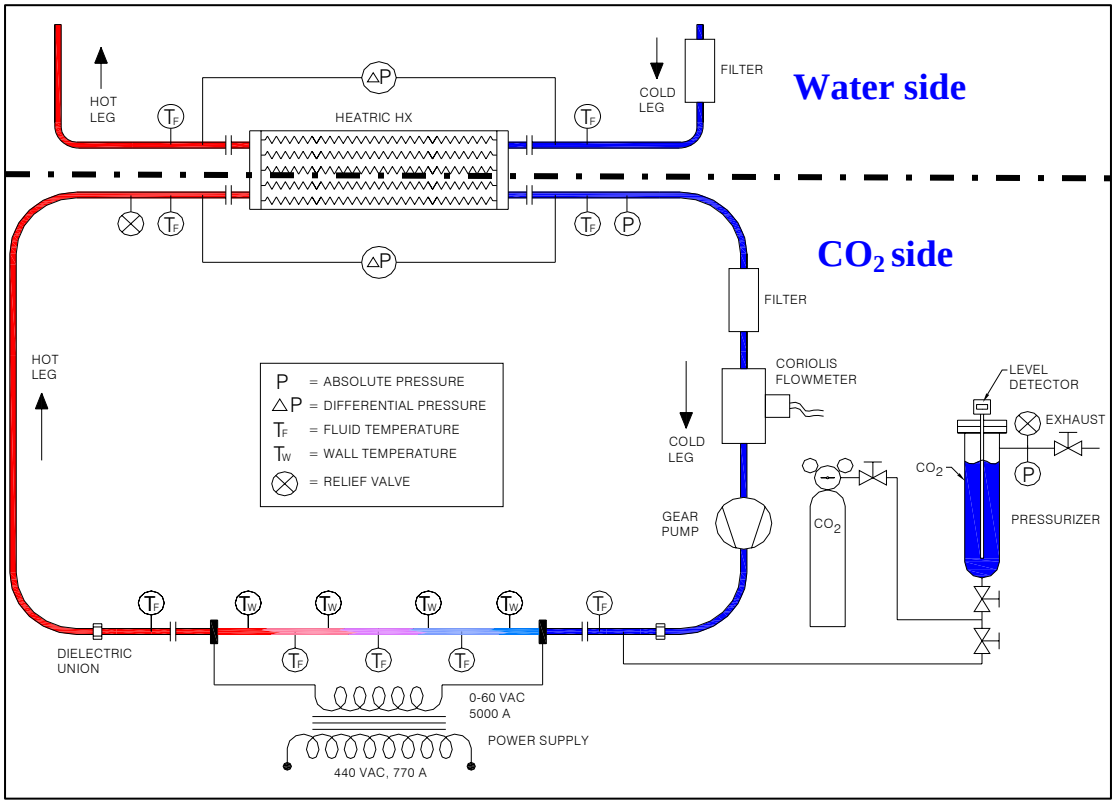

Figure 3.1 2-D picture of the experimental loop

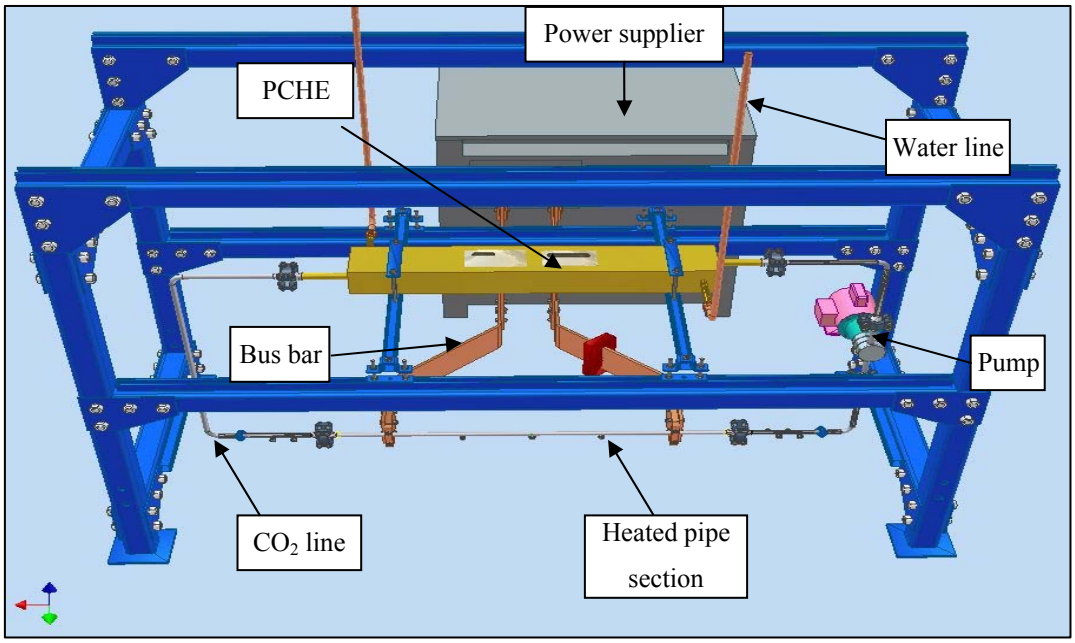

Figure 3.2 3-D picture of the experimental loop

3.1. Printed Circuit Heat Exchanger (PCHE)

The Printed circuit heat exchanger (PCHE) is a compact heat exchanger manufactured by Heatric. In comparing the PCHE against conventional heat exchangers of the same duty, the PCHE is up to 85 % smaller than the equivalent shell and tube heat exchanger [5] as shown in Figure 3.3.

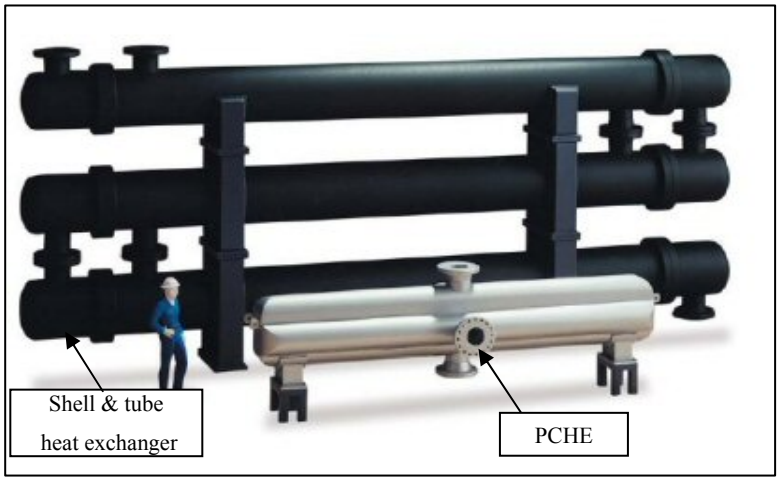

Figure 3.3 Comparison a PCHE with a shell and tube heat exchanger [5]

The heat exchange path is created by chemically etching the flow path on metal sheets (Stainless steel 316) as shown in Figure 3.4(a). The plates are joined one by one through the method of diffusion bonding as shown in Figure 3.4(b). The diffusion bonding process forms bonds at the molecular level under high pressure and temperature. The diffusion bonding generates continuity between sheets so that contact resistance is eliminated and thus effective heat transfer promoted. Figure 3.4(c) shows the grain growth between surfaces of etched plates.

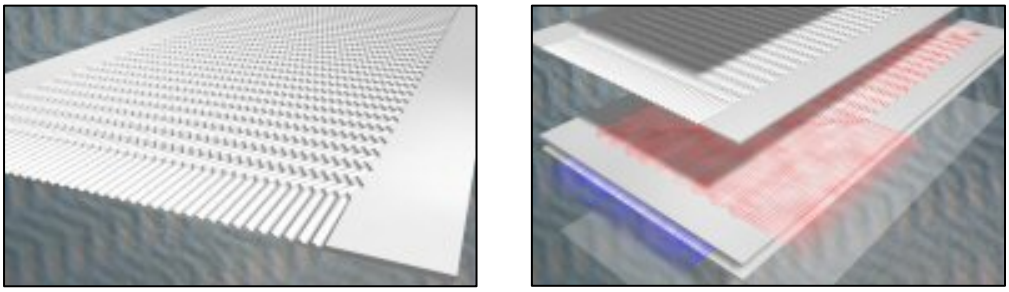

(a) Etched plate (b) Stacked plates

(c) Micrograph of a PCHE

Figure 3.4 The details of a PCHE [5]

The PCHE for this study is rated for a maximum pressure of 21.6MPa for the hot channel and 8.3MPa for the cold channel. The unit measures 120×200×1200mm, weights 203kg, and has a heat exchange capacity of 17.5kW. Figure 3.5 shows a top down view of the unit. This compact heat exchanger is designed for the test between high and low pressure streams of S-CO_2, but in order to benchmark its performance, the PCHE was tested here with water and S-CO_2 as the heat transfer media. Additional details of PCHE

are provided in Table 3.1. The unit has the same hydraulic diameter, 0.92mm, volumetric capacity, 2 liters, and heat transfer area, 5.6m^2 on both the hot and cold sides as quoted in Table 3.1.

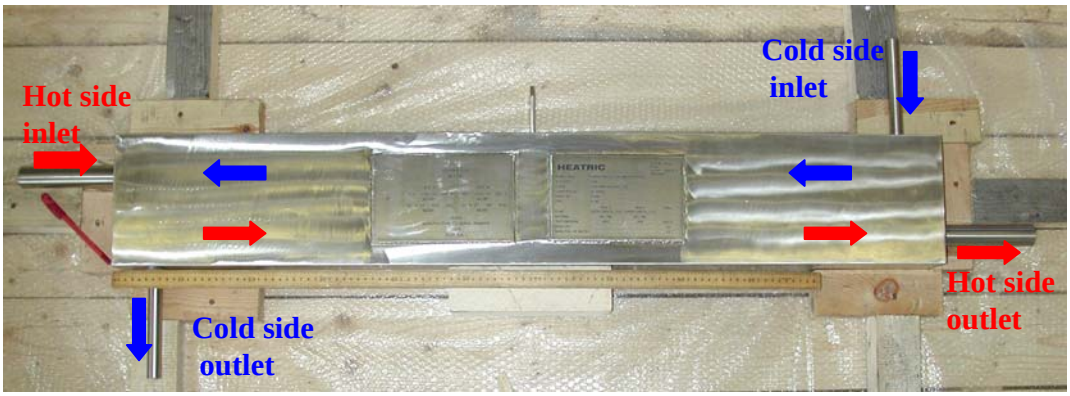

Figure 3.5 The picture of the PCHE

Table 3.1 Design specifications for PCHE

	Hot side	Cold side
Design pressure (bar)	83	216
Design temperature (^{o}C)	200	200
Flow area (mm^2)	1047	930
Number of channels	1176	1050
Hydraulic diameter (mm)	0.92	0.92
Capacity (liters)	2	2
Total heat transfer area (m^2)	5.6	
Total mass (kg)	203	
Dimensions (mm)	120 x 200 x 1200	

3.2. Heating system

The CO_2 in the primary loop is heated via electrical resistance heating by direct current through the one meter section of the horizontal pipe as shown in Figure 3.1 and 3.2. Figure 3.6 shows the power supply and copper bus bar. The copper bus bars provide the electrical connection between the power supply and the pipe section. The capacity of the power supply is 300kW. The CO_2 is heated as it flows through the pipe section. The electrical resistance has a maximum temperature limit of 538^{o}C. To protect the experimental loop, this loop automatically shuts down when the wall temperature inside the pipe section exceeds 538^{o}C. The temperature of the pipe section can be controlled by controlling the power output of the power supply.

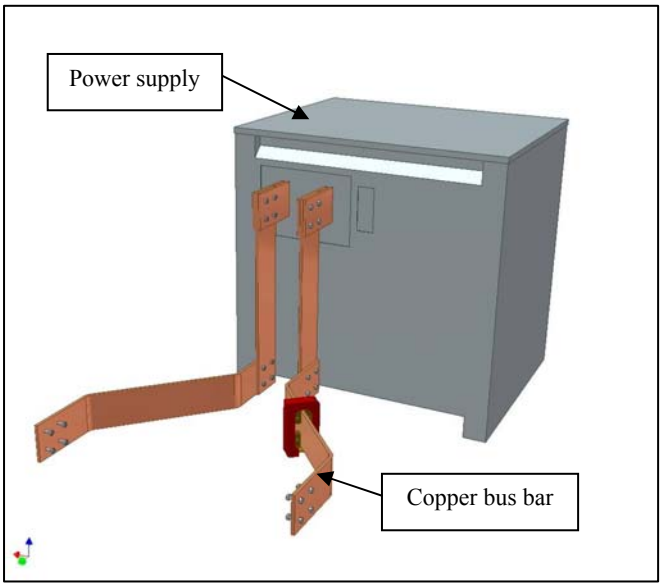

Figure 3.6 The power supply and the copper bus bars

3.3. Cooling system

3.3.1. Heat sink

When the experiment is conducted, water is the working fluid on the cold side and exchanges heat with the hot side. The water is supplied from a water tank located in the basement of the experimental room. The maximum flow rate of the water is 4gpm (0.25

L/sec). Two valves are connected with the hot water line and the cold water line as shown in Figure 3.7. The temperature of the water through the loop can be controlled by adjusting the valves that vary the volumetric flow rate of hot and cold water in the supply.

Also, cold water is provided to cool the power supply. The used water is dumped through a drain. Figure 3.7 shows a picture of the water valves and drain line.

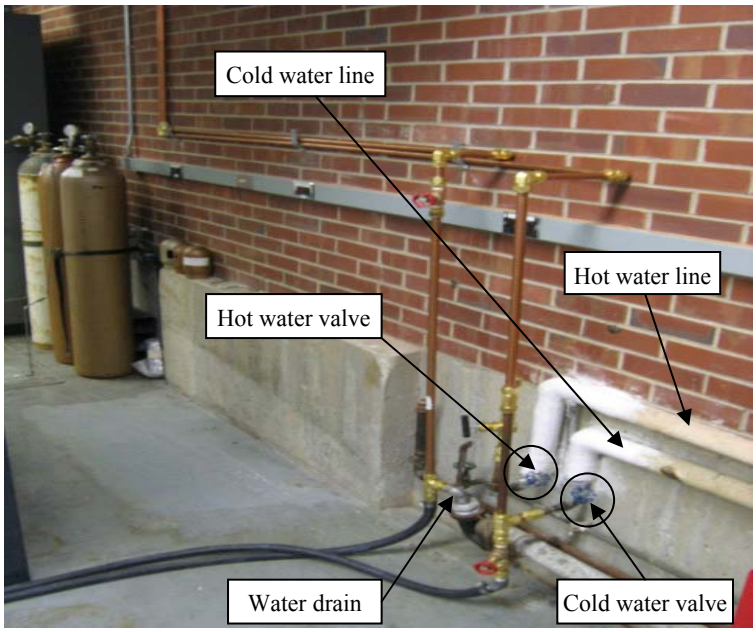

Figure 3.7 The water controller and water lines

3.2.2. Cooling

Prior to the experiment, the CO_2 line was first filled into the intended loop from the CO_2 reservoir tank. If the CO_2 loop pressure on filling did not reach the targeted pressure, we need to increase the loop pressure. The experimental loop as built does not have a booster pump, so we had to improvise a way to reach the targeted pressure of the CO_2 loop. In order to charge the loop to higher pressure, we cool the CO_2 loop. As the CO_2 cools, the pressure of the CO_2 decreases correspondingly. Subsequently, as the loop attains a lower pressure, we can add more CO_2 just using the CO_2 reservoir tank.

In order to cool down CO_2, water was used as a coolant. The temperature of water from the water tank was about 20^{o}C. It was not cold enough to cool down the CO_2. So, using a tube in the tube heat exchanger manufactured by Parker Hannifin as shown in Figure 3.8, water from the water line was cooled down by a coolant (ethylene glycol) from a chiller (a GCI Icewagon chiller). Then, the cooled water flowed into the PCHE to cool CO_2 as described above.

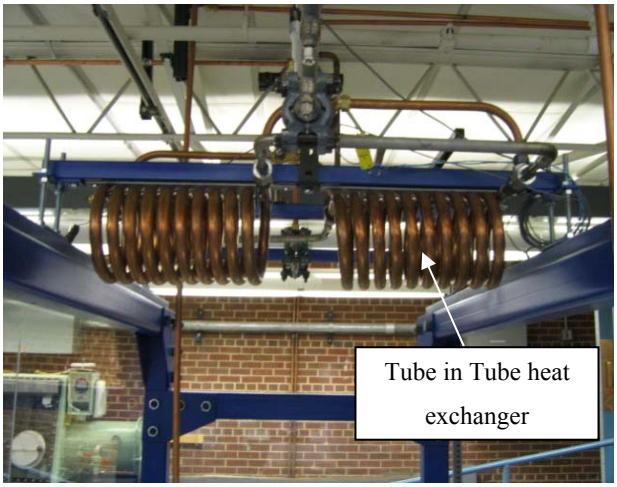

Figure 3.8 The tube-in-tube heat exchanger

A GCI Icewagon chiller (Model DE8AC by GCI Refrigeration Technology, Inc.) was used. This chiller had a 25 kW cooling capacity rating at 10% solution of ethylene glycol in water. Figure 3.9 shows the chiller.

Figure 3.9 GCI Icewagon chiller

3.4. Pump and Motor

A magnetic drive gear pump (Micropump model 10K pump) circulates the CO_2 through the CO_2 loop. The pump is made out of stainless steel 316 with PPS (Ryton) gears, carbon bearings, and PTFE O-ring, close coupled to a 3/4 horsepower TEFC (Totally Enclosed, Fan Cooled) motor. The motor speed is controlled by a variable frequency drive. Figure 3.10 shows the magnetic drive gear pump and the 3/4 horse power TEFC motor. The pump was installed between the flow meter and the inlet of the electrically heated pipe section on the hot side.

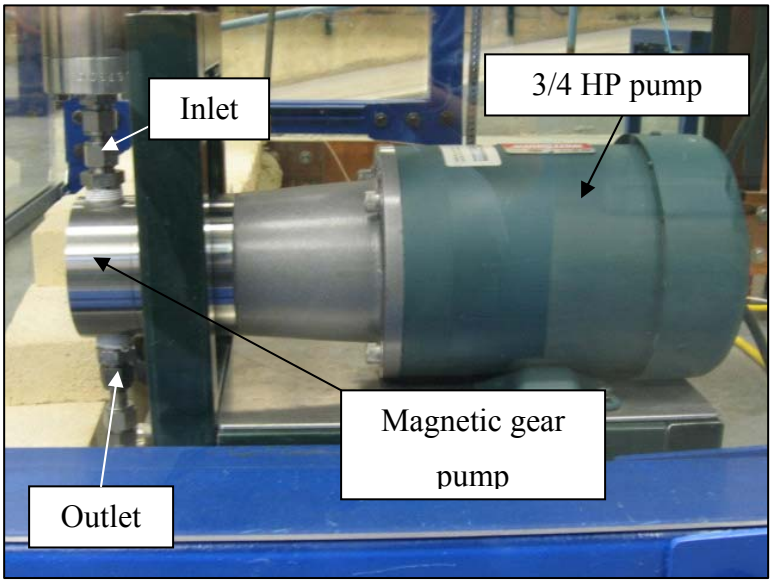

Figure 3.10 The magnetic gear pump and the TEFC motor

3.5. Pressurizer

We found early through trial experimental runs that the loop with S-CO_2 was very sensitive to small changes in parameters such as temperature and pressure. The pressurizer shown in Figure 3.11 accommodates thermal expansion of CO_2 as it is heated from room temperature to the critical point and beyond. The pressurizer dampens CO_2 pressure fluctuations that might occur. The pressurizer is constructed from 3", schedule

40 pipe and is fitted with a level sensor. The CO_2 level within the pressurizer is measured by a Mercap capacitance sensor manufactured by Milltronics Process Inc. It measures the sensor capacitance relative to that of a reference electrode. The measurement range is 0-500mm Hg with an accuracy of 0.1% of the measured value and a temperature rating up to 200^{o}C.

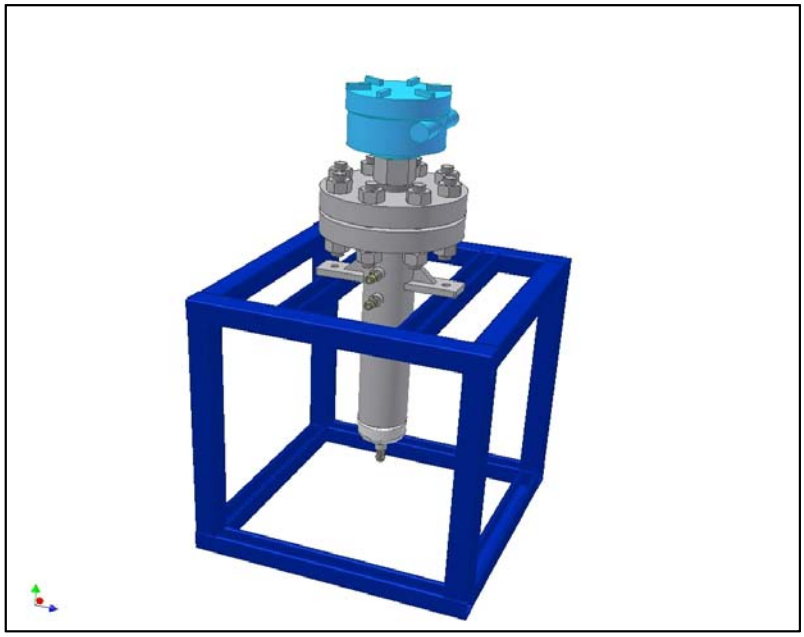

Figure 3.11 Pressurizer

3.6. Flow meter

A PROline Promass 80M Coriolis mass flow meter manufactured by Endress-Hauser was used to measure the mass flow of CO_2 on the hot side. The flow meter has an accuracy of ±0.50%. This flow meter was operated independently of the physical fluid properties, such as viscosity and density. Its maximum temperature limit was 350^{o}C, and pressure limit, 350bar. The flow meter was installed after the heat exchanger and before the gear pump because the focus of the test was the state of the CO_2 after the compact heat exchanger as shown in Figure 3.12. For this reason, the Coriolis flow meter was used to measure the mass flow of CO_2.

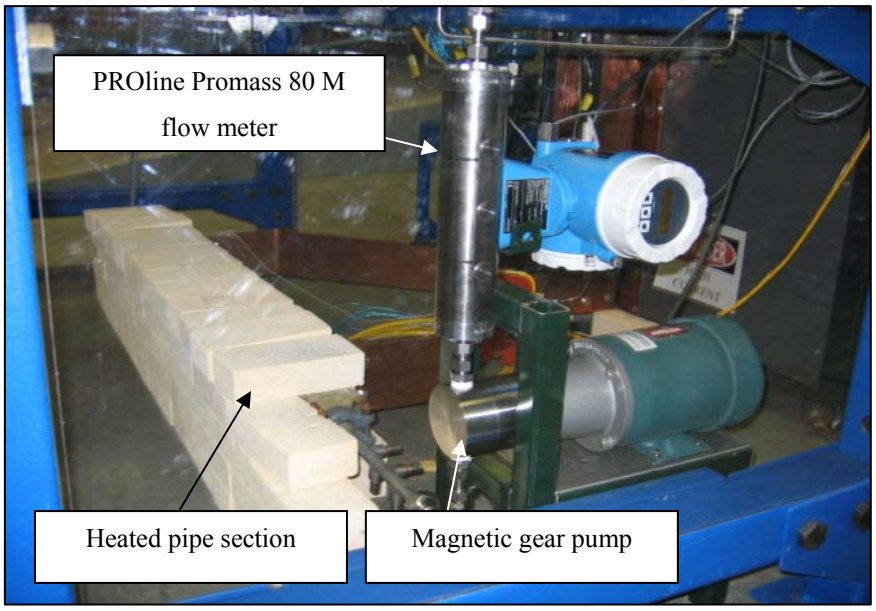

Figure 3.12 CO_2 flow meter

On the water side, a paddlewheel flow meter (OMEGA® FP7001A) was installed just before the three way valve. The flow meter measured the inlet water flow rate. A picture of the flow meter is shown in Figure 3.13. The flow meter had an accuracy of ±2%.

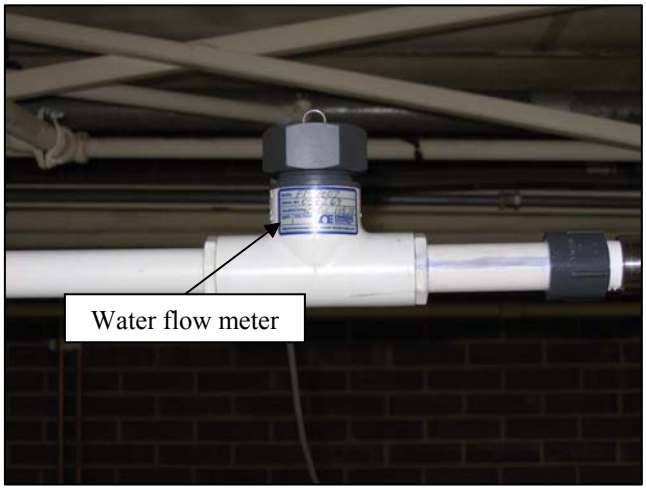

Figure 3.13 Water flow meter

3.7. Differential pressure transmitter

Absolute and differential pressures were measured using a Rosemount Model 2088 and 3051CD pressure transmitters manufactured by Rosemount Inc. In this experiment, we judged the stead state of experimentation based on the absolute pressure. We defined that if CO_2 pressure fluctuate within 0.01bar, experimental data can be in steady state. Differential pressures were measured on both hot and cold sides with 3051 CD pressure transmitters. The absolute pressure within the loop and pressurizer was measured with 2088 pressure transmitter. The additional specifications of pressure transmitters are given in Table 3.2.

Table 3.2 Pressure transmitters

Model	2088	3051
Accuracy	± 0.10 %	± 0.065 %
Weight	2.44 lb (1.11 kg)	6.0 lb (2.72 kg)
Dimension	3.9 x 5.0 x 5.4 in (99 x 127 x 137 mm)	6.4 x 3.2 x 7.8 in. (163 x 81 x 198 mm)

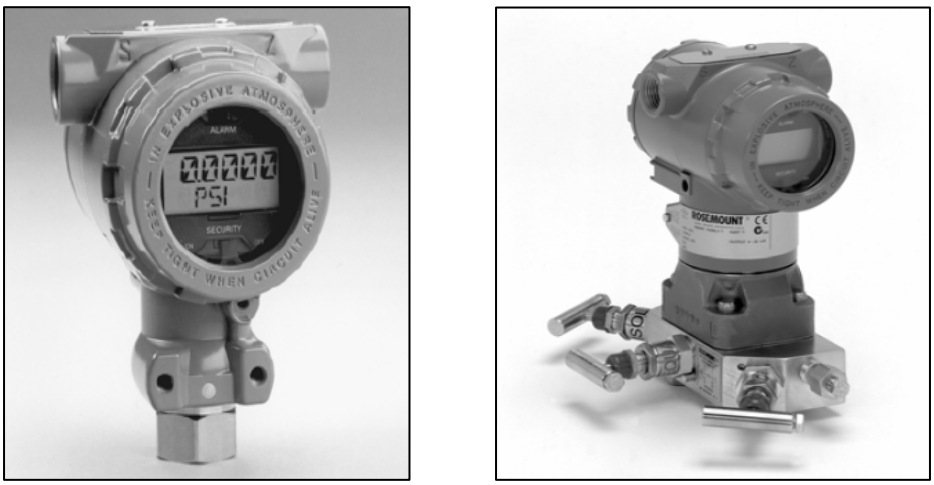

Figure 3.14 Rosemount Model 2088 and 3051 pressure transmitter

3.8. Data acquisition System

All data acquisition and process control tasks are managed by a PC executing LabVIEW 6.i under Windows 2000. Sensors are connected to HP Model E1345A 16-channel multiplexer and the signals are digitized by an HP Model E1326B 5 1/2 digit multimeter. Figure 3.15 shows the data acquisition system and control panel. In the control panel, temperature is observed and controlled.

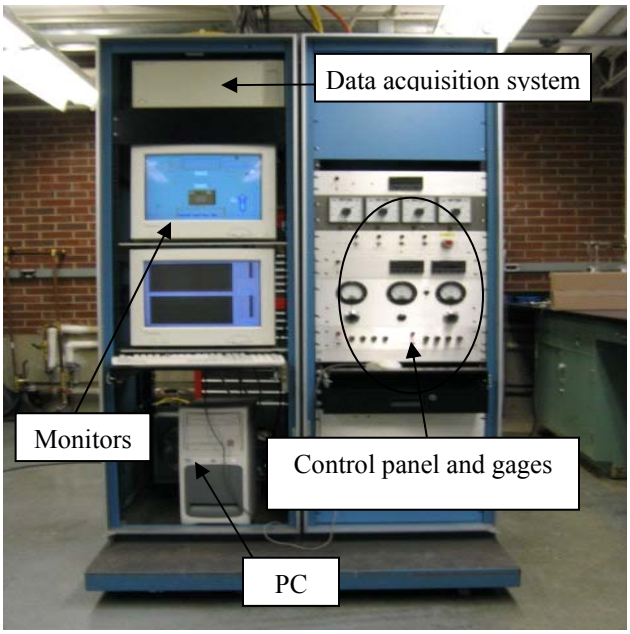

Figure 3.15 Data acquisition system and control panel

CHAPTER 4 - Estimate of the Printed Circuit Heat Exchanger Internal Configuration

4.1. Zigzag angle

One of the primary objectives of this study was to measure the heat transfer coefficient of S-CO_2 in the prototype PCHE at ANL. To study the PCHE, the specifications of the PCHE were verified first. In fact, under the contract with Heatric, the detailed design of the heat exchanger was proprietary information and thus the heat exchanger could not be opened and inspected. Without all of the detailed heat exchanger dimensions, analyses of experimental data were not possible. However, Heatric provided a partial list of specifications. Table 4.1 shows the selected overall dimensions of the PCHE provided by Heatric. Table 4.2 subsequently depicts additional specifications provided by Heatric.

Table 4.1 Design specifications for PCHE from Heatric

	Hot side	Cold side
Design pressure (bar)	83	216
Design temperature (^oC)	200	200
Flow area (mm^2)	1047	930
Number of channels	1176	1050
Hydraulic diameter (mm)	0.92	0.92
Capacity (liters)	2	2
Total heat transfer area (m^2)	5.6	
Total mass (kg)	203	
Dimensions (mm)	120 x 200 x 1200	

Table 4.2 Test results provide by Heatric

	SERVICE PER ITEM		hot SIDE				cold SIDE				Rev
1	FLUID CONDITIONS		In		Out		In		Out		
2	Fluid		Super Critical CO2				Super Critical CO2				
3	Flow rate, total	kg/hr	353				543				
4	Flow rate, gas/vapour	kg/hr	353		353		543		543		
5	Flow rate, liquid	kg/hr	0		0		0		0		
6	Temperature	°C	84.0		178.0		181.0		85.0		
7	Design temp: max/min	°C	200 / 0				200 / 0				
8	Pressure: inlet/design	barg	201.0 / 216.2				74.0 / 82.5				
9	Pressure drop: calc/allwd	bar	0.07 / 0.25				0.24 / 0.25				
10	FLUID PROPERTIES		Liq	Vap	Liq	Vap	Liq	Vap	Liq	Vap	
11	Density	kg/m³	-	573.0	-	286.0	-	94.0	-	140.0	
12	Specific heat	J/kg K	-	2608	-	1445	-	1127	-	1373	
13	Viscosity	cP	-	0.0450	-	0.0310	-	0.0240	-	0.0200	
14	Thermal conductivity	W/mK	-	0.0620	-	0.0420	-	0.0320	-	0.0270	
15	Dew point	°C									
16	CONNECTIONS										
17	No. of nozzles		1		1		1		1		
18	Nozzle size	mm NB	15 NB		15 NB		25 NB		25 NB		
19	Flange class		--		--		--		--		
20	Max strainer aperture	microns	260				260				
21	MATERIALS										
22	Nozzle material		SS 316/316L		SS 316/316L		SS 316/316L		SS 316/316L		
23	Flange material		SS 316/316L		SS 316/316L		SS 316/316L		SS 316/316L		
24	Header material		-		-		-		-		
25	Header belt material		-		-		-		-		
26	Core material		SS 316/316L								
27	THERMAL DESIGN										
28	Design heat load	kW	17.5		LMTD	°C	1.8				
29	Corrected TD	°C	4.2		Fouling allowance	%	0				
30	Overall htc, clean	W/m²K	754		Oversizing	%	1				
31	Area provided	m²	6		Area required, clean	m²	6				
32	MASS & SIZE										
33	Mass: dry/operating/test	kg	202 / 203 / 206 [2]								
34	Core dimensions	mm	196 x 1196 x 119 [2]								

Since details such as heat transfer length (path), zigzag angle and related parameters were not provided, we had to first check these parameters associated with the flow zigzag flow configuration of the PCHE using Table 4.1 and Table 4.2. First, we calculated the diameter of the hot side channel using the hydraulic diameter (D_h= 0.92mm), defined as follows [26],

$$D_h = \frac{4 \cdot A_c}{P} = 0.92mm \tag{1}$$

In Equation 1, A_c is the cross-sectional area of the channel, P is the perimeter of the channel, and D_h is the hydraulic diameter.

Considering that the cross sectional shape of the channel was semicircular as seen in Figure 4.1, the diameter of the channel can be calculated using the hydraulic diameter as shown below.

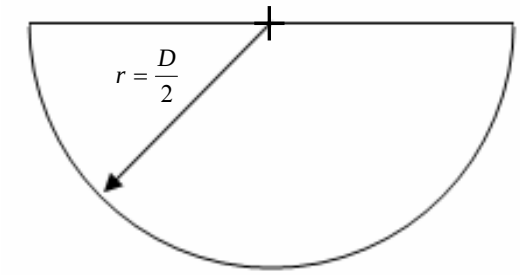

Figure 4.1 The cross section shape of the channel

Using the equation for hydraulic diameter and Figure 4.1, the diameter, D, of the channel is calculated as 1.5057 mm. Using the diameter, the free flow area of the hot side can be estimated using Equation 2.

$$\begin{aligned} Flow\ area &= No.\ of\ \ channels \times Area\ of\ \ one\ channel \\ &= 1176 \times \frac{1}{2} \cdot \frac{\pi \cdot (1.5057mm)^2}{4} \\ &= 1047mm^2 \end{aligned} \tag{2}$$

The calculated free flow area is same as that specified in Table 4.1. With the calculated diameter 1.5057 mm, and the channel length, the zigzag angle can be estimated.

First, the length of the hot side channel can be calculated using Equation 3.

$$Volume\ \ of\ \ channels = Length of\ \ channel \times Flow\ Area of\ \ channels \tag{3}$$

Rearranging Equation 3 yields Equation 4, which can be used to solve for the length of the hot side channel. The volume of the channels is taken from Table 4.1.

$$Travel\ length = \frac{Volume\ of\ channels}{Flow\ Area\ of\ channels}$$
$$= \frac{2\ liters}{1047 mm^2} \tag{4}$$
$$= 1.91\ m$$

The travel length is the length over which the working fluid flows in the body of the heat exchanger. This length is related to the overall length of the heat exchanger, 1.2m as well as the zigzag angle. From the heat exchanger geometry, shown in Figure 4.2, we can see that the hot side channels pass directly through the heat exchanger body. The cold side, however, has a right angle entry section which must be accounted for in the length calculation.

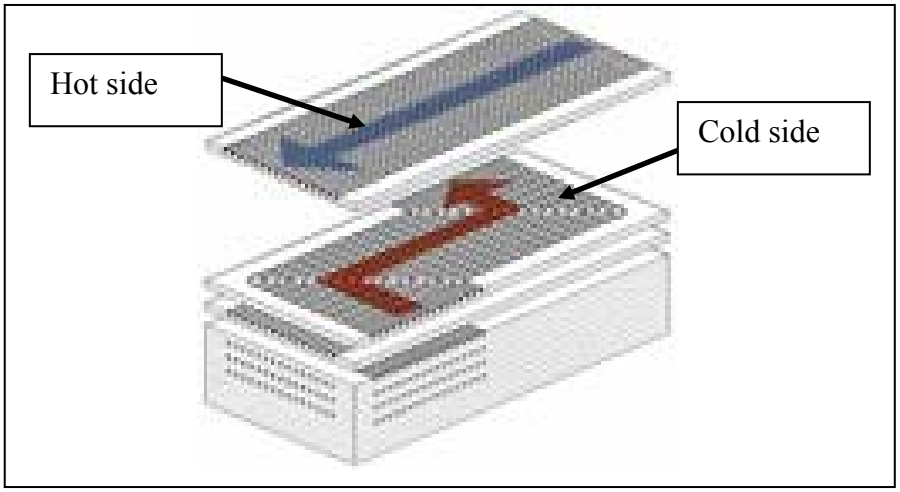

Figure 4.2 Microchannel structure of a PCHE

The hot side channel will be checked first because of its simple flow geometry, relative to cold side. The total hot side travel length can be compared to the heat exchanger body length, which allows calculation of the zigzag angle. This is shown in Figure 4.3, with the dotted line representing the heat exchanger body length and the red line representing the total fluid travel length. The whole channel can be divided into triangles as is shown in Figure 4.3.

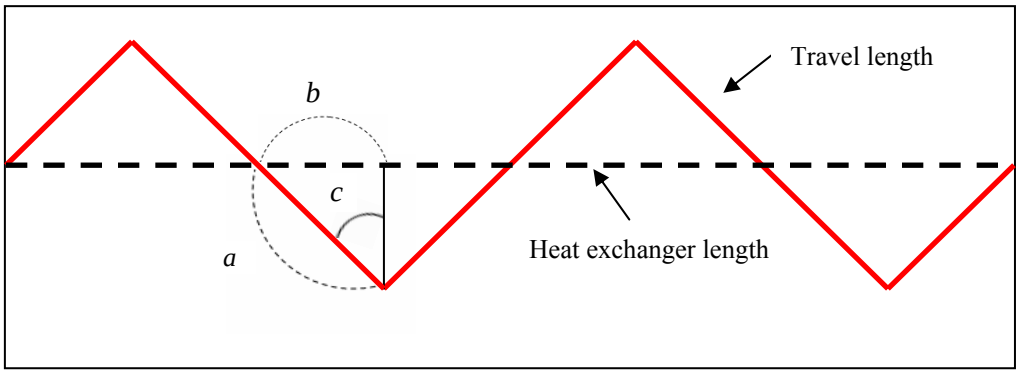

Figure 4.3 Simplified longitudinal channel shape

Along the zigzag channel, the zigzag angle, *c*, can be calculated using a simple geometric relationship. We can define the relationship with the lengths and angle as,

$$\sin c = \frac{b}{a} \tag{5}$$

If the hot side channel consists of *n* triangles as seen in Figure 5.3, the heat exchanger length and travel length of the hot side channel can be related by the expression,

$$Heat\ \ exchanger\ \ length = b \times n = 1.2\ m \tag{6}$$

$$Travel\ \ length\ \ of\ \ the\ hot\ side\ channel = a \times n = 1.91\ m \tag{7}$$

Using the values from Equations 6 and 7, the zigzag angle, c, can be calculated per Equation 8 as,

$$c = \sin^{-1}\left[\frac{b}{a}\right] = \sin^{-1}\left[\frac{1.2}{1.91}\right] = 38.9^{\circ} \tag{8}$$

Thus, the full zigzag angle of the hot side is double this value,

$$Zigzag\ \ angle\ of\ \ the\ hot\ side = c \times 2 = 78^{\circ} \tag{9}$$

Equations 1 to 9 can be applied to calculate the zigzag angle of the cold side as well. Most of all, the flow channel shape needs to be considered because the cold side has two right angle bends for the entry and exit regions, as shown in Figure 4.2. Figure 4.4 (a) is a schematic of the cold side channel used in calculating the cold side zigzag angle. Each channel is the same distance apart. Suppose that the channel is put into a grid, which is composed of squares, like Figure 4.4 (b). In this way, we can see that the length of each channel is the same as the solid line in Figure 4.4(b). From TiTech's printed circuit heat exchanger specification[8], we know that the cold and hot sides have the same length. In fact this length is also the heat exchanger length (0.89 m).

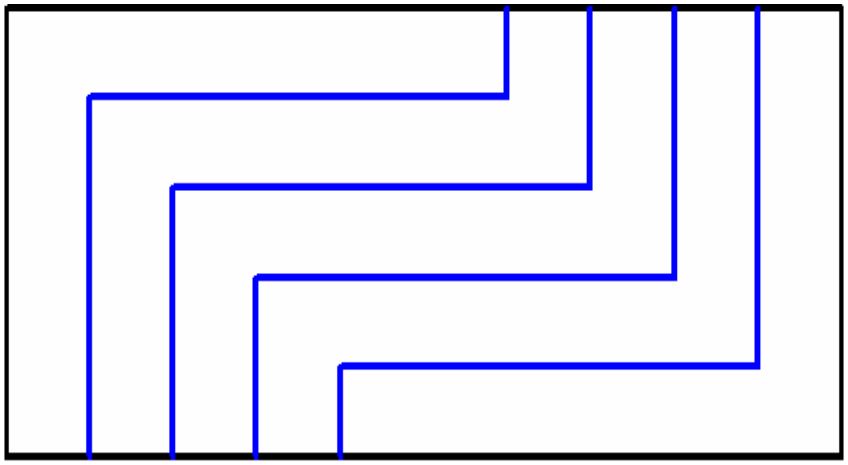

Figure 4.4 (a). The simplified cold channel of the PCHE

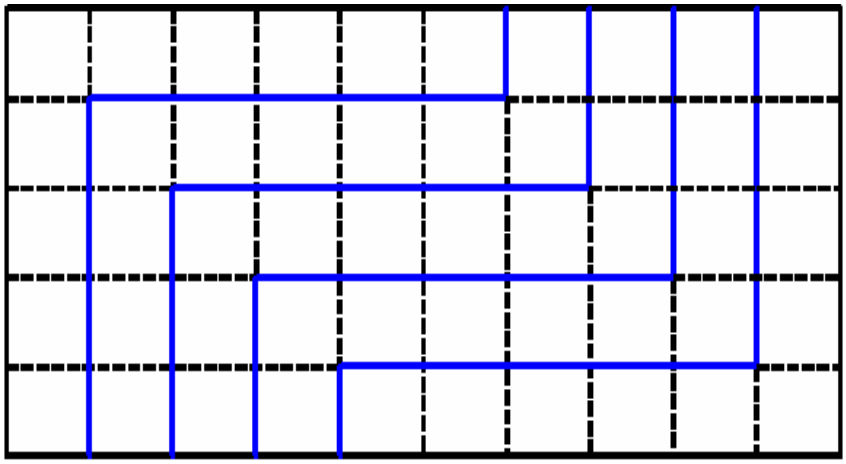

Figure 4.5 (b). The same size matrix with the simplified PCHE

Therefore, the assumption that the length of the cold channel is the same as that of the heat exchanger (1.2 m) is reasonable. Using Equations from 1 to 9 in the same manner as for the hot side, the zigzag angle of the cold side is calculated:

$$\text{Hydraulic diameter: } D_h = \frac{4 \cdot A}{P} = 0.92mm \tag{10}$$

$$\text{Cross sectional area: } A_c = \frac{1}{2} \cdot \frac{\pi \cdot D^2}{4} \tag{11}$$

$$\text{Perimeter of the channel: } P = \frac{\pi \cdot D}{2} + D = D \cdot (\frac{\pi}{2} + 1) \tag{12}$$

$$D_h = \frac{4 \cdot A_c}{P} = \frac{4 \cdot \frac{1}{2} \cdot \frac{\pi \cdot D^2}{4}}{D \cdot (\frac{\pi}{2} + 1)} = \frac{\pi \cdot D}{\pi + 2} = 0.92mm \tag{13}$$

Using Equation 13, the diameter of the cold side channel is calculated as 1.5057m which is the same as the hot side. The free flow area is,

$$\begin{aligned} Free\ flow\ area &= No.\ of\ channels \times Area\ of\ one\ channel \\ &= 1050 \times \frac{1}{2} \cdot \frac{\pi \cdot (1.5057mm)^2}{4} \\ &= 934mm^2 \end{aligned} \tag{14}$$

If we compare this to the cold side flow area, 930 mm^2, from Table 4.1 (provided by Heatric), we see that the calculated area is almost identical to Heatric's. The travel length of the cold side is 2.16m as shown below Equation 15.

$$\begin{aligned} Travel\ length &= \frac{Volume\ of\ channels}{Area\ of\ one\ channel} \\ &= \frac{2\ liters}{927mm^2} \\ &= 2.16\ m \end{aligned} \tag{15}$$

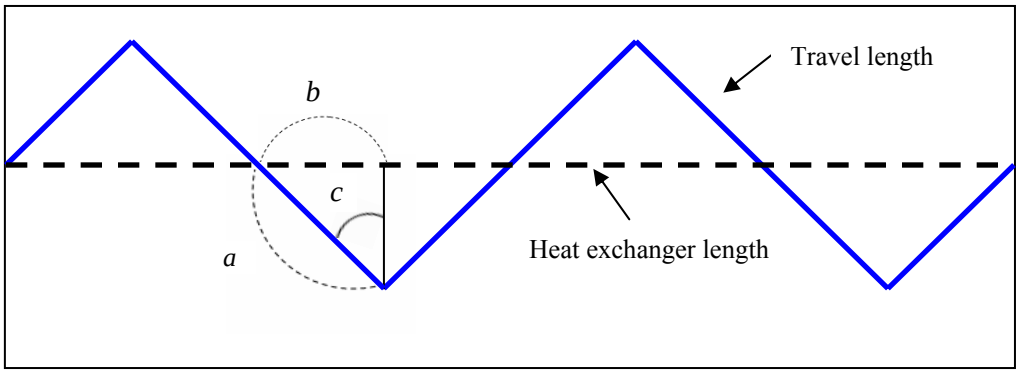

Figure 4.6 Simplified longitudinal channel shape of cold side

Per geometric relationship applied to the cold side, we estimate the cold side angle to be as follows,

$$\sin c = \frac{b}{a} \tag{16}$$

$$Heat\ exchanger\ length = b \times n = 1.2\ m \tag{17}$$

$$Travel\ length\ of\ the\ cold\ side\ channel = a \times n = 2.16\ m \tag{18}$$

$$c = \sin^{-1}\left[\frac{b}{a}\right] = \sin^{-1}\left[\frac{1.2}{2.16}\right] = 33.74\ ^{\circ} \tag{19}$$

$$Zigzag\ angle\ of\ the\ cold\ side = c \times 2 = 67.5\ ^{\circ} \tag{20}$$

Comparing the cold side with the hot side, the zigzag angle of the cold side (67.5^{o}) is slightly smaller than the hot side ($78\ ^{o}$).

The zigzag angles can be evaluated in another way. This method also starts from simple geometrical formulation. If the above zigzag angle is based on the volume of channels, another method is to base it on the heat transfer area. We can consider this method using TiTech's heat exchanger specification. In their case, they measured the interior flow channel configuration in detail. Table 4.3 provides TiTech's PCHE specification.

In Table 4.3, we consider heat transfer areas, hydraulic diameter, and the channel active length. The channel active length can be translated to the travel length.

Table 4.3 Geometry and configuration of TiTech's PCHE [8]

	Hot side channel	Cold side channel
Plate material	SS316L	SS316L
Plate thickness	1.63mm	1.63mm
Number of plates	144	66
Zigzag angle	115 ^{o}	100 ^{o}
Cross-sectional shape	Semicircle	Semicircle
Channel diameter	1.88mm	1.88mm
Hydraulic diameter	1.15 mm	1.15 mm
Heat transfer area	0.697m^2	0.356 m^2
Travel length	1000mm	1100mm
Plenum space length	49mm	46.5mm
Channel length	896mm	896mm

First, we need to calculate the diameter of channel using the hydraulic diameter, 1.15 mm, provided in Table 4.3 as,

$$D_h = \frac{4 \cdot A_c}{P} = \frac{4 \cdot \frac{1}{2} \cdot \frac{\pi \cdot D^2}{4}}{D \cdot (\frac{\pi}{2} + 1)} = \frac{\pi \cdot D}{\pi + 2} = 1.15mm \tag{21}$$

From Equation 1, we can verify that TiTech's PCHE has channel diameter, 1.88mm. Using this result and the number of channels, the cross sectional flow area is verified as 0.0002 m^2 and 0.000092 m^2 for the hot and cold sides respectively. Next, the travel length needs to be calculated with the diameter and heat transfer area of each side as,

$$\begin{aligned} &Heat\ Transfer\ Area \\ &= No.\ of\ \ channels \times Cross\ \text{sec}tional\ \ perimeter \times Travel\ length \end{aligned} \tag{22}$$

Equation 22 is rearranged with respect to the travel length,

$$Travel\ length = \frac{Heat\ Transfer\ Area}{No.\ of\ \ channels \times Cross\ \text{sec}tional\ \ perimeter} \tag{23}$$

For the hot side of TiTech's PCHE, the travel length is calculated using Equation 23,

$$\begin{aligned} &\textit{Travel length of the hot side} \\ &= \frac{\textit{Heat Transfer Area}}{\textit{No. of channels} \times \textit{Cross sectional perimeter}} \\ &= \frac{0.697m^2}{144 \times (1.88mm + \frac{1.88mm \times \pi}{2})} \\ &= 1.001m \end{aligned} \tag{24}$$

For the cold side,

$$\begin{aligned} &\textit{Travel length of the cold side} \\ &= \frac{\textit{Heat Transfer Area}}{\textit{No. of channels} \times \textit{Cross sectional perimeter}} \\ &= \frac{0.356m^2}{66 \times (1.88mm + \frac{1.88mm \times \pi}{2})} \\ &= 1.116m \end{aligned} \tag{25}$$

This calculated result is almost identical to the travel lengths (1.0m and 1.1m) of the hot and cold side given in Table 4. 3. So this method provides another means estimating interior channel configuration of our PCHE. The heat transfer area, diameter of channels, and the number of channels are given in Table 4.1. Following the same step from Equation 23, the travel length of each side is calculated as,

$$\begin{aligned} &\textit{Travel lengthof the hot side} \\ &= \frac{\textit{Heat Transfer Area}}{\textit{No. of channels} \times \textit{Cross sectional perimeter}} \\ &= \frac{5.6m^2}{1176 \times (1.5057mm + \frac{1.5057mm \times \pi}{2})} \\ &= 1.23m \end{aligned} \tag{26}$$

For the cold side,

$$\begin{aligned} &Travel\ length of\ the\ cold\ side \\ &= \frac{Heat\ Transfer\ Area}{No.\ of\ channels \times Cross\ sectional\ perimeter} \\ &= \frac{5.6m^2}{1050 \times (1.5057mm + \frac{1.5057mm \times \pi}{2})} \\ &= 1.378m \end{aligned} \tag{27}$$

These results are different from the results based on the heat exchanger volumetric capacity. The difference likely occurs from the plenum chamber just before and after the channel flow on each side. If a large fraction of the PCHE's volumetric capacity is the plenum chamber, the travel length based on the volumetric capacity would be shorter than the calculated result. Using the travel length results of each side and Equation 19, the plenum chambers and zigzag angles on each side are calculated. For the hot side,

$$\begin{aligned} &Plenum\ chamber\ volume \\ &= Total\ volumetric\ capacity\ of\ hot\ side\ channel \\ &\quad - Travel\ length \times No.\ of\ channels \times Cross\ sectional\ area \\ &= 2Liter - 1.23m \times 1176 \times \frac{1}{2} \cdot \frac{\pi \cdot (1.5057mm)^2}{4} \\ &= 0.712Liter \end{aligned} \tag{28}$$

$$c = \sin^{-1}\left[\frac{b}{a}\right] = \sin^{-1}\left[\frac{1.2}{1.23}\right] = 77.32^{\circ} \tag{29}$$

For the cold side in similar manner,

$$\begin{aligned} &Plenum\ chamber\ volume \\ &= Total\ volumetric\ capacity\ of\ cold\ side\ channel \\ &\quad - Travel\ length \times No.\ of\ channels \times Cross\ sectional\ area \\ &= 2Liter - 1.378m \times 1050 \times \frac{1}{2} \cdot \frac{\pi \cdot (1.5057mm)^2}{4} \\ &= 0.712Liter \end{aligned} \tag{30}$$

$$c = \sin^{-1}\left[\frac{b}{a}\right] = \sin^{-1}\left[\frac{1.2}{1.378}\right] = 60.55^{\circ} \tag{31}$$

One more thing should be considered. We assumed that the straight channel length is identical to the heat exchanger length. In order for more accurate calculation, we need to think about the plenum size before and after channels. For this step, we use TiTech's PCHE dimension. They opened the heat exchanger and then measured most of inside dimensions. They also measured the plenum length along the hot and cold sides. Their heat exchanger has a hot and cold side arrangement opposite to the ANL PCHE. In our case, the cold side channel has a right bend, but TiTech's PCHE has a right bend on the hot side. When the same method for calculating the zigzag channel is applied to TiTech's PCHE with the plenum length, the result is as follows.

For the hot side,

$$c = \sin^{-1}\left[\frac{b}{a}\right] = \sin^{-1}\left[\frac{(896-49)mm}{1000mm}\right] = 57.89^{\circ} \tag{32}$$

For the cold side,

$$c = \sin^{-1}\left[\frac{b}{a}\right] = \sin^{-1}\left[\frac{(896-46.5)mm}{1100mm}\right] = 50.56^{\circ} \tag{33}$$

So the zigzag angles of TiTech's PCHE are 115.77^{o} and 101.11^{o} on the hot and cold side, respectively. The relative error is 0.67 % and 1.1 %, respectively, on the hot and cold side. Therefore, the portion of the plenum length to the whole heat exchanger length should be considered.

It is very difficult to estimate the plenum size of our PCHE with the heat exchanger specification provided by Heatric. For these reasons, the plenum lengths of TiTech's heat exchanger wree used. For this calculation, the plenum length of 46.5mm and 49 mm were used for the hot and cold side respectively.

For the hot side,

$$\begin{aligned} c &= \sin^{-1}\left[\frac{b}{a}\right] \\ &= \sin^{-1}\left[\frac{(1200-46.5)mm}{1230mm}\right] \\ &= 69.69^{\circ} \end{aligned} \tag{34}$$

For the cold side,

$$c = \sin^{-1}\left[\frac{b}{a}\right]$$
$$= \sin^{-1}\left[\frac{(1200-49)mm}{1378mm}\right] \quad (35)$$
$$= 56.64^{\circ}$$

From the calculation, the full zigzag angles of ANL's PCHE are 139.38^{o} and 113.28^{o}, respectively, for the hot and cold side with considering the plenums. Without the plenum length, the full zigzag angles are 154.64^{o} and 121.10^{o} for the hot and cold side respectively. Although we could not estimate the zigzag angles using TiTech PCHE's plenum length, we will use the estimated zigzag angles, 139.38^{o} and 113.28^{o} because a PCHE is manufactured by stacking metal plates thus the plenum length of our PCHE might be similar to TiTech's PCHE. These calculated dimensions will be used in the data analysis.

4.2. Heat transfer area and wall thickness of metal wall

Table 4.2 provided by Heatric is the test between CO_2/CO_2 in the same heat exchanger as ANL. Using this table, the results such as Reynolds numbers, Fanning friction factors and energy balance were recalculated. Without the heat exchanger specification shown in Table 4.1, one can measure the some data such as temperature, pressure, flowrate, and pressure drop. Without accurate information about the interior dimensions of the PCHE, it is not possible to analyze the data recorded and obtain useful results for such parameters as, friction factor, temperature distribution, and heat transfer coefficient. To check the heat exchanger dimensions, the test results in Table 4.4 will be recalculated to verify the following dimensions: the heat transfer area, free flow area, and thickness of the metal wall between the hot and cold channels.

Table 4.4 Reynolds number provide by Heatric

	Cold side		Hot side	
Re	Inlet	Outlet	Inlet	Outlet
	2150	3100	5500	6600
j factor	0.0076	0.0075	0.0121	0.0101

The Reynolds number is defined as,

$$\mathrm{Re} = \frac{Du\rho}{\mu} = \frac{D}{\mu}\frac{\dot{m}}{(Free\ \ flow\ area)} \tag{36}$$

Using this formula, the Reynolds number on each side can be calculated using the data and dimensions provided by Heatric. First, we will calculate the Reynolds number at the hot side inlet as follows,

$$\begin{aligned}\mathrm{Re} &= \frac{D_h u\rho}{\mu} \\ &= \frac{(0.92mm)(10^{-3}\frac{m}{mm})}{(23.87\mu\mathrm{Pa\ s})(10^{-6}\frac{1}{\mu})}\frac{543\frac{kg}{hr}}{(3600\frac{s}{hr})}\frac{1}{(1047mm^2)(10^{-6}m^2/mm^2)} \\ &= 5522\end{aligned} \tag{37}$$

This value is almost the same as the value given by Heatric, Re=5500. The relative error is 0.4%. Due to the fact that our calculations are very close to the values presented by Heatric, it is reasonable to assume that our calculated values for hydraulic diameter and free flow area are correct. As another check, the Reynolds number at the hot side outlet is calculated as,

$$\begin{aligned}\mathrm{Re} &= \frac{D_h u\rho}{\mu} \\ &= \frac{(0.92mm)(10^{-3}\frac{m}{mm})}{(20\mu\mathrm{Pa\ s})(10^{-6}\frac{1}{\mu})}\frac{543\frac{kg}{hr}}{(3600\frac{s}{hr})}\frac{1}{(1047mm^2)(10^{-6}m^2/mm^2)} \\ &= 6626\end{aligned} \tag{38}$$

Comparing this result to the Heatric's, Re=6600, the relative error is 0.4 %. So we can conclude that the hydraulic diameter is indeed 0.92 mm and the free flow area 1047mm^2 on the hot (CO_2) side. Next, the dimension of the cold side needs to be checked. In the same way, the Reynolds number of the inlet is calculated with the dimensions provided by Heatric as,

$$\begin{aligned}\mathrm{Re} &= \frac{D_h u \rho}{\mu} \\ &= \frac{(0.92mm)(10^{-3}\frac{m}{mm})}{(45\mu\mathrm{Pa\ s})(10^{-6}\frac{1}{\mu})}\frac{353\frac{kg}{hr}}{(3600\frac{s}{hr})}\frac{1}{(930mm^2)(10^{-6}m^2/mm^2)} \\ &= 2155\end{aligned} \tag{39}$$

The relative error here is 0.2 % (Re=2150). At the outlet of the cold side,

$$\begin{aligned}\mathrm{Re} &= \frac{D_h u \rho}{\mu} \\ &= \frac{(0.92mm)(10^{-3}\frac{m}{mm})}{(31\mu\mathrm{Pa\ s})(10^{-6}\frac{1}{\mu})}\frac{353\frac{kg}{hr}}{(3600\frac{s}{hr})}\frac{1}{(930mm^2)(10^{-6}m^2/mm^2)} \\ &= 3129\end{aligned} \tag{40}$$

The relative error is 0.9 % (Re=3100). Through these calculations, we can assume the hydraulic diameter of both the hot and cold side channels is 0.92 mm. We can also assume that the free flow areas of the channels are 1047 and 930 mm^2 for the hot and cold side, respectively.

The *j* factors were provided by Heatric as shown in Table 4.4. Using *j* factor, the overall heat transfer coefficient can be calculated because the heat transfer coefficient of each side can be calculated using the *j* factor and also the overall heat transfer coefficient can be calculated by the energy balance in the heat exchanger and by the equation as,

$$\frac{1}{U \cdot A} = \frac{1}{h_h \cdot A} + \frac{L}{k \cdot A} + \frac{1}{h_c \cdot A} \tag{41}$$

where U, h_h, h_c, k, A, and L are respectively the overall heat transfer coefficient, the heat transfer coefficient of hot and cold side, the conductive heat transfer coefficient, the heat transfer area and the metal wall thickness.

Using Equation 41, the metal wall thickness between the hot and cold channels can be verified. The *j* factor is the modified Stanton number that takes into account the moderate variations in the fluid with the fluid Prandtl number. It is defined as,

$$j = St \cdot \mathrm{Pr}^{2/3} = \frac{Nu}{\mathrm{Re}} \cdot \mathrm{Pr}^{-\frac{1}{3}} \tag{42}$$

The Colburn *j*-factor is nearly independent of the flowing fluid for 0.5<Pr<10, under laminar to turbulent flow conditions. The j factors in the each inlet and outlet are provided by the Heatric. They measured the overall heat transfer using the same PCHE as ANL. The Nusselt number of each side is calculated using the Colburn factors as,

$$Nu = j \cdot \mathrm{Re} \cdot \mathrm{Pr}^{-\frac{1}{3}} \tag{43}$$

Also, the convection heat transfer coefficient of each part can be calculated from the Nusselt numbers per Equation 43.

$$h = \frac{Nu \cdot k}{D_h} \tag{44}$$

where k is the thermal conductivity.

Using the above equations with the properties of the CO_2 shown in Table 4.2, the convection heat transfer coefficient of each inlet and outlet can be calculated. The results are shown in Table 4.5.

Table 4.5 Convection heat transfer coefficient provide by Heatric

	h (W/m^2K)	h_{avg} (W/m^2K)
A inlet(hot side)	2167	1813
A outlet	1459	
B inlet(cold side)	1374	1417
B outlet	1460	

As the overall coefficient is given by Heatric in Table 4.2, we can check the conduction heat transfer coefficient of the metal wall. The thickness of the metal wall needs to be estimated because the information about the metal wall was not provided. First of all, let's look at the overall heat transfer equation. It is defined per Equation 38.

The overall heat transfer coefficient of the PCHE is given to be 754 W/m^2 K as shown in Table 4.2. So we can substitute the heat transfer coefficient values into Equation 41 as,

$$\frac{1}{754} = \frac{1}{1813} + \frac{1}{1417} + \frac{L}{k} \tag{45}$$

and it thus follows that,

$$\frac{L}{k} = 0.00006897 \tag{46}$$

According to Table 4.2, the heat exchanger is made of stainless 316. Its thermal conductivity is 14.6W/m·K at 20 ~ 100^{o}C. So the thickness of the metal wall is estimated to be,

$$\begin{aligned} L &= 0.00006897 \cdot k \\ &= 0.00006897 \cdot 14.6 \\ &= 0.001[m] \\ &= 1[mm] \end{aligned} \tag{47}$$

Considering that TiTech's PCHE has a measured wall thickness of 0.69 mm. The calculated thickness of the metal sheet is thought to be reasonable.

Lastly we checked the total heat transfer area using Table 4.2. From the table, the total heat transfer area, overall heat transfer coefficient, and temperature difference are taken to be as 5.6m^2, 754W/m^{2}K, and 4.2^{o}C respectively. Using these values, the heat transfer capacity can be calculated as,

$$\begin{aligned} q &= U \cdot A \cdot \Delta T_{lm} \\ &= 754\ W/m^2K \times 5.6\ m^2 \times 4.2\ K \\ &= 17.73\ kW \end{aligned} \tag{48}$$

Also, we can calculate the heat transfer rate using the energy balance equation on the hot and cold side. First, on the hot side, the heat transfer rate is calculated:

$$\begin{aligned} q &= \dot{m} \cdot (h_{in} - h_{out}) \\ &= 353 kg/hr \times (567.5 - 388.0) kJ/kg \\ &= 17.60\ kW \end{aligned} \tag{49}$$

And on the cold side,

$$\begin{aligned} q &= \dot{m} \cdot (h_{in} - h_{out}) \\ &= 543 kg/hr \times (620.6 - 505.1) kJ/kg \\ &= 17.42\ kW \end{aligned} \tag{50}$$

Comparing the calculated heat transfer rates above, the above calculation shows that the overall heat transfer area is 5.6 m^2. The estimated uncertainty is 1.8 % (0.1m^2) based on 5.6 m^2.

Based on the calculations detailed above, the values listed by Heatric can be assumed to be correct and will be used in further calculations. Table 4.6 shows the checked and calculated dimension of the PCHE. These values will be used for the calculation and for data analysis.

Table 4.6 Dimension of the PCHE

	Hot side	Cold side
Flow area (mm^2)	1047	930
Number of channels	1176	1050
Travel length (m)	1.23	1.378
Zigzag angles	139.38 ^{o}	113.28 ^{o}
Channel diameter (mm)	1.5	1.5
Total heat transfer area (m^2)	5.6	
Thickness of metal wall (mm)	1	

4.3. Consideration of the metal wall between channels

In the previous section, the interior configuration and dimensions of the PCHE were estimated using heat exchanger specifications provided by Heatric. We also made use of information regarding TiTech's heat exchanger. The thickness of the metal wall was calculated in the previous section. However, this value cannot be verified because of the limited dimensions of the PCHE provided by Heatric. Thus, in this chapter, we will evaluate the thermal resistance of the metal wall.

According to the PCHE specification quoted by Heatric, the printed circuit heat exchanger is made of the 316 SS (stainless steel). The properties of the 316 SS are shown in Table 4.7.

Table 4.7 The properties of Stainless Steel 316

Grade	Density (kg/m^3)	Thermal Conductivity (W/m·K)		Specific Heat 0~100°C (J/kg·K)
		At 25°C	At 100°C	
316/L/H	8000	13.4	16.3	500

By comparison, the thermal conductivities of water and CO_2 are 0.017 and 0.61W/m·K; the SS316 has much larger thermal conductivity. If the thickness of the metal wall is very thin and thermal conductivity large, the thermal resistance in the metal wall can be neglected in our analysis. In order to estimate the temperature drop between the hot and cold side channels, two assumptions are made, as follows:

1. The maximum thickness of the metal wall is estimated based on TiTech's PCHE. They measured their configuration directly. Figure 4.6 is the cross sectional shape of TiTech's heat exchanger. We will assume that our PCHE has the same ratio of the thickness of the metal wall to the diameter of the channel as TiTech's PCHE.
2. The thermal conductivity is 13.4W/m·K for the present calculation.

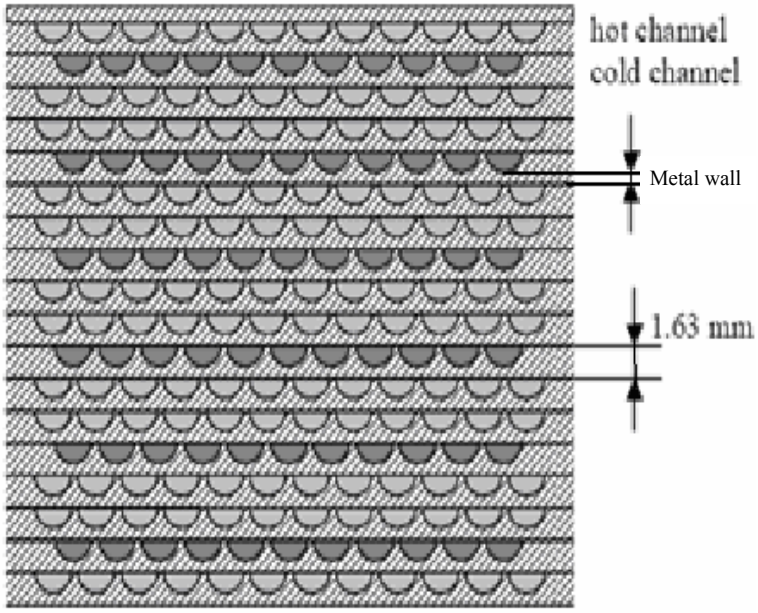

Figure 4.7 Sectional area of TiTech's PCHE [8]

Table 4.8 The specification of TiTech's heat exchanger [8]

	hot channel	cold channel
Plate material	SS316L	SS316L
Plate thickness, mm	1.63	1.63
Number of plates	12	6
Number of channels	144	66
Flow channel bending angle, degree	115	100
Horizontal pitch, mm	4.50	3.62
Pitch of right angle to flow direction, mm	2.97	3.25
Flow channel configuration	semi-circle	semi-circle
Wall width, mm	0.60	0.70
Channel width, mm	1.90	1.80
Channel depth, mm	0.90	0.90
Hydraulic diameter of channel, mm	1.15	1.15
Heat transfer area, m^2	0.697	0.356
Cross sectional area of channel, m^2	0.00020	0.000092
Channel active length, mm	1000	1100
Inlet and outlet part length, mm	49.0	46.5
Channel length, mm	896	896

Using Figure 4.6 and Table 4.8, the thickness of the metal wall is calculated as shown in the following equations. First, the diameter of the metal wall is calculated as below,

$$A_c = \frac{1}{2} \cdot \frac{\pi \cdot D^2}{4} \tag{51}$$

$$P = \frac{\pi \cdot D}{2} + D = D \cdot (\frac{\pi}{2} + 1) \tag{52}$$

$$D_h = \frac{4 \cdot A_c}{P} = \frac{4 \cdot \frac{1}{2} \cdot \frac{\pi \cdot D^2}{4}}{D \cdot (\frac{\pi}{2} + 1)} = \frac{\pi \cdot D}{\pi + 2} = 1.15mm \tag{53}$$

$$D = 1.88\ mm \tag{54}$$

where A_c is the cross sectional area, P is the perimeter of the cross section of the channel, D is the diameter of the channels, and D_h is the hydraulic diameter of the channels

So the thickness of the metal wall defined in Figure 5.1 can be calculated assuming that the cross section of the channel is semicircular. Thus,

$$\begin{aligned} L &= Plate\ thickness - \frac{The\ diameter\ of\ the\ channels}{2} \\ &= 1.63\ mm - \frac{1.88\ mm}{2} \\ &= 0.69\ mm \end{aligned} \tag{55}$$

where L is the thickness of the metal wall.

The ratio between the thickness and the diameter is:

$$\frac{L}{D} = \frac{0.69\ mm}{1.88\ mm} = 0.357 \tag{56}$$

So applying this ratio to our heat exchanger, the diameter of the channels is calculated to be 1.5 mm and the metal wall thickness is estimated to be,

$$L_{ANL} = 0.357 \times D = 0.357 \times 1.5\ mm = 0.54\ mm \tag{57}$$

So the maximum thickness of the metal wall is estimated to be 0.54 mm. With the above assumptions and result, the thermal resistance of the metal wall is defined as,

$$R_{t,wall} = \frac{L}{k \cdot A} \tag{58}$$

where $R_{t,wall}$ is the thermal resistance, L is the thickness of the metal wall, A is the heat transfer area, and k is the thermal conductivity.

Using Equation 58, we see that $R_{t,wall}$ varies according to the thickness, L. Note as well that the thermal resistance inversely influences the heat transfer coefficient. That is, $R_{t,wall}$ is the inverse of the product of overall heat transfer coefficient and the heat transfer area, that is, $U \cdot A$, such that:

$$R_{total} = \frac{1}{U \cdot A} = R_{t,wall} + R_{t,CO_2} + R_{t,H_2O} \tag{59}$$

In order to see how small $R_{t,wall}$ is, the R_{total} will be used, where R_{total} is one over the overall heat transfer coefficient.

To gauge the magnitude of $R_{t,wall}$ relative to R_{total}, the overall heat transfer coefficient from the experiment generated from the CO_2/water test was used and is shown in Table 4.9.

Table 4.9 A test condition of CO_2/water

Hot side				Cold side			U
p (bar)	$\dot{m}$ (kg/hr)	$T_{h,in}$ (^oC)	$T_{h,out}$ (^oC)	Q (gpm)	$T_{c,in}$ (^oC)	$T_{c,out}$ (^oC)	(W/m^2K)
74.27	208.61	87.86	31.76	2.99	31.32	41.44	144

If the thermal resistance of the metal wall is very small relative to the total resistance, it can be neglected because the temperature drop across the metal wall is equally small. The thermal resistance of the metal wall is expressed as the ratio of $\frac{R_{t,wall}}{R_{total}}$. In this data, $\frac{R_{t,CO_2}}{R_{total}}$ and $\frac{R_{t,H_2O}}{R_{total}}$ are is 0.96 and 0.03, respectively. Figure 4.8 shows the ratio of the thermal resistance versus the metal wall thickness. As shown in Figure 4.8, $R_{t,wall}$ is very small in magnitude relative to the overall resistance to heat transfer. As the thickness of the wall decreases, the resistance to heat transfer rate decreases as well. Even at the maximum wall thickness of 0.54 mm, the fraction of the wall resistance to the total resistance is still small (up to 0.0005 %). Even if the thickness of the metal wall is 2mm (greater than the channel diameter), the thermal resistance of the metal wall is very small, about 0.002 %. This result shows that it is reasonable to neglect the metal wall between hot and cold channels in further analyses.

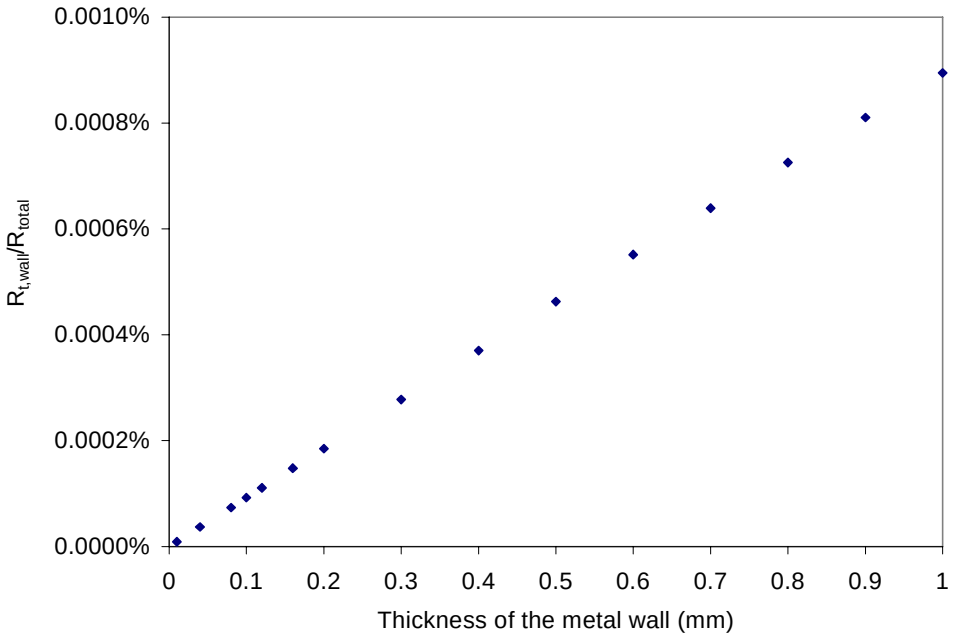

Figure 4.8 Ratio of the thermal resistance of the metal wall to the total resistance

CHAPTER 5 - Pressure drop

In many heat exchange applications, fluids need to be pumped through the heat exchanger because there is flow resistance through the heat exchanger and heat transfer generally increases with forced flow. In this study, the pressure drop across the flow configuration is important to check the similarity of the cold and hot side channel. It will be discussed later in this chapter. For this reason, the pressure drop in the heat exchanger is investigated. In general, the total pressure drop consists of an entrance region, heat exchanger core, and exit region pressure drops. They are linearly related as follows,

$$\text{Total pressure drop} = \text{Entrance effect} + \text{Core effect} + \text{Exit effect} \quad (1)$$

The core frictional pressure drop is the dominating term, about 90% or more of the Δp for gas flows in many compact heat exchangers [31]. The design of the Heatric PCHE is proprietary information, and thus the pressure drop cannot be calculated analytically because the internal channel geometry is not known. Therefore, the pressure drop must be measured experimentally to determine the hydraulic characteristics of the internal flow configuration. The hydraulic characteristics can be surmised by measuring the relationship between pressure drop and flow rate. For this study, both the hot and cold sides were tested with ambient pressure water at two different temperatures. The hot side was also tested with CO_2. The data was used to calculate pressure loss coefficients for each side using the equations below [7]. Because the friction factor is dependent on the flow configuration [31], we expect the friction factor will show the flow characteristics on both sides. Here, the Fanning friction factor and Moody (or Darcy) friction factor are defined as follows,

$$\text{Moody (or Darcy) friction factor: } f = \frac{D_h}{L}\left(\frac{\Delta P}{\frac{1}{2}\rho v^2}\right) \quad (2)$$

For fully developed laminar flow, the Moody friction factor is related to the Reynolds number as shown below [7].

$$f = \frac{64}{\mathrm{Re}_D} \tag{3}$$

For fully-developed turbulent flow in a circular tube with smooth surfaces, the Moody friction factor is experimentally correlated with the Reynolds number as follows [7].

$$f = 0.316 \cdot \mathrm{Re}_D^{-1/4} \qquad \mathrm{Re}_D \le 2 \times 10^4 \tag{4}$$

$$f = 0.184 \cdot \mathrm{Re}_D^{-1/5} \qquad \mathrm{Re}_D \ge 2 \times 10^4 \tag{5}$$

The Fanning friction factor is defined as follows,

$$\text{Fanning friction factor: } C_f = \frac{1}{4}\frac{D_h}{L}\left(\frac{\Delta P}{\frac{1}{2}\rho v^2}\right) \tag{6}$$

Pressure loss measurements with water were made over the full available flow rate range for water, from $\dot{m}$ = 105 to 1390 kg/hr. The temperature range of the water was from 20°C and 50°C. The tests were conducted for both the hot and cold sides. Figure 6.1 shows the Moody friction factor on both the hot and cold sides.

Pressure drop was also measured with CO_2 on the hot side. The pressure range of CO_2 was from 60bar to 80bar. The temperature was at 20°C. The mass flow rate was from 460 to 1700 kg/hr.

The pressure drop data using water on both the hot and cold side was reproduced in a form of the Moody friction factor by Equation 2.

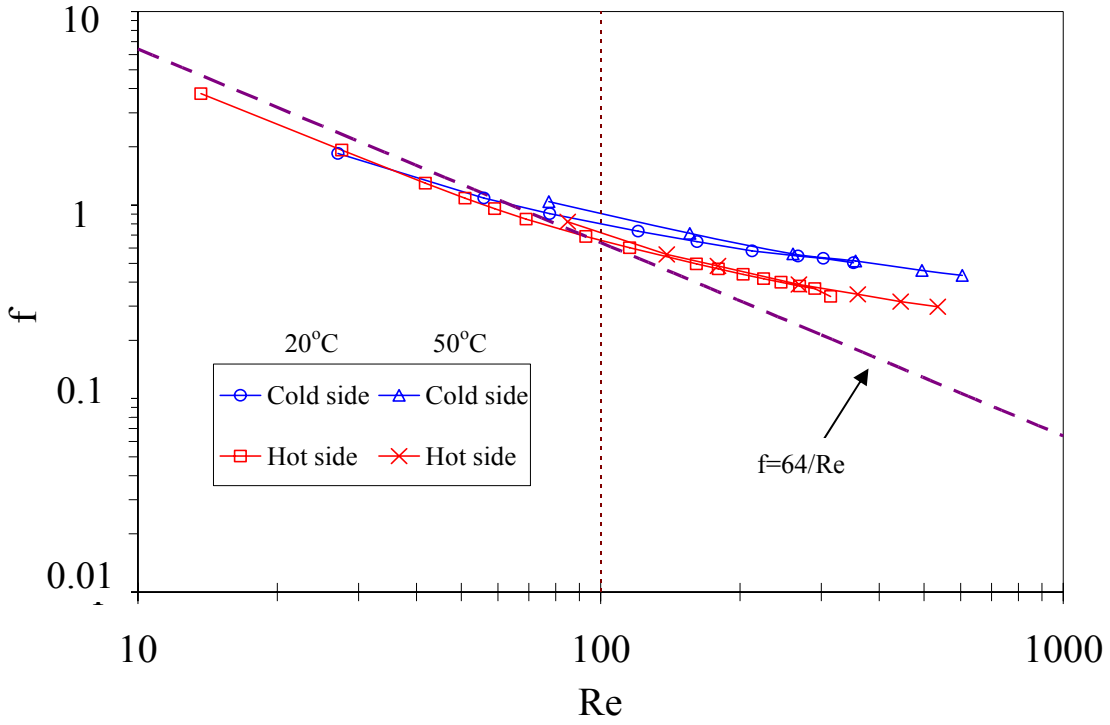

Figure 5.1 Moody friction factor with water on the hot and cold sides

Figure 5.1 shows the Moody (or Darcy) friction factor. The dotted line is for laminar flow in a circular tube described by an equation, f = 64/Re. The square and X data points indicate the hot side, and circle and triangle data points indicate cold side. As shown in Figure 5.1, our friction trend line departs from the laminar line. It seems that the transition from laminar to turbulent occurs earlier at a Reynolds number, Re~100, rather than the critical Reynolds number for tube flow, Re~2300. A similar transition from laminar to turbulent in zigzag channels was observed by Ziao et al. [9]. They found that the critical Reynolds number at which the laminar flow in zigzag channels changes to turbulent flow is, Re~100 to 150. It's possible that turbulent flow is present in the heat exchanger above Re~100 due to the zigzag flow configuration. At low Reynolds numbers ($Re_D < 100$), the Moody friction factors on both the hot and cold sides are nearly identical. For $Re_D > 100$, the Moody friction factor departs from 64/Re due to influence of the zigzag configuration. The hot side, which has a bigger zigzag angle, has a lower friction factor than the cold side. This means that a larger tortuosity has the higher friction factor [4].

The pressure drop test also provided a means to check the overall similarity in flow characteristics of the hot and cold channels as discussed at the beginning of this chapter. In Figure 5.2, the pressure drop data is reproduced in terms of the Fanning friction factor with TiTech's experimental result shown as bounding solid lines.

Ishizuka et al. [8] measured the pressure drop on both sides of their PCHE with CO_2 as the heat transfer medium. In our case, we could only measure the pressure drop on the hot side using CO_2 at pressures from 60bar to 80bar. In addition, Heatric provided four (4) pressure drop points on both sides using CO_2 at pressures of 201bar and 74bar.

As shown, our square points are consistent with the hot side points provided by Heatric. In fact, the Fanning friction factors on the hot and cold sides of our PCHE have a smaller difference compared to TiTech's correlations.

Based on the result shown in Figure 5.2, we will assume that both sides of our PCHE have similar flow characteristics compared to TiTech's PCHE. This assumption will be used in calculating convection heat transfer coefficients for water in the PCHE and will be discussed in the next chapter.

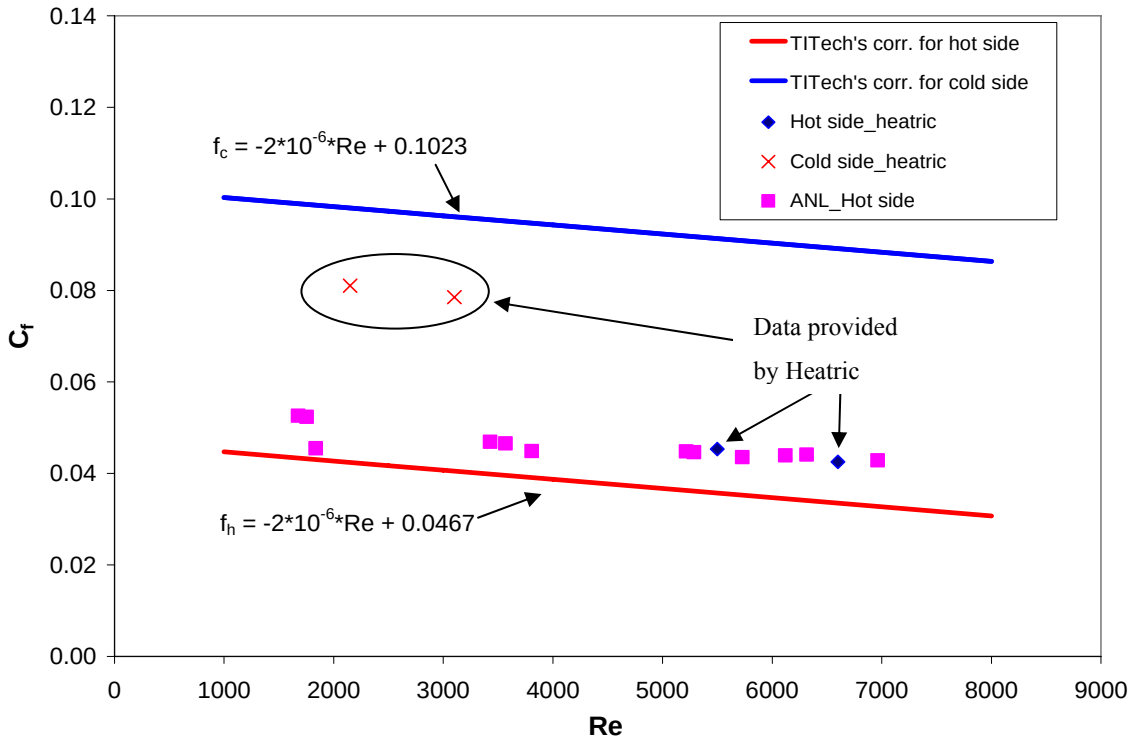

Figure 5.2 Fanning friction factor with CO_2 on the hot side

CHAPTER 6 - Heat transfer with water and water in the PCHE

Before the heat exchanger was tested under Brayton cycle conditions with water and CO_2, it was operated using water as the working fluid on both the hot and cold sides. The purpose of these tests was to measure the heat transfer coefficient with water. For these tests, the heat exchanger was operated with cold side inlet and outlet temperatures of approximately $T_{c,in}$= 15°C and $T_{c,out}$= 50°C, respectively. The hot side inlet and outlet temperatures were $T_{h,in}$=50°C and $T_{h,out}$=15°C. The mass flow rates ranged from $\dot{m}$ =0.03kg/s to 0.3kg/s. The inlet and outlet flow rates are set nearly equal in order to more easily determine the heat transfer coefficient of water. In order to calculate the heat transfer coefficient with water on both the hot and cold side of the PCHE, some assumptions were made, as follows:

1. The thermal resistance of the metal wall between the channels is negligible.
2. The heat transfer is only a function of the Reynolds number.
3. Both the hot and cold sides have similar flow characteristics, since the flow configuration is not known.

With the above assumptions, the water side "h (heat transfer coefficient)" was calculated using the following approach. We can measure an overall heat transfer coefficient, U, for water-water heat transfer using the usual relationship below. Figure 6.1 shows the simplified heat exchange in the PCHE.

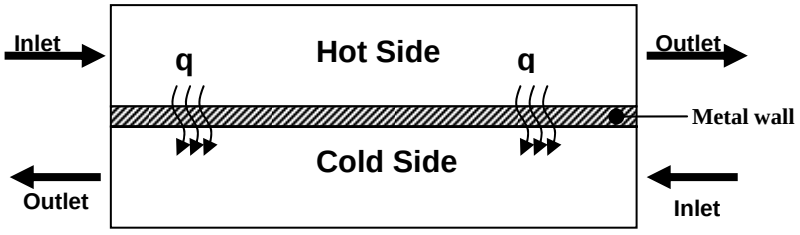

Figure 6.1 Simplified heat exchanger figure

Accordingly, the heat transfer energy equation can be expressed as,

$$q = UA\Delta T \tag{1}$$

where ΔT is the overall temperature difference, A is the total heat transfer area, 5.6m^2, and U is the overall heat transfer coefficient

For this experiment ΔT is calculated using the logarithmic mean temperature difference [26]. Equation 1 can be rewritten as,

$$q = AU\Delta T_{lm} \tag{2}$$

where ΔT_{LM} is defined as,

$$\Delta T_{lm} = \frac{\left(T_{h,out} - T_{c,in}\right) - \left(T_{h,in} - T_{c,out}\right)}{\ln\left[\left(T_{h,out} - T_{c,in}\right)/\left(T_{h,in} - T_{c,out}\right)\right]} \tag{3}$$

where the subscripts h, c, in, and out refer to hot side, cold side, inlet, and outlet, respectively.

The heat load was determined from an energy balance along with the flow rate and inlet and outlet fluid temperatures on the hot side as,

$$q = \dot{m}_h (i_{h,in} - i_{h,out}) \tag{4}$$

where i is the enthalpy.

The overall heat transfer coefficient in Equation 2 is defined as,

$$\frac{1}{U \cdot A} = \frac{1}{h_h \cdot A} + \frac{L}{k \cdot A} + \frac{1}{h_c \cdot A} \tag{5}$$

where h_h and h_c are the convection heat transfer coefficient of the hot and cold side, respectively.

Although we do not know details of the geometry of either side, we assume that the heat transfer coefficients on each side are a function of the given Reynolds number.

This assumption is supported by Ishizuka's result [8]. They showed that the heat transfer on each side was expressed well in terms of Reynolds number with CO_2 as shown in Figure 6.2.

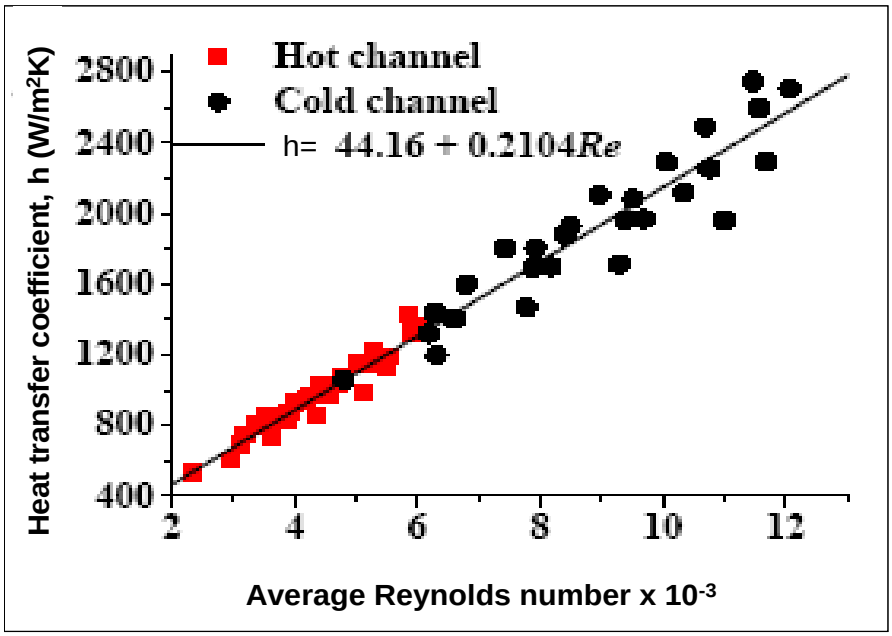

Figure 6.2 The correlation between heat transfer coefficient and Reynolds number for CO_2 [8]

In the calculation of heat transfer coefficients, the thermal resistance of metal wall between hot and cold side channels is assumed negligible. The wall thickness of metal between the hot and cold channels was estimated to be 1 mm. Taking the thermal conductivity of 316 SS as 13.4W/m·K at 25°C, the thermal resistance ($R_{t,wall}$) of the metal wall is only about 0.0005% of the total thermal resistance (R_{total}):

$$R_{t,wall} = \frac{L}{k \cdot A} \tag{6}$$

$$R_{t,h} = \frac{1}{h_h \cdot A} \tag{7}$$

$$R_{t,c} = \frac{1}{h_c \cdot A} \tag{8}$$

$$R_{total} = \frac{1}{U \cdot A} = R_{t,wall} + R_{t,h} + R_{t,c} \quad (9)$$

where $R_{t,wall}$, $R_{t,h}$, $R_{t,c}$, and R_{total} is the thermal resistance for conduction in the wall, for convection in the cold side, for convection in the cold side, and the total thermal resistance. L is the thickness of the metal wall. A is the heat transfer area. k is the thermal conductivity.

By neglecting the thermal resistance of the metal wall between channels, the overall heat transfer coefficient can be simplified from Equation 5 to,

$$\frac{1}{U} = \frac{1}{h_h} + \frac{1}{h_c} \quad (10)$$

The test loop configuration does not permit separate measurements of the hot and cold side heat transfer coefficients. However, if the heat transfers coefficients are expressed in terms of the given Reynolds number and the Reynolds numbers are the same on each side, the heat transfer coefficients can be expected to be the same; that is $h_h \approx h_c$.

We assumed that the convection heat transfer coefficients in our PCHE can be explained in terms of Reynolds number for water. Using Equation 10 and the assumption, we can assume that $h \approx 2U$ with the same Reynolds number on each side.

$$h_h \approx h_c = h \quad \rightarrow \quad h \approx 2U \quad (11)$$

The variables, U and h were calculated from measured ΔT_{Lm} and Q over a range of matched hot/cold side Reynolds numbers. The heat transfer coefficient has been measured for water over a Reynolds number range of about 30~400 as shown in Figure 6.3. By applying a best fit curve to the data, the heat transfer coefficient of water is a linear function of the Reynolds number as, described by

$$h_{H_2O} = 11.04 \times Re_{H_2O} + 570.36, \quad R^2 = 0.99 \quad (12)$$

Equation 12 will be used for the CO_2/water test to calculate the heat transfer coefficient of CO_2 on the hot side based on the Reynolds number of the water on the cold side.

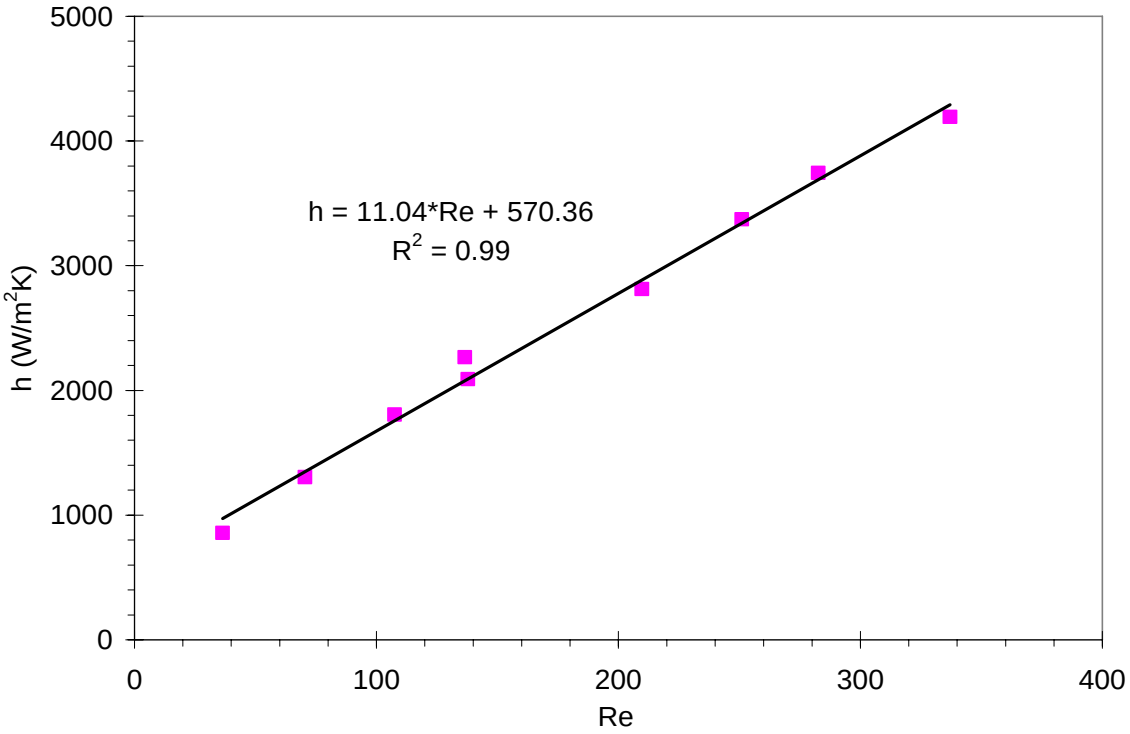

Figure 6.3 Average heat transfer coefficient for water

The heat transfer coefficient of water is measured using an assumption that $h_h \approx h_c$. However, we need to think about the possibility that h_h is not similar to h_c. In order to check this, a simple calculation can be used. Table 6.1 shows the heat transfer coefficient ratios based on the cold side. If h_h is larger than the cold side in the real situations, h_c has error occurred from the assumption that $h_h \approx h_c$. For example, if the real h_h is 1.7 times larger than h_c, the calculated h_c is 1.59U by Equation 10 (not 2U which is based on the assumption). If the real h_h is two times larger than h_c, the calculated h_c will have a relative error of 25% because the real h_c will have 1.5U.

In considering the channel diameter, and the similar Fanning friction factor of both the hot and cold sides as discussed in Chapter 4 and 6, the relative error is likely smaller than 25%. Even though the relative error is not small, we will use the assumption

that $h_h \approx h_c$ in measuring the heat transfer coefficient of water. Then we will check how much the relative error from the heat transfer coefficients of water affects the heat transfer coefficient of CO_2 in the next chapter verify whether the assumption that $h_h \approx h_c$ is reasonable. This topic will be discussed again in Chapter 7.

Table 6.1 The comparison of heat transfer coefficients

h_c	h_h / h_c	h_c /U	Relative error (%)
1.00	1.00	2.00	0
1.00	1.10	1.91	4.5
1.00	1.20	1.83	8.5
1.00	1.30	1.77	11.5
1.00	1.40	1.71	14.5
1.00	1.50	1.67	16.5
1.00	1.60	1.63	18.5
1.00	1.70	1.59	20.5
1.00	1.80	1.56	22
1.00	1.90	1.53	23.5
1.00	2.00	1.50	25

CHAPTER 7 - Heat transfer with CO_2 and water

7.1 Heat transfer in the pseudocritical region

One of the interesting characteristics of CO_2 is the change in thermophysical properties in the pseudocritical region as stated before. As shown in Figure 7.1, both the density and specific heat have a significant change through the pseudocritical temperature at a given pressure of 7.5MPa. Figure 7.2 show the thermal conductivity and the viscosity at 7.5MPa. The thermal properties of CO_2 at supercritical pressures of interest, 7.4, 7.5, 8.0, 8.5, and 9.0MPa, are contained in Appendix E. In general, the thermal properties of CO_2 near the pseudocritical point at the pressures of interest have patterns similar to that shown in Figures 7.1 and 7.2.

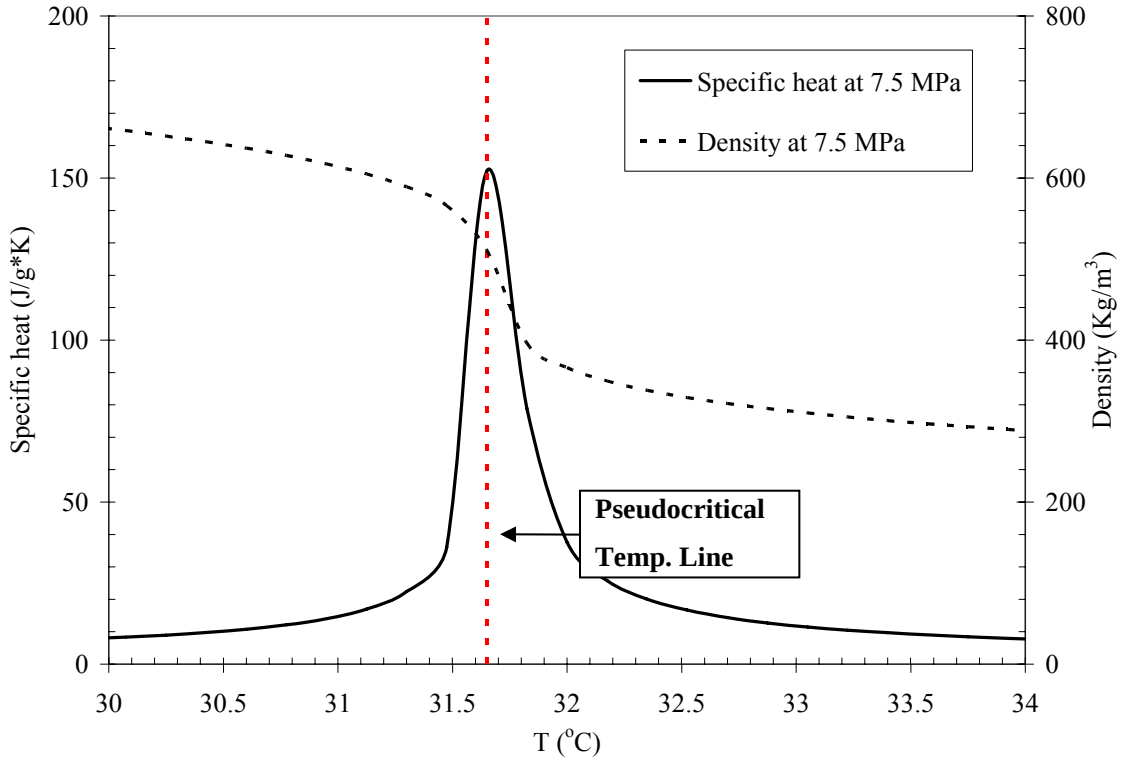

Figure 7.1 Specific heat and density of CO_2 at 7.5MPa

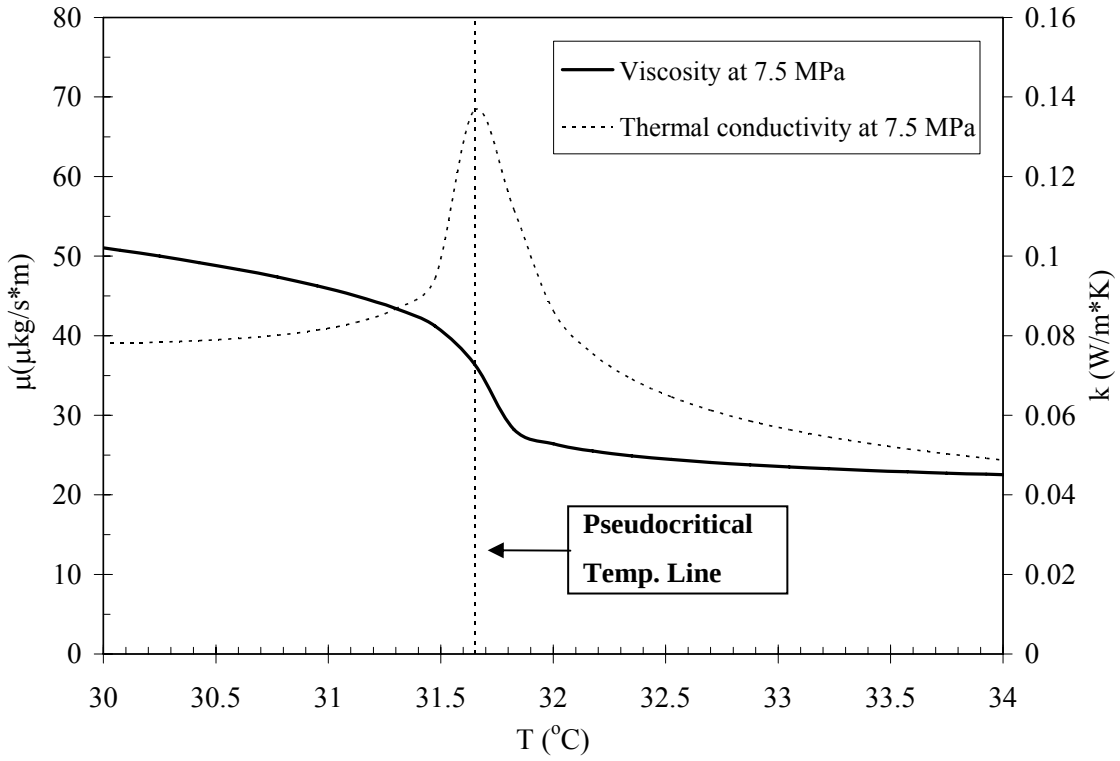

Figure 7.2 Viscosity and thermal conductivity of CO_2 at 7.5MPa

As the thermophysical properties change near the pseudocritical point, they will influence the heat transfer of CO_2 in the heat exchanger. Several previous studies have shown heat transfer augmentation near the pseudocritical region. In a study by Liao et al. [14, 15], they measured the heat transfer using CO_2 in horizontal mini-channels with diameters of 0.7, 1.4, and 2.16mm. They carried out heat transfer experiments at 8.0 and 10MPa with the mass flow rate at 0.030kg/min. As Figure 7.3 shows, Liao et al's results indicate that the heat transfer coefficient reaches a relative maximum value, and then decreases at the given pressures with an increase in the bulk temperature beyond the pseudocritical temperature. The bulk temperature was defined as,

$$T_{bulk} = \frac{T_{in} + T_{out}}{2} \tag{1}$$

where T_{in}, and T_{out} are temperatures for the CO_2 inlet and outlet.

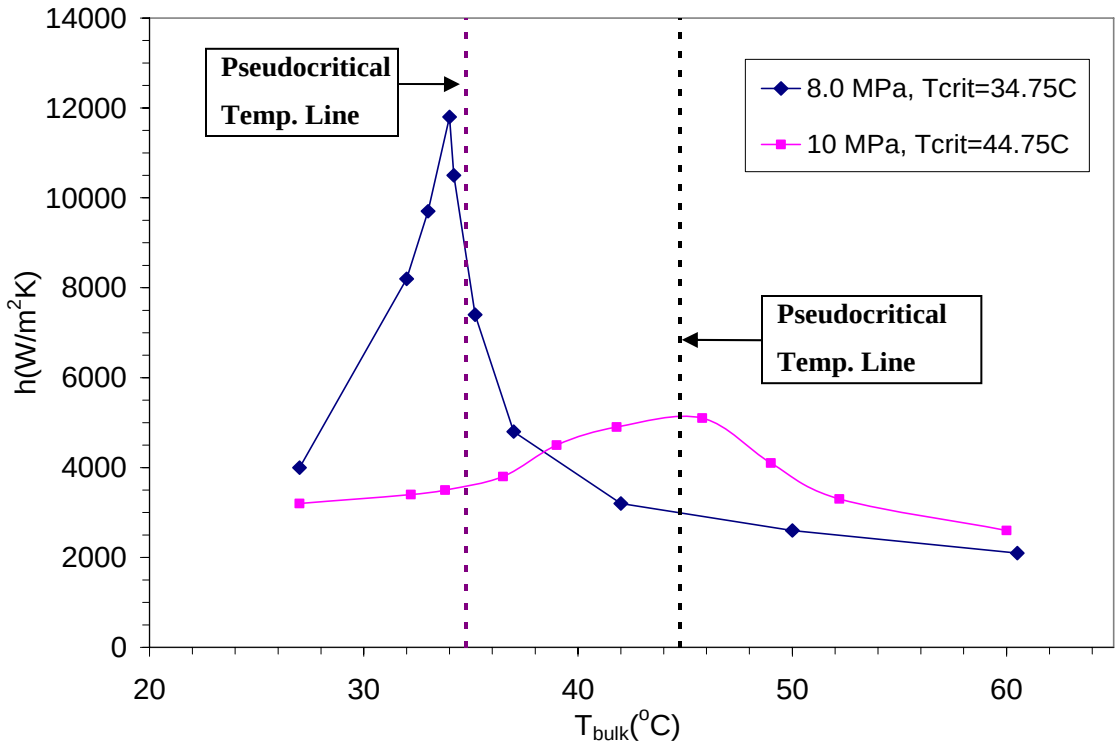

Figure 7.3 Heat transfer coefficient versus bulk temperature from Liao's paper[14]

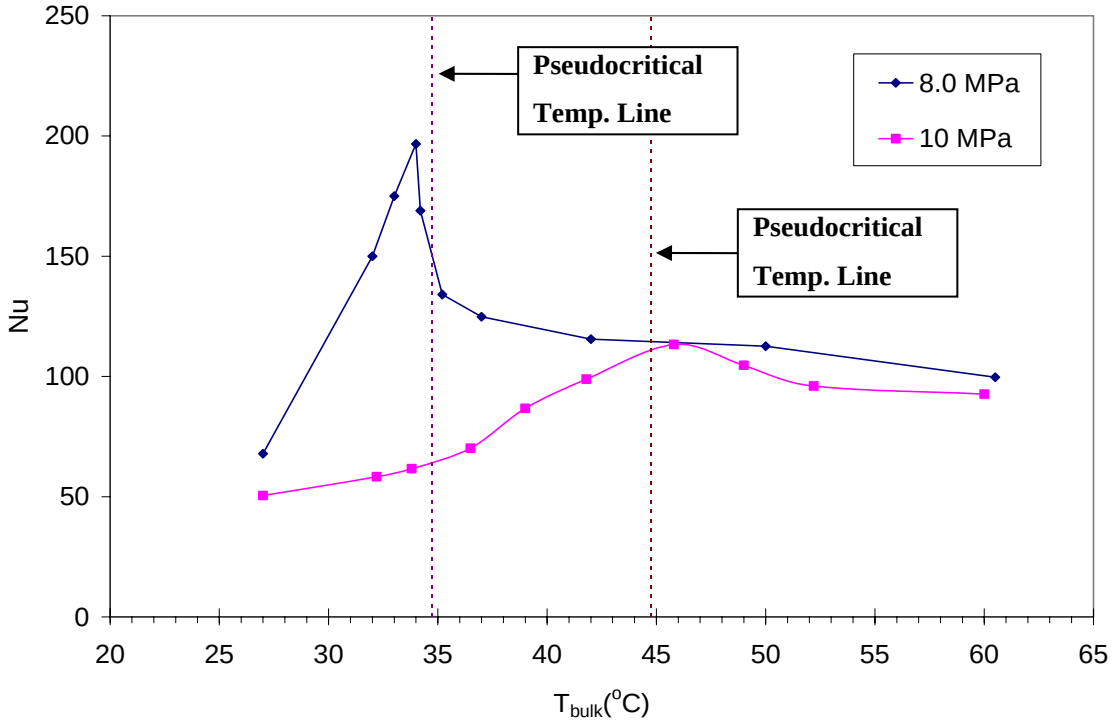

Figure 7.4 Nusselt number versus bulk temperature from Liao's paper [14]

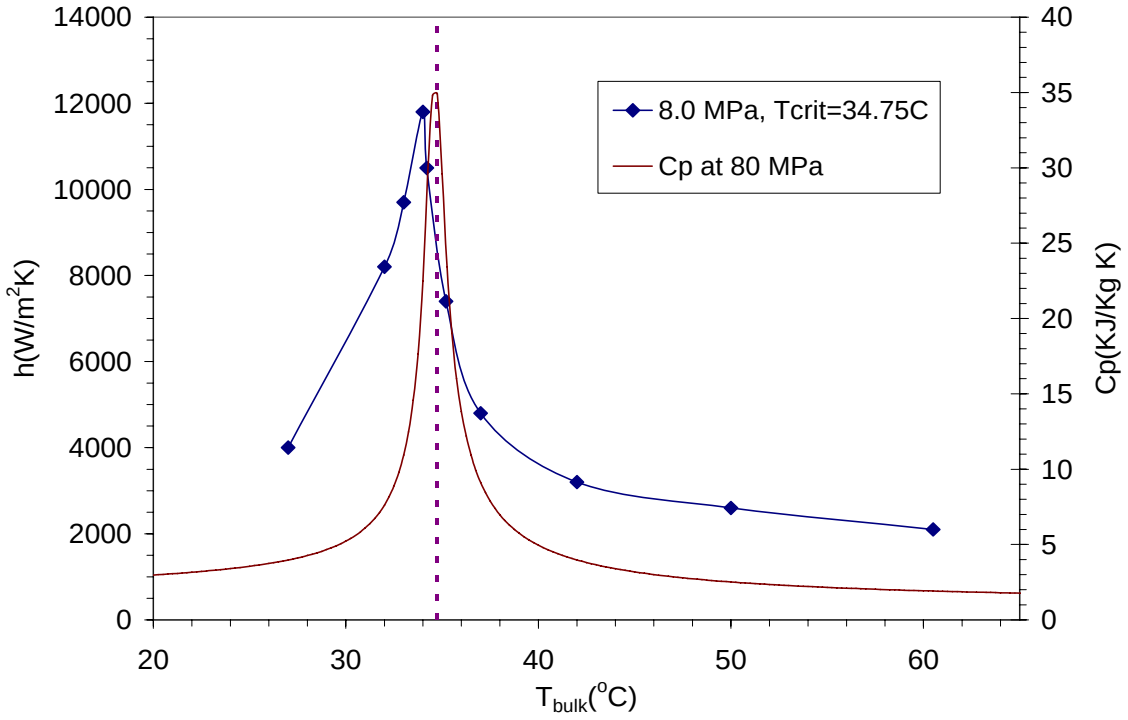

Figure 7.5(a) Liao's result at 8.0MPa with CO_2

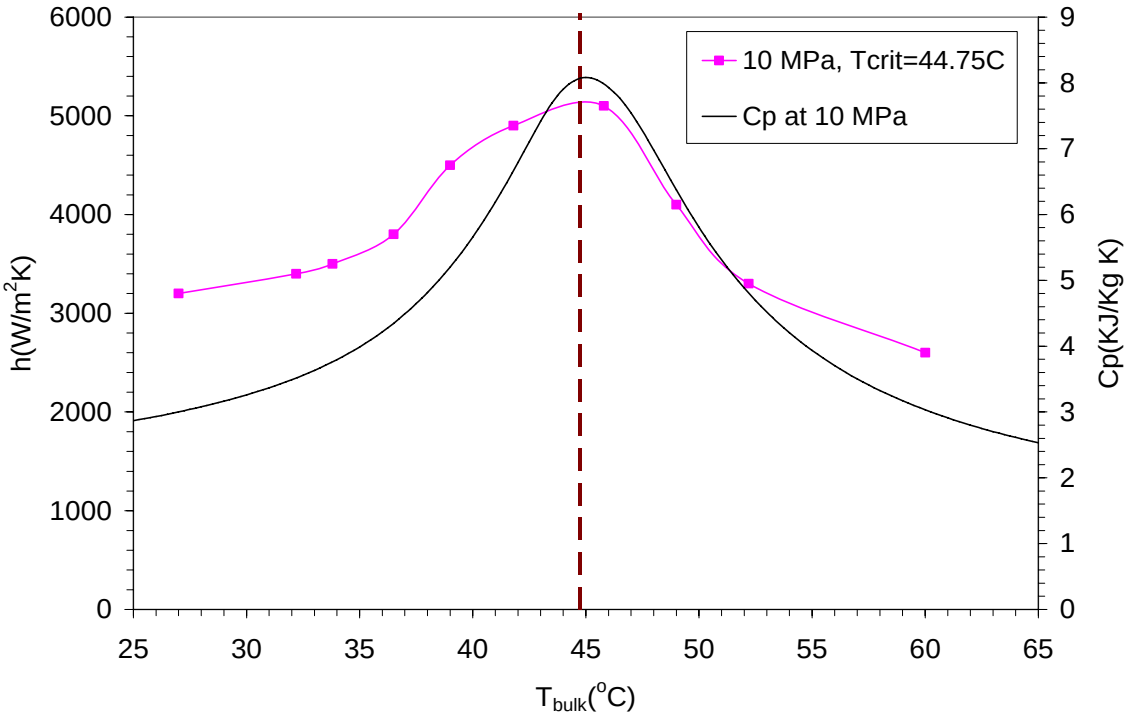

Figure 7. 6(b) Liao's result at 10MPa with CO_2

The peak points of the heat transfer coefficient and Nusselt number are located within the psedocritical region at each pressure. Figure 7.4 shows the Nusselt numbers. The general trend is similar to the heat transfer coefficient, but the right hand side from the pseudocritical line has the higher Nusselt number due to the low thermal conductivity. The thermal conductivity decreases rapidly at the pseudocritical line as shown in Figure 7.2. In Figure 7.5(a) and 7.5(b), heat transfer augmentation is observed in the pseudocritical region. The heat transfer coefficient increases, reaches a peak, and then decreases as the bulk temperature increases. The heat transfer coefficient at 8.0MPa near its pseudocritical point at 8.0MPa is higher than 10MPa. This trend in heat transfer coefficient along with the bulk temperature was also observed by others such as Huai et al. [6] as shown in Figure 7.6(a), (b), and (c) for 7.5, 8.0, and 8.5MPa respectively. It is evident that the heat transfer coefficient of the S-CO_2 is closely correlated to the specific heat at the given pressure because the heat transfer coefficient changes in a similar pattern to the specific heat along the temperature as shown in Figure 7.5 and 7.6.

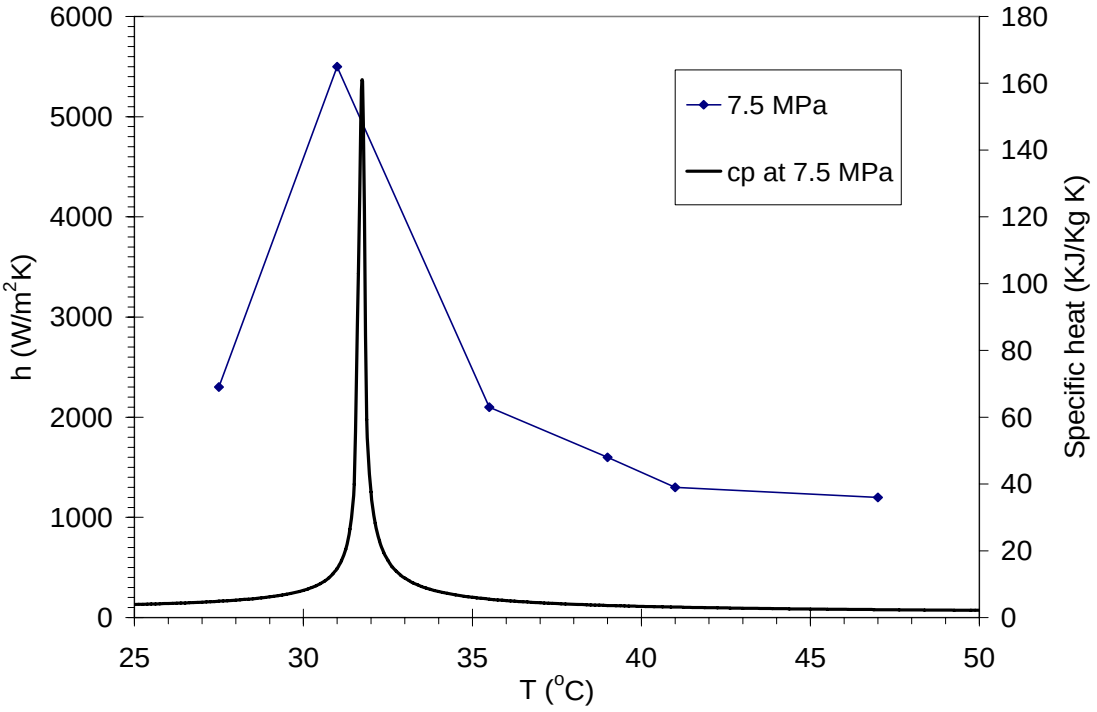

Figure 7. 7(a) The heat transfer coefficient versus the temperature at 7.5MPa [6]

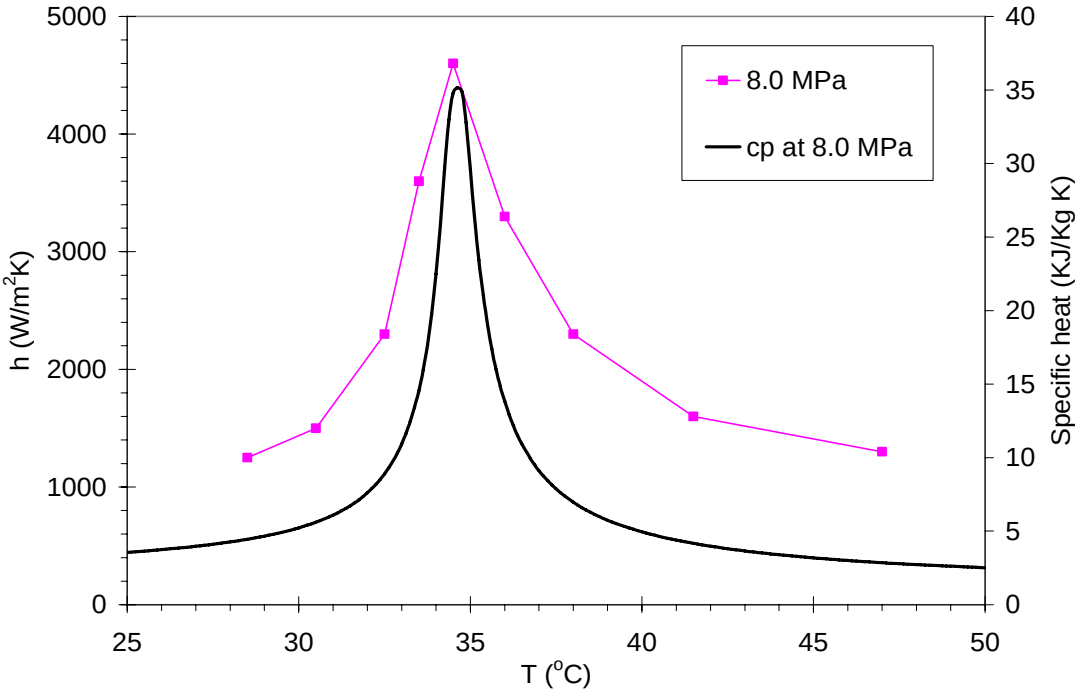

Figure 7. 8(b) The heat transfer coefficient versus the temperature at 8.0MPa [6]

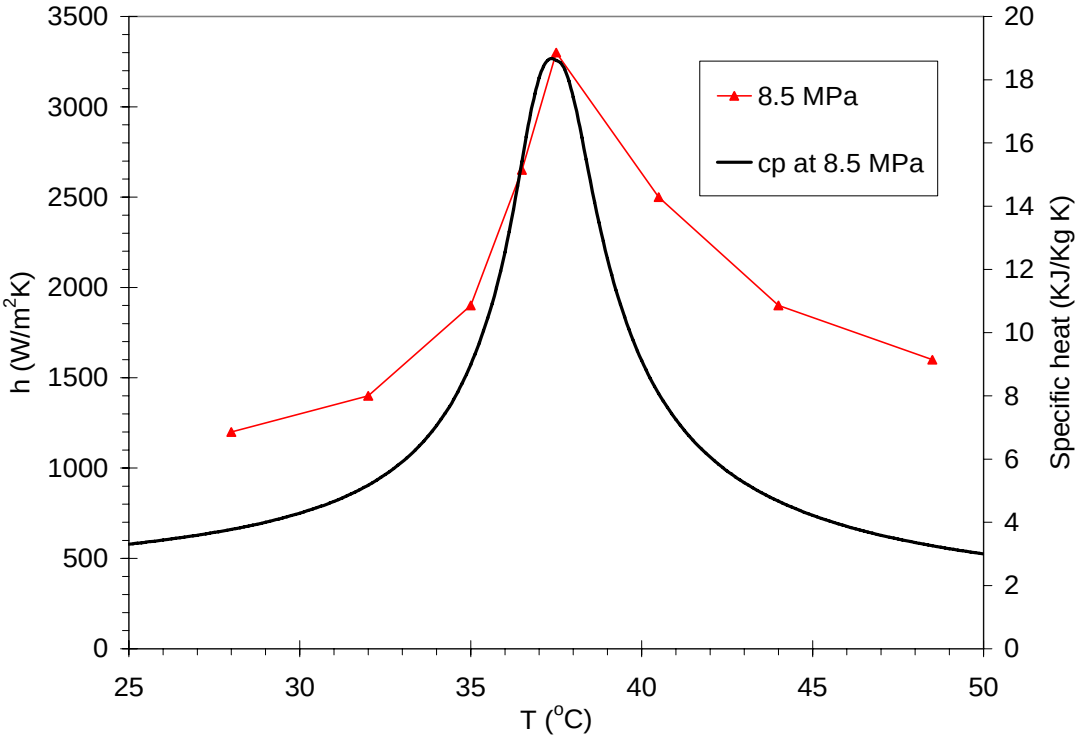

Figure 7. 9(c) The heat transfer coefficient versus the temperature at 8.5MPa [6]

In order to study the above trend in heat transfer using our PCHE, two sets of test were conducted at 7.5MPa and 8.5MPa. For this test, the outlet and inlet temperature difference of the hot (CO_2) side was set as small as possible to see the change in heat transfer rate for a smaller change in the specific heat. The temperature difference was less than 5^{o}C in our PCHE. Otherwise, the specific heat changes so rapidly that its influence on the heat transfer change is difficult to assess. The water flow rate was 3gpm ($1.893\times10^{-4}m^3$/sec), the CO_2 flow rate was 250kg/hr (0.069kg/sec), and the heat load was less than 2kW.

Figure 7.7 shows the heat transfer coefficients at 7.5MPa and 8.5MPa calculated from the test. The heat transfer coefficients in this study show a trend similar to Liao and Huai's result as shown in Figure 8.5 and Figure 8.6. The largest heat transfer coefficient can be found at each pseudocritical point.

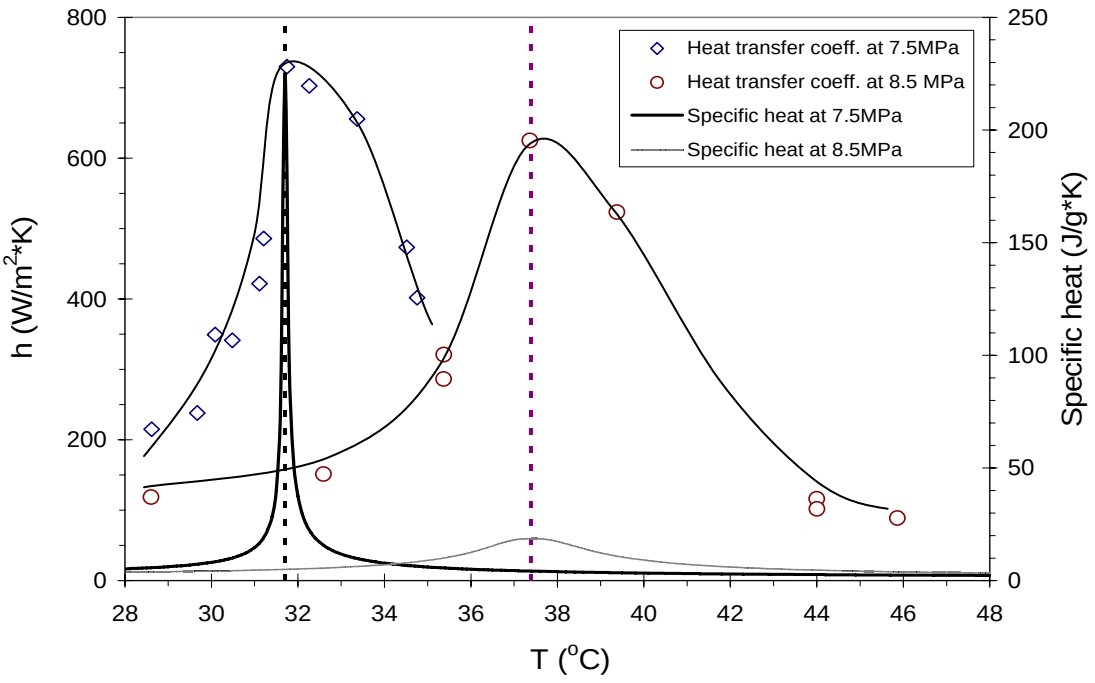

Figure 7. 10 **Average heat transfer coefficient versus the bulk temperature**

In summary, heat transfer augmentation near the pseudocritical region in our PCHE was observed over a small temperature difference between the inlet and outlet on the CO_2 side. Near the pseudocritical point, CO_2 has the maximum specific heat, thus the enthalpy changes rapidly relative to the region far from the pseudocritical region. If CO_2 was in the pseudocritical region, it would have a large convection heat transfer coefficient because a large amount of heat can be transferred with the small temperature change.

In the next section, we will study the heat transfer change and the increase in heat transfer near the pseudocritical point under the precooler operating conditions in the STAR-LM system.

7.2 Heat transfer between CO_2 and water under STAR-LM system conditions

As shown in the previous section, the heat transfer coefficient changes with fluid temperature and pressure in PCHE with small temperature difference between the inlet and outlet on the CO_2 side. The heat transfer augmentation was observed near the pseudocritical region in our PCHE. It was also observed that the pressure affected the heat transfer. In this section, the result of the previous section will be applied to the precooler operating conditions. Using the operating conditions of the precooler, the heat transfer is investigated by changing the CO_2 outlet temperature and pressure.

For this study, three sets of tests were conducted. Two data sets were obtained for CO_2 pressure slightly above 7.4MPa. These experiments were for the investigation of the heat transfer augmentation near the pseudocritical point which was observed in section 7.1. The two sets differed slightly in the proximity of the outlet temperature to the pseudocritical point. These tests were to see the influence of the pseudocritical region because the heat transfer coefficient is the highest near the pseudocritical region. Thus, one test has the outlet closer to the pseudocritical point than another with the same inlet temperature. These experiments were basically based on the anticipated STAR-LM system conditions suggested by Moisseytsev [20], which is shown in Figure 7.8.

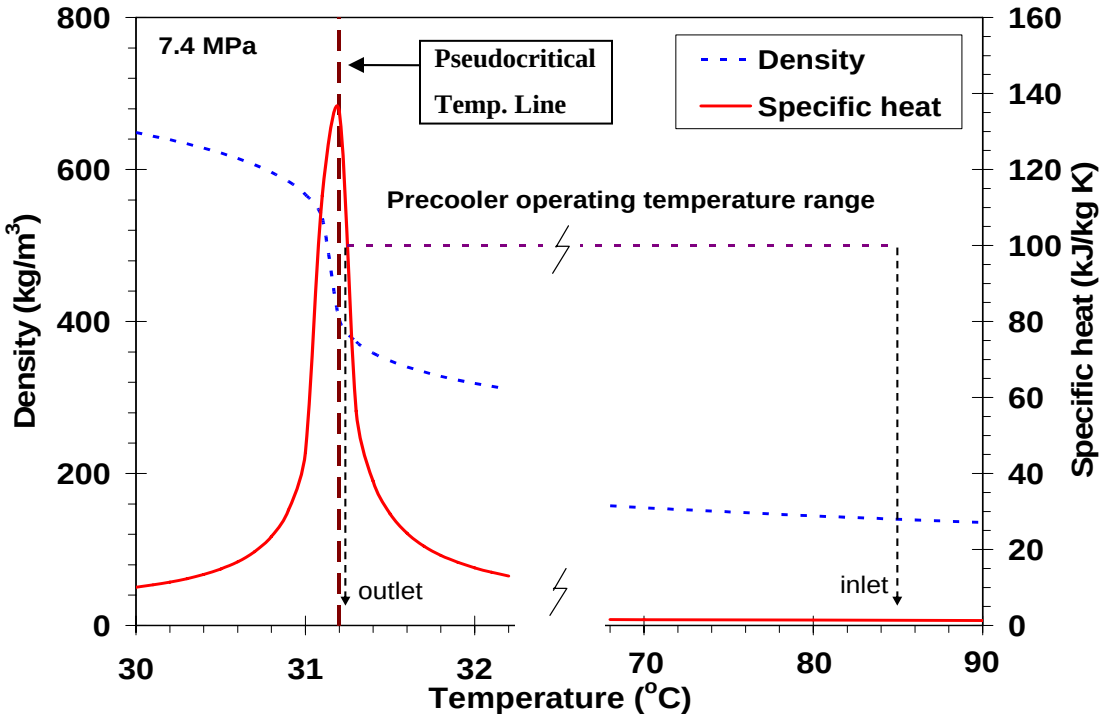

Figure 7. 11 The precooler operating range in the STAR-LM system

Based on the precooler operating range, the experiment range was set up as shown in Figure 7.9. The targeted inlet temperature in each case was 85°C though it could not always be reached while maintaining the desired outlet temperature. Thus the inlet temperatures varied within the range of 70~90°C. The water flow rate was set to 3gpm (11.4Liter/min) for all tests. The heat load ranged from about 10kW at the lowest flow rates to 30kW at the highest. Tests A and B were conducted based on the PCHE operating range as shown in Figure 7.9. Test A and Test B has very small difference of the outlet temperature on the CO_2 side. That is why the test conditions of both tests are shown in one figure. Test A has the outlet temperature closer to the pseudocritical point than Test B. Thus, Test A has lower outlet temperatures on the CO_2 side than Test B. The reason that the experimental pressure is slightly higher than 7.4MPa (the Precooler operating range in the STAR-LM system) is that the 7.4MPa is very close to the critical point as shown in Figure 7.8. If the pressure control is not accurate, the CO_2 is likely to change to the subcritical state. To keep the CO_2 in the supercritical region, the experimental condition is set slightly higher than 7.4MPa.

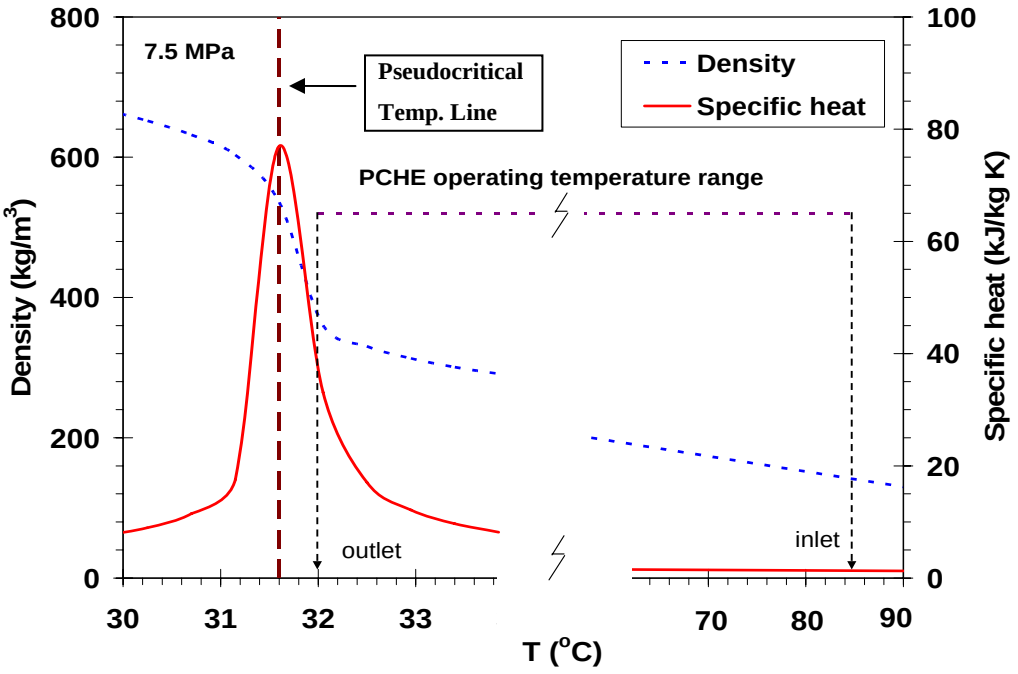

Figure 7. 12 The PCHE operating range

Figure 7.10 shows the outlet temperature and specific heat of the hot side relative to the pseudocritical temperature. The "x" axis designates the ratio of the temperature of the measurement point to that of the pseudocritical point, and the "y" axis shows the ratio of the specific heat of the measurement point to that of the pseudocritical point. As shown in this figure, each test point is very close to the pseudocritical point. Note that although the temperature ratio changes very little, the specific heat ratio of the CO_2 changes significantly in Figure 7.10. In comparing Test A to Test B, we note that Test A's outlet temperatures are quite close to the pseudocritical point at 7.5 MPa as shown in Figure 7.10.

Figure 7.11 shows the average heat transfer coefficient calculated from Test A at the temperatures and pressures. The heat transfer coefficient is calculated using Equations 2 to 4.

$$q = UA\Delta T_{lm} \tag{2}$$

$$\Delta T_{LM} = \frac{\left(T_{hout} - T_{cin}\right) - \left(T_{hin} - T_{cout}\right)}{\ln\left[\left(T_{hout} - T_{cin}\right)/\left(T_{hin} - T_{cout}\right)\right]} \tag{3}$$

$$\frac{1}{U} = \frac{1}{h_{CO_2}} + \frac{1}{h_{H_2O}} \tag{4}$$

The average heat transfer coefficient on the water side was calculated based on the Reynolds number contained in the correlation that was generated from the water/water heat transfer tests. The derived correlation was,

$$h_{H_2O} = 11.04 \times Re_{H_2O} + 570.36 \quad R^2 = 0.99 \tag{5}$$

Using the above equations 2 to 5, the heat transfer coefficient of the hot side, CO_2 side, is calculated and shown in Figure 7.11. The average heat transfer coefficient linearly increases with Reynolds number of CO_2.

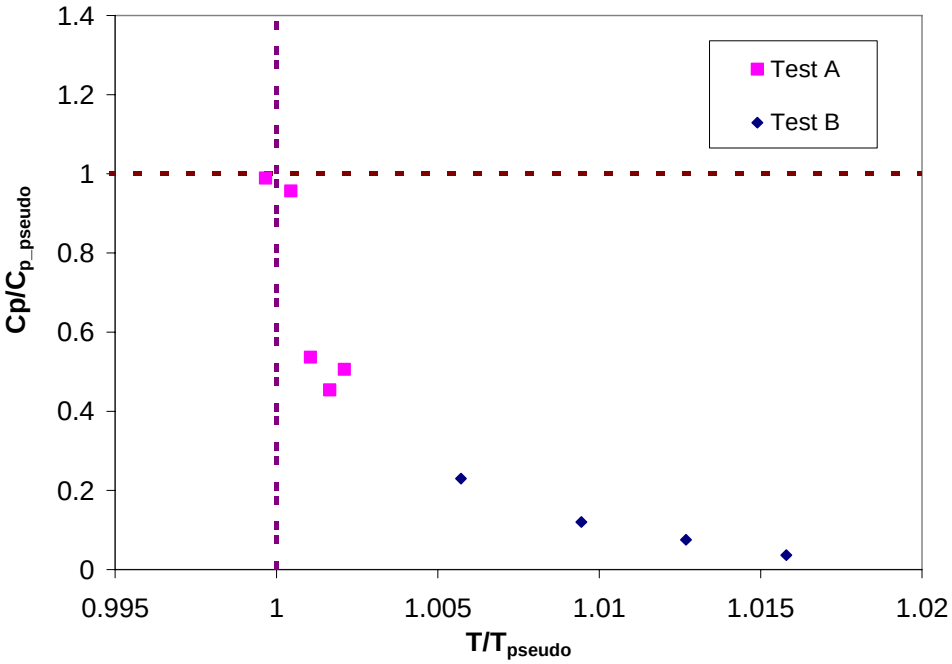

Figure 7.13 The specific heat versus temperature normal to the pseudocritical point

The heat transfer coefficient of Test B is calculated in the same way as Test A using Equation 2 to 5. Figure 7.11 shows the average heat transfer coefficient versus Reynolds number. The increase in heat transfer with Reynolds number is similar to Test

A, but Test B has a slightly higher average heat transfer coefficient than Test A, below Re≤3000. When the error analysis is taken into account, the heat transfer coefficients are nearly identical. The expected heat transfer augmentation near the pseudocritical region is not observed in this test, because of the high specific heat of CO_2 at the outlet. That is, if the CO_2 has high specific heat near the outlet, the CO_2 temperature would not change much for a given heat transfer rate. In this respect, the outlet temperature may stay almost constant. As a result, there is no evidence of heat transfer augmentation in the pseudocritical region.

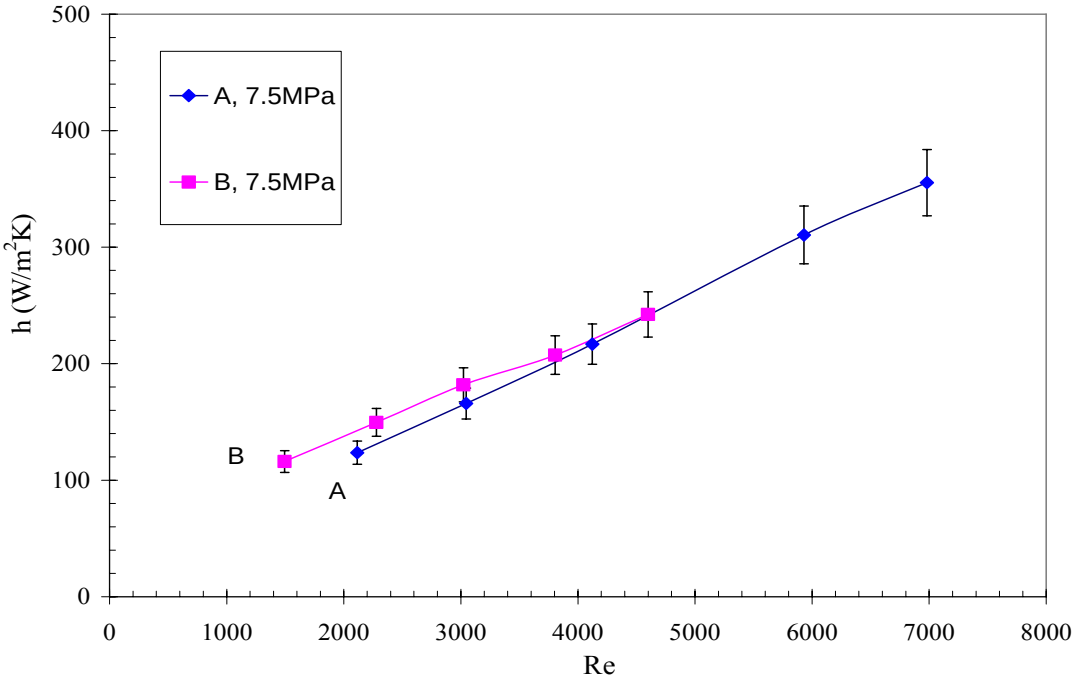

Figure 7.14 Heat transfer coefficient with Reynolds number of Test A and B

Heat transfer with change in the outlet temperature was also investigated. Here, the relationship between the heat transfer and the pressure of the CO_2 has been studied. Some previous studies [23, 63] also investigated this relation. For example, Huai et al.[23] experimented with CO_2 at pressures, 7.5, 8.0, and 8.5 MPa, and mass velocity, $G=262.2 kg/m^2s$. They investigated the change in heat transfer along with the bulk temperature. Their results showed that the heat transfer coefficient reached a maximum

value near the pseudocritical point and decreased beyond as the bulk temperature increased as shown in Figure 7.12.

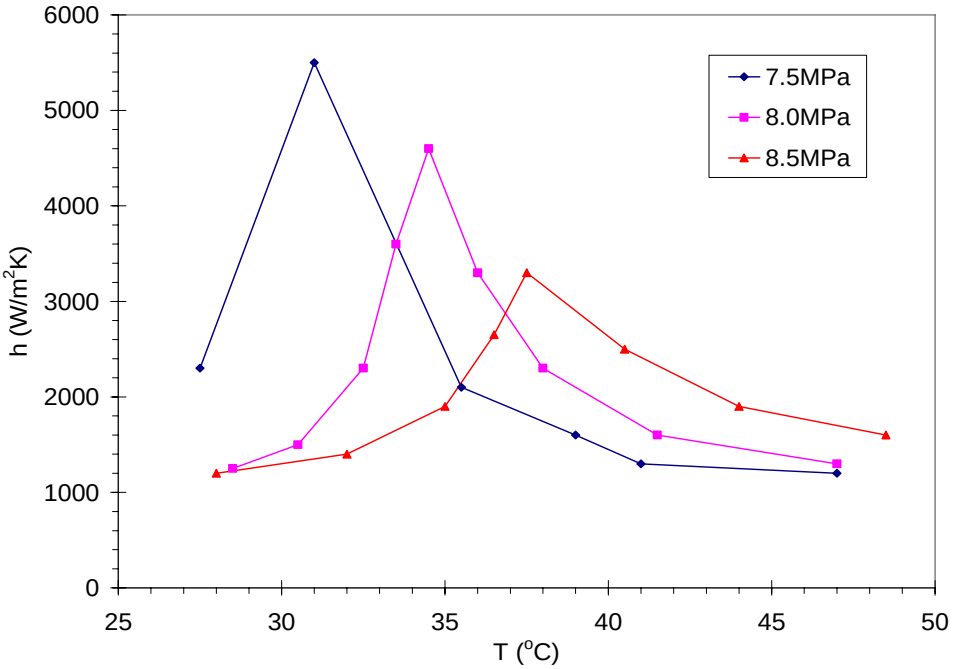

Figure 7.15 The heat transfer coefficient with the temperature of Huai et al. [6]

As seen in Figure 7.12, at a pressure of 7.5MPa, the heat transfer coefficient is the largest; at 8.0MPa, the local maximum is slightly lower and so on at each pseudocritical point.

In order to check the heat transfer in our PCHE with variation in CO_2 pressure, one more test was conducted at 8.5MPa. This experiment is called Test C. This test also has the outlet temperature closer to the pseudocritical point, as in Test A and Test B, and the inlet temperature from 86°C to 91°C. The average heat transfer coefficient is calculated in the same manner as Tests A and B. The heat transfer for Test C varies linearly with Reynolds number, and has the trend similar to Test A and Test B. However, Figure 7.13 shows that the heat transfer coefficient of CO_2 is larger at the higher pressure. As shown in Figure 7.7, the specific heat at 8.5MPa is larger than at 7.5MPa except near the pseudocritical region in our operating range. The large specific heat means that the enthalpy changes rapidly in a given change of temperature. In addition to this, we could

not observe the heat transfer augmentation near the pseudocritical region at 7.5MPa. In considering the specific heat and the heat transfer near the pseudocritical region, it can be concluded that if CO_2 temperature is almost constant near the outlet, there is no effect from the high specific heat near the outlet.

In this condition, the specific heat at 8.5MPa is larger than that at 7.5MPa. This conclusion will be verified by the computational analysis in the next chapter.

Figure 7.14 shows the results of order of magnitude analysis. The 'x' axis shows the effect of the specific heat and the 'y' axis shows the heat transfer characteristics. For example, Test A has the largest Prandtl number compared to Test B and Test C due to the specific heat of CO_2. Thus, from the x axis, we can see how close the outlet temperature is to the critical point. From the y axis, we can see the heat transfer characteristics. As shown in Figure 7.13, higher pressure CO_2 has the higher heat transfer coefficient. The derivation of the order of magnitude method is shown in Appendix C.

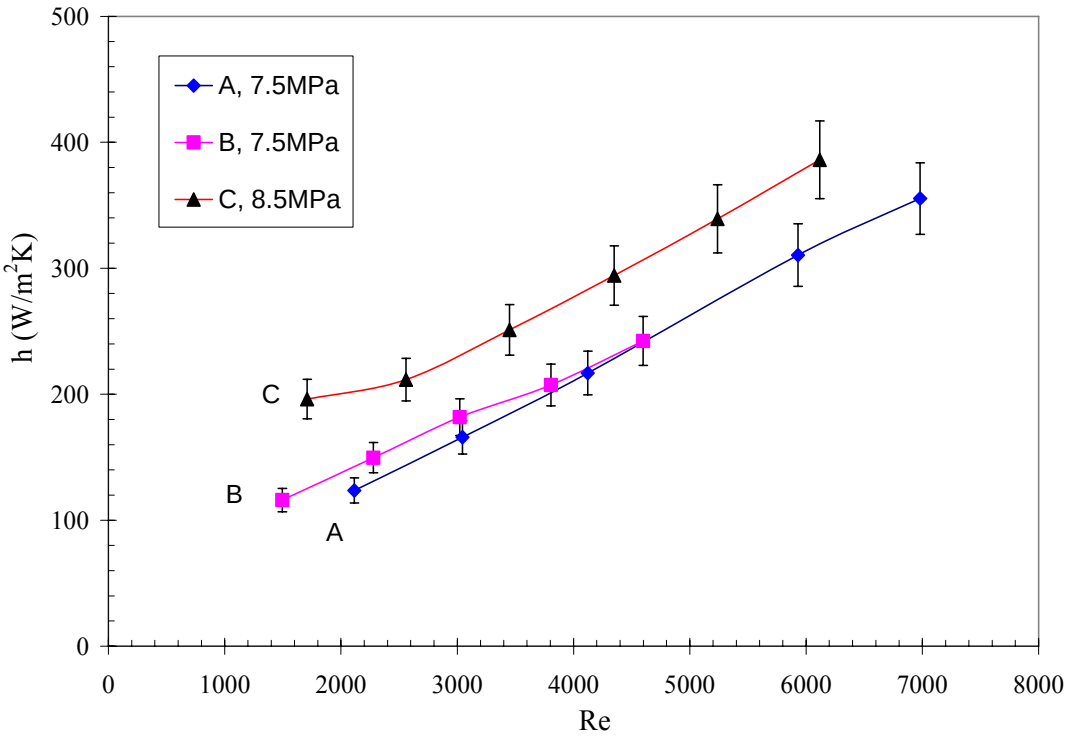

Figure 7.16 The heat transfer coefficient with CO_2 of Test A, B, and C

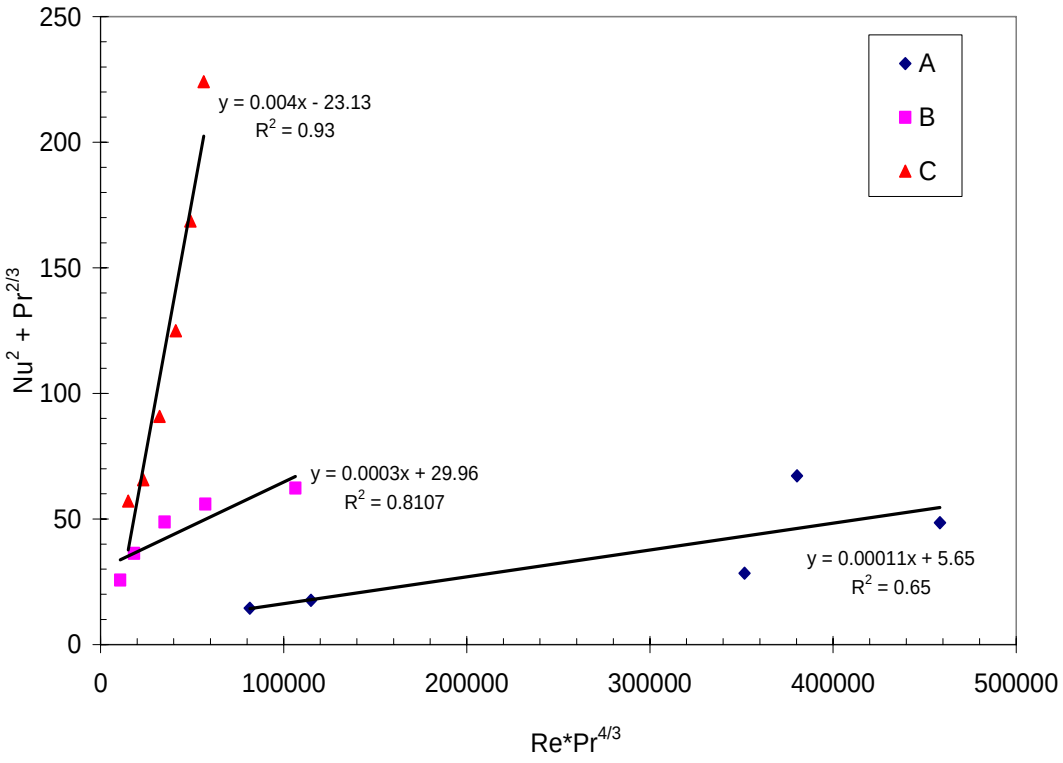

Figure 7.17 The result of the order of magnitude method

In this study, we could not observe heat transfer enhancement near the pseudocritical region which was shown with the small temperature difference between the inlet and outlet of the CO_2 side. Since most heat transfer occurs near the inlet of the CO_2 side, as the CO_2 temperature approached the pseudocritical point, the specific heat dramatically increases relative to a small temperature change. The small temperature change means that an increasingly small amount of heat is transferred. In this way, it is possible for the expected enhancement near the pseudocritical region to not appear in the heat exchanger.

As presented, we considered the relative error introduced from the assumption that $h_h \approx h_c$. The measured experimental overall heat transfer coefficient is 100-600W/m^{2}K, and the heat transfer coefficient of water ranged from 3000 to 3500W/m^{2}K. In Chapter 6, there is a relative error of 25% when h_h is twice as large as h_c. Although this error is not small, if one can show that the calculated heat transfer coefficient of CO_2 is not strongly influenced, we can procede under the assumption that $h_h \approx h_c$. For example, if the overall heat transfer coefficient is 100W/m^{2}K and the heat transfer coefficient of

water side is 3000W/m^{2}K, the heat transfer coefficient of CO_2 can be calculated as follows.

$$\frac{1}{U} = \frac{1}{h_c} + \frac{1}{h_h} \tag{2}$$

$$\frac{1}{h_h} = \frac{1}{U} - \frac{1}{h_c} \tag{3}$$

The calculated h_h is 96.77W/m^{2}K without the relative error of 25%, and 95.74W/m^{2}K with the relative error. For other values of U and h_c, the calculated results are shown in Table 7.1. There are two h_h results. One is calculated with assumption that there is no relative error on the heat transfer coefficient for water. Another is with the relative error at 25%. The error is calculated between the two h_h results. As shown in the table, the relative error is typically less than 5.5%. So the error on the water side does not significantly affect the heat transfer coefficient of CO_2.

So, even though the relative error on the water side is not small, it does not significantly influence the heat transfer coefficient of CO_2 because the heat transfer coefficient of water is much larger than the overall heat transfer coefficient. Therefore, the assumption that $h_h \approx h_c$ is considered reasonable.

Table 7.1 The error propagation on the CO_2 by the water heat transfer coefficient

U	h_c	h_h without 25% error	h_h with 25 %error	Relative Error
W/m^{2}K	W/m^{2}K	W/m^{2}K	W/m^{2}K	%
100	3000	96.77	95.74	1.06
200	3000	187.50	183.67	2.04
300	3000	272.73	264.71	2.94
400	3000	352.94	339.62	3.77
500	3000	428.57	409.09	4.55
600	3000	500.00	473.68	5.26
100	3500	97.22	96.33	0.92
200	3500	189.19	185.84	1.77
300	3500	276.32	269.23	2.56
400	3500	358.97	347.11	3.31
500	3500	437.50	420.00	4.00
600	3500	512.20	488.37	4.65

CHAPTER 8 - Predicted temperature distribution in the PCHE

The heat transfer coefficients were measured for the overall area of the heat exchanger experimentally. Since the thermal properties of CO_2 change very quickly near the pseudocritical region, it is important to calculate the temperature distribution inside the heat exchanger using the experimental results, even though the heat transfer coefficients are the average value. If the estimated temperatures are close to the measured temperature with the average heat transfer coefficients, it is possible to predict the temperature distribution.

8.1. Analytical calculation method

Figure 8.1 shows a simplified drawing of the heat exchanger with *n* nodal segments. The heat exchanger consists of CO_2 on the hot side, and water on the cold side. In order to calculate the temperature distribution, several assumptions were made as follows:

1. The temperature drop through the metal wall between channels is negligible because of the small thermal resistance as shown in Chapter 5.
2. The temperature at a given node in each channel is constant.
3. Since the measured pressure drop on the CO_2 side is very small relative to the pressure at the CO_2 inlet, the CO_2-side pressure drop in the heat exchanger is neglected; that is, the thermophysical properties of the CO_2 are a function of temperature alone.

With these assumptions and the experimental results, the analytical model is based on the first law of the thermodynamics.

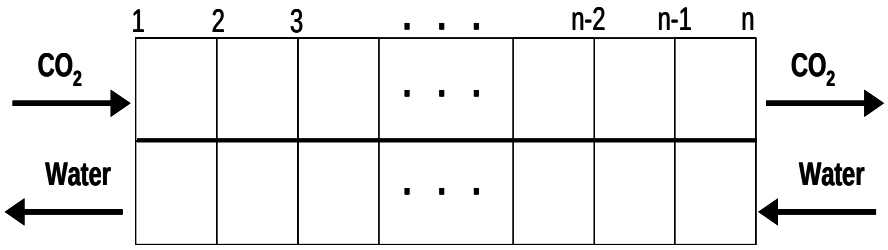

Figure 8.1 A simplified drawing of the PCHE

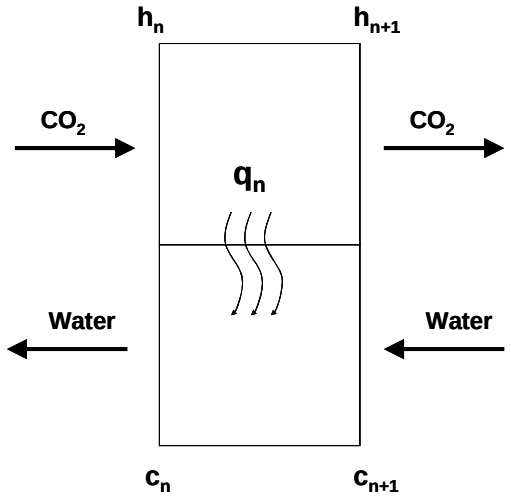

Figure 8.2 A section of the simplified drawing of the PCHE

In Figure 8.2, "h_n" and "c_n" represent the *n*th node on the hot side and the cold side. On the hot side (CO_2 side), the enthalpy of CO_2 is taken as a function of temperature, and values are taken from the NIST database [21]. The mass flow rates of water and CO_2 are known from the experiment. The heat transferred from the hot side, q_n, in a given segment can be expressed as,

$$q_n = \dot{m}_h \cdot (i_{h_n} - i_{h_{n+1}}) \tag{1}$$

where i and $\dot{m}_H$ are the enthalpy and mass flow rate of the CO_2, respectively.

The energy transferred to the cold side can be calculated as follows,

$$q_n = \dot{m}_c \cdot (i_{c_n} - i_{c_{n+1}}) \tag{2}$$

where q_n, $\dot{m}_c$, and i_c are the heat transfer rate, mass flow rate and enthalpy of the water, respectively. The mass flow rates are taken from the experimental data.

The well-known, Log Mean Temperature Difference (LMTD), analysis is applied to each segment of the heat exchanger with the measured overall heat transfer coefficients as shown in Equation 3. The heat transfer area, 5.6 m^2, was provided from Heatric.

$$q_n = U \cdot \frac{A}{No.\ of\ \ nodes} \cdot \frac{(T_{h_n} - T_{c_n}) - (T_{h_{n+1}} - T_{c_{n+1}})}{\ln\left[\frac{T_{h_n} - T_{c_n}}{T_{h_{n+1}} - T_{c_{n+1}}}\right]} \tag{3}$$

where U is the overall heat transfer coefficient, and A is the heat transfer area, 5.6 m^2

We now have three equations for each section of the heat exchanger. These equations can be related to each other through the following equalities,

Heat transfer rate calculated by equation (Eqn 1), $q_n(1)$
= Heat transfer rate calculate by equation (Eqn 2), $q_n(2)$
= Heat transfer rate calculated by LMTD method (Eqn 3), $q_n(3)$

The temperature distribution calculation was conducted with the total number of nodes, *n*=15 and 20. For both *n*=15 and 20, we predicted essentially the same inlet and outlet temperatures. As shown in Figure 8.3, the dotted and solid lines corresponding to *n*=15 and 20 nodes are nearly identical. Therefore, the temperature distribution in the heat exchanger are calculated with *n*=15 piece.

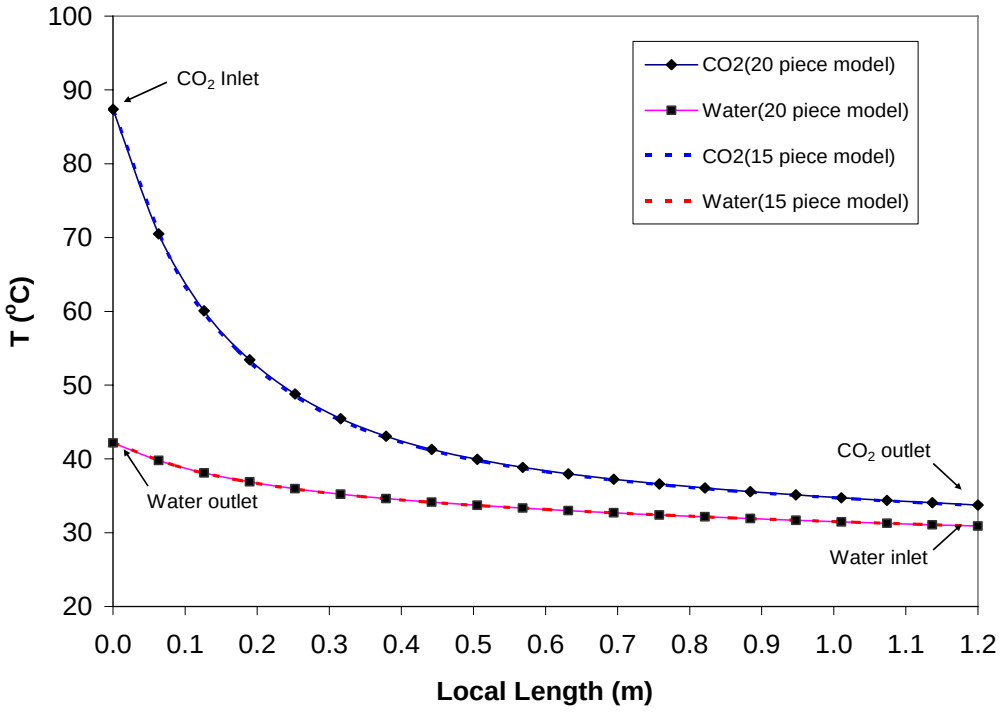

Figure 8.3 The comparison of results of the 15 and 20 piece model

8.2. Calculation results

We can use the above method for the entire length of the heat exchanger. Using this method 15 individual heat exchanger sections lead to 28 unknowns. There are also 28 equations generated ((No. of nodes-1) × 2). Since we have as many equations as unknowns, the temperature distribution inside the heat exchanger can be estimated using this method.

Figure 8.4 shows the modeled temperature distributions along with the experimental results. The calculated CO_2 outlet temperatures are within 6% of the experimental values. As shown in the figures below, most of the temperature changes occur near the CO_2 inlet region where the temperature decreases dramatically. The temperature changes near the outlet are very small in contrast. On the water side, the calculated water outlet temperatures differ from that measured by 15 %. Most of the

temperature change occurs near the water outlet region as shown in the Figure 8.4. This means that the temperature change near the CO_2 psuedocritical point (toward outlet) is relatively insignificant because specific heat is so large (i.e. $q_n = \dot{m} \cdot c_p \cdot \Delta T$). So a material with a large specific heat cannot be heated and cooled easily compared to a material with a the low specific heat. In terms of the specific heat, we can interpret that the temperature change near the inlet region of the CO_2 side is large because of the low specific heat and the temperature change near the CO_2 outlet is small due to the high specific heat. Due to the heat transfer characteristics, the temperature may not change much near the outlet region of the CO_2 side. In other words, there may be rare heat exchange, and the heat transfer enhancement may not be expected near the outlet region of the CO_2 side. Similarly, Moisseytsev [20] explained that if the CO_2 outlet temperature is set to 31.0°C, the required heat exchanger length, for a given q, to 26.5m. If the CO_2 outlet temperature is raised slightly to 31.25°C at 7.4MPa, the heat exchanger length decreases to 12.1m.

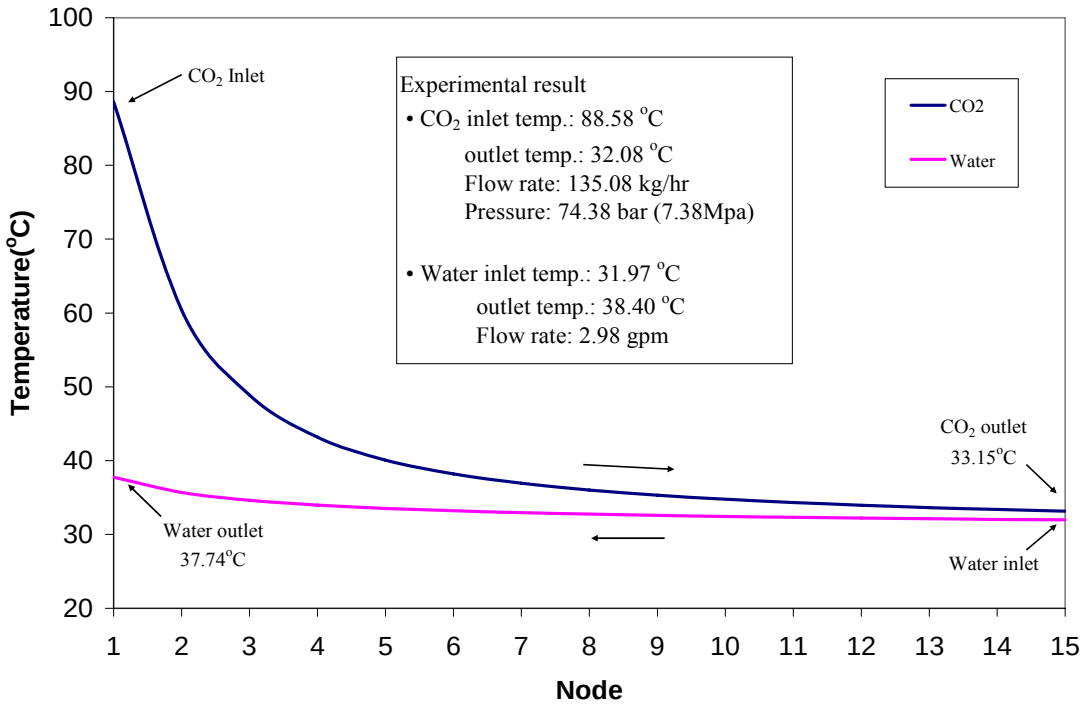

Figure 8.4 The temperature distribution of Test A1

By the magnitude of thermal diffusivity, we can estimate the thermal characteristics of a material. For example, a large thermal diffusivity value means that the material's temperature changes quickly to its thermal environment, while a material with a small thermal diffusivity value responds slowly to its thermal environment. Figure 8.5 shows the thermal diffusivity of CO_2 at 7.5MPa. The thermal diffusivity has the smallest value at the psuedocritical point, and then, increases past the pseudocritical point. According to Figure 8.5, we can conclude that the CO_2 temperature near the outlet of the PCHE does not change much.

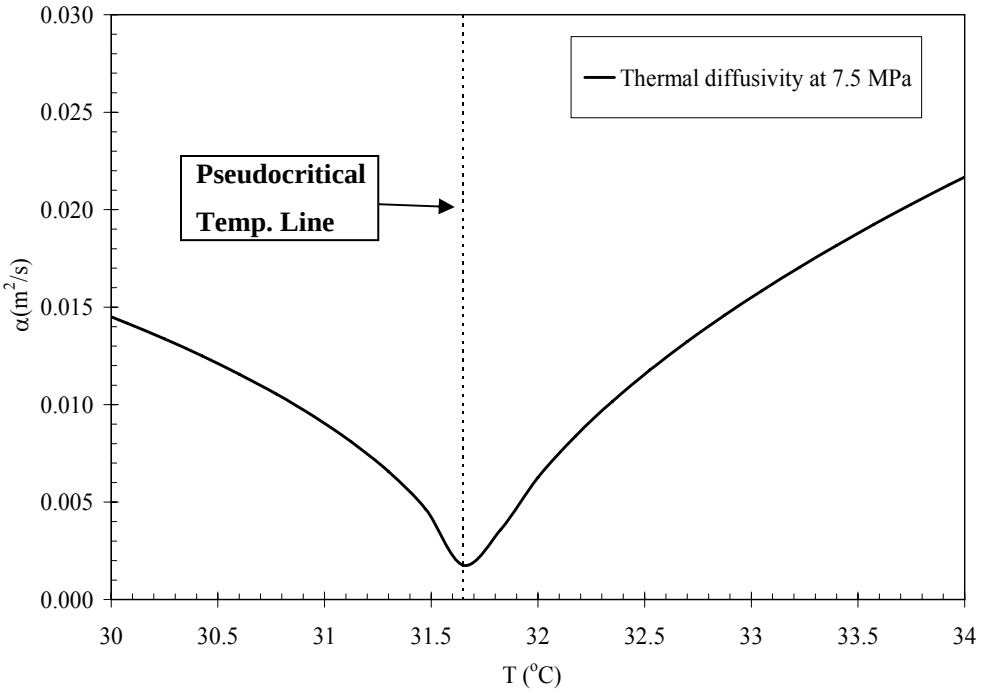

Figure 8.5 Thermal diffusivity of CO_2 at 7.5MPa

The previous nodal calculation is based on the energy balances on each side, so the calculation does not consider the geometrical effects (flow configuration) of the PCHE. To validate the calculation, Computational Fluid Dynamics (CFD) was used. Here, the commercial software package, FLUENT, was used to simulate a simplified, four-layer zigzag channel flow with heat transfer between hot and cold streams. Based on finite volume method, simulations were performed on a co-located multiblock grid. A

packaged, QUICK (Quadratic upstream interpolation for convective kinetics) and central differencing numerical schemes were applied for convective and diffusive terms, respectively. The discrete nonlinear equations were implemented implicitly. The pressure-velocity coupling algorithm SIMPLE (Semi Implicit Method for Pressure-Linked Equations) was used to evaluate the pressure field and the linearized equations were solved by multigrid method. Additional details are given in the Fluent user manual.

Simulation of the convective and conductive heat transfer in a counter-flow type heat exchange was performed. There were approximately 600,000 cells in our two-dimensional model. The computational domain consists of nine computational blocks as shown in Figure 8.6.

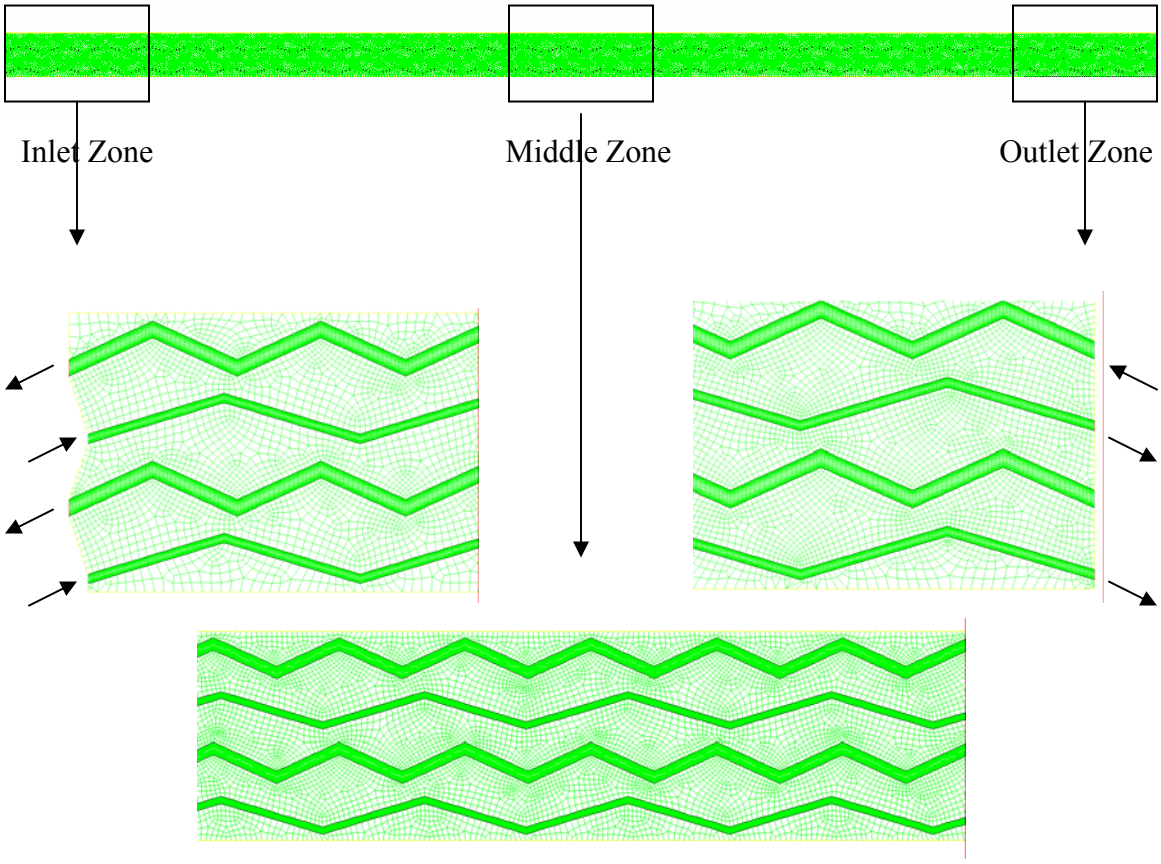

Figure 8.6 Computational domain of the zigzag channel flow past a Staggered Tube Bundle Array

Blocks I and II (zigzag channel) are fluid domains. Block I was designated for water and Blocks II, for carbon dioxide. The remaining Block III represents solid material, steel. Along the zigzag channel, a distribution of non-uniform structured quadrilateral meshes, perpendicular to the channel wall was used. The mesh was refined in vicinity of zigzag wall.

The CFD results are shown in Figure 8.6. The temperature distribution with this simplified zigzag heat exchanger is almost identical to the nodal model result. The CFD simulation result also shows that the CO_2 temperature reaches a nearly constant value near the outlet, as well as relative to water temperature. This relative constant temperature difference indicates that there is relatively little heat transfer in this regions, as equally predicted by the nodal model.

Therefore the nodal LMTD model, as applied along the heat exchanger gives a sensible (anticipated) temperature distribution. Heat transfer augmentation near the outlet of CO_2 was not observed but higher heat transfer is maintained because CO_2 approaches its critical point under the STAR-LM system parameters.

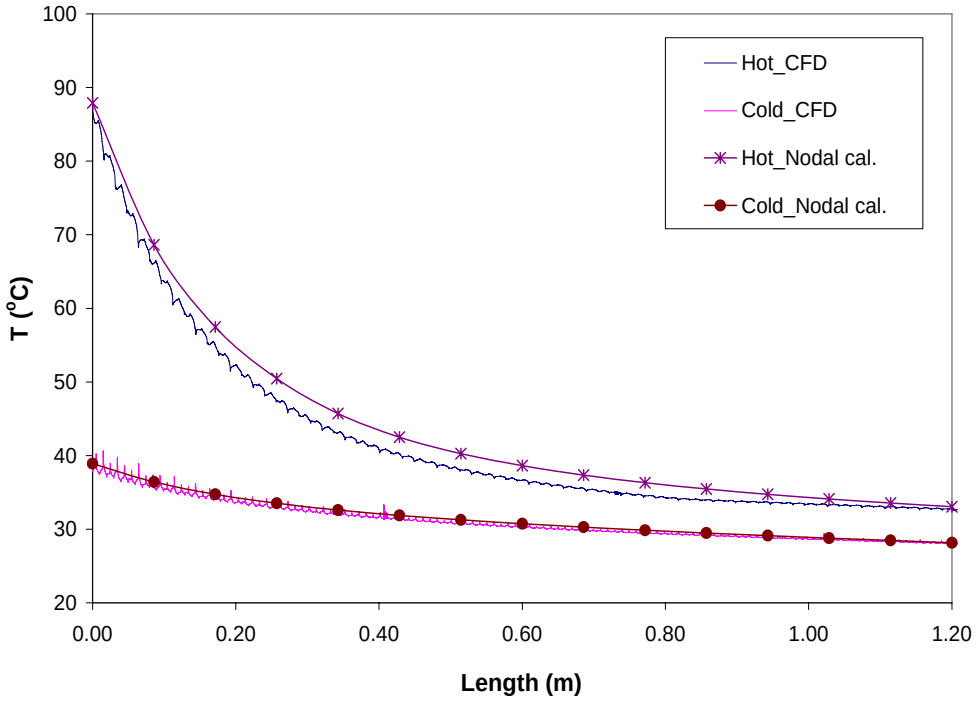

Figure 8.7 The calculation results from the nodal calculation and CFD

CHAPTER 9 - Conclusion

The performance of a printed circuit heat exchanger manufactured by Heatric was investigated for operating conditions corresponding to those of the precooler in the STAR-LM lead fast reactor (LFR) concept. The STAR-LM LFR is designed with an indirect supercritical CO_2 Brayton cycle for power production.

Since the design specification of our PCHE is proprietary and thus specifications limited, we had to first estimate the angle of the zigzag flow path, length of the channel, and channel diameter. These dimensions were calculated using geometrical information provided by Heatric and additionally consulting the dimensions of TiTech's PCHE, though of smaller capacity, is similar to our PCHE. The calculated zigzag angles are 139.38^o and 113.28^o for the hot and cold side, respectively. However, there are dimensions that cannot be calculated such as pitch of channels, thickness of the metal wall, and the length of the plenum regions (entrance and exit).

Subsequently, we experimentally checked the hydraulic characteristics of the heat exchanger. The pressure drop on both the hot and cold sides using water and CO_2 was determined to check for hydraulic similarity between the hot and cold sides. The pressure drop data was presented in terms of the Moody friction factor and revealed departure away from the laminar at approximately $Re \approx 100$ in our PCHE with zigzag channels. This agrees with results from other studies of laminar to turbulent transition in microchannels with zigzag paths [9]. However, as heat transfer was the primary focus of our work, we did not investigate this further.

The pressure drop with CO_2 flowing on the hot side was measured since the experimental facility was not configured to measure the pressure drop on the cold side using CO_2. Limited additional data for the cold side was provided by Heatric. The pressure drop data with CO_2 was reproduced in terms of the Fanning friction factor. These data were compared to the friction factor data given by TiTech's PCHE study [8]. The comparison revealed that our PCHE has a smaller difference in the friction factor (hot to cold) than TiTech's PCHE. As the Fanning friction factor represents the combined

influence of channel geometry, surface roughness, and channel shape, we concluded that both sides of our PCHE have similar flow characteristics.

For heat transfer characteristics of our PCHE, we first measured the heat transfer with water on both the hot and cold sides in order to establish a water-based reference in the precooler. Based on the Fanning friction factor data, it was assumed that if both the hot and cold sides have similar flow characteristics, then the heat transfer characteristics are likely to be similar. In addition, we justifiably neglected the thermal resistance of the metal wall between the hot and cold side channels. Heat transfer tests were conducted while maintaining the Reynolds number and temperature as constant as possible on both sides, in a temperature range for water flowing through the precooler under projected operating condition. The heat transfer coefficient with water was determined to be linear with the Reynolds number; the correlation between the heat transfer coefficient and the Re-number using a linear regression trend line is as follows,

$$h_{H_2O}[W/m^2K] = 11.04 \times Re_{H_2O} + 570.36 \quad R^2 = 0.99$$

where, R^2 is the coefficient of correlation.

As for heat transfer characteristics of S-CO_2 in the PCHE, heat transfer tests were conducted in a small temperature range, and precooler operating range. A small temperature range test was selected to study the effect of the specific heat on the heat transfer rate of S-CO_2, while additional tests were conducted with the precooler operating range to check for heat transfer enhancement near the outlet region on the CO_2 side.

In the small temperature range test, the difference between the inlet and outlet temperature on the CO_2 side was kept as small as possible; here as noted, the specific heat changes rapidly near the critical point. The heat transfer markedly increases and decreases about the pseudocritical temperatures with rapid change in specific heat. Similarly the thermal conductivity and enthalpy increase about the critical point; however, density, viscosity and thermal diffusivity decrease about the critical point. Thus very near the pseudocritical point, both the heat transfer and heat transfer coefficient can assume large values. The small temperature range test showed that the heat transfer coefficient is strongly correlated with the specific heat, relative to other thermophysical quantities. Similar results were observed by previous studies, including other refrigerants. Based on this one might expect heat transfer enhancement near the outlet region of the

CO_2 in the precooler operating range because the outlet of the CO_2 side was set near the pseudocritical point.

In order to study the heat transfer augmentation near the pseudocritical point theorectical pressure, under the precooler operating range, two sets of tests were carried out at 7.5MPa (just above 7.4MPa). One set had the CO_2 outlet temperature closer to the pseudocritical point than the other. Prior to the experiment, we expected that the test set with outlet temperature closer to the pseudocritical point might have a larger convective heat transfer coefficient than a test case further away from the pseudocritical point. As shown in the small temperature test, the heat transfer coefficient for CO_2 in the PCHE increases with the specific heat near the pseudocritical point (at a given pressure). The CO_2 outlet temperature of the precooler is slightly higher than the pseudocritical point at the given pressure, 7.5MPa. From the experimental results, the expected heat transfer augmentation near the outlet region of the CO_2 side was not observed under the precooler operating range with our PCHE.

One more test at 8.5MPa was conducted to study the relationship between the heat transfer and pressure because the specific heat changes less dramatically here with pressure. As the outlet temperature of the CO_2 side is set close to the pseudocritical point at test pressure, the change in heat transfer coefficient was investigated at 7.5 and 8.5MPa. In fact, the specific heat at 7.5MPa is much larger than at 85bar, at the corresponding critical temperature. However, beyond the pseudocritical region, the specific heat at 8.5MPa is generally larger than at 7.5MPa (broad versus a sharp peak). From this test, we found that the heat transfer rate on the hot side was not influenced by the pseudocritical region but the average heat transfer coefficient at 8.5MPa is higher than that at 7.5MPa. We thus found that the heat transfer enhancement does not occur in the precooler operating region.

In terms of data analysis and PCHE modeling, a traditional approach cannot be taken as thermophysical properties rapidly change about the critical point. We thus developed a nodal model of our PCHE. The nodal calculation is based on the application of thermodynamics (1^{st} law) to ideal/pure fluids. The PCHE is split into 15 sections, and an energy balance (a log-mean temperature method) is applied to each section of the PCHE. In this model, the geometry of the channel is not considered, but simply the

average temperature in each section. The model showed that most of the heat transfer takes place near the inlet region of the CO_2 side, and the CO_2 temperature does not change much near the outlet region. However, large changes in specific heat maintain high heat transfer. Our nodal model accurately predicted the experimentally observed PCHE inlet/outlet temperatures.

Lastly, in order to verify and compare the nodal model, limited CFD simulations were also conducted with an idealized zigzag channel configuration. The commercial CFD code, Fluent, was used. The CFD simulations were based on the estimated dimensions of the PCHE and only the change in specific heat was modeled. The simulation substantiated the suitability of the nodal model in terms of temperature distribution along the heat exchanger. The predicted temperature distribution shows that the CO_2 temperature changes appreciably near the inlet region, but much less near the outlet region of the PCHE. This means that most of the heat exchange occurs near the inlet region on the CO_2 side, while rapid increase in the specific heat near the pseudo-critical maintains high heat transfer near the outlet.

References

[1] Adams, T. M., 1998, "An Experimental Investigation of Single-Phase Forced Convection in Microchannels," International Journal of Heat and Mass Transfer, **41**(6) pp. 851.

[2] Babu, B.V., 2005 "Evaluation of existing treatment techniques and various problems associated with nuclear waste management," Energy Education Science and Technology, 14(2) pp. 93

[3] Bringer, R. P., 1957, "Heat transfer in the Critical Region," AIChE J., 3(1), pp. 49

[4] Haynes, B. S., 2002, "High-effectiveness micro-exchanger performance," Heatric (A division of Meggitt)

[5] Heatric website: www.heatric.com

[6] Huai, X. L., 2005, "An Experimental Study of Flow and Heat Transfer of Supercritical Carbon Dioxide in Multi-Port Mini Channels Under Cooling Conditions," Chemical Engineering Science, **60**(12) pp. 3337.

[7] Incropera, F. P., "Introduction to Heat transfer," 4th edition, Wiley.

[8] Ishizuka, T., 2005, "Thermal-Hydraulic Characteristics of a Printed Circuit Heat Exchanger in a Supercritical CO_2 Loop," The 11th International Topical Meeting on Nuclear Reactor Thermal-Hydraulics (NURETH-11), Popes' Palac Conference Cener, Avignon, France, October 2-6,2005

[9] Jiao, Z., 1987, "RESISTANCE AND HEAT TRANSFER IN ZIGZAG DUCT AND THE PERFORMANCE OF PLATE HEAT EXCHANGERS." HTD, **76** pp. 85.

[10] Kandlikar, S. G., 2003, "Evolution of Microchannel Flow Passages-Thermohydraulic Performance and Fabrication Technology," Heat Transfer Engineering, 24(1) pp. 3.

[11] Kiran, E., "Supercritical fluids: Fundamentals and applications," Publisher: Springer; 1 edition (August 30, 2005)

[12] Lee, S. H., 1998, "Turbulent Developing Convective Heat Transfer in a Tube for Fluids Near the Critical Point," International Journal of Heat and Mass Transfer, **41**(10) pp. 1205.

[13] Lee, Y. S., 2003, "Experimental Study on Heat Transfer in Wavy Channels," Journal of Enhanced Heat Transfer, **10**(1) pp. 21.

[14] Liao, S. M., 2002, "An Experimental Investigation of Convection Heat Transfer to Supercritical Carbon Dioxide in Miniature Tubes," International Journal of Heat and Mass Transfer, **45**(25) pp. 5025.

[15] Liao, S. M., 2002, "Measurements of Heat Transfer Coefficients from Supercritical Carbon Dioxide Flowing in Horizontal mini/micro Channels," Journal of Heat Transfer, **124**(3) pp. 413.

[16] Liao, S. M., 2002, "A Numerical Investigation of Laminar Convection of Supercritical Carbon Dioxide in Vertical mini/micro Tubes," Progress in Computational Fluid Dynamics, **2**(2) pp. 144.

[17] Lomperski, S., 2006, "Testing of a Compact Heat Exchanger for use as the Cooler in a Supercritical CO_2 Brayton Cycle," Proceedings of the 2006 International Congress on Advances in Nuclear Power Plants, ICAPP'06, 2006, pp. 1745.

[18] Lomperski, S., 2004, "Stability of a Natural Circulation Loop with a Fluid Heated through the Thermodynamic Pseudocritical Point," pp. 1736.

[19] McAdams, W. H.," Heat Transmission," 2nd edition, McGraw-Hill, New York, NY, USA

[20] Moisseytsev, A., 2003, "Passive load follow analysis of the STAR-LM and STAR-H2 systems," Ph. D. degree thesis.

[21] NIST website: http://webbook.nist.gov/chemistry/fluid/

[22] Nuclear Energy Institute: http://www.nei.org

[23] O'Brien, J. E., 1982, "Corrugated-Duct Heat Transfer, Pressure Drop, and Flow Visualization," Journal of Heat Transfer, 104(3) pp. 410.

[24] Peiyi, W., 1983, "Measurement of Friction Factors for the Flow of Gases in very Fine Channels used for Microminiature Joule-Thomson Refrigerators," Cryogenics, 23(5) pp. 273.

[25] Peng, X. F., 1996, "Convective Heat Transfer and Flow Friction for Water Flow in Microchannel Structures," International Journal of Heat and Mass Transfer, **39**(12) pp. 2599.

[26] Peng, X. F., 1995, "Effect of Thermofluid and Geometrical Parameters on Convection of Liquids through Rectangular Microchannels," International Journal of Heat and Mass Transfer, **38**(4) pp. 755.

[27] Peng, X. F., 1994, "Heat Transfer Characteristics of Water Flowing through Microchannels," Experimental Heat Transfer, **7**(4) pp. 265.

[28] Peterson, P. F., 2003, "Multiple-Reheat Brayton Cycles for Nuclear Power Conversion with Molten Coolants," Nuclear Technology, 144(3) pp. 279.

[29] Pettersen, J., 2000, " Heat transfer and pressure drop characteristics of supercritical carbon dioxide in microchannel tubes under cooling," IIF-IIR Commission B1, B2 with E1, E2, Purdue University, pp. 315

[30] Sabersky, R. H., 1967, "Forced Convection Heat Transfer to Carbon Dioxide Near the Critical Point," International Journal of Heat and Mass Transfer, **10**(11) pp. 1499.

[31] Shah, R. K., "Fundamentals of Heat Exchanger Design", 1st edition, Wiely.

[32] Sienicki, J. J., 2003, "The STAR-LM Lead-Cooled Closed Fuel Cycle Fast Reactor Coupled to a Supercritical Carbon Dioxide Brayton Cycle Advanced Power Converter," pp. 916.

[33] Swenson, H. S., 1965, "Heat transfer to supercritical water in smooth-bore tubes," Journal of Heat Transfer, pp. 477.

[34] Wood, R. D., "Heat transfer in the critical region temperature and velocity profiles in turbulent flow," A. I. Ch. E Journal, **10**(2) pp. 180.

Appendix A - Experimental Data

Table A.1 Experiment range of pressure drop on the hot side using water

Test No.	$\dot{m}_h$	Δp_h	q	$T_{h,in}$	$T_{h,out}$	Re	f
	kg/hr	kPa	kW	^oC	^oC	-	-
1	53.29	0.50	0.00	22.52	21.80	13.68	376.50
2	104.69	1.00	0.00	23.35	23.12	27.57	192.55
3	163.09	1.63	0.00	21.58	22.58	41.81	129.59
4	207.21	2.20	0.00	19.80	20.88	50.93	108.50
5	250.50	2.83	0.00	18.41	18.93	59.04	95.73
6	297.34	3.53	0.00	17.89	18.18	69.03	84.67
7	403.89	5.28	0.00	17.59	17.80	92.94	68.75
8	503.01	7.18	0.00	17.57	17.78	115.61	60.24
9	709.16	11.77	0.00	17.15	17.28	161.12	49.68
10	796.10	13.99	0.00	16.89	16.99	179.72	46.85
11	905.08	16.93	0.00	16.69	16.82	203.27	43.87
12	1001.12	19.65	0.00	16.75	16.87	225.13	41.62
13	1097.14	22.61	0.00	16.54	16.65	245.46	39.88
14	1207.30	26.21	0.00	16.44	16.57	269.41	38.18
15	1302.15	29.56	0.00	16.47	16.55	290.58	37.00
16	1409.57	31.53	0.00	16.40	16.51	314.15	33.69
17	190.12	1.40	7.96	50.13	49.87	84.88	82.12
18	310.53	2.55	12.48	50.31	50.02	138.98	55.61
19	400.73	3.71	16.17	50.21	50.05	179.25	48.52
20	600.28	6.61	23.88	50.08	50.05	268.25	38.90
21	805.05	10.57	31.98	50.05	50.03	359.57	34.59
22	999.34	15.06	39.43	49.93	49.92	445.46	31.66
23	1199.13	20.20	47.46	50.02	50.03	535.31	29.80

Table A.2 Experiment range of pressure drop on the cold side using water

Test No.	$\dot{m}_c$	Δp_c	q	$T_{c,in}$	$T_{c,out}$	Re	f
	kg/hr	kPa	kW	°C	°C	-	-
1	153.27	1.66	7.02	50.57	49.84	77.30	104.34
2	309.32	4.62	13.61	50.24	50.05	155.81	71.38
3	517.01	10.11	21.42	50.19	50.17	260.58	55.92
4	703.00	17.17	28.87	50.43	50.34	355.57	51.37
5	981.15	29.94	39.71	50.21	50.22	494.81	45.98
6	1199.21	42.11	43.04	50.26	50.27	605.13	43.29
7	105.43	1.37	0.00	17.57	17.15	27.07	184.76
8	216.92	3.42	0.00	17.61	17.43	55.95	108.70
9	300.59	5.46	0.00	17.56	17.52	77.58	90.26
10	470.28	10.84	0.00	17.22	17.40	120.61	73.28
11	634.82	17.44	0.00	16.92	17.08	161.55	64.69
12	837.31	27.18	0.00	16.86	16.93	212.53	57.95
13	1048.25	40.07	0.00	17.00	17.07	267.11	54.51
14	1194.14	50.52	0.00	16.84	16.94	303.10	52.97
15	1389.72	65.04	0.00	16.80	16.89	352.29	50.35

Table A.3 Experiment range of water to water test

Test No.	$\dot{m}_h$	$\dot{m}_h$	Δp_h	Δp_h	$T_{h,in}$	$T_{h,out}$	$T_{c,in}$	$T_{c,out}$
	kg/s	kg/s	kPa	kPa	°C	°C	°C	°C
W1	0.3	0.3	19.9	51.6	49.9	16.9	13.6	46.3
W2	0.26	0.25	15.8	39.4	50.2	16.5	13.2	46.8
W3	0.23	0.23	13.3	32.4	50.2	16.2	12.8	46.8
W4	0.19	0.19	9.7	23.5	50.0	15.9	12.8	46.5
W5	0.11	0.13	4.9	10.8	49.9	15.3	12.6	46.6
W6	0.12	0.12	5.3	10.6	49.8	16.3	13.0	47.6
W7	0.09	0.1	3.5	7.1	49.8	15.9	13.1	47.3
W8	0.06	0.06	1.9	3.7	50.0	15.4	13.3	47.1
W9	0.03	0.03	1.1	1.7	50.1	15.6	13.8	47.9

Table A.4 The test conditions of Test A using CO_2

Test No.	p_h	T_{pseudo}	C_{p_pseudo}	$\dot{m}_h$	T_{h_in}	T_{h_out}	Q_c	T_{c_in}	T_{c_out}
	bar	°C	J/g·K	kg/sec	°C	°C	gpm	°C	°C
A1	74.71	31.54	309.26	212.52	87.90	31.59	2.92	28.17	42.39
A2	74.72	31.53	302.31	318.48	88.40	31.59	2.88	25.51	47.10
A3	74.74	31.56	298.38	431.20	85.05	31.54	2.93	22.21	50.77
A4	74.75	31.56	292.80	623.93	76.18	31.57	2.90	16.14	54.54

Table A.5. The test conditions of Test B using CO_2

Test No.	p_h	T_{pseudo}	C_{p_pseudo}	$\dot{m}_h$	T_{h_in}	T_{h_out}	Q_c	T_{c_in}	T_{c_out}
	bar	°C	J/g·K	kg/sec	°C	°C	gpm	°C	°C
B1	74.38	31.34	500.46	135.08	88.58	32.08	3.05	31.97	38.40
B2	74.27	31.27	622.28	208.61	87.86	31.76	2.99	31.32	41.44
B3	74.58	31.46	364.84	280.43	87.38	31.86	3.02	30.90	44.47
B4	74.74	31.56	298.38	358.72	88.30	31.85	2.94	30.01	47.87
B5	74.95	31.68	239.11	444.05	86.60	31.86	2.93	28.53	51.11

Table A.6 The test conditions of Test C using CO_2

Test No.	p_h	T_{pseudo}	C_{p_pseudo}	$\dot{m}_h$	T_{h_in}	T_{h_out}	Q_c	T_{c_in}	T_{c_out}
	bar	°C	J/g·K	kg/sec	°C	°C	gpm	°C	°C
C1	84.11	36.9	20.348	180.46	90.89	37.43	3.04	37.32	46.90
C2	83.97	36.8	20.643	270.97	90.45	37.31	3.07	36.44	50.67
C3	84.33	37	19.907	374.19	89.03	37.28	3.06	34.80	54.80
C4	84.40	37.04	19.77	478.40	87.53	37.18	3.04	32.52	58.32
C5	84.56	37.12	19.464	581.02	86.78	37.19	3.05	30.19	61.44
C6	84.81	37.26	19.005	682.29	86.27	37.28	3.06	27.82	64.29

Appendix B - Error analysis

If variable Z is relations with variables such as A and B, the rule for calculating the error in Z is tabulated in following table. The error analysis in this study is estimated by following Table 1.

Table B.1 Rule of error analysis

	Relation between Z and (A,B)	Relation between errors ΔZ and (ΔA, ΔB)
1	Z = A + B	$(\Delta Z)^2 = (\Delta A)^2 + (\Delta B)^2$
2	Z = A - B	$(\Delta Z)^2 = (\Delta A)^2 + (\Delta B)^2$
3	Z = AB	$\left(\frac{\Delta Z}{Z}\right)^2 = \left(\frac{\Delta A}{A}\right)^2 + \left(\frac{\Delta B}{B}\right)^2$
4	Z = A/B	$\left(\frac{\Delta Z}{Z}\right)^2 = \left(\frac{\Delta A}{A}\right)^2 + \left(\frac{\Delta B}{B}\right)^2$
5	$Z = A^n$	$\frac{\Delta Z}{Z} = n\frac{\Delta A}{A}$
6	Z = ln A	$\Delta Z = \frac{\Delta A}{A}$
7	$Z = e^A$	$\frac{\Delta Z}{Z} = \Delta A$

(cf.: http://teacher.nsrl.rochester.edu/phy_labs/AppendixB/AppendixB.html)

The heat transfer coefficient for CO_2 is defined by Equation 1 in this study. Equation 1 is rearranged into Equation 2.

$$\frac{1}{h_{CO_2}} = \frac{1}{U} - \frac{1}{h_{H_2O}} = \frac{h_{H_2O} - U}{U \cdot h_{H_2O}} \tag{1}$$

$$h_{CO_2} = \frac{U \cdot h_{H_2O}}{h_{H_2O} - U} \tag{2}$$

Propagated errors in h_{CO_2} due to errors in U and h_{H_2O} is expressed by the fourth rule in Table 1 as follows.

$$\frac{\Delta h_{CO_2}}{h_{CO_2}} = \left[\left(\frac{\Delta(U \cdot h_{H_2O})}{U \cdot h_{H_2O}} \right)^2 + \left(\frac{\Delta(h_{H_2O} - U)}{h_{H_2O} - U} \right)^2 \right]^{1/2} \tag{3}$$

The overall coefficient, U, is defined by equation 4.

$$q = AU\Delta T_{lm} \tag{4}$$

The errors in U are written by the fourth rule in Table 1.

$$\frac{\Delta U}{U} = \left[(\frac{\Delta q}{q})^2 + (\frac{\Delta T_{lm}}{T_{lm}})^2 \right]^{1/2} \tag{5}$$

q can be defined in terms of enthalpy and mass flow rate of CO_2.

$$q = \dot{m}_{CO2} \cdot [i_h - i_l] \tag{6}$$

Errors in q is written by the forth rule as,

$$\frac{\Delta q}{q} = \{ (\frac{\Delta \dot{m}_{CO2}}{\dot{m}_{CO2}})^2 + (\frac{\Delta[i_h - i_l]}{[i_h - i_l]})^2 \}^{1/2} \tag{7}$$

In Equation 7, the errors in the enthalpy term are written by the second rule as follows.

$$\Delta[i_h - i_l] = \left[(\Delta i_h)^2 + (\Delta i_l)^2 \right] \tag{8}$$

The enthalpy is affected by temperature which is measured by RTDs. They have the accuracy of 0.1°C. From Table 1, we can take the hot side inlet and outlet temperature. Based on Table 1, enthalpies at 0.1°C higher and lower than the inlet and outlet temperature are shown in Table 2.

Table B.2 Experimental data

$T_{h,in}$	$T_{h,out}$	$T_{c,in}$	$T_{c,out}$	ΔT_{lm}	U	Re_h	Re_c	h_{H2O}	h_{CO2}
°C	°C	°C	°C	°C	W/m^2	-	-	W/m^2	W/m^2
85.05	31.54	22.21	50.77	19.17	201.53	4643.16	221.83	3018.29	215.95

Table B.3 Enthalpy for the hot side

Temperature	i_{in}	Temperature	i_{out}
79.95°C	503.74 kJ/kg	31.44°C	316.59 kJ/kg
80.05°C	503.88 kJ/kg	31.54 °C	340.03 kJ/kg
80.15°C	504.02 kJ/kg	31.64°C	351.74 kJ/kg

Using Table 2, we can calculate the errors of enthalpy as shown in the below equations.

$$\Delta i_{in} = (504.02 - 503.88) = 0.14 \tag{9}$$

$$\frac{\Delta i_{in}}{i_{in}} = \frac{(504.02 - 503.88)}{503.88} = 0.000278 \tag{10}$$

$$\Delta i_{out} = (351.74 - 340.03) = 11.71 \tag{11}$$

$$\frac{\Delta i_{out}}{i_{out}} = \frac{(351.74 - 340.03)}{340.03} = 0.0344 \tag{12}$$

These calculated results are substituted into Equation 8 as follows.

$$\begin{aligned}\Delta[i_{in} - i_{out}] &= \left[(\Delta i_{in})^2 + (\Delta i_{out})^2\right]^{1/2} \\ &= [(0.14)^2 + (11.71)^2]^{1/2} \\ &= 11.71\end{aligned} \tag{13}$$

For the mass term, mass flow meter has accuracy better than 0.5 %. So we can define the errors in the mass flow rate.

$$\frac{\Delta \dot{m}_{CO2}}{\dot{m}_{CO2}} = 0.005 \tag{14}$$

$$\begin{aligned}\frac{\Delta q}{q} &= \{(\frac{\Delta \dot{m}_{CO2}}{\dot{m}_{CO2}})^2 + (\frac{\Delta[i_h - i_l]}{[i_h - i_l]})^2\}^{1/2} \\ &= \left[(0.005)^2 + \left(\frac{11.71}{(503.88 - 340.03)}\right)^2\right]^{1/2} \\ &= 0.716\end{aligned} \tag{15}$$

Next, we need to estimate the errors in the log mean temperature difference, which is defined by Equation 16.

$$\Delta T_{lm} = \frac{\left(T_{h,out} - T_{c,in}\right) - \left(T_{h,in} - T_{c,out}\right)}{\ln\left[\left(T_{h,out} - T_{c,in}\right)/\left(T_{h,in} - T_{c,out}\right)\right]} \tag{16}$$

From the fourth rule, errors in the log mean temperature difference is written as follows.

$$\frac{\Delta T_{lm}}{T_{lm}} = \left[\left(\frac{\Delta\left[\left(T_{h,out} - T_{c,in}\right) - \left(T_{h,in} - T_{c,out}\right)\right]}{\left[\left(T_{h,out} - T_{c,in}\right)/\left(T_{h,in} - T_{c,out}\right)\right]} \right)^2 + \left(\frac{\Delta\left(\ln\left[\left(T_{h,out} - T_{c,in}\right) - \left(T_{h,in} - T_{c,out}\right)\right]\right)}{\ln\left[\left(T_{h,out} - T_{c,in}\right)/\left(T_{h,in} - T_{c,out}\right)\right]} \right)^2 \right]^{1/2} \quad (17)$$

For $\left(T_{h,out} - T_{c,in}\right) - \left(T_{h,in} - T_{c,out}\right)$, the errors are estimated based on the accuracy of 0.1°C by the first rule as shown in Table 1.

$$[(0.1)^2 + (0.1)^2 + (0.1)^2 + (0.1)^2]^{1/2} = 0.2 \quad (18)$$

$$\left(T_{h,out} - T_{c,in}\right) - \left(T_{h,in} - T_{c,out}\right) = (85.05 - 50.77) - (31.54 - 22.21) = 19.95 \quad (19)$$

In $\ln\left[\frac{\left(T_{h,out} - T_{c,in}\right)}{\left(T_{h,in} - T_{c,out}\right)}\right]$ term, we define the term inside the bracket as follows.

$$D \equiv \frac{\left(T_{h,out} - T_{c,in}\right)}{\left(T_{h,in} - T_{c,out}\right)} \equiv \frac{A}{B} \quad (20)$$

We can calculate the errors in A and B due to the RTDs' error (0.1 °C) by the second rule of Table 1.

$$\Delta A = \Delta B = [(0.1)^2 + (0.1)^2]^{1/2} = 0.14 \quad (21)$$

As follow the fourth rule, we can estimate the errors in D.

$$\frac{\Delta D}{D} = \left[\left(\frac{\Delta A}{A}\right)^2 + \left(\frac{\Delta B}{B}\right)^2\right]^{1/2}$$
$$= \left[\left(\frac{0.14}{29.28}\right)^2 + \left(\frac{0.14}{9.33}\right)^2\right]^{1/2}$$
$$= 0.015 \tag{22}$$

where $A = 85.05 - 50.77 = 29.28$, $B = 31.54 - 22.21 = 9.33$

Using Equation 22, we can estimate the error in $\ln\left[\frac{\left(T_{h,out} - T_{c,in}\right)}{\left(T_{h,in} - T_{c,out}\right)}\right]$ by following the sixth rule as shown in Equation 23.

$$\Delta\left\{\ln\left[\frac{\left(T_{h,out} - T_{c,in}\right)}{\left(T_{h,in} - T_{c,out}\right)}\right]\right\} = \frac{\Delta D}{D} = 0.015 \tag{23}$$

Therefore, errors in the log mean temperature difference is calculated as follows using the above results.

$$\frac{\Delta T_{lm}}{T_{lm}}$$
$$= \left[\left(\frac{\Delta\left[\left(T_{h,out} - T_{c,in}\right) - \left(T_{h,in} - T_{c,out}\right)\right]}{\left[\left(T_{h,out} - T_{c,in}\right)/\left(T_{h,in} - T_{c,out}\right)\right]}\right)^2 + \left(\frac{\Delta\left(\ln\left[\left(T_{h,out} - T_{c,in}\right) - \left(T_{h,in} - T_{c,out}\right)\right]\right)}{\ln\left[\left(T_{h,out} - T_{c,in}\right)/\left(T_{h,in} - T_{c,out}\right)\right]}\right)^2\right]^{1/2} \tag{24}$$
$$= \left[\left(\frac{0.2}{19.95}\right)^2 + \left(\frac{0.015}{1.14}\right)^2\right]^{1/2}$$
$$= 0.0165$$

$$\Delta T_{lm} = (0.0165) * (19.17) = 0.316 \tag{25}$$

Substituting the above results into 5, we can estimate errors in the overall coefficient as shown in Equation 26.

$$\frac{\Delta U}{U} = \left[(\frac{\Delta q}{q})^2 + (\frac{\Delta T_{lm}}{T_{lm}})^2 \right]^{1/2}$$
$$= \left[(0.07)^2 + (0.0165)^2 \right]^{1/2} \quad (26)$$
$$= 0.072$$

$$\Delta U = 0.072 * (204.18) = 14.7 \quad (27)$$

For errors in the water side, we need to look at the heat transfer coefficient of water, which is defined by Equation 28.

$$h_{H2O} = 11.035 * \mathrm{Re}_{H_2O} + 570.36 \quad (28)$$

Re_{H_2O} is defined as Equation 29 and errors in Reynolds number is estimated by Equation 30 from the fourth rule of Table 1.

$$\mathrm{Re}_{H2O} = \frac{\rho \cdot u \cdot D}{\mu} \quad (29)$$

$$\frac{\Delta \mathrm{Re}_{H_2O}}{\mathrm{Re}_{H_2O}} = \left[\left(\frac{\Delta \rho}{\rho} \right)^2 + \left(\frac{\Delta u}{u} \right)^2 + \left(\frac{\Delta \mu}{\mu} \right)^2 \right]^{1/2} \quad (30)$$

Density and viscosity are function of temperature in this study. The errors are caused by the temperature inaccuracy, 0.1°C.

Table B.4 Density and viscosity for CO_2

Temperature	Density	Viscosity
84.95°C	141.55 kg/m^3	19.792 μPa·s
85.05°C	141.46 kg/m^3	18.794 μPa·s
85.15°C	141.38 kg/m^3	19.797 μPa·s

Using the values shown in Table 3, each error in Equation 30 is calculated. The water velocity has errors occurred by the water flow meter, whose accuracy is 2 %.

$$\frac{\Delta u}{u} = 0.02 \tag{31}$$

$$\frac{\Delta \rho}{\rho} = \frac{(141.46 - 141.38)}{141.46} = 0.00056 \tag{32}$$

$$\frac{\Delta \mu}{\mu} = \frac{(19.794 - 19.797)}{19.794} = 0.00015 \tag{33}$$

Substitute the above results into Equation 30,

$$\frac{\Delta \mathrm{Re}_{H_2O}}{\mathrm{Re}_{H_2O}} = \left[\left(\frac{\Delta u}{u} \right)^2 + \left(\frac{\Delta \rho}{\rho} \right)^2 + \left(\frac{\Delta \mu}{\mu} \right)^2 \right]^{1/2} = 0.02 \tag{34}$$

So the error in heat transfer coefficient for water is calculated as follows.

$$\frac{\Delta h_{H_2O}}{h_{H_2O}} = \frac{48.96}{3018.29} = 0.016 \tag{35}$$

Now, the errors in heat transfer coefficient for CO_2 can be estimated by substitute the above results into Equation 3. Before that, we need to calculate the two terms in the right hand side of Equation 3 as follows.

$$\begin{aligned} \left(\frac{\Delta (U \cdot h_{H_2O})}{U \cdot h_{H_2O}} \right) &= \left[\left(\frac{\Delta U}{U} \right)^2 + \left(\frac{\Delta h_{H_2O}}{h_{H_2O}} \right)^2 \right]^{1/2} \\ &= \left[(0.072)^2 + (0.0162)^2 \right]^{1/2} \\ &= 0.074 \end{aligned} \tag{36}$$

$$\begin{aligned} \Delta (h_{H_2O} - U) &= \left[(\Delta h_{H_2O})^2 + (\Delta U)^2 \right]^{1/2} \\ &= \left[(48.96)^2 + (14.7)^2 \right]^{1/2} \\ &= 51.12 \end{aligned} \tag{37}$$

Therefore, errors in the heat transfer coefficient for CO_2 are estimated by Equation 38.

$$\frac{\Delta h_{CO_2}}{h_{CO_2}} = \left[\left(\frac{\Delta(U \cdot h_{H_2O})}{U \cdot h_{H_2O}} \right)^2 + \left(\frac{\Delta(h_{H_2O} - U)}{h_{H_2O} - U} \right)^2 \right]^{1/2}$$
$$= \left[(0.074)^2 + \left(\frac{51.12}{(3018.29 - 201.53)} \right)^2 \right]^{1/2} \quad (38)$$
$$= 0.076$$

So the error in heat transfer coefficient for CO_2 is ±8 %.

Appendix C - Order of magnitude analysis

We consider an order of magnitude analysis (OMA) of two-dimensional, steady-state laminar flow in a channel with convective heat transfer. The conservation equations for mass, momentum and energy are as follows with the corresponding algebraic form as indicated.

Taking the x-axis along the flow channel and the y-axis transverse to the same channel, in terms of mass conservation, we have,

$$\frac{\partial}{\partial x}(\rho u)+\frac{\partial}{\partial y}(\rho v)=0 \text{ and its OMA form is,} \tag{1}$$

$$\frac{1}{L}(\rho u)\sim\frac{1}{\delta}(\rho v) \tag{2}$$

where

u~ is the velocity scale of the velocity along the channel

v~ is the velocity scale of the transverse velocity component along the channel

L~ is the length scale along the channel

δ~ is, for the moment, either the momentum or thermal boundary layer thickness transverse to the channel

ρ ~ is the density of the heat transfer medium

So, the transverse velocity component scales as follows

$$v\sim\frac{\delta}{L}u \tag{3}$$

This scaling is as expected; that is, the transverse component is a fraction of the velocity along the channel, as defined by the ratio of the boundary layer thickness to length along the channel.

Next, the momentum equations appear as,

x-component: $$u\frac{\partial}{\partial x}(\rho u)+v\frac{\partial}{\partial y}(\rho u)=-\frac{\partial p}{\partial x}+\mu\left[\frac{\partial^2 u}{\partial x^2}+\frac{\partial^2 u}{\partial y^2}\right] \quad (4)$$

y-component: $$u\frac{\partial}{\partial x}(\rho v)+v\frac{\partial}{\partial y}(\rho v)=-\frac{\partial p}{\partial y}+\mu\left[\frac{\partial^2 v}{\partial x^2}+\frac{\partial^2 v}{\partial y^2}\right] \quad (5)$$

where additionally, μ is the dynamic viscosity.

Here OMA provides three possibilities as follows, that: 1) the inertial force balances the pressure gradient, 2) the inertial force balances the viscous force and 3) the inertial force balances a combination of the both the pressure gradient and viscous force. A fourth possibility that neglects the inertial force is nonsensical because inertial forces are inherent to convective flow. Since the velocity can be scaled in terms of the momentum and thermal boundary layer thickness (see below), we simply acknowledge the three possibilities and proceed to the energy conservation equation.

So, the energy conservation appears as,

$$\frac{\partial}{\partial x}(\rho u e)+\frac{\partial}{\partial y}(\rho v e)=\frac{\partial}{\partial x}\left[\frac{k}{c_p}\frac{\partial e}{\partial x}\right]+\frac{\partial}{\partial y}\left[\frac{k}{c_p}\frac{\partial e}{\partial y}\right] \quad (6)$$

where

e~ represents enthalpy and scales as E. Typically, enthalpy can represent the enthalpy difference between the inlet and outlet of a channel.

C_p ~ represents the specific heat of the medium.

Here, OMA gives,

$$\frac{1}{L}\rho u E+\frac{1}{\delta}\rho E\frac{u\delta}{L}\sim\frac{1}{L}\frac{k}{c_p}\frac{E}{L}+\frac{1}{\delta}\frac{k}{c_p}\frac{E}{\delta} \quad (7)$$

Since the convective terms are of the same magnitude, we further have,

$$\frac{1}{L}\rho u E\sim\frac{k}{c_p}\frac{E}{\delta^2}\left[\frac{\delta^2}{L^2}+1\right] \quad (8)$$

Now since the x-component of velocity scales as, $u \sim \frac{\delta_T}{\delta} U$, where U is the velocity beyond the thermal boundary thickness, δ_T, Equation (8) becomes,

$$\frac{\delta_T}{\delta} UL \sim \frac{\alpha L^2}{\delta^2}\left[\frac{\delta^2}{L^2}+1\right] \tag{9}$$

In fact, the above ratio of thermal-to-momentum boundary layer thickness is related to the Prandtl number as, $\frac{\delta_T}{\delta} = \mathrm{Pr}^{-1/3}$. Here, we limit our interest to fluids with Prandtl number is bigger than 1. So, it follows that,

$$\mathrm{Pr}^{-1/3}\frac{UL}{\alpha} \sim \frac{L^2}{\delta^2}\left[\frac{\delta^2}{L^2}+1\right] = 1+\frac{L^2}{\delta^2}\left[\frac{{\delta_T}^2}{{\delta_T}^2}\right] \tag{10}$$

$$\mathrm{Pr}^{-1/3}\,\mathrm{Re}\,\mathrm{Pr} \sim 1+\frac{L^2}{{\delta_T}^2}\left[\frac{{\delta_T}^2}{\delta^2}\right]$$

By noting that the Nusselt is scales as follows, $Nu^2 \sim L^2/\delta_T^2$, we have that, (11)

$$\mathrm{Re}\,\mathrm{Pr}^{2/3} \sim 1 + Nu^2\,\mathrm{Pr}^{-2/3} \tag{12}$$

or equally,

$$\mathrm{Re}\,\mathrm{Pr}^{4/3} \sim \mathrm{Pr}^{2/3} + Nu^2 \tag{13}$$

Typically, as Pr is on the order of "1, $O(Pr) \sim 1$, and the Nusselt number is (much) larger than "1", $O(Nu) >> 1$, $Nu^2 >> Pr^{2/3}$. In this case Equation 13 simplifies to,

$$\mathrm{Re}\,\mathrm{Pr}^{4/3} \sim Nu^2 \tag{14}$$

We note in this case that $Nu \sim Re^{1/2} Pr^{2/3}$ and in so doing, confirm the correctness of our analysis, as this functional dependence on *Re* and *Pr* is typically observed in convective correlations.

This result thus suggests plotting our data as follows,

$$(Nu^2 + \mathrm{Pr}^{2/3}) \sim f(\mathrm{Re}\,\mathrm{Pr}^{4/3}) \qquad (15)$$

so as to reveal differences in the dependence on the Reynolds and Prandtl numbers. In fact, as the change in the specific heat strongly influences the Prandtl number (relative to changes in viscosity and thermal conductivity, Equation (15) should reveal differences in the heat transfer near the critical point for CO_2. The results presented support this perspective via this OMA.

Appendix D - Experimental procedure

D.1. Initial charge of CO_2

1) Turn on the data acquisition system, LabVIEW program, to monitor the loop.
2) Connect the vacuum pump with the swage lock ¼" fitting on the Primary line just after the heating pipe section using ¼" hose of the pump.
3) Operate the vacuum pump until the primary line gets to 0.1bar.
4) Turn off the vacuum pump, and open the CO_2 reservoir tank to charge the primary loop with CO_2 to slightly above 1 bar.
5) Repeat step 2 and 4 three times.
6) After step 4, charge the primary loop with CO_2 to 3bar.
7) Disconnect the vacuum pump hose from the swage lock and place the swage lock cover quickly.
8) Then, open the valve of the CO_2 reservoir tank, and charge the primary loop with CO_2 until the pressure of the hot side loop becomes near that of the CO_2 reservoir tank.
9) Close the valve of the CO_2 reservoir tank.

D.2. Supplemental Charging of CO_2

In order to make supercritical state of CO_2, it is necessary to cool down the hot (CO_2) side loop. When the temperature of the hot side loop becomes lower than the room temperature, it is possible to put more CO_2 into the test loop.

1) Turn the 3 way valve on the cold side loop to make lab water flow through the copper cooling coils.
2) Turn on the pump and then the refrigerator of the cooler.
3) Open the faucet of the cold water in the lab.
4) Open the valve of the outlet water.
5) Turn on the Micro magnetic pump fixing the speed to 10 Hz.

6) When the pressure of the hot side loop becomes about 55 bar, open the CO_2 reservoir tank.
7) Continue charging the CO_2 until the temperature of the hot side becomes 10 C.
8) After completing step 7, turn off the cooler and turn the 3 way valve to circulate the lab water not through the copper cooling coils.
9) Turn on the three way valve on the secondary line to make water come through the coil cooler.
10) Open the cold water valve and the drain valve.
11) Turn on the switch of the pump of the chiller out of the lab, and then push "P" to set the outlet temperature of the coolant on the manual board of the chiller.
12) Turn the refrigeration switch on.
13) When the primary temperature becomes 10^oC lower than the before the temperature, open the valve of the CO_2 reservoir tank.
14) Charge the primary loop until the temperature of the primary inlet CO_2 becomes 10^oC.
15) When the temperature of the primary inlet CO_2 reaches 10^oC, close the valve on the CO_2 reservoir and the valve before the pressurizer.

D.3. Experiment procedure

1) Turn on the switches on the gage board.
2) Turn on the data acquisition system, LabVIEW program : HP daq.vi, run charts.vi, heatrtic globals.vi, and run front panel.vi
3) Open the valve of the cold water.
4) Check the initial condition of the experimental loop.
5) If the differential pressure does not designate near zero value, check the differential pressure transmitter and vent the air in it.
6) If everything is checked and fine, then, name the experiment that will be conducted.
7) If the data acquisition starts, turn on the valve of the cold water and the drain valve.

Appendix E - Thermophysical properties of CO_2

In this part, thermophysical properties of CO_2 will be introduced at 74, 75, 80, 85, and 90bar. At each pressure, specific heat, density, thermal conductivity, enthalpy, viscosity, and thermal diffusivity will be shown in the order.

Table E.1 Thermal properties at 74bar

Temperature (°C)	Density (kg/m3)	Internal Energy (kJ/kg)	Enthalpy (kJ/kg)	Cv (J/g*K)	Cp (J/g*K)	Viscosity (uPa*s)	Therm. Cond. (W/m*K)	Phase
20	816.82	10.543	10.942	42.228	138.61	73.661	0.091125	liquid
21	806.68	10.679	11.083	42.441	143.7	71.828	0.089651	liquid
22	795.93	10.82	11.23	42.687	149.69	69.952	0.08815	liquid
23	784.43	10.968	11.383	42.973	156.87	68.021	0.086623	liquid
24	772.03	11.122	11.544	43.312	165.67	66.018	0.085073	liquid
25	758.5	11.286	11.715	43.722	176.78	63.923	0.083507	liquid
26	743.52	11.461	11.899	44.232	191.43	61.703	0.081946	liquid
27	726.57	11.651	12.1	44.892	211.98	59.307	0.080437	liquid
28	706.7	11.865	12.326	45.795	243.54	56.643	0.0791	liquid
29	682.02	12.117	12.595	47.147	299.66	53.528	0.078267	liquid
30	647.42	12.447	12.95	49.631	434.86	49.484	0.079145	liquid
31	565.95	13.139	13.715	64.201	2085.7	41.192	0.10034	supercritical
32	314.99	15.628	16.662	54.789	629.89	23.702	0.060668	supercritical
33	288.25	16.006	17.135	50.567	372.81	22.474	0.049917	supercritical
34	271.82	16.258	17.456	48.191	280.28	21.79	0.044723	supercritical
35	259.77	16.456	17.71	46.536	230.85	21.327	0.04144	supercritical
36	250.2	16.622	17.924	45.282	199.57	20.984	0.039112	supercritical
37	242.23	16.768	18.112	44.283	177.77	20.717	0.03735	supercritical
38	235.4	16.898	18.281	43.461	161.6	20.501	0.035958	supercritical
39	229.41	17.017	18.436	42.769	149.07	20.324	0.034826	supercritical
40	224.07	17.127	18.58	42.174	139.04	20.176	0.033884	supercritical
41	219.26	17.23	18.715	41.655	130.81	20.051	0.033089	supercritical
42	214.88	17.327	18.842	41.198	123.91	19.944	0.032407	supercritical
43	210.86	17.419	18.963	40.79	118.05	19.852	0.031818	supercritical
44	207.14	17.506	19.079	40.422	112.98	19.773	0.031303	supercritical
45	203.68	17.59	19.189	40.089	108.57	19.704	0.030851	supercritical
46	200.45	17.671	19.296	39.786	104.67	19.645	0.030451	supercritical
47	197.42	17.749	19.399	39.508	101.21	19.594	0.030095	supercritical
48	194.57	17.825	19.499	39.251	98.12	19.549	0.029778	supercritical
49	191.87	17.898	19.595	39.015	95.332	19.511	0.029494	supercritical
50	189.31	17.969	19.689	38.795	92.807	19.478	0.029239	supercritical
51	186.89	18.038	19.781	38.591	90.508	19.45	0.02901	supercritical
52	184.57	18.106	19.87	38.401	88.406	19.426	0.028804	supercritical

53	182.36	18.172	19.958	38.224	86.476	19.407	0.028617	supercritical
54	180.25	18.237	20.043	38.058	84.698	19.39	0.028449	supercritical
55	178.23	18.3	20.127	37.903	83.053	19.377	0.028297	supercritical
56	176.28	18.362	20.21	37.758	81.528	19.367	0.028159	supercritical
57	174.41	18.423	20.29	37.621	80.109	19.36	0.028035	supercritical
58	172.62	18.483	20.37	37.493	78.786	19.355	0.027922	supercritical
59	170.88	18.542	20.448	37.373	77.55	19.353	0.027821	supercritical
60	169.21	18.6	20.525	37.259	76.391	19.352	0.02773	supercritical
61	167.59	18.658	20.601	37.153	75.304	19.354	0.027647	supercritical
62	166.03	18.714	20.676	37.052	74.281	19.357	0.027574	supercritical
63	164.52	18.77	20.749	36.958	73.317	19.362	0.027508	supercritical
64	163.05	18.825	20.822	36.868	72.407	19.369	0.027449	supercritical
65	161.63	18.879	20.894	36.784	71.547	19.377	0.027397	supercritical
66	160.24	18.933	20.965	36.704	70.733	19.387	0.027351	supercritical
67	158.9	18.986	21.036	36.629	69.96	19.398	0.027311	supercritical
68	157.6	19.039	21.105	36.557	69.227	19.41	0.027277	supercritical
69	156.33	19.091	21.174	36.49	68.53	19.423	0.027247	supercritical
70	155.09	19.142	21.242	36.426	67.866	19.437	0.027222	supercritical
71	153.89	19.194	21.31	36.366	67.234	19.452	0.027202	supercritical
72	152.71	19.244	21.377	36.309	66.63	19.469	0.027185	supercritical
73	151.57	19.294	21.443	36.255	66.054	19.486	0.027172	supercritical
74	150.45	19.344	21.509	36.203	65.503	19.504	0.027163	supercritical
75	149.36	19.394	21.574	36.155	64.977	19.523	0.027158	supercritical
76	148.3	19.443	21.639	36.109	64.472	19.543	0.027156	supercritical
77	147.26	19.491	21.703	36.065	63.989	19.563	0.027156	supercritical
78	146.24	19.54	21.767	36.024	63.525	19.584	0.02716	supercritical
79	145.24	19.588	21.83	35.985	63.08	19.606	0.027166	supercritical
80	144.27	19.636	21.893	35.948	62.652	19.628	0.027175	supercritical
81	143.31	19.683	21.955	35.913	62.241	19.651	0.027187	supercritical
82	142.38	19.73	22.018	35.88	61.846	19.675	0.0272	supercritical
83	141.46	19.777	22.079	35.849	61.465	19.699	0.027216	supercritical
84	140.56	19.824	22.14	35.819	61.099	19.724	0.027234	supercritical
85	139.68	19.87	22.201	35.791	60.746	19.749	0.027254	supercritical
86	138.82	19.916	22.262	35.765	60.406	19.774	0.027276	supercritical
87	137.97	19.962	22.322	35.74	60.077	19.801	0.0273	supercritical
88	137.14	20.007	22.382	35.717	59.761	19.827	0.027325	supercritical
89	136.33	20.053	22.442	35.695	59.455	19.854	0.027352	supercritical
90	135.53	20.098	22.501	35.675	59.16	19.882	0.027381	supercritical

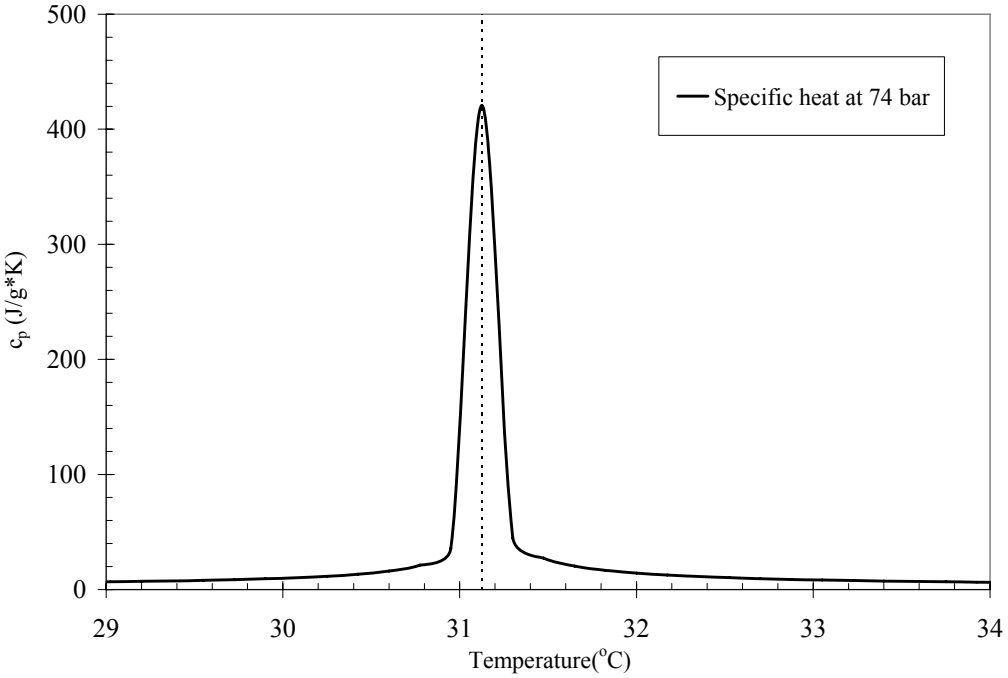

Figure E.1 Specific heat at 74bar

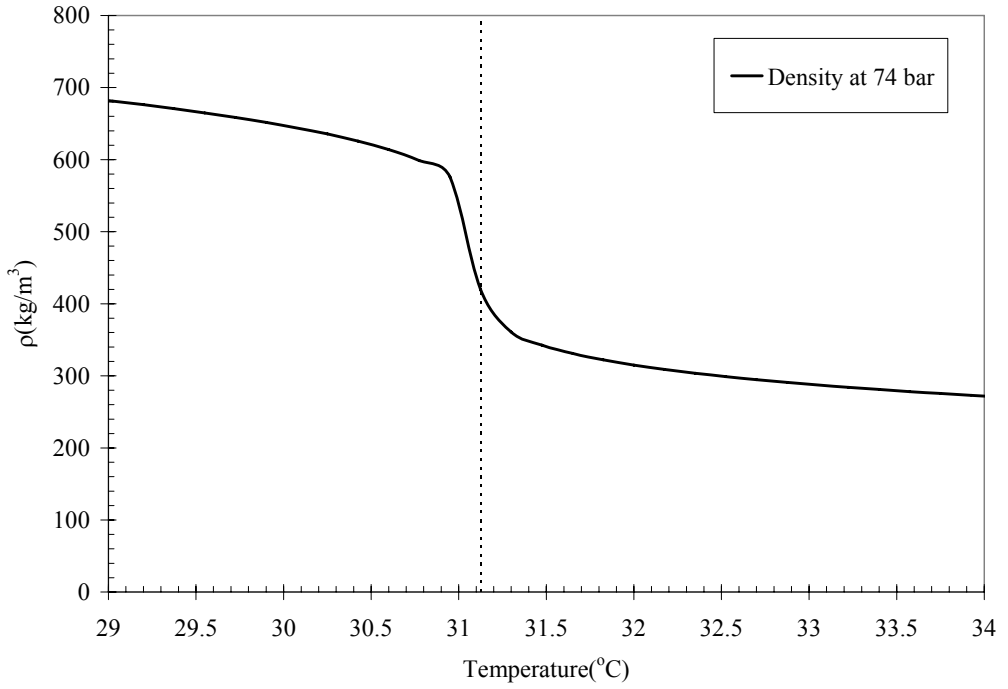

Figure E.2 Density at 74bar

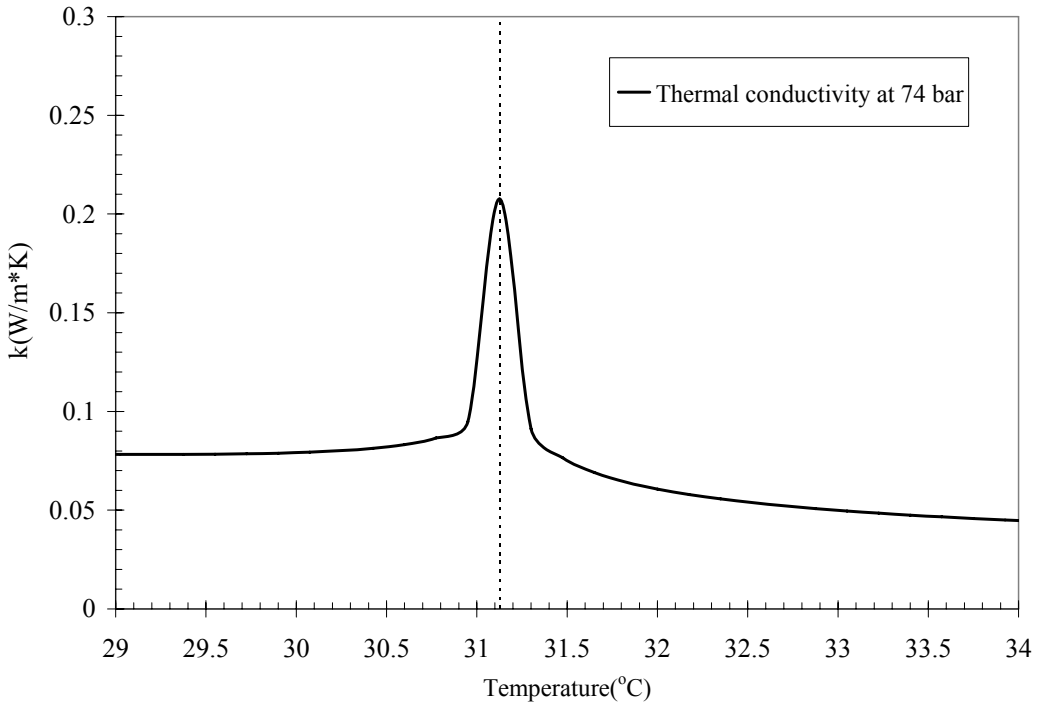

Figure E.3. Thermal Conductivity at 74bar

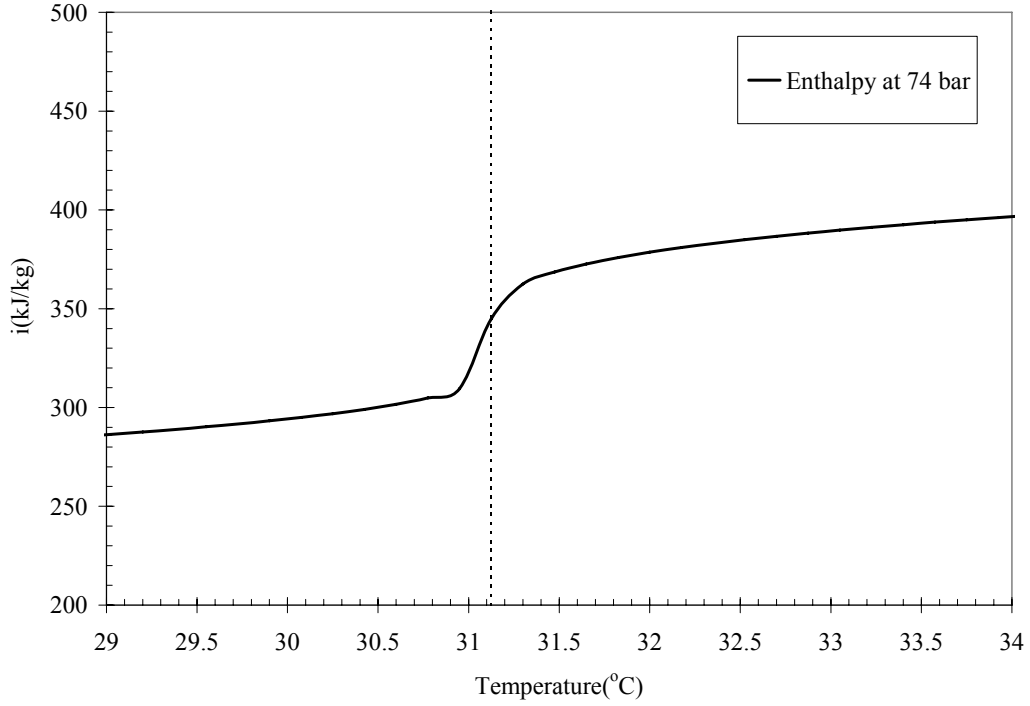

Figure E.4 Enthalpy at 74bar

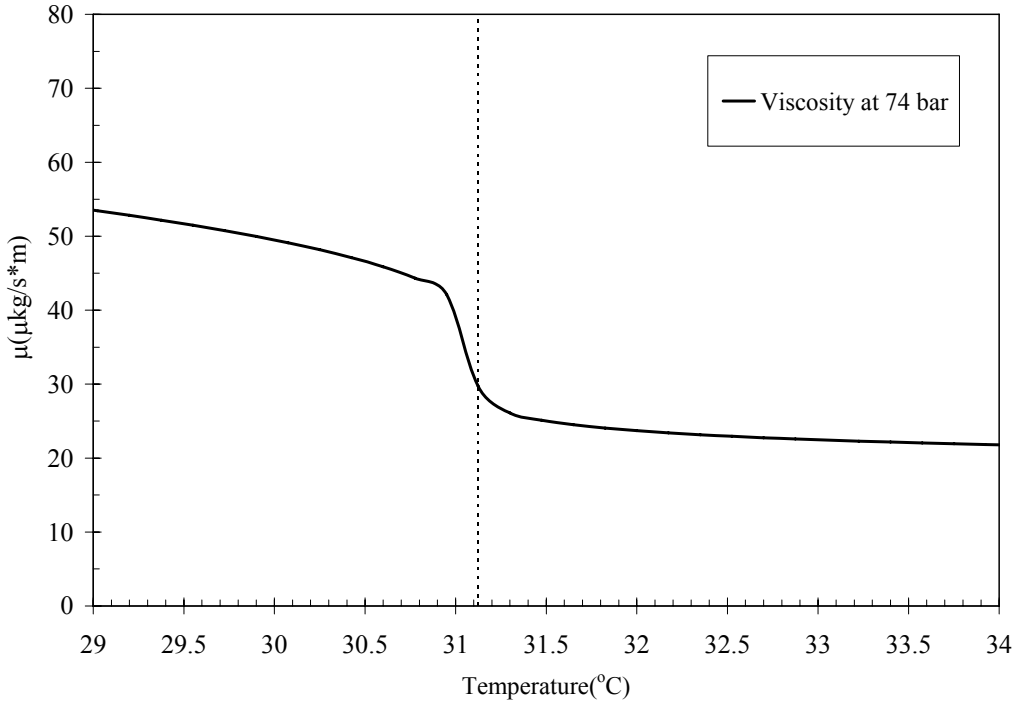

Figure E.5. Viscosity at 74bar

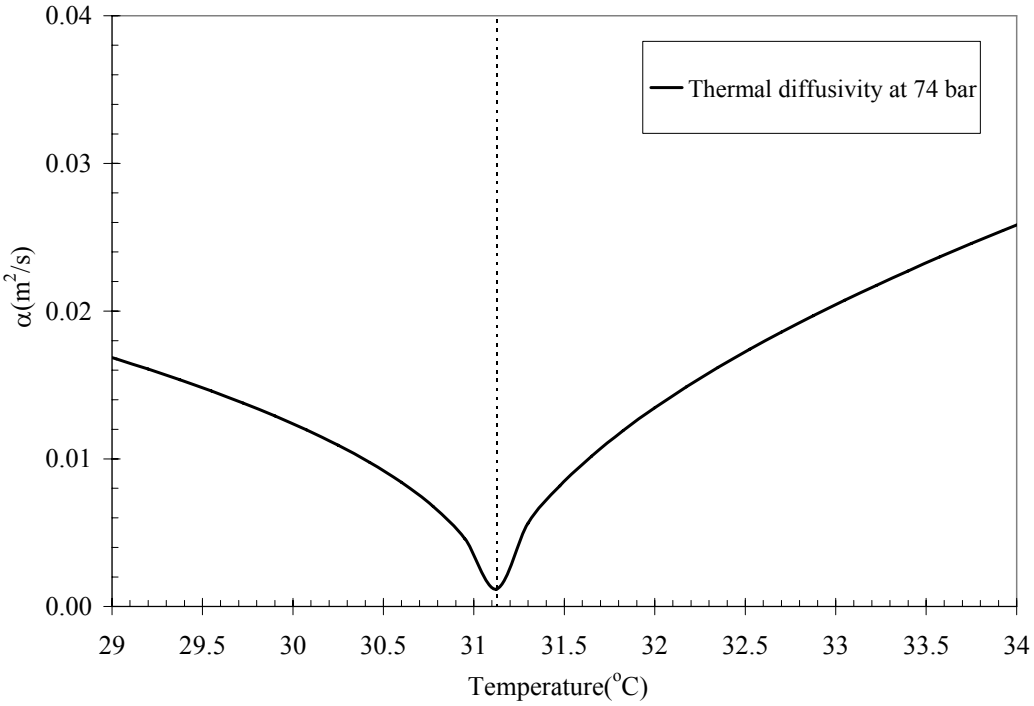

Figure E.6. Thermal diffusivity at 74bar

Table E.2. Thermophysical properties of CO_2 at 75bar

Temperature (°C)	Density (kg/m3)	Internal Energy (kJ/kg)	Enthalpy (kJ/kg)	Cv (J/g*K)	Cp (J/g*K)	Viscosity (uPa*s)	Therm. Cond. (W/m*K)	Phase
20	818.74	10.525	10.928	42.157	137.16	74.019	0.091411	liquid
21	808.79	10.66	11.068	42.359	141.98	72.207	0.08995	liquid
22	798.25	10.799	11.213	42.592	147.61	70.356	0.088463	liquid
23	787.02	10.944	11.364	42.862	154.31	68.455	0.086951	liquid
24	774.96	11.096	11.522	43.179	162.42	66.49	0.085414	liquid
25	761.87	11.256	11.689	43.558	172.52	64.442	0.083859	liquid
26	747.47	11.426	11.868	44.024	185.58	62.286	0.082299	liquid
27	731.34	11.61	12.062	44.617	203.35	59.978	0.08077	liquid
28	712.77	11.814	12.277	45.404	229.43	57.45	0.079352	liquid
29	690.38	12.048	12.526	46.52	272.25	54.572	0.078251	liquid
30	661.1	12.336	12.835	48.301	358.15	51.055	0.078087	liquid
31	614.17	12.763	13.3	52.41	648.55	45.925	0.081862	supercritical
32	365.93	15.039	15.941	62.312	1655	26.429	0.086212	supercritical
33	311.47	15.724	16.784	53.063	519.48	23.576	0.056981	supercritical
34	288.3	16.055	17.2	49.744	343.29	22.524	0.048759	supercritical
35	272.97	16.292	17.501	47.663	267.15	21.888	0.04424	supercritical
36	261.4	16.482	17.745	46.161	223.67	21.443	0.041244	supercritical
37	252.07	16.644	17.953	45.001	195.16	21.107	0.039063	supercritical
38	244.24	16.786	18.138	44.067	174.88	20.843	0.037387	supercritical
39	237.48	16.915	18.305	43.293	159.61	20.629	0.036048	supercritical
40	231.53	17.033	18.458	42.636	147.66	20.452	0.03495	supercritical
41	226.22	17.142	18.601	42.068	138.03	20.303	0.034032	supercritical
42	221.42	17.244	18.735	41.571	130.07	20.176	0.033253	supercritical
43	217.04	17.341	18.861	41.131	123.37	20.068	0.032582	supercritical
44	213.01	17.432	18.982	40.737	117.65	19.974	0.032	supercritical
45	209.28	17.52	19.097	40.381	112.69	19.894	0.031491	supercritical
46	205.81	17.604	19.207	40.057	108.36	19.824	0.031042	supercritical
47	202.57	17.684	19.314	39.762	104.53	19.763	0.030645	supercritical
48	199.52	17.762	19.417	39.49	101.13	19.71	0.030291	supercritical
49	196.65	17.838	19.516	39.24	98.073	19.664	0.029975	supercritical
50	193.93	17.911	19.613	39.008	95.319	19.624	0.029691	supercritical
51	191.36	17.982	19.707	38.793	92.821	19.59	0.029436	supercritical
52	188.91	18.051	19.799	38.593	90.545	19.561	0.029207	supercritical
53	186.58	18.119	19.888	38.407	88.461	19.536	0.029	supercritical
54	184.36	18.185	19.976	38.233	86.547	19.515	0.028812	supercritical
55	182.23	18.25	20.061	38.07	84.781	19.498	0.028643	supercritical
56	180.19	18.313	20.145	37.917	83.147	19.483	0.02849	supercritical
57	178.23	18.376	20.228	37.774	81.631	19.472	0.028351	supercritical
58	176.34	18.437	20.309	37.64	80.22	19.464	0.028226	supercritical
59	174.53	18.497	20.388	37.514	78.904	19.458	0.028112	supercritical
60	172.78	18.556	20.466	37.395	77.672	19.455	0.02801	supercritical
61	171.09	18.614	20.543	37.284	76.518	19.453	0.027917	supercritical
62	169.46	18.672	20.619	37.179	75.435	19.454	0.027834	supercritical
63	167.88	18.728	20.694	37.08	74.415	19.457	0.027759	supercritical

64	166.35	18.784	20.768	36.986	73.454	19.461	0.027692	supercritical
65	164.87	18.839	20.841	36.898	72.546	19.467	0.027632	supercritical
66	163.43	18.894	20.913	36.815	71.688	19.474	0.027579	supercritical
67	162.04	18.948	20.985	36.736	70.874	19.483	0.027532	supercritical
68	160.68	19.001	21.055	36.662	70.103	19.493	0.027491	supercritical
69	159.36	19.054	21.125	36.591	69.371	19.504	0.027455	supercritical
70	158.08	19.106	21.194	36.525	68.674	19.517	0.027425	supercritical
71	156.83	19.158	21.262	36.462	68.011	19.53	0.027399	supercritical
72	155.62	19.209	21.33	36.402	67.378	19.545	0.027377	supercritical
73	154.43	19.26	21.397	36.346	66.775	19.561	0.02736	supercritical
74	153.27	19.31	21.463	36.292	66.199	19.577	0.027346	supercritical
75	152.15	19.36	21.529	36.241	65.648	19.595	0.027336	supercritical
76	151.04	19.41	21.595	36.193	65.121	19.613	0.02733	supercritical
77	149.97	19.459	21.66	36.148	64.616	19.632	0.027326	supercritical
78	148.92	19.508	21.724	36.105	64.132	19.652	0.027326	supercritical
79	147.89	19.556	21.788	36.064	63.668	19.672	0.027329	supercritical
80	146.88	19.604	21.851	36.025	63.222	19.694	0.027334	supercritical
81	145.89	19.652	21.914	35.989	62.794	19.715	0.027342	supercritical
82	144.93	19.7	21.977	35.954	62.382	19.738	0.027353	supercritical
83	143.99	19.747	22.039	35.921	61.986	19.761	0.027366	supercritical
84	143.06	19.794	22.101	35.89	61.605	19.785	0.027381	supercritical
85	142.15	19.84	22.162	35.861	61.238	19.809	0.027398	supercritical
86	141.26	19.887	22.223	35.833	60.884	19.834	0.027417	supercritical
87	140.39	19.933	22.284	35.807	60.543	19.859	0.027438	supercritical
88	139.54	19.979	22.345	35.783	60.214	19.885	0.027461	supercritical
89	138.7	20.025	22.405	35.759	59.896	19.911	0.027486	supercritical
90	137.87	20.07	22.464	35.738	59.59	19.937	0.027512	supercritical

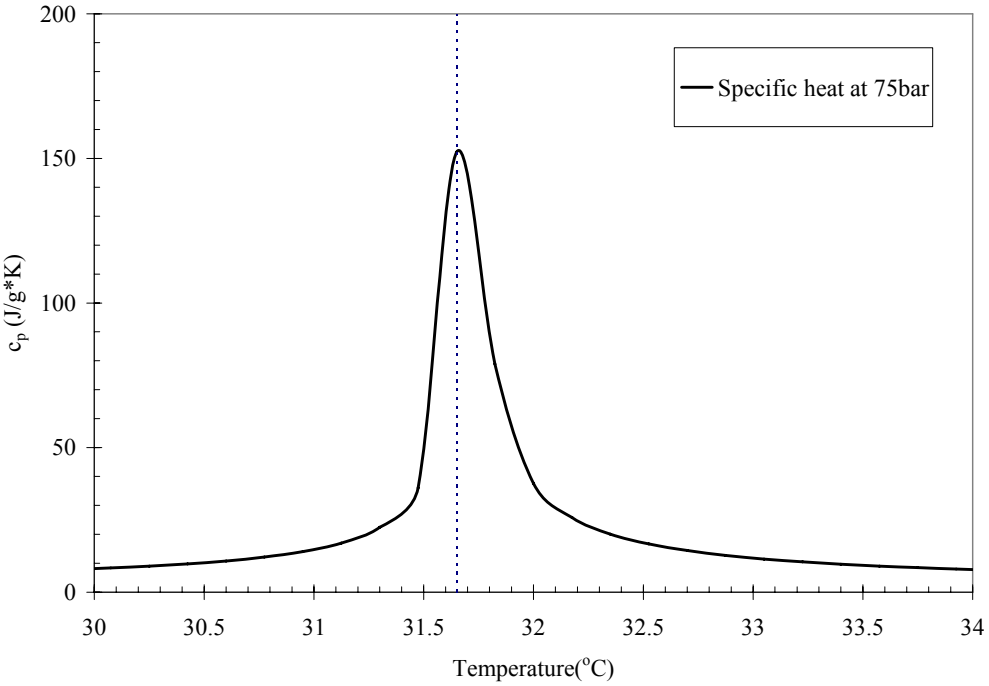

Figure E.7. Specific heat at 75bar

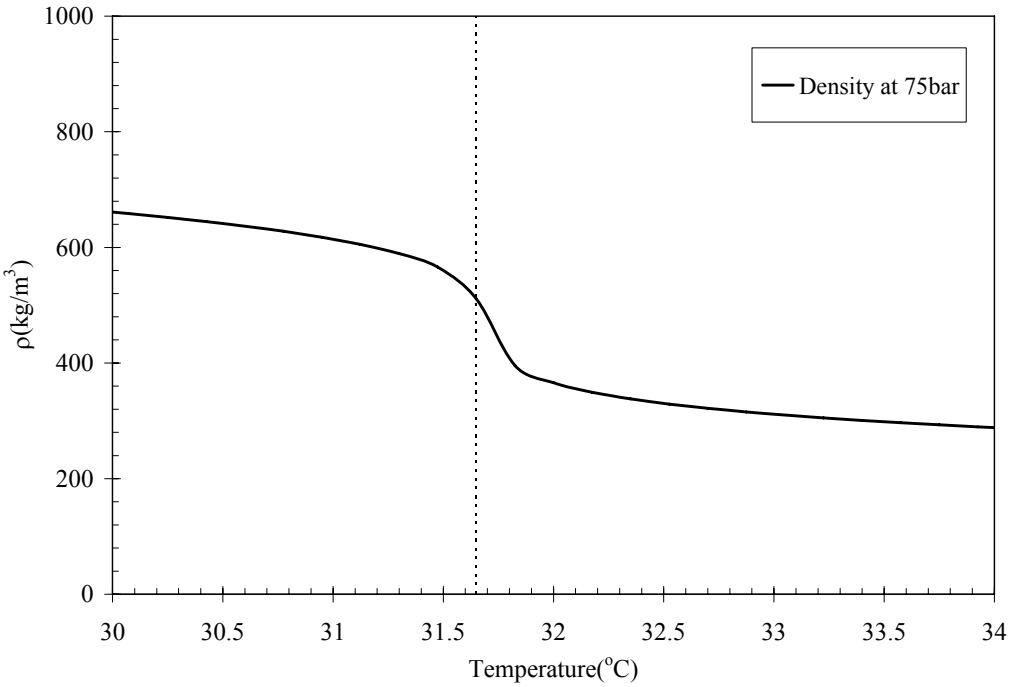

Figure E.8. Density at 75bar

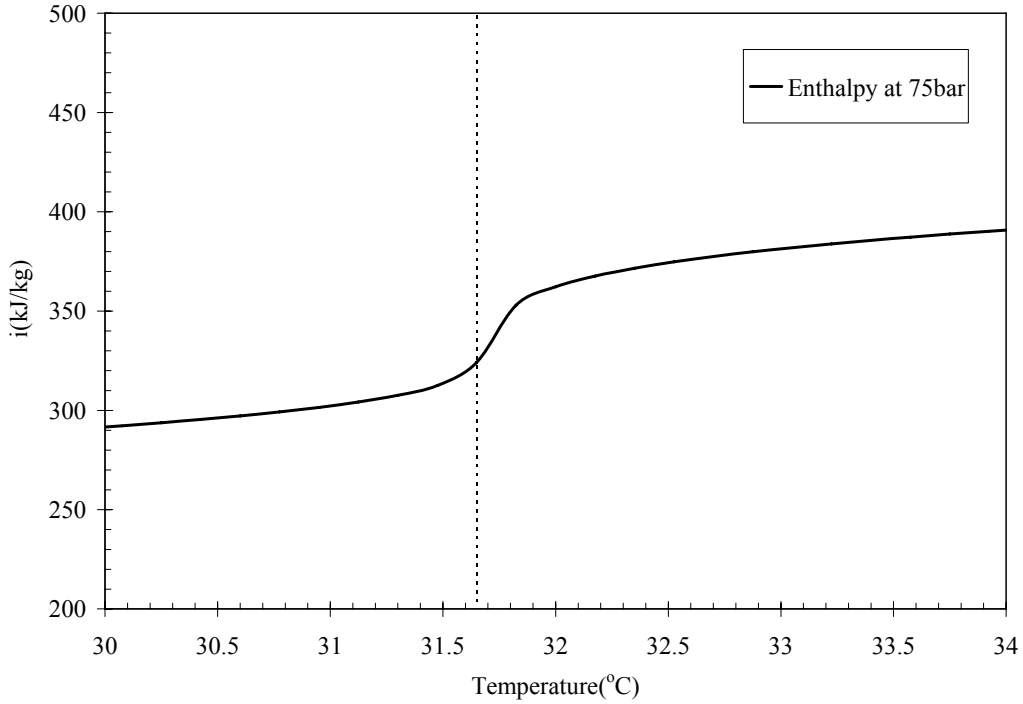

Figure E.9. Enthalpy at 75bar

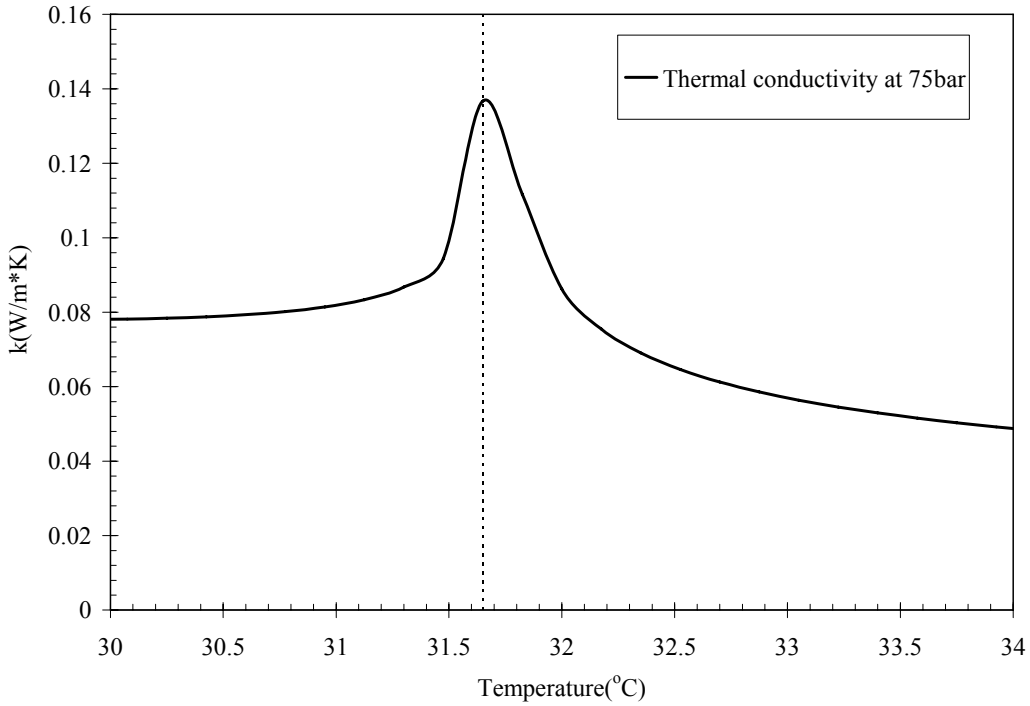

Figure E.10. Thermal conductivity at 75bar

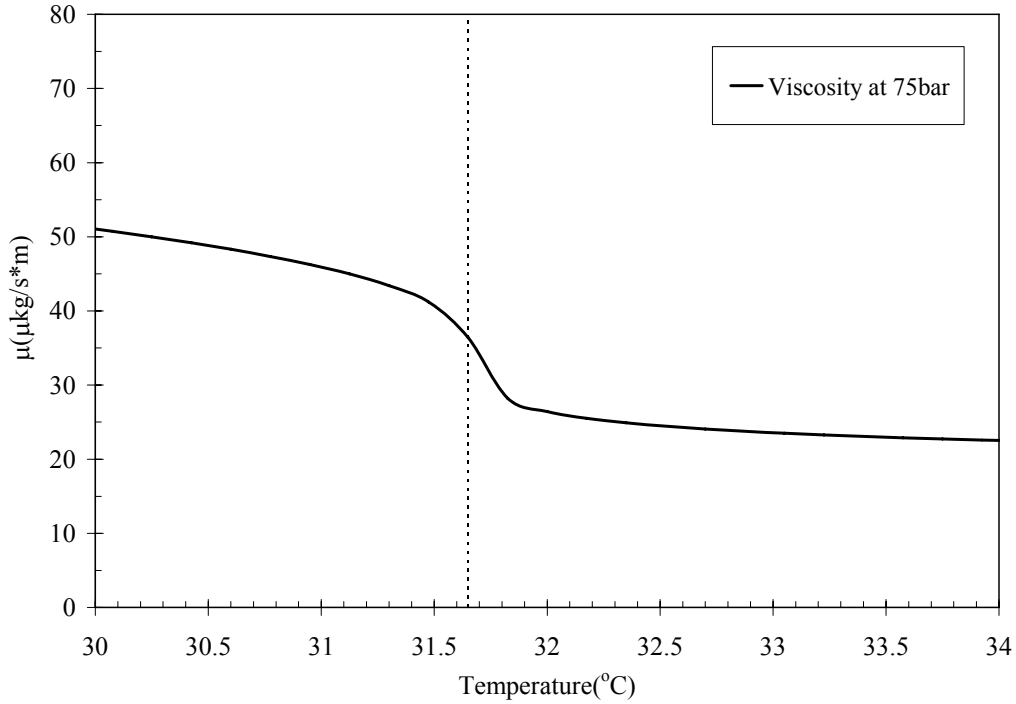

Figure E.11. Viscosity at 75bar

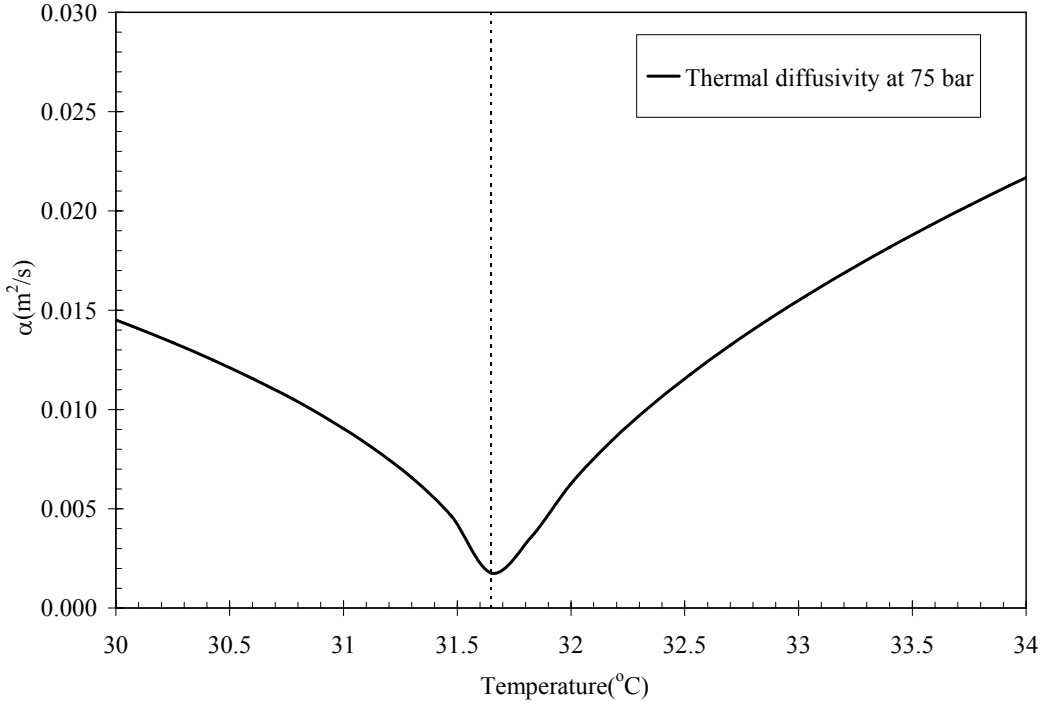

Figure E.12. Thermal diffusivity at 75bar

Table E.3 Thermophysical properties at 80bar

Temperature (°C)	Density (kg/m3)	Internal Energy (kJ/kg)	Enthalpy (kJ/kg)	Cv (J/g*K)	Cp (J/g*K)	Viscosity (uPa*s)	Therm. Cond. (W/m*K)	Phase
20	827.71	237.25	246.91	0.95097	2.9745	75.717	0.092784	liquid
21	818.55	240.16	249.93	0.95458	3.0598	73.994	0.091383	liquid
22	808.93	243.15	253.04	0.95868	3.1572	72.247	0.089961	liquid
23	798.8	246.23	256.25	0.96335	3.2693	70.468	0.088516	liquid
24	788.07	249.43	259.58	0.96869	3.3998	68.651	0.087048	liquid
25	776.64	252.76	263.06	0.97486	3.5541	66.785	0.085557	liquid
26	764.38	256.23	266.7	0.9821	3.74	64.859	0.084047	liquid
27	751.1	259.9	270.55	0.99075	3.97	62.855	0.082524	liquid
28	736.53	263.8	274.66	1.0013	4.2646	60.748	0.081004	liquid
29	720.29	268.01	279.11	1.0146	4.6595	58.502	0.07952	liquid
30	701.72	272.63	284.04	1.0318	5.2214	56.059	0.078142	liquid
31	679.73	277.89	289.66	1.055	6.0894	53.32	0.077022	supercritical
32	652.12	284.16	296.42	1.088	7.6094	50.097	0.076521	supercritical
33	613.68	292.41	305.44	1.1391	10.936	45.958	0.077605	supercritical
34	546.47	306.05	320.69	1.239	22.484	39.561	0.084016	supercritical
35	419.09	333.2	352.29	1.3171	29.594	29.843	0.082512	supercritical
36	354.75	349.68	372.23	1.2117	13.824	25.988	0.062933	supercritical
37	324.02	358.65	383.34	1.1412	9.1169	24.397	0.053859	supercritical
38	304.14	364.97	391.27	1.0939	6.9703	23.46	0.048551	supercritical
39	289.49	369.94	397.58	1.0594	5.7449	22.819	0.044981	supercritical
40	277.9	374.11	402.9	1.0329	4.9501	22.345	0.042376	supercritical
41	268.31	377.74	407.56	1.0115	4.3907	21.975	0.040371	supercritical
42	260.13	380.98	411.73	0.99377	3.9744	21.678	0.038772	supercritical
43	253.01	383.92	415.54	0.97874	3.6514	21.434	0.037462	supercritical
44	246.71	386.63	419.05	0.96574	3.3931	21.229	0.036368	supercritical
45	241.05	389.15	422.34	0.95432	3.1813	21.054	0.035439	supercritical
46	235.92	391.52	425.43	0.94416	3.0043	20.905	0.03464	supercritical
47	231.23	393.76	428.36	0.93505	2.8539	20.776	0.033947	supercritical
48	226.91	395.89	431.14	0.9268	2.7244	20.663	0.03334	supercritical
49	222.91	397.92	433.81	0.91928	2.6117	20.565	0.032805	supercritical
50	219.18	399.87	436.37	0.91238	2.5125	20.479	0.03233	supercritical
51	215.7	401.75	438.84	0.90604	2.4246	20.403	0.031908	supercritical
52	212.42	403.56	441.22	0.90018	2.3461	20.336	0.031529	supercritical
53	209.33	405.32	443.53	0.89475	2.2756	20.277	0.031189	supercritical
54	206.41	407.02	445.78	0.88971	2.2118	20.226	0.030883	supercritical
55	203.64	408.68	447.96	0.88501	2.1538	20.18	0.030607	supercritical
56	201.01	410.29	450.09	0.88063	2.1009	20.14	0.030357	supercritical
57	198.5	411.86	452.16	0.87654	2.0524	20.105	0.03013	supercritical
58	196.11	413.4	454.19	0.87271	2.0078	20.075	0.029924	supercritical
59	193.82	414.9	456.18	0.86913	1.9666	20.049	0.029737	supercritical
60	191.62	416.38	458.13	0.86577	1.9284	20.026	0.029567	supercritical
61	189.52	417.82	460.04	0.86262	1.893	20.007	0.029412	supercritical
62	187.49	419.24	461.91	0.85966	1.86	19.991	0.029271	supercritical

63	185.54	420.64	463.76	0.85687	1.8291	19.978	0.029142	supercritical
64	183.66	422.01	465.57	0.85425	1.8003	19.968	0.029026	supercritical
65	181.84	423.37	467.36	0.85178	1.7733	19.96	0.02892	supercritical
66	180.09	424.7	469.12	0.84945	1.7478	19.954	0.028823	supercritical
67	178.4	426.01	470.85	0.84725	1.7239	19.95	0.028736	supercritical
68	176.76	427.31	472.57	0.84518	1.7014	19.949	0.028657	supercritical
69	175.16	428.59	474.26	0.84322	1.68	19.949	0.028586	supercritical
70	173.62	429.85	475.93	0.84137	1.6599	19.951	0.028522	supercritical
71	172.12	431.1	477.58	0.83961	1.6407	19.955	0.028464	supercritical
72	170.67	432.34	479.21	0.83795	1.6226	19.96	0.028413	supercritical
73	169.26	433.56	480.82	0.83638	1.6054	19.966	0.028367	supercritical
74	167.88	434.77	482.42	0.83489	1.589	19.974	0.028327	supercritical
75	166.54	435.97	484	0.83348	1.5734	19.984	0.028292	supercritical
76	165.24	437.15	485.57	0.83214	1.5585	19.994	0.028262	supercritical
77	163.97	438.33	487.12	0.83087	1.5443	20.005	0.028236	supercritical
78	162.73	439.49	488.66	0.82967	1.5307	20.018	0.028214	supercritical
79	161.52	440.65	490.18	0.82852	1.5177	20.032	0.028196	supercritical
80	160.34	441.8	491.69	0.82744	1.5052	20.046	0.028182	supercritical
81	159.18	442.93	493.19	0.82641	1.4933	20.061	0.028172	supercritical
82	158.06	444.06	494.68	0.82543	1.4819	20.078	0.028164	supercritical
83	156.96	445.19	496.16	0.82451	1.471	20.095	0.02816	supercritical
84	155.88	446.3	497.62	0.82363	1.4604	20.113	0.028159	supercritical
85	154.82	447.4	499.08	0.8228	1.4503	20.131	0.02816	supercritical
86	153.79	448.5	500.52	0.82201	1.4406	20.151	0.028165	supercritical
87	152.78	449.6	501.96	0.82126	1.4312	20.171	0.028171	supercritical
88	151.79	450.68	503.38	0.82055	1.4222	20.191	0.028181	supercritical
89	150.82	451.76	504.8	0.81989	1.4136	20.213	0.028192	supercritical
90	149.87	452.83	506.21	0.81925	1.4052	20.235	0.028206	supercritical

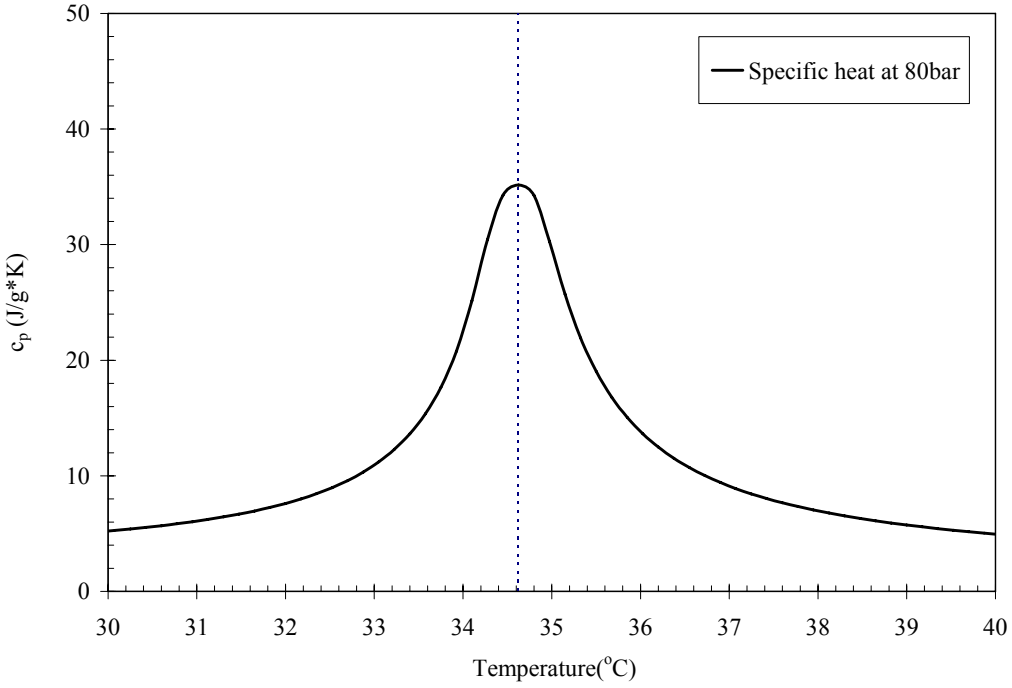

Figure E.13. Specific heat at 80bar

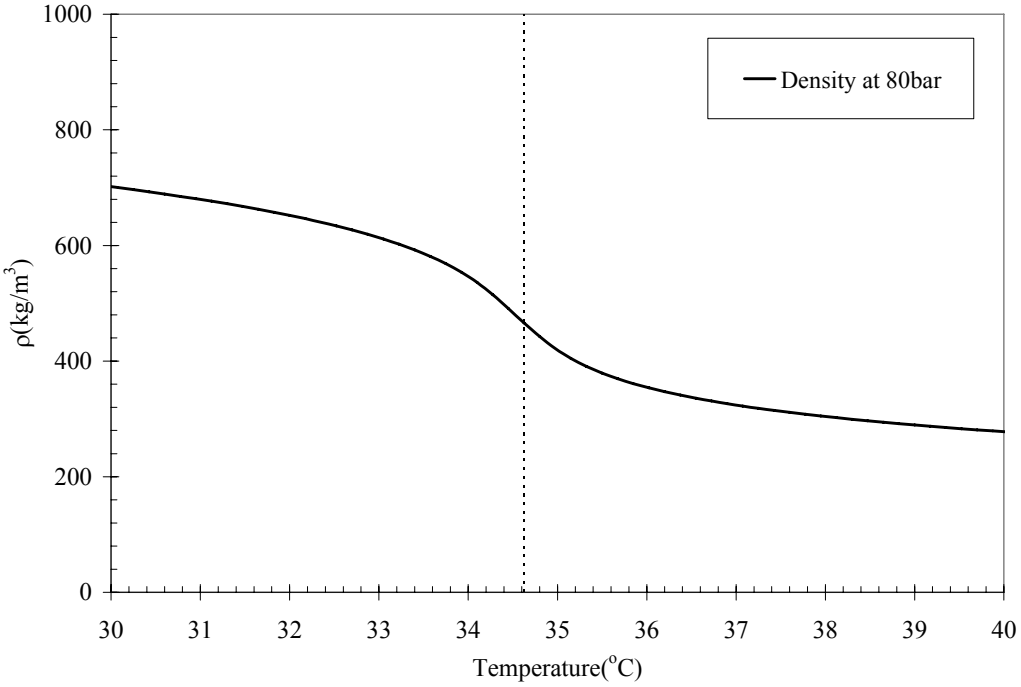

Figure E.14. Density at 80bar

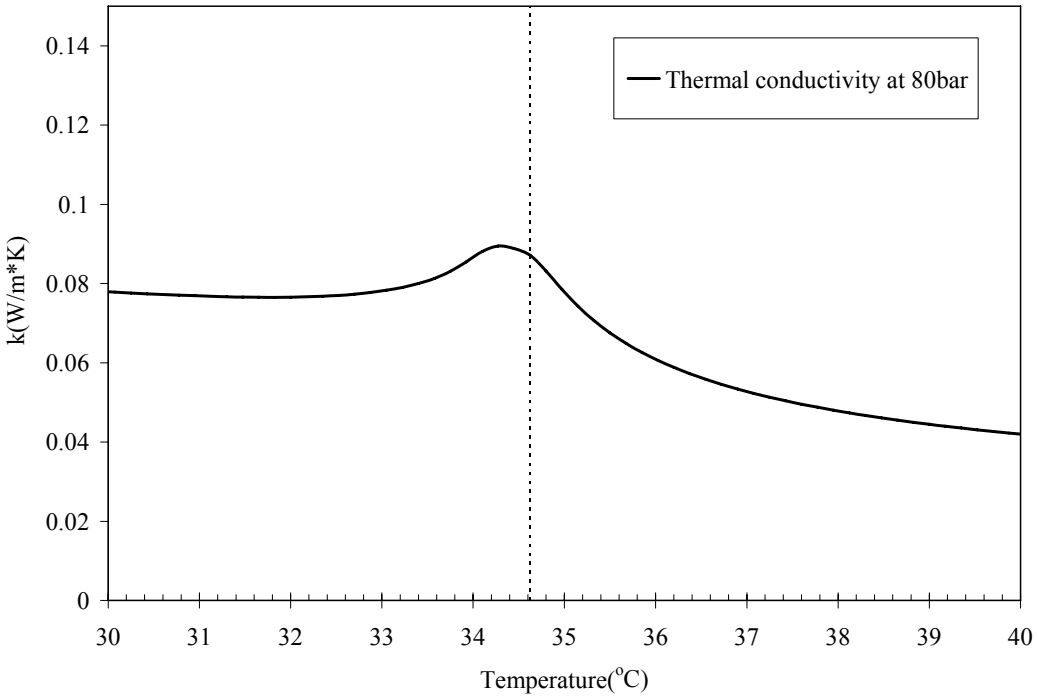

Figure E.15. Thermal conductivity at 80bar

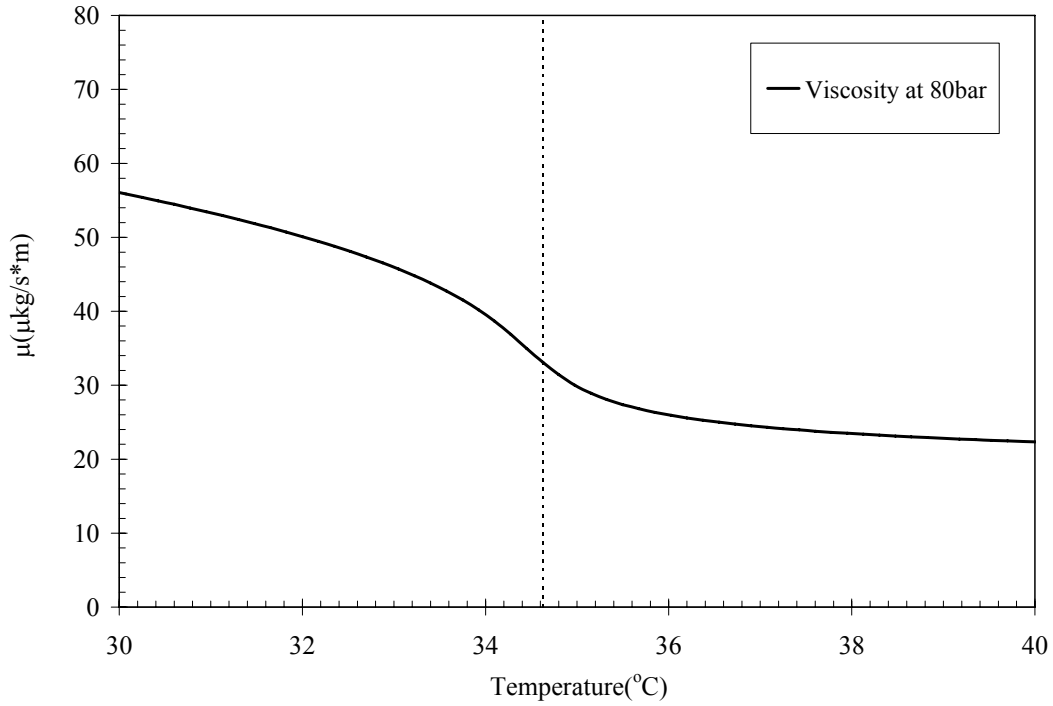

Figure E.16. Viscosity at 80bar

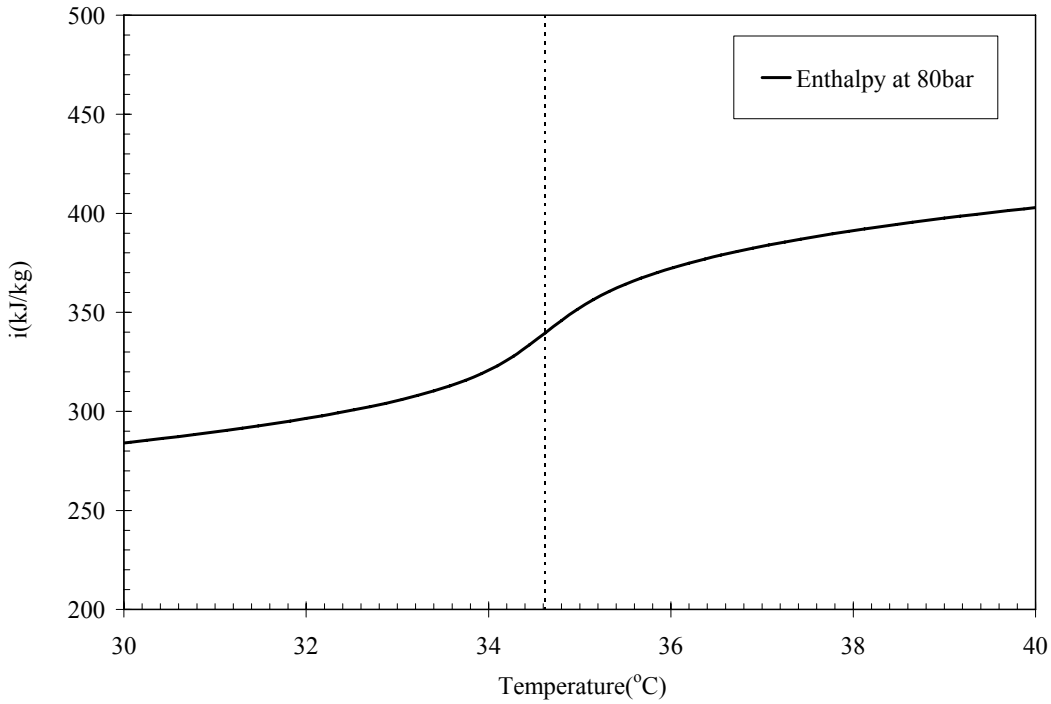

Figure E.17. Enthalpy at 80bar

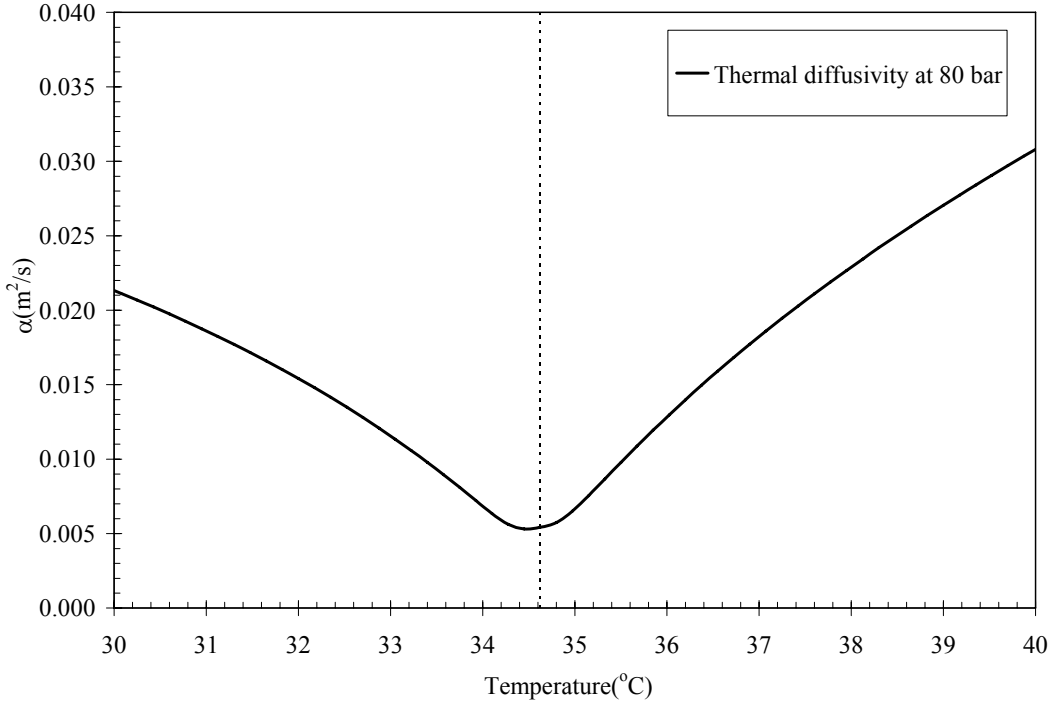

Figure E.18. Thermal diffusivity at 80bar

Table E.4. Thermophysical properties at 85bar.

Temperature (°C)	Density (kg/m3)	Internal Energy (kJ/kg)	Enthalpy (kJ/kg)	Cv (J/g*K)	Cp (J/g*K)	Viscosity (uPa*s)	Therm. Cond. (W/m*K)	Phase
20	835.8	10.365	10.812	41.612	125.91	77.292	0.094073	liquid
21	827.24	10.487	10.94	41.74	128.94	75.637	0.092725	liquid
22	818.33	10.613	11.07	41.883	132.34	73.967	0.091358	liquid
23	809.02	10.742	11.204	42.045	136.17	72.278	0.089973	liquid
24	799.26	10.875	11.343	42.226	140.52	70.566	0.088567	liquid
25	788.98	11.012	11.486	42.432	145.5	68.824	0.087142	liquid
26	778.11	11.153	11.634	42.665	151.26	67.045	0.085696	liquid
27	766.54	11.301	11.789	42.934	158.04	65.221	0.084231	liquid
28	754.15	11.455	11.951	43.248	166.16	63.341	0.08275	liquid
29	740.76	11.617	12.122	43.62	176.11	61.388	0.081263	liquid
30	726.15	11.789	12.304	44.07	188.7	59.343	0.079784	liquid
31	709.94	11.973	12.5	44.626	205.2	57.174	0.078341	supercritical
32	691.62	12.175	12.716	45.327	227.79	54.836	0.07699	supercritical
33	670.35	12.401	12.959	46.229	260.37	52.262	0.07583	supercritical
34	644.7	12.662	13.243	47.412	310.71	49.339	0.075046	supercritical
35	612.12	12.981	13.592	48.983	395.38	45.881	0.07495	supercritical
36	567.77	13.398	14.057	51.125	551.99	41.583	0.076002	supercritical
37	504.09	13.992	14.734	53.551	794.87	36.126	0.077506	supercritical
38	434.5	14.682	15.543	53.728	767.77	31.017	0.072484	supercritical
39	385.19	15.224	16.195	51.585	543.03	27.897	0.063115	supercritical
40	353.91	15.603	16.66	49.447	401.14	26.134	0.056118	supercritical
41	332.01	15.89	17.017	47.787	319.11	25.001	0.051266	supercritical
42	315.42	16.122	17.308	46.501	266.96	24.203	0.047721	supercritical
43	302.16	16.318	17.557	45.473	231.23	23.605	0.045014	supercritical
44	291.17	16.489	17.774	44.626	205.33	23.136	0.042875	supercritical
45	281.81	16.642	17.969	43.91	185.72	22.758	0.041138	supercritical
46	273.68	16.78	18.147	43.291	170.36	22.447	0.039699	supercritical
47	266.49	16.907	18.311	42.748	158	22.185	0.038486	supercritical
48	260.06	17.025	18.464	42.266	147.84	21.962	0.03745	supercritical
49	254.25	17.136	18.607	41.832	139.33	21.771	0.036555	supercritical
50	248.95	17.24	18.743	41.438	132.09	21.604	0.035775	supercritical
51	244.08	17.339	18.872	41.08	125.86	21.459	0.03509	supercritical
52	239.58	17.433	18.995	40.751	120.44	21.332	0.034484	supercritical
53	235.4	17.524	19.113	40.448	115.68	21.219	0.033945	supercritical
54	231.5	17.61	19.226	40.168	111.46	21.119	0.033464	supercritical
55	227.84	17.694	19.336	39.908	107.69	21.031	0.033032	supercritical
56	224.4	17.775	19.442	39.667	104.31	20.952	0.032643	supercritical
57	221.15	17.853	19.545	39.443	101.26	20.882	0.032291	supercritical
58	218.07	17.929	19.644	39.234	98.487	20.82	0.031973	supercritical
59	215.15	18.003	19.742	39.039	95.961	20.764	0.031684	supercritical
60	212.37	18.075	19.836	38.857	93.647	20.714	0.031422	supercritical
61	209.72	18.145	19.929	38.686	91.521	20.67	0.031182	supercritical
62	207.19	18.214	20.02	38.526	89.561	20.631	0.030964	supercritical

63	204.77	18.281	20.108	38.376	87.747	20.597	0.030764	supercritical
64	202.45	18.347	20.195	38.235	86.063	20.566	0.030582	supercritical
65	200.22	18.412	20.28	38.103	84.497	20.54	0.030416	supercritical
66	198.07	18.475	20.364	37.979	83.036	20.517	0.030263	supercritical
67	196	18.538	20.446	37.862	81.67	20.497	0.030124	supercritical
68	194.01	18.599	20.527	37.751	80.389	20.48	0.029996	supercritical
69	192.09	18.66	20.607	37.647	79.187	20.466	0.02988	supercritical
70	190.23	18.719	20.686	37.549	78.055	20.454	0.029773	supercritical
71	188.44	18.778	20.763	37.456	76.989	20.445	0.029676	supercritical
72	186.7	18.836	20.84	37.368	75.982	20.438	0.029587	supercritical
73	185.01	18.893	20.915	37.285	75.03	20.432	0.029507	supercritical
74	183.37	18.95	20.99	37.206	74.128	20.429	0.029433	supercritical
75	181.79	19.006	21.064	37.132	73.273	20.428	0.029367	supercritical
76	180.25	19.061	21.137	37.061	72.461	20.428	0.029307	supercritical
77	178.75	19.116	21.209	36.994	71.688	20.43	0.029253	supercritical
78	177.29	19.17	21.28	36.93	70.953	20.434	0.029205	supercritical
79	175.87	19.223	21.351	36.87	70.251	20.439	0.029162	supercritical
80	174.49	19.277	21.42	36.813	69.583	20.445	0.029125	supercritical
81	173.14	19.329	21.49	36.758	68.944	20.452	0.029091	supercritical
82	171.82	19.381	21.558	36.706	68.333	20.461	0.029063	supercritical
83	170.54	19.433	21.626	36.657	67.748	20.471	0.029038	supercritical
84	169.29	19.484	21.694	36.611	67.189	20.481	0.029017	supercritical
85	168.07	19.535	21.761	36.566	66.652	20.493	0.029	supercritical
86	166.87	19.585	21.827	36.524	66.137	20.506	0.028986	supercritical
87	165.7	19.635	21.893	36.484	65.643	20.52	0.028976	supercritical
88	164.56	19.685	21.958	36.446	65.168	20.534	0.028969	supercritical
89	163.44	19.735	22.023	36.41	64.712	20.55	0.028965	supercritical
90	162.35	19.784	22.088	36.376	64.273	20.566	0.028963	supercritical

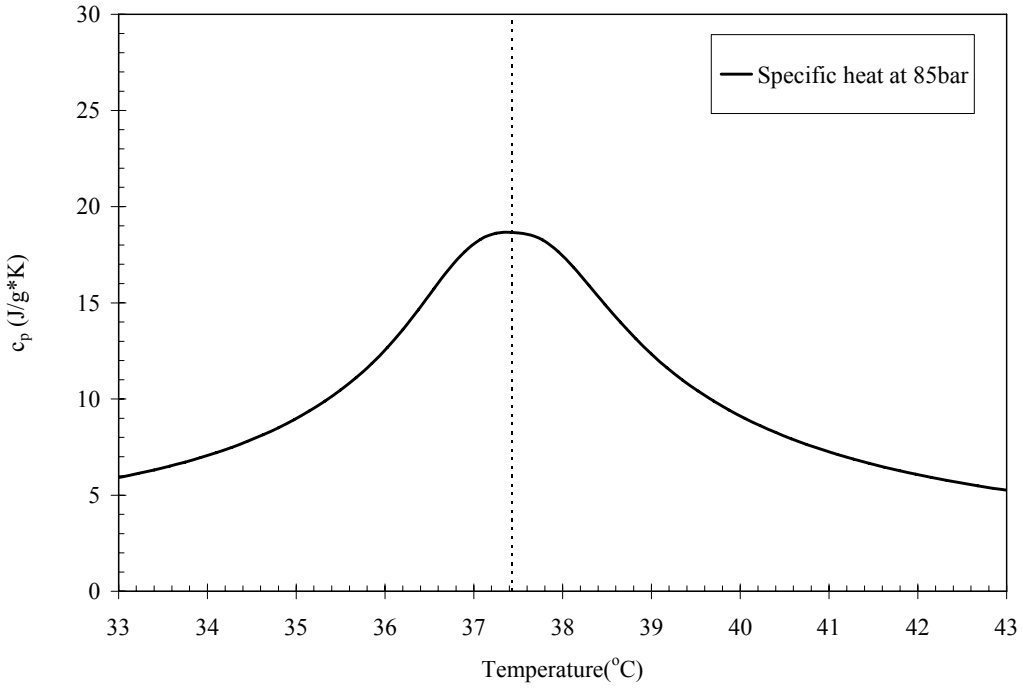

Figure E.19. Specific heat at 85bar

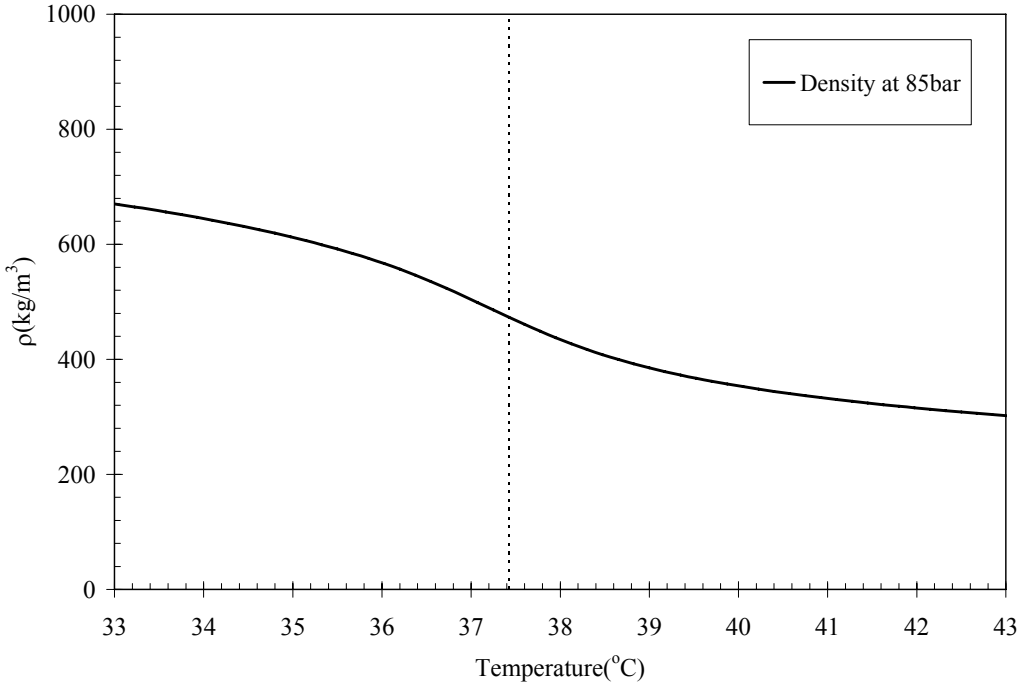

Figure E.20. Density at 85bar

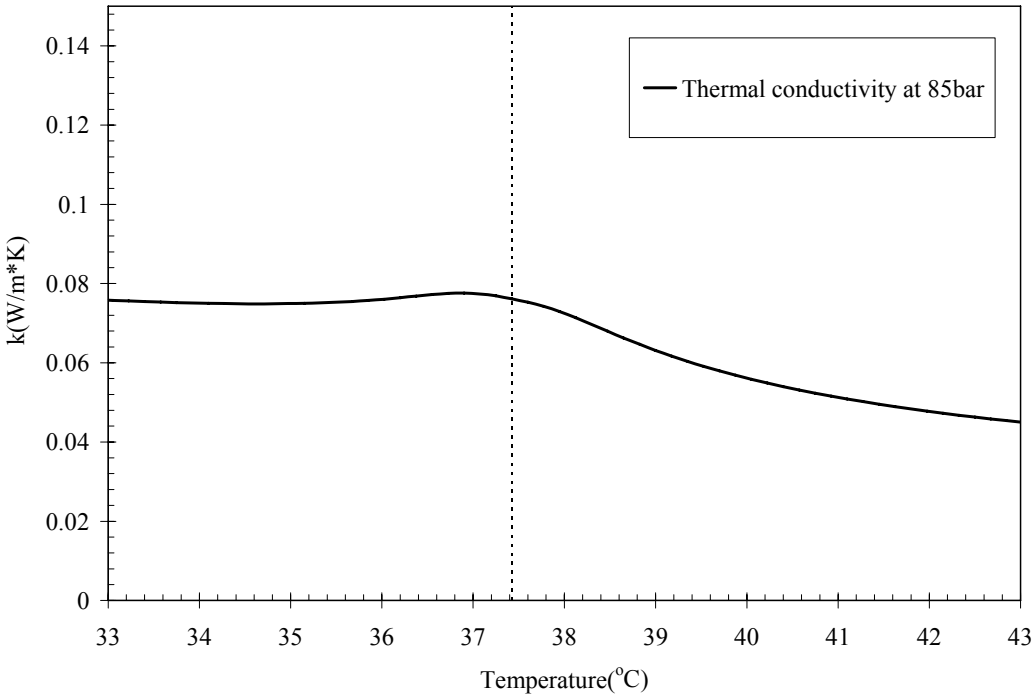

Figure E.21. Thermal conductivity at 85bar

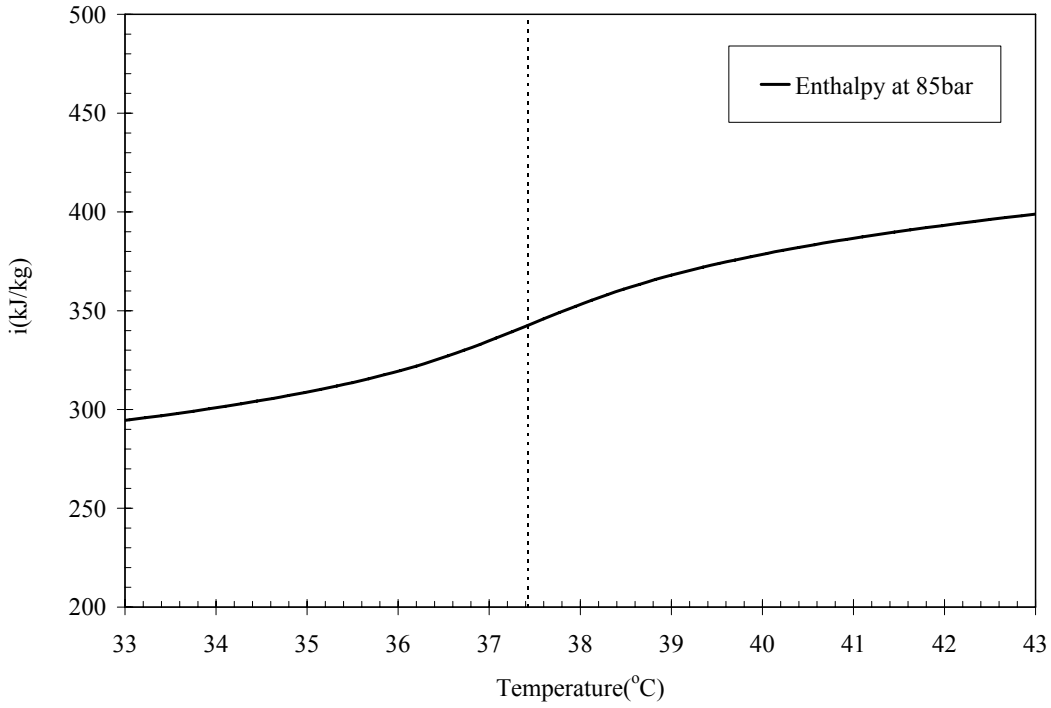

Figure E.22. Enthalpy at 85bar

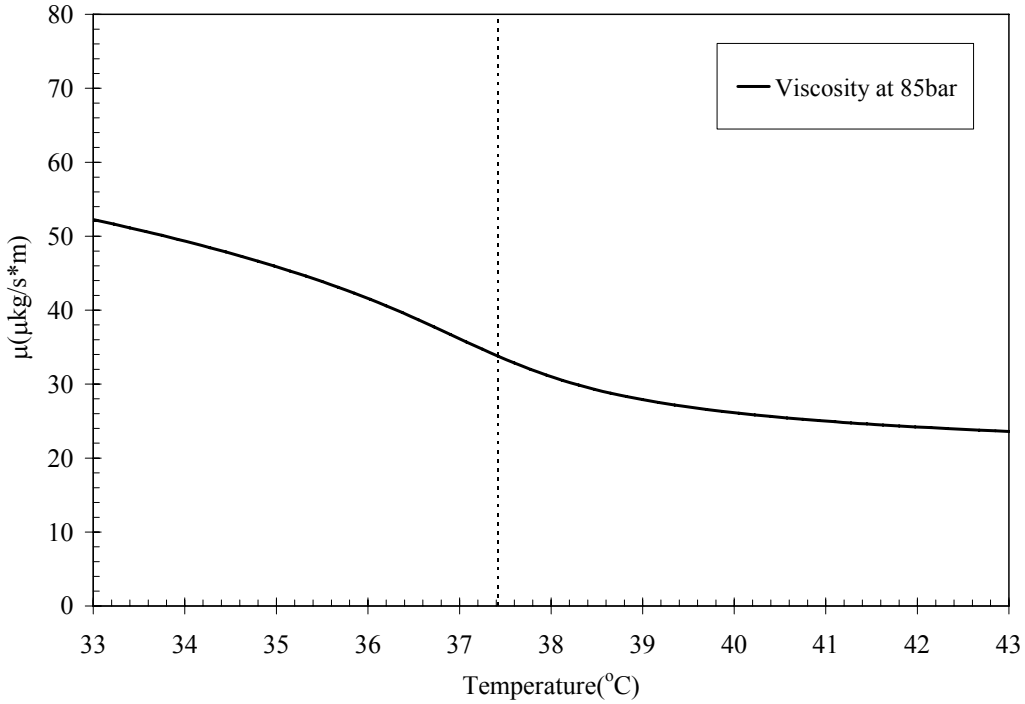

Figure E.23. Viscosity at 85bar

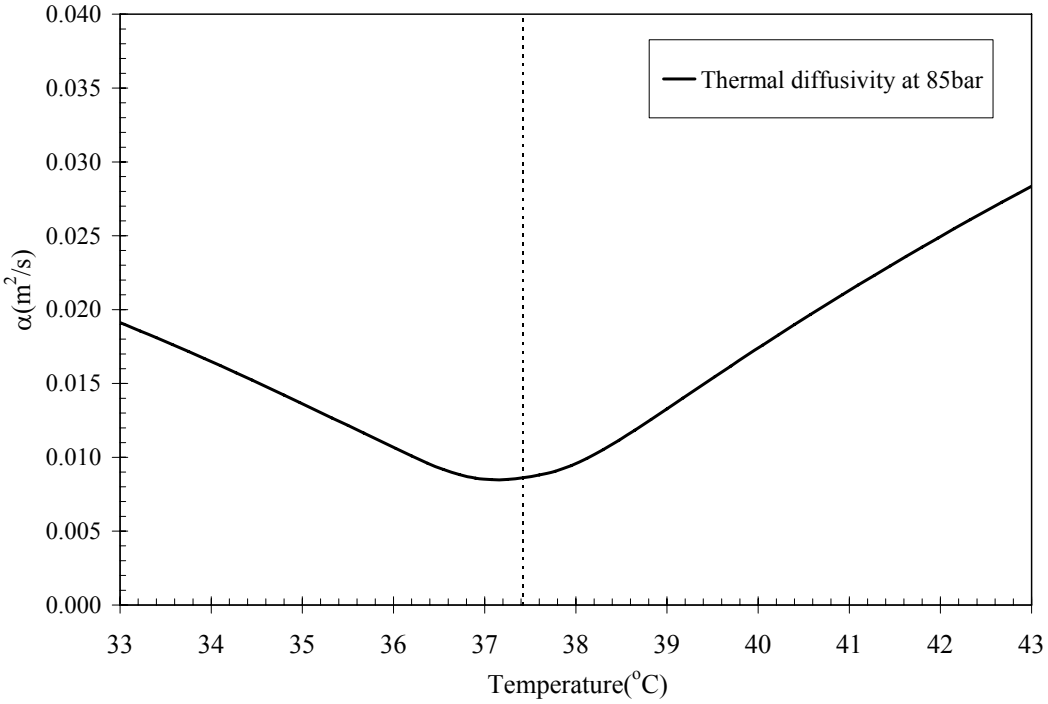

Figure E.24. Thermal diffusivity at 85bar

Table E.5. Thermophysical properties at 90bar

Temperature (°C)	Density (kg/m3)	Internal Energy (kJ/kg)	Enthalpy (kJ/kg)	Cv (J/g*K)	Cp (J/g*K)	Viscosity (uPa*s)	Therm. Cond. (W/m*K)	Phase
20	843.17	10.294	10.764	41.42	121.8	78.767	0.095291	liquid
21	835.12	10.413	10.887	41.524	124.31	77.166	0.093987	liquid
22	826.78	10.534	11.013	41.64	127.09	75.558	0.092669	liquid
23	818.11	10.657	11.141	41.77	130.17	73.938	0.091335	liquid
24	809.08	10.784	11.273	41.914	133.61	72.304	0.089985	liquid
25	799.65	10.913	11.409	42.075	137.46	70.652	0.088617	liquid
26	789.77	11.047	11.548	42.254	141.82	68.978	0.087232	liquid
27	779.38	11.184	11.692	42.455	146.78	67.276	0.085828	liquid
28	768.41	11.327	11.842	42.683	152.49	65.54	0.084408	liquid
29	756.75	11.474	11.998	42.942	159.16	63.763	0.082972	liquid
30	744.31	11.629	12.161	43.243	167.08	61.934	0.081525	liquid
31	730.91	11.791	12.332	43.595	176.7	60.041	0.080076	supercritical
32	716.36	11.962	12.515	44.014	188.65	58.066	0.078637	supercritical
33	700.34	12.145	12.711	44.517	203.89	55.986	0.077231	supercritical
34	682.47	12.344	12.924	45.13	223.84	53.768	0.075896	supercritical
35	662.13	12.563	13.161	45.878	250.7	51.369	0.07469	supercritical
36	638.48	12.809	13.429	46.789	287.9	48.73	0.073697	supercritical
37	610.3	13.093	13.742	47.892	340.46	45.779	0.073005	supercritical
38	575.93	13.43	14.118	49.2	415.84	42.436	0.07269	supercritical
39	533.61	13.84	14.582	50.496	514.4	38.668	0.072523	supercritical
40	485.5	14.314	15.13	51.07	564.78	34.806	0.07059	supercritical
41	440.2	14.783	15.683	50.521	530.89	31.549	0.066528	supercritical
42	403.5	15.19	16.172	49.316	443.34	29.171	0.061187	supercritical
43	375.79	15.52	16.574	48.049	363.94	27.528	0.056335	supercritical
44	354.49	15.79	16.907	46.936	306.2	26.356	0.052442	supercritical
45	337.51	16.018	17.191	45.993	264.39	25.482	0.049335	supercritical
46	323.56	16.215	17.439	45.188	233.25	24.804	0.046818	supercritical
47	311.8	16.39	17.66	44.49	209.38	24.263	0.044744	supercritical
48	301.69	16.547	17.86	43.877	190.61	23.821	0.043011	supercritical
49	292.84	16.69	18.043	43.331	175.52	23.452	0.041544	supercritical
50	285	16.822	18.212	42.838	163.15	23.141	0.040288	supercritical
51	277.97	16.945	18.37	42.392	152.84	22.874	0.039201	supercritical
52	271.61	17.06	18.518	41.983	144.12	22.643	0.038253	supercritical
53	265.8	17.168	18.658	41.608	136.65	22.442	0.037421	supercritical
54	260.47	17.271	18.792	41.263	130.19	22.265	0.036684	supercritical
55	255.55	17.369	18.919	40.943	124.54	22.109	0.03603	supercritical
56	250.97	17.463	19.041	40.647	119.56	21.971	0.035445	supercritical
57	246.7	17.553	19.158	40.372	115.14	21.848	0.03492	supercritical
58	242.7	17.639	19.271	40.117	111.19	21.738	0.034447	supercritical
59	238.94	17.723	19.381	39.879	107.64	21.639	0.034019	supercritical
60	235.39	17.804	19.487	39.657	104.42	21.551	0.033632	supercritical
61	232.04	17.883	19.59	39.45	101.51	21.471	0.033279	supercritical
62	228.85	17.959	19.69	39.256	98.848	21.4	0.032959	supercritical

63	225.83	18.033	19.787	39.075	96.411	21.336	0.032666	supercritical
64	222.94	18.106	19.883	38.905	94.171	21.278	0.032398	supercritical
65	220.19	18.177	19.976	38.747	92.105	21.226	0.032153	supercritical
66	217.55	18.246	20.067	38.597	90.192	21.179	0.031928	supercritical
67	215.03	18.314	20.156	38.457	88.418	21.138	0.031722	supercritical
68	212.61	18.381	20.244	38.326	86.766	21.1	0.031533	supercritical
69	210.28	18.446	20.33	38.202	85.226	21.067	0.031359	supercritical
70	208.04	18.51	20.414	38.085	83.785	21.037	0.031199	supercritical
71	205.88	18.574	20.497	37.975	82.435	21.011	0.031052	supercritical
72	203.8	18.636	20.579	37.871	81.168	20.988	0.030917	supercritical
73	201.79	18.697	20.66	37.772	79.975	20.968	0.030793	supercritical
74	199.84	18.757	20.739	37.679	78.85	20.951	0.030679	supercritical
75	197.96	18.817	20.818	37.591	77.789	20.936	0.030574	supercritical
76	196.14	18.875	20.895	37.508	76.785	20.924	0.030478	supercritical
77	194.37	18.933	20.971	37.429	75.834	20.914	0.030391	supercritical
78	192.66	18.991	21.046	37.354	74.933	20.906	0.03031	supercritical
79	191	19.047	21.121	37.283	74.076	20.9	0.030237	supercritical
80	189.38	19.103	21.195	37.215	73.262	20.896	0.030171	supercritical
81	187.81	19.158	21.268	37.151	72.487	20.893	0.03011	supercritical
82	186.28	19.213	21.34	37.09	71.748	20.892	0.030056	supercritical
83	184.79	19.268	21.411	37.032	71.043	20.893	0.030006	supercritical
84	183.33	19.321	21.482	36.977	70.37	20.895	0.029962	supercritical
85	181.92	19.375	21.552	36.924	69.726	20.899	0.029923	supercritical
86	180.54	19.427	21.621	36.875	69.11	20.904	0.029888	supercritical
87	179.19	19.48	21.69	36.827	68.52	20.91	0.029858	supercritical
88	177.88	19.532	21.758	36.782	67.955	20.917	0.029831	supercritical
89	176.59	19.583	21.826	36.739	67.413	20.925	0.029808	supercritical
90	175.34	19.634	21.893	36.698	66.892	20.935	0.029789	supercritical

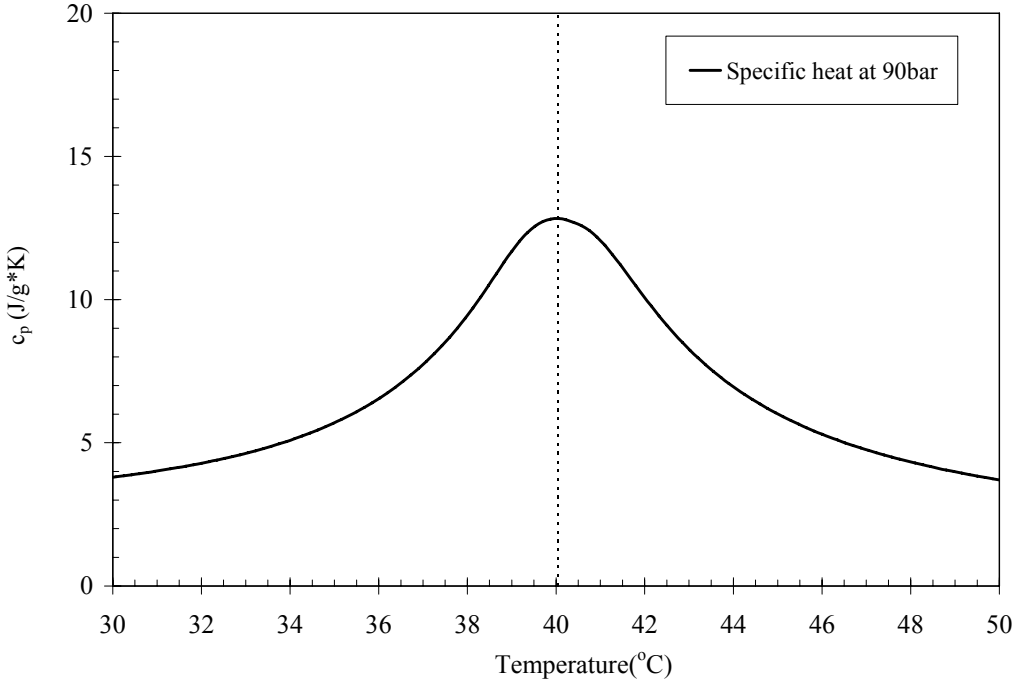

Figure E.25. Specific heat at 90bar

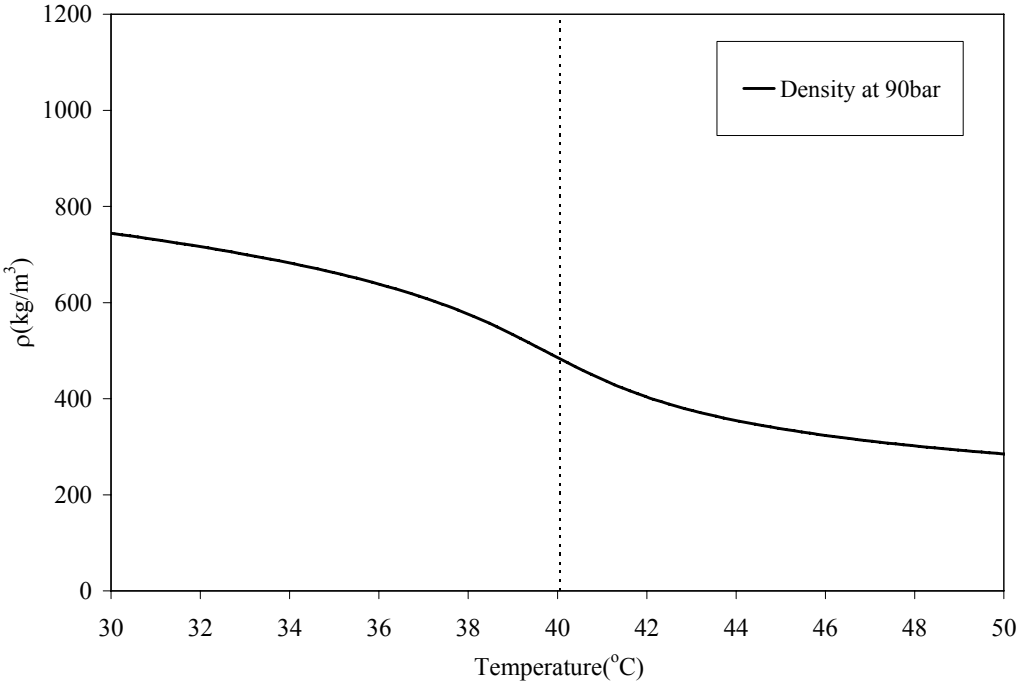

Figure E.26. Density at 90bar

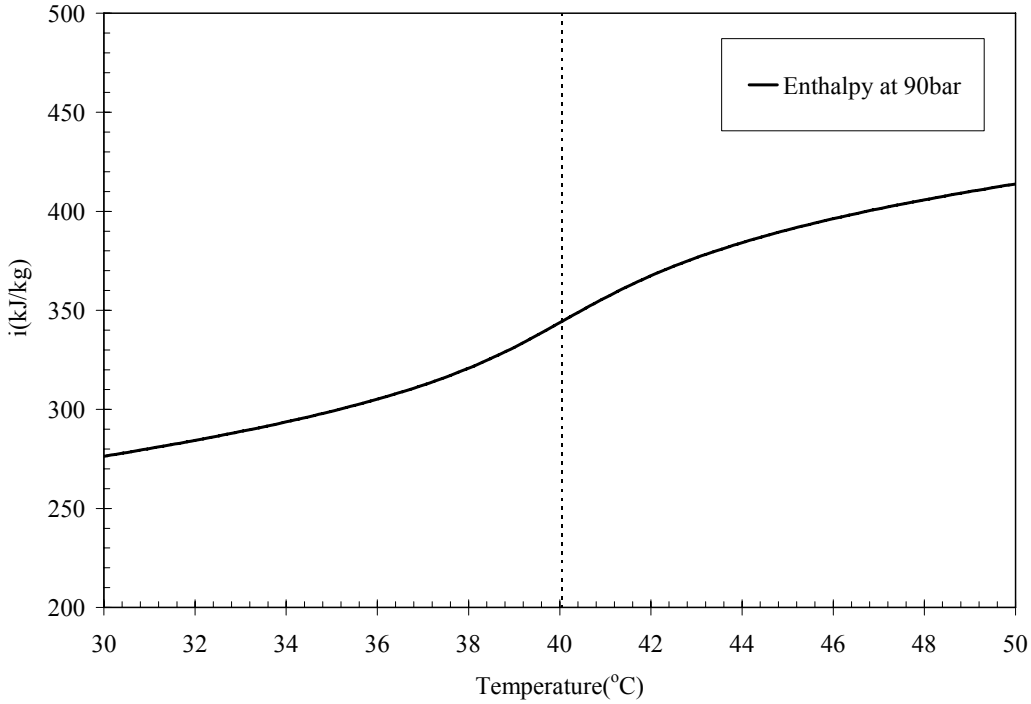

Figure E.27. Enthalpy at 90bar

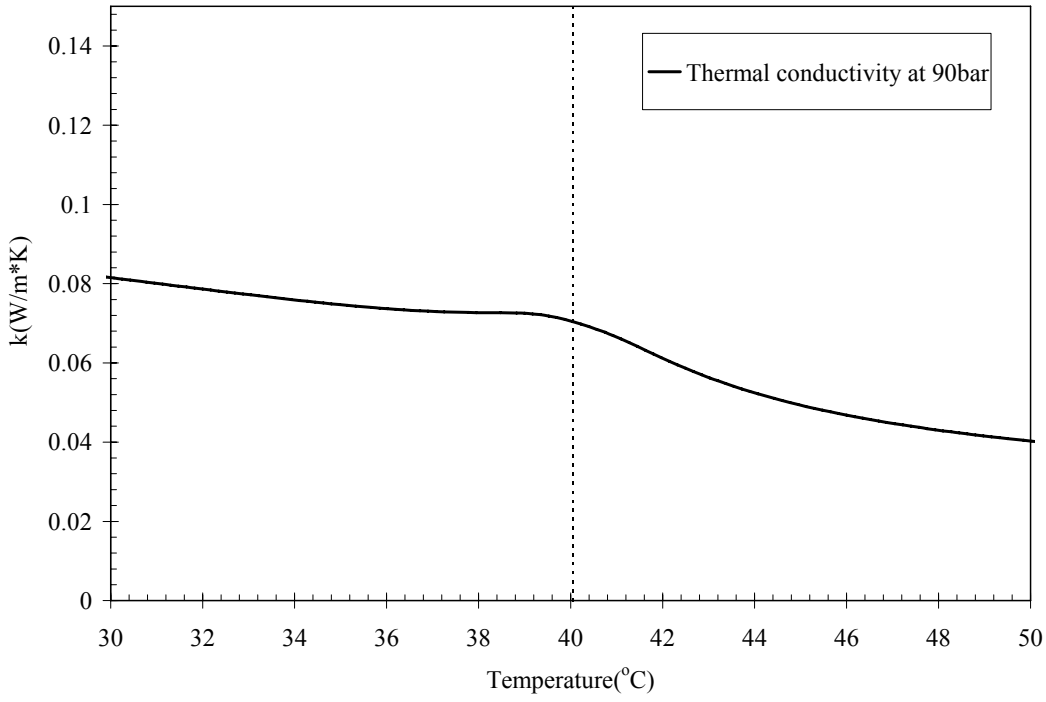

Figure E.28. Thermal conductivity at 90bar

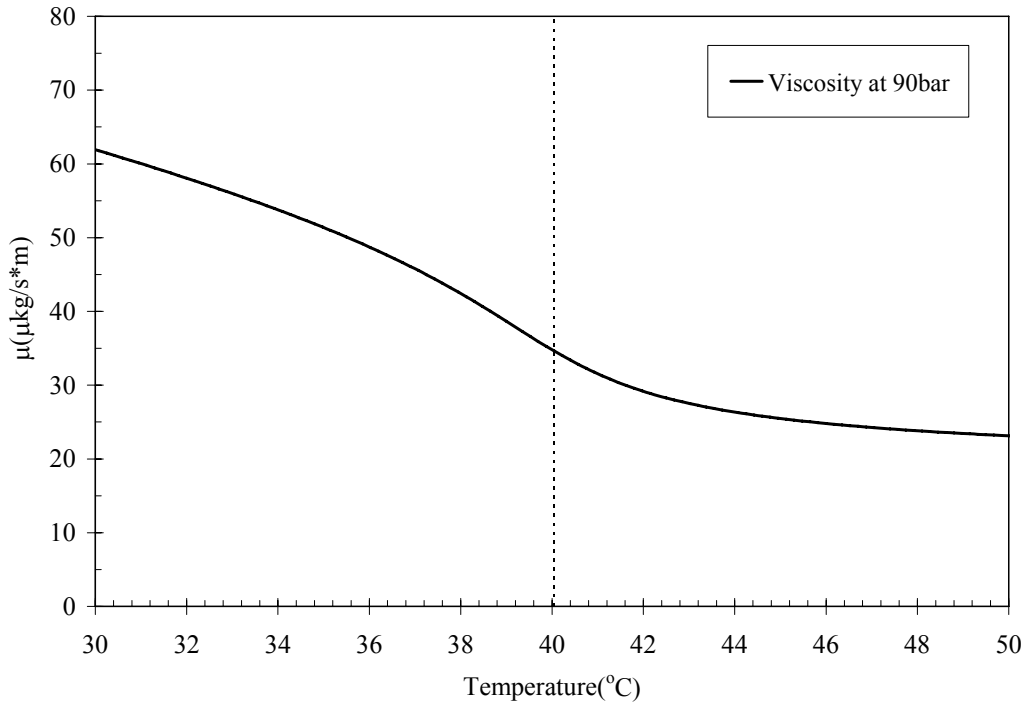

Figure E.29. Viscosity at 90bar

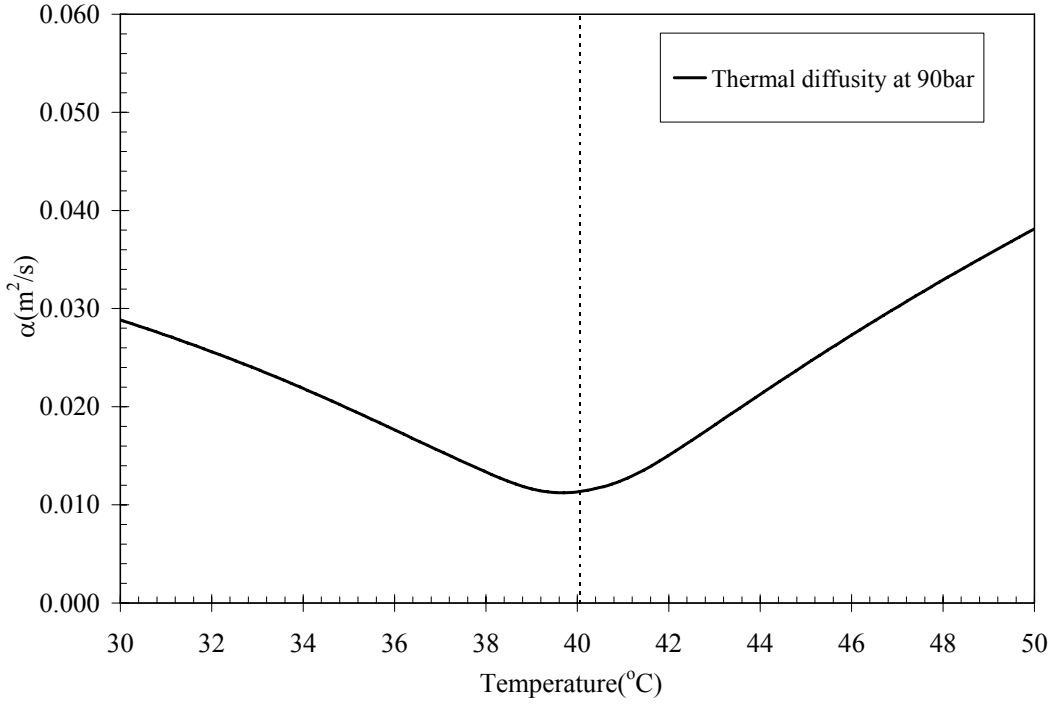

Figure E.30. Thermal diffusivity at 90bar

Appendix F - Results of the nodal calculation

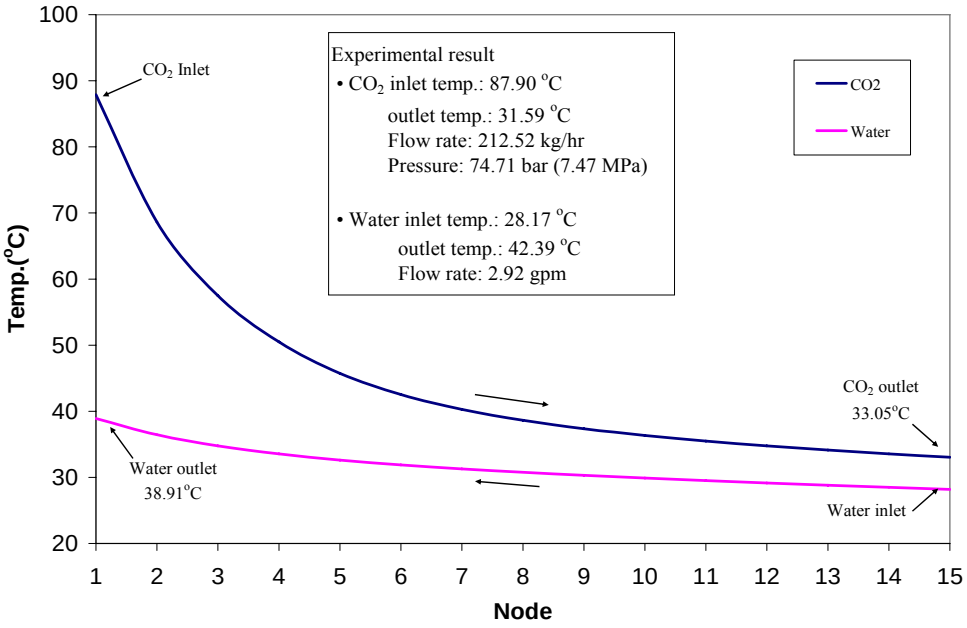

Figure F.1. Temperature distribution of Test A1

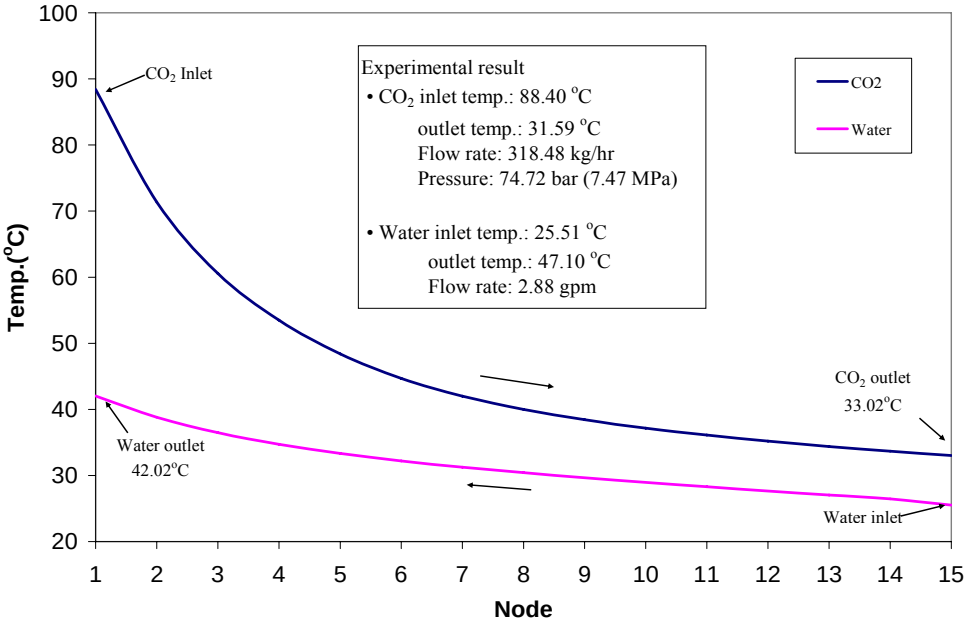

Figure F.2. Temperature distribution of Test A2

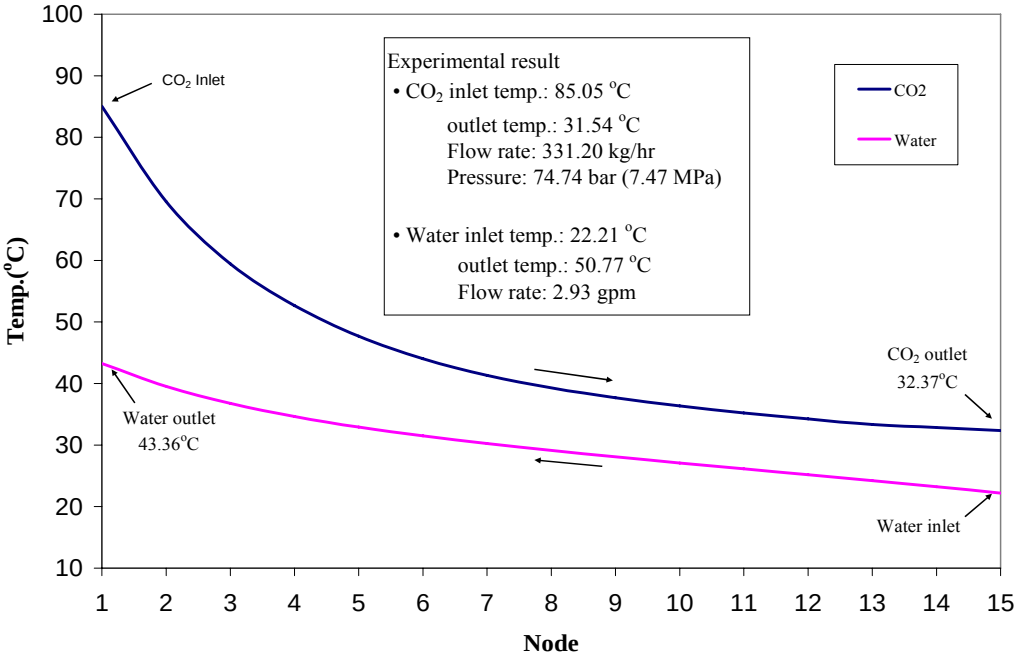

Figure F.3. The temperature distribution of Test A3

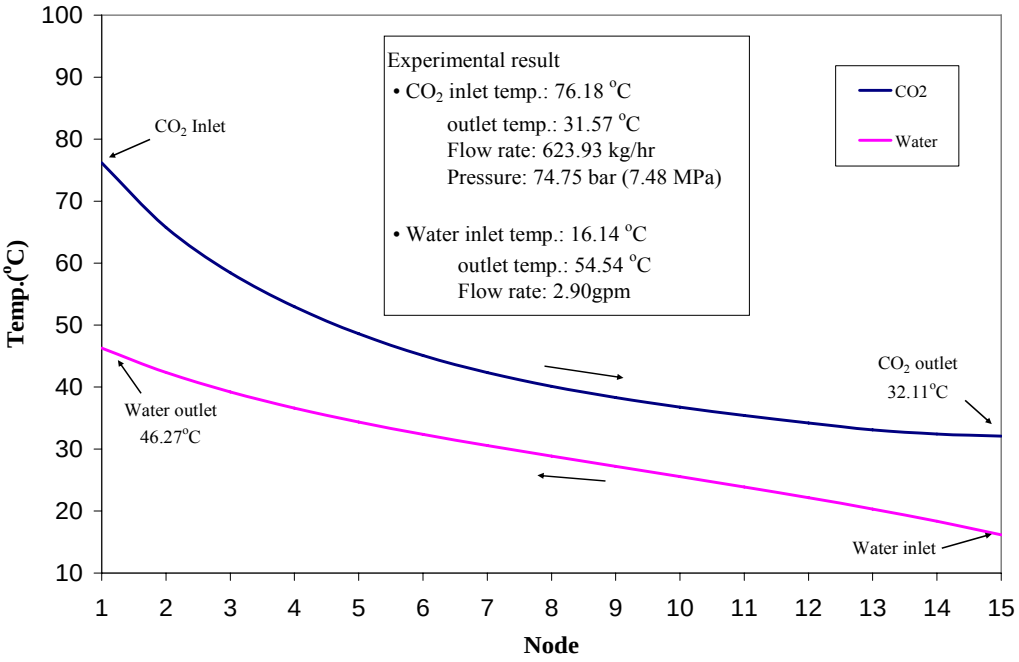

Figure F.4. The temperature distribution of Test A4

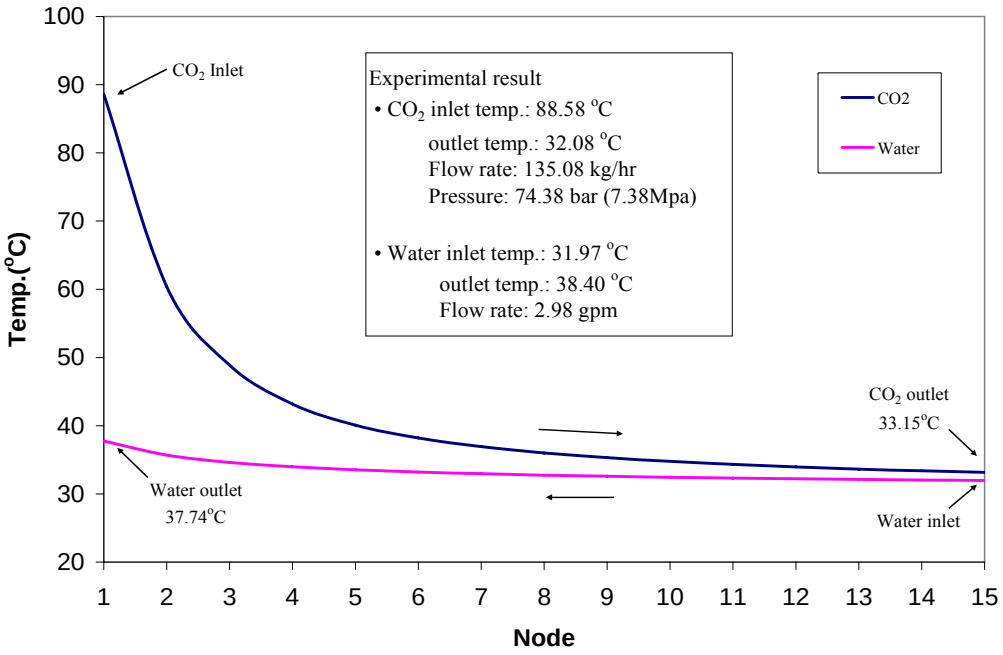

Figure F.5. The temperature distribution of Test B1

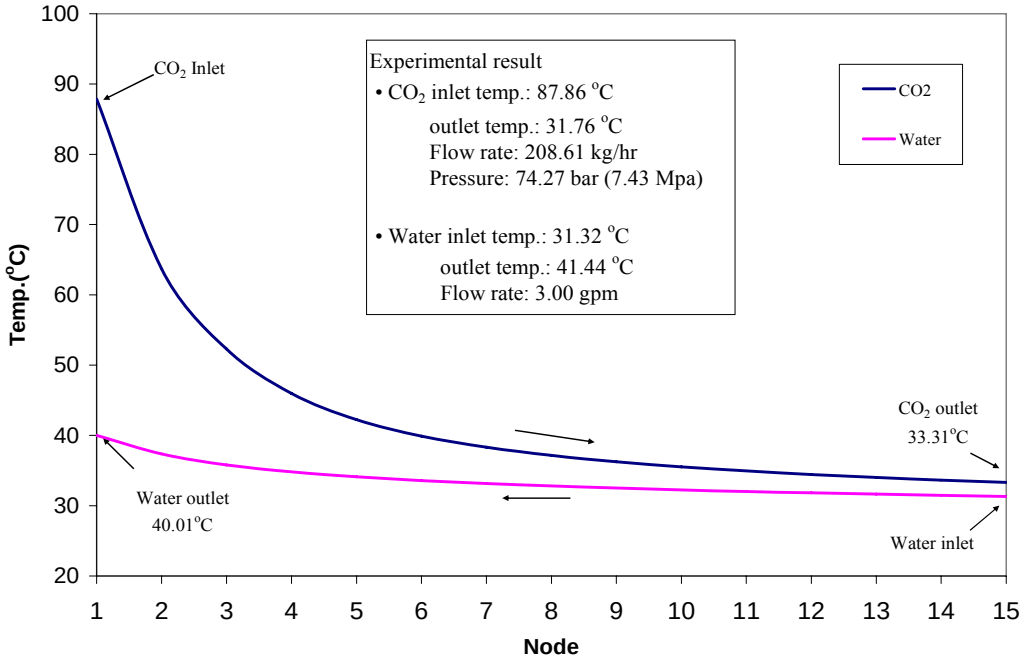

Figure F.6. The temperature distribution of Test B2

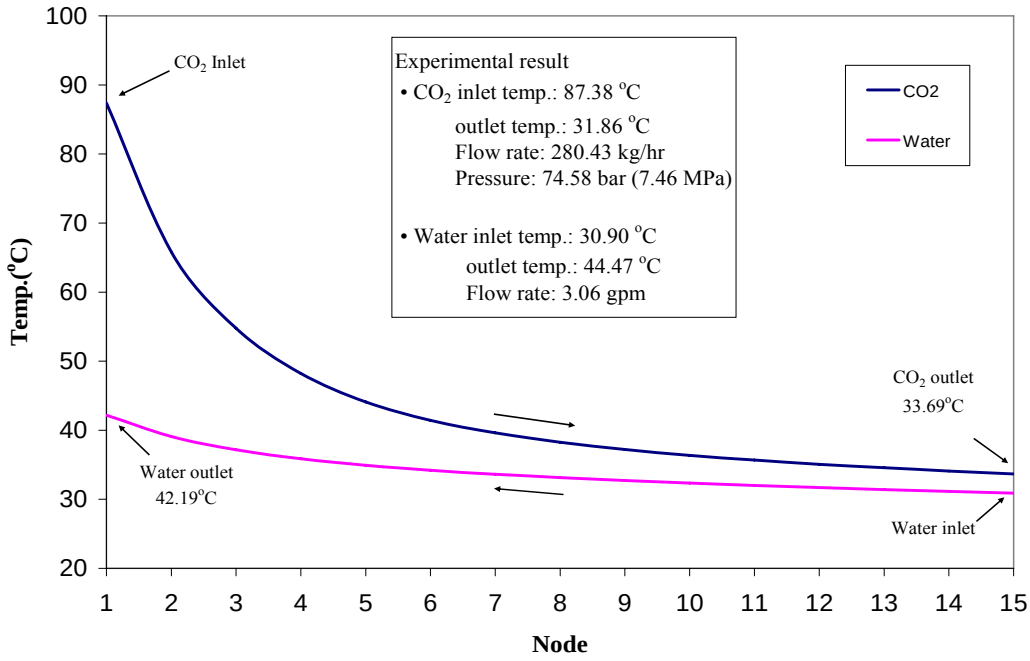

Figure F.7. The temperature distribution of Test B3

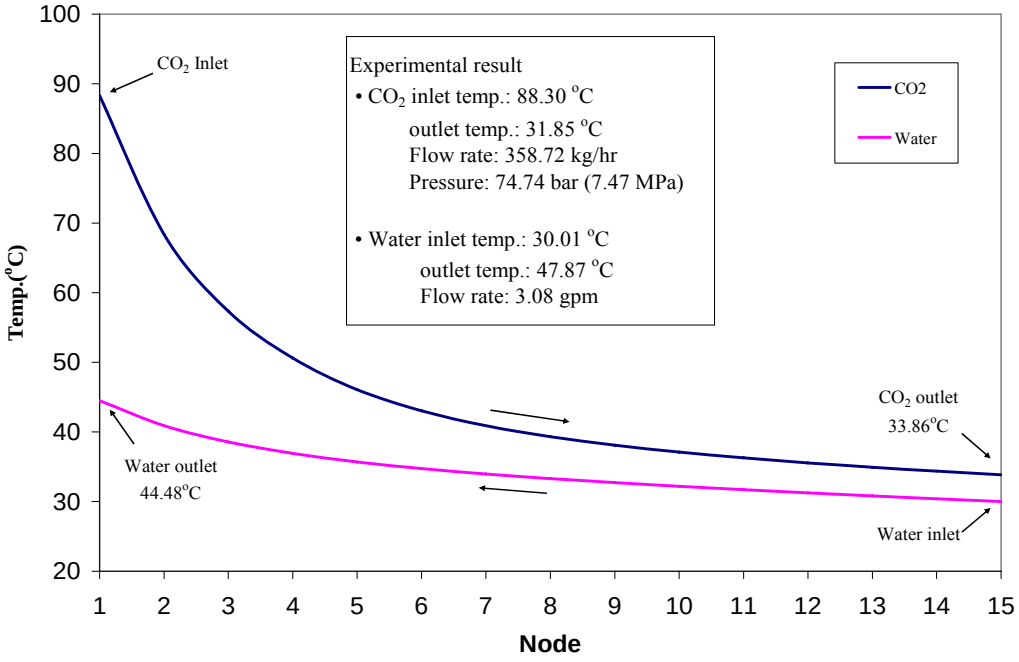

Figure F.8. The temperature distribution of Test B4

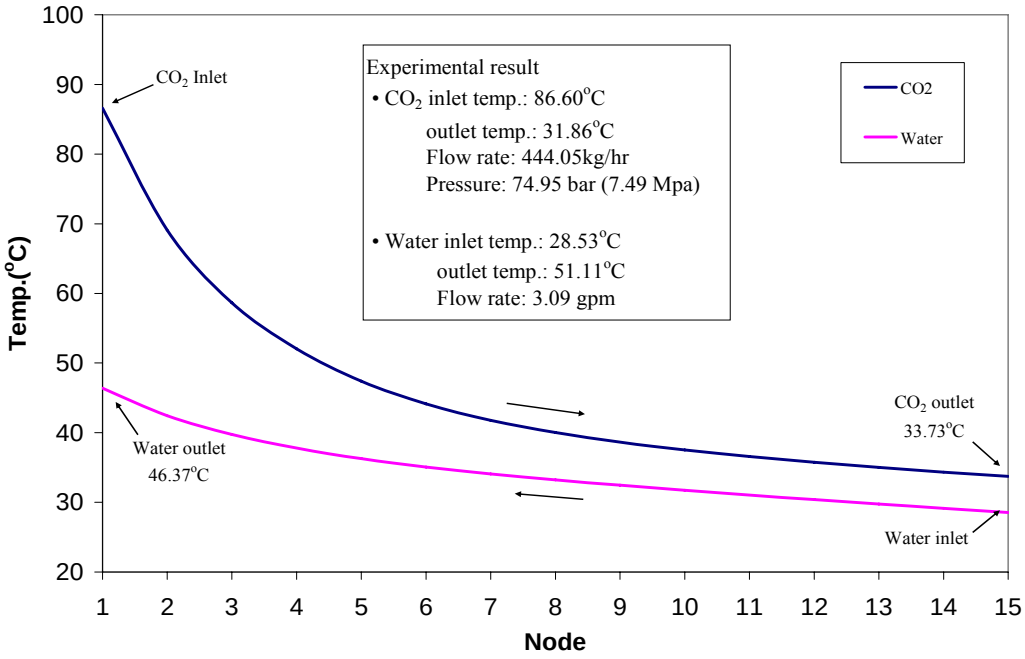

Figure F.9. The temperature distribution of Test B5

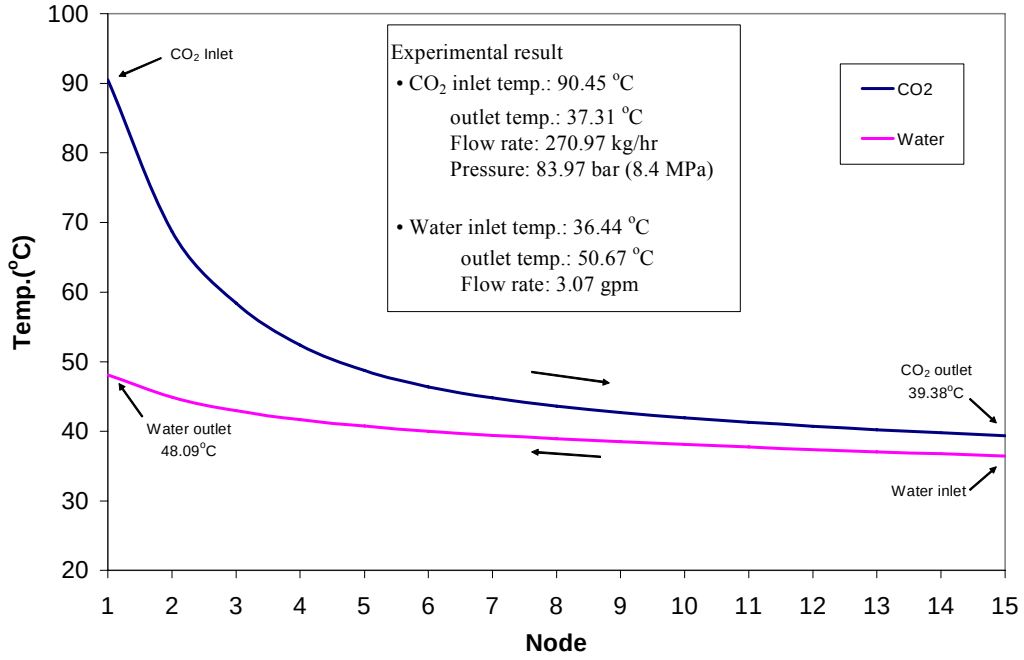

Figure F.10. The temperature distribution of Test C1

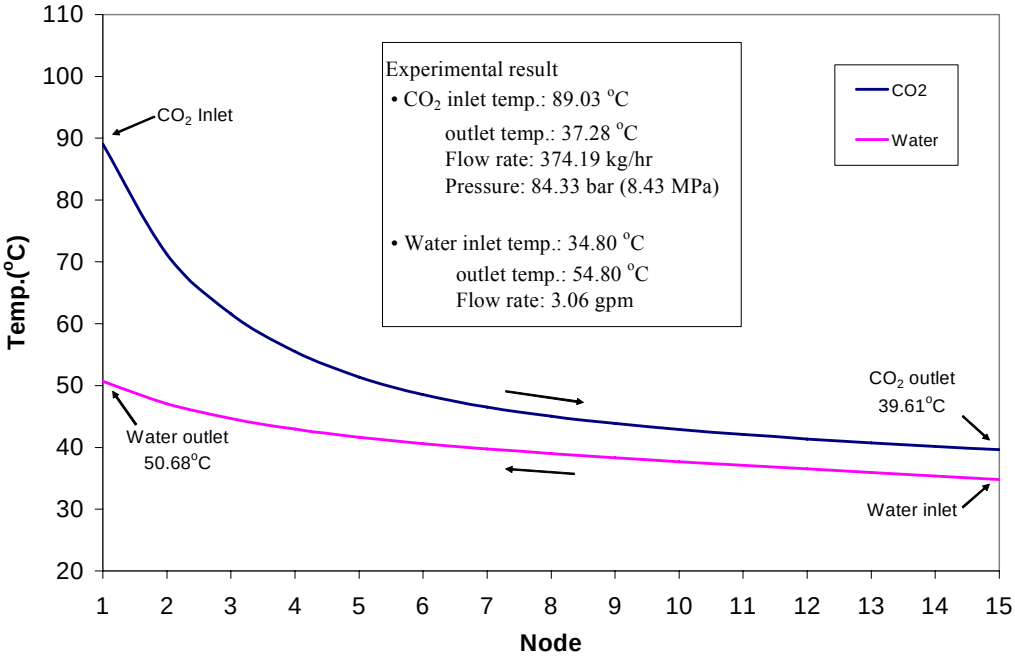

Figure F.11.The temperature distribution of Test C2

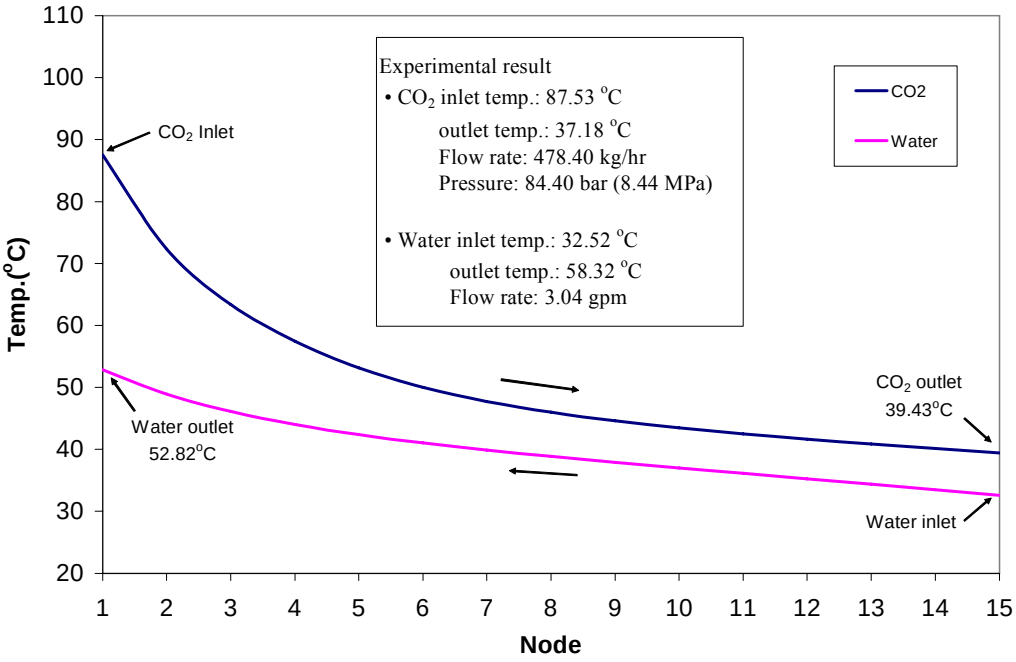

Figure F.12. The temperature distribution of Test C3

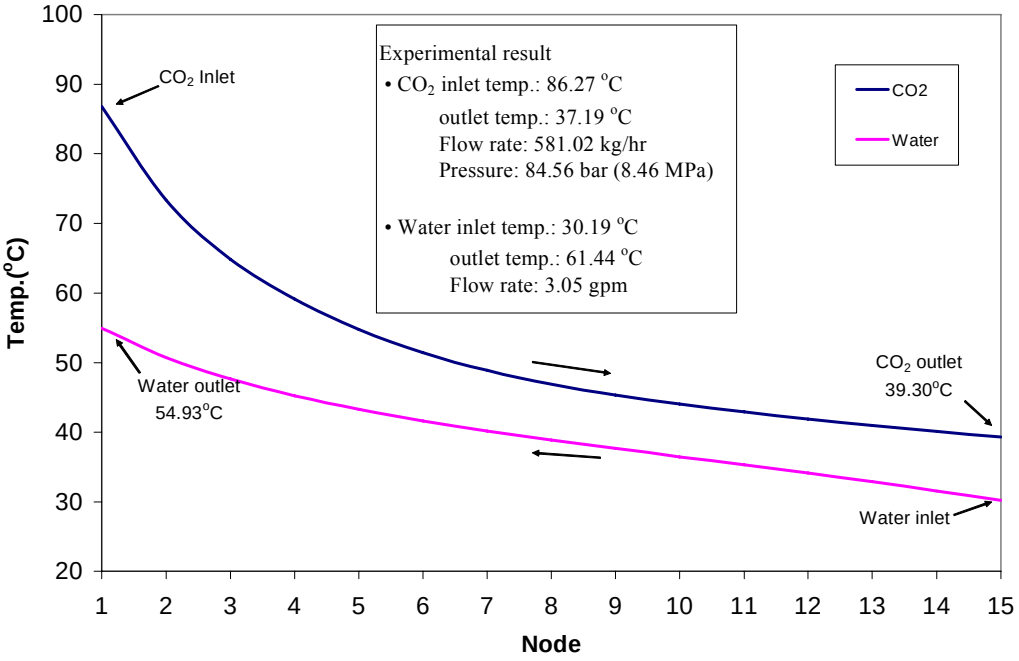

Figure F.13. The temperature distribution of Test C4

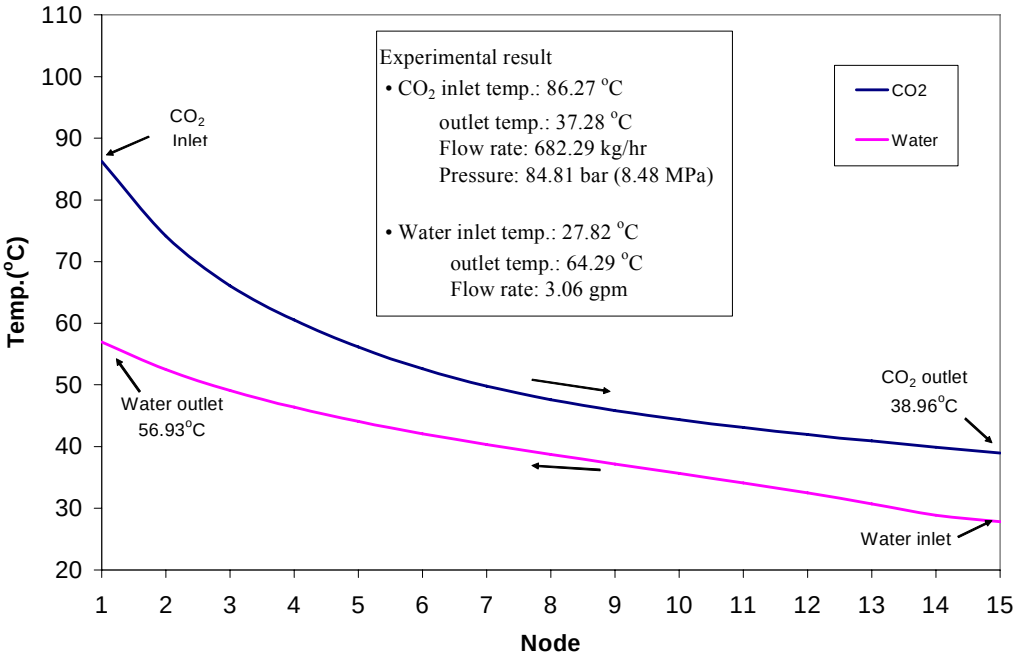

Figure F.14. The temperature distribution of Test C5

Appendix G - Published papers

Proceedings of ICAPP '06
Reno, NV USA, June 4-8, 2006
Paper 6075

Testing of a Compact Heat Exchanger for Use as the Cooler in a Supercritical CO_2 Brayton Cycle

S. Lomperski, D. Cho
Argonne National Laboratory
9700 S. Cass Avenue, Argonne, IL 60439
Tel:630-252-1144 , Fax: 630-252-6080,
lomperski@anl.gov, cho@anl.gov

H. Song, A. Tokuhiro
Kansas State University
3002 Rathbone hall, Manhattan, KS 66506-5205
hoseok@ksu.edu, tokuhiro@ksu.edu

Abstract –*The performance of a compact, printed circuit heat exchanger manufactured by Heatric has been tested for operating conditions corresponding to those of the cooler in the STAR-LM lead fast reactor (LFR) concept, which is designed with an indirect supercritical CO_2 Brayton cycle for power production. The heat exchanger was operated with water at atmospheric pressure on the cold side and supercritical CO_2 on the hot side. Tests were conducted with the CO_2 at pressures of 7.5 and 8.5 MPa, mass flow rates in the range of 100 to 700 kg/h, and heat loads between 10 and 30 kW. The hot side inlet and outlet temperatures were near 85 and 31°C, respectively, to match the planned cooler conditions. The measured overall heat transfer coefficients for Reynolds numbers between 2000 and 6000 are 200-700 W/m^2K. The accompanying water side heat transfer coefficient, measured in separate tests, was ~3500 W/m^2K and so the heat transfer rate for these cooler operating conditions is controlled by the CO_2 side. The measured heat exchanger effectiveness varied between ~1 for the lower Reynolds numbers and 0.7 for the highest.*

I. INTRODUCTION

New nuclear power stations must prove economically competitive if they are to become viable rivals of alternative energy sources. This necessity is a driving factor behind the design of next generation nuclear reactor concepts. Two key features used to improve the economics of new reactors are 1) plant simplifications to limit capital costs and, 2) thermal efficiency enhancement to reduce the cost per unit of power delivered. Both of these features are associated with the supercritical CO_2 Brayton cycle, which has been proposed for power conversion in several of the Generation IV nuclear reactor concepts. The use of a gas turbine cycle rather than a steam-driven Rankine cycle is expected to significantly reduce plant size, complexity, and cost. Recent advances in heat exchanger design and manufacturing techniques promise improvements in the thermal efficiency of the gas turbine Brayton cycle, which reduces the cost of producing electricity and increases the economic competitiveness of the plant.

The supercritical CO_2 Brayton cycle has been chosen as the power conversion system for the Secure Transportable Autonomous Reactor (STAR) project at Argonne National Laboratory. The STAR-LM (Liquid Metal) version is a high temperature, fast flux reactor driven by natural circulation. It employs molten lead (or lead-bismuth eutectic) as the primary coolant and uses an indirect Brayton cycle for the generation of electricity. The plant is designed to operate with a turbine inlet temperature of ~550°C and is expected to have a cycle efficiency of about 45 percent[1].

The STAR-LM reactor achieves high thermal efficiency through, in part, the use of high effectiveness heat exchangers that recover process heat on the secondary side of the plant. Figure 1 is a flow diagram of the STAR-LM plant showing the main elements of the system. Energy transfer between the primary and secondary sides is accomplished with tube-type heat exchangers positioned within the reactor vessel and immersed directly in the molten lead. The high and low temperature recuperators,

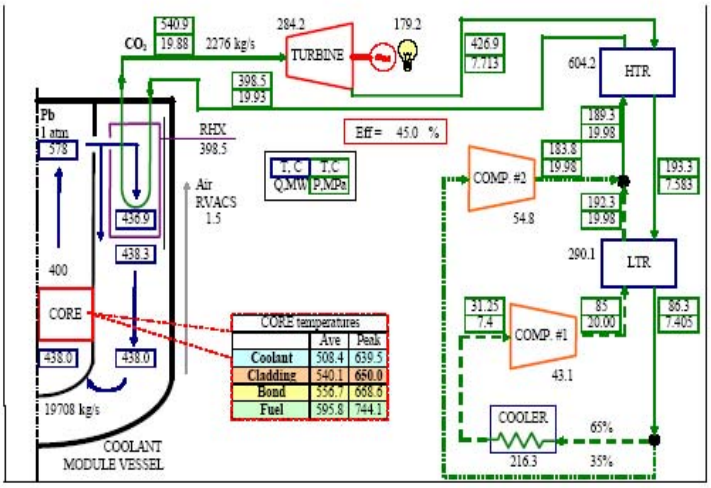

Fig. 1. Flow diagram for the STAR-LM reactor[1].

HTR and LTR, respectively, each operate with supercritical CO_2 on both sides of the heat exchanger. The cooler uses supercritical CO_2 on the hot side and water from the ultimate heat sink on the cold side. The thermal duty of the recuperators is particularly high because of the large energy transfer rate between the hot and cold streams. The performance of these heat exchangers influences cycle efficiency and hence the economics of the plant. In particular, cycle efficiency is sensitive to the effectiveness of both the recuperators and cooler[2,3]. The hydraulic characteristics of the heat exchangers are also of interest because pressure drops must be considered in the task of detailed cycle optimization[4].

Though heat exchangers with high effectiveness are required for optimum cycle efficiency, their size must be limited to control plant capital costs. Traditional equipment such as a shell and tube heat exchanger generally achieves high effectiveness through long flow paths in devices that can be large and costly. An alternative is the so-called "compact" heat exchanger, which is characterized by a large heat transfer area per unit of heat exchanger volume. Compact heat exchangers are particularly suitable for applications with strict size constraints for a given heat load and effectiveness. One type of compact heat exchanger being considered for use in the STAR-LM reactor is a printed circuit heat exchanger (PCHE) manufactured by Heatric, a subsidiary of Meggitt (UK) Ltd. in the UK. A PCHE is constructed from a series of plates that have been chemically-etched to create rows of millimeter-sized flow channels when stacked together (Fig. 2). PCHEs are useful for a variety of industrial applications in which it is critical to limit the size of the heat exchanger. They are of interest for nuclear applications because of their compactness and ability to withstand the high operating temperatures and pressures foreseen for the next generation of nuclear power systems. Indeed, the special characteristics of this type of heat exchanger are an important element in realizing an economically competitive Lead Fast Reactor (LFR). There is, however, no experience with large-scale PCHEs operating in a supercritical CO_2 Brayton cycle and their performance level in an actual power plant is uncertain.

Ishizuka et al.[5] have conducted thermal hydraulic tests with a 3 kW Heatric heat exchanger using CO_2. The hot and cold side pressures ranged between 2-4 and 6-11 MPa, respectively, with fluid temperatures between about 110 and 280°C. The CO_2 on the cold side was in many cases

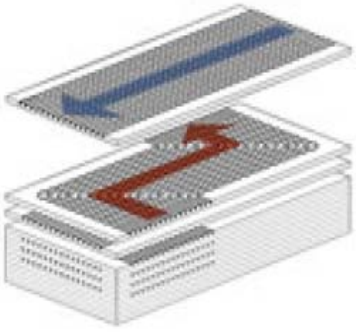

Fig. 2. Minichannel structure of printed circuit heat exchanger (courtesy of Heatric).

supercritical (critical point at 7.38 MPa, 31.1°C) though all tests were carried out far from the pseudocritical region where there are sharp changes in fluid properties with temperature. The effectiveness of the heat exchanger was found to be very high, ~99%, for all test cases. Pressure loss and heat transfer coefficients correlated well with Reynolds number and there were no notable differences between subcritical and supercritical conditions.

The test conditions of Ishizuka's study differ considerably from those of the LFR cooler, which uses water on one side and CO_2 on the other. Moreover, the CO_2 is cooled into the pseudocritical region very close to the critical point. The pseudocritical temperature coincides with the peak in heat capacity and Prandtl number of a fluid at a fixed pressure above the critical pressure. Figure 3 shows the cooler operating range along with the specific heat and density of CO_2 at the operating pressure of 7.4 MPa. It can be seen that the outlet lies in a region of abruptly changing heat capacity and density (though not shown, also thermal conductivity and viscosity). The outlet temperature was chosen to utilize the density increase near the critical point to reduce compressor work and increase cycle efficiency. The fluid must be kept above the critical pressure, however, to avoid two-phase flow into the compressor. Note that even though the abrupt change in fluid properties occurs within a narrow temperature range, it is associated with a significant portion of the HX channel length. This is a consequence of the elevated fluid heat capacity so that an appreciable fraction of the heat transfer takes place in the pseudocritical region. It is therefore of interest to determine whether the fluid property variations within the pseudocritical region influence the performance of the PCHE.

Locating the cooler outlet temperature within the pseudocritical region improves cycle efficiency, but also makes it difficult to predict the performance of the heat exchanger. The thermal hydraulics of a near-critical fluid

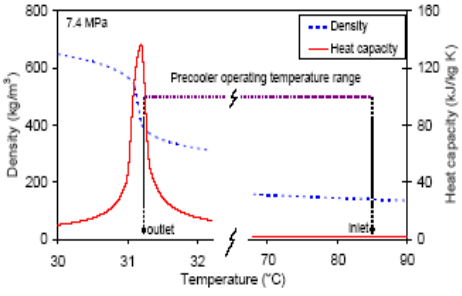

Fig. 3. CO_2 density and heat capacity at cooler operating pressure of 7.4 MPa; inlet 86°C, outlet 31.2°C; note discontinuous temperature scale.

flowing through minichannels such as those of the PCHE is not yet well understood. There is a large body of related research devoted to heat transfer of supercritical fluids in tubes and bundles (see, for example, the reviews of Pioro et al.[6] and Pitla et al.[7]). Researchers have observed complex behavior with both augmentation and deterioration of heat transfer coefficients in the pseudocritical region depending upon such factors as channel orientation, flow regime, and heat flux level. These findings are difficult to apply to the PCHE, especially considering that other studies have shown that the hydraulic and heat transfer characteristics of micro/mini-channels differ from those of conventional-sized channels[8]. There have been, however, few heat transfer studies with mini-channels and fluids near the pseudocritical point. Liao and Zhao[9] heated supercritical CO_2 in ~1 mm-diameter tubes in horizontal, upflow, and downflow configurations. They found augmented heat transfer in the pseudocritical region for the horizontal and upflow configurations, but deterioration for downflow. Buoyancy effects were observed for Reynolds numbers up to ~10^5, which is remarkable for such narrow channels. There have been similar studies involving the cooling of supercritical CO_2 in single[10] and multi-port minichannels[11, 12]. These studies found a marked increase in the heat transfer coefficient in the vicinity of the pseudocritical temperature, and the effect grew with proximity to the critical pressure. The authors of these studies also compared the data to well established correlations with varying degrees of success. Despite the correspondence between the fluid conditions used in these studies and those of the cooler, the data would be difficult to apply to the Heatric PCHE because it consists of semicircular, zigzag minichannels whereas the data was generated with circular, straight minichannels. Forced convection through semicircular minichannels has been investigated numerically for fluids with a strongly temperature-dependent viscosity[13], which is one of the property variations observed near the critical point. The study found that viscosity variations influenced both the velocity and temperature distributions, as well as the friction factor and Nusselt number. There is currently no experimental data to verify these findings or to assess the hydraulic and heat transfer characteristics of zigzag minichannels with fluids in the near-supercritical region.

This paper reports the results of testing performed on a PCHE for conditions that are close to those of the cooler in the LFR, which uses supercritical CO_2 in the near critical region. Experimentally determining the hydraulic and heat transfer characteristics of the heat exchangers is useful for evaluating heat exchanger performance, aiding in the development of models, and supporting claims of favorable economics for the STAR-LM reactor concept. It is noted that the heat exchanger was designed and optimized for the conditions of the LTR, which operates

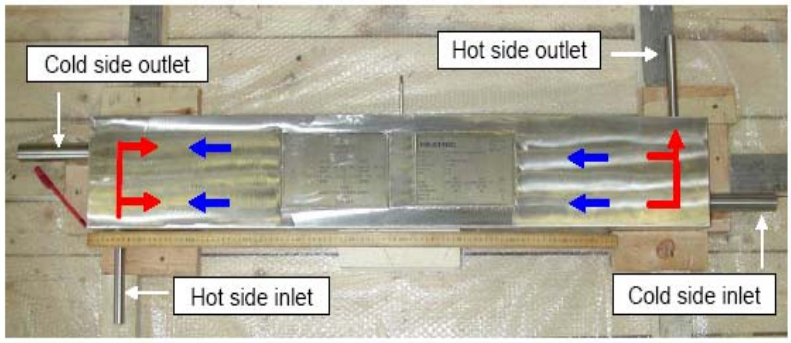

Fig. 4. PCHE under test; cross flow limited to region around inlet and outlet headers.

with supercritical CO_2 on both the hot and cold sides. As a prelude to testing the PCHE for LTR conditions, the heat exchanger has been tested for operating conditions relevant to the cooler. The study has two purposes: to measure HX performance under cooler conditions and to determine whether it is influenced by proximity of the CO_2 side outlet to the pseudocritical region. When considering the results, it should be kept in mind that the PCHE was not optimized for the conditions of the cooler.

II. TEST APPARATUS

II.A. Printed Circuit Heat Exchanger

The device under test is a printed circuit heat exchanger manufactured by Heatric. The etched plates shown in Fig. 2 are joined by high temperature diffusion bonding to form a block that can be welded to others to build up the desired flow area. The strength of the diffusion bond is equal to that of the base metal, making it possible to construct heat exchangers that are suitable for high service temperatures and pressures. The particular unit tested for this study is rated for 200°C at hot and cold side pressures of 82 and 216 bar, respectively. A photo of the heat exchanger showing connections to inlet and outlet manifolds is provided in Fig. 4. The unit is constructed from 316 SS, has dimensions of 120 x 200 x 1200 mm, and weighs about 200 kg. Heat exchanger specifications were established with the notion that the unit would represent a section of the full-scale, 290 MW LTR in the LFR power plant. The small-scale heat exchanger is thought of as one of many units operating in parallel and so its length and pressure drop at nominal operating conditions were specified to correspond with those foreseen for the full scale unit. The mass flow rates for the test unit at nominal operating conditions were scaled down from those of the plant by the ratio of the heat exchanger power ratings. The small-scale unit is rated for a power of 17 kW for the low temperature recuperater conditions shown in Fig. 1. Additional details of the design are provided in Table 1.

II.B. Test loop

The test apparatus consists of two forced circulation loops that link a heat source and heat sink to the heat exchanger under test. A closed loop is used for the supercritical CO_2 on the hot side and an open loop with lab water on the cold side. A schematic of the test apparatus is shown in Fig. 5. The heated section, risers, and elbows are constructed from ½" schedule 80 pipe (i.d.=14 mm). All wetted components are made of type 316 stainless steel. Heating is provided within a 1 m-long horizontal section of the loop by passing a low voltage, AC current directly through the pipe. A magnetic drive gear pump (Micropump model 10k) circulates the CO_2 while flow rate is measured with a coriolis mass flow meter (Endress & Hauser Promass 80M). Absolute and differential pressures are measured with Rosemount model 2088 and 3051CD

TABLE I

Design specifications for PCHE.

	Hot side	*Cold side*
Design pressure (bar)	83	216
Design temperature (°C)	200	200
Flow area (mm^2)	1047	930
Number of channels	1176	1050
Hydraulic diameter (mm)	0.92	0.92
Capacity (liters)	2	2
Total heat transfer area (m^2)	5.6	
Total mass (kg)	203	
Dimensions (mm)	120 x 200 x 1200	

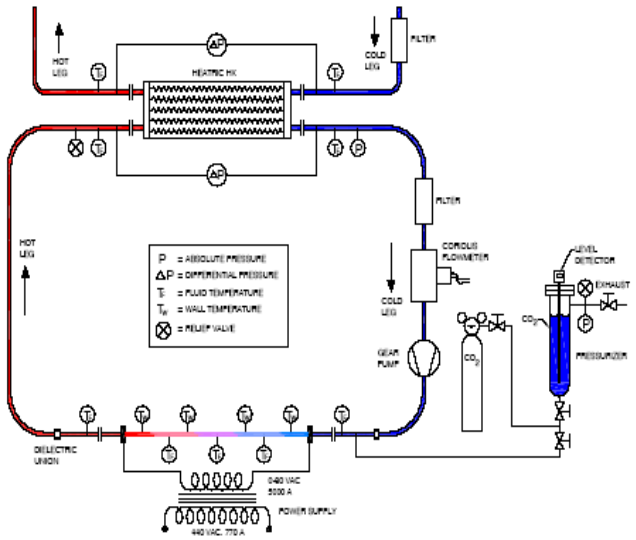

Fig. 5. Schematic of test loop.

pressure transmitters, respectively. Fluid temperatures near the inlets and outlets of the heat exchanger were measured with platinum RTDs having an accuracy of ±0.1°C. A pressurizer is connected to the main loop to accommodate the thermal expansion of the CO_2 as it is heated from the liquid state at room temperature to supercritical conditions. Additional details regarding loop specifications and operating procedure can be found in reference[14].

III. TEST RESULTS

The hydraulic characteristics of the heat exchanger were determined by measuring the relationship between pressure drop and flow rate. Both the hot and cold sides were tested with ambient pressure water at two different temperatures. The hot side was also tested with room temperature CO_2 at 60, 70 and 80 bar. The data has been used to calculate loss coefficients for each side. The flow channels, though of semicircular cross section and following a zigzag pattern, are not unlike circular conduits and so the well-known relationship for the Fanning friction factor for circular tubes has been used:

$$f = \frac{1}{4}\frac{D_h}{L}\left(\frac{\Delta P}{\frac{1}{2}\rho v^2}\right) \quad (1)$$

The expression for pressure losses could also include an additional term as a form factor to account for the elbows of the zigzag pattern, but the simple formulation above is sufficient to reveal general trends in the data.

The pressure loss measurements with water were made over the full available flow rate range. As seen in Fig. 6, the Reynolds numbers for water are rather low and well below the laminar-turbulent transition region of ~2000 for straight circular tubes. For laminar flow in noncircular flow passages, the simple formulation of Eqn. 1 using the hydraulic diameter is not recommended even for long, straight noncircular tubes[15]. Still, the measured friction factor does not exhibit the characteristic Re^{-1} dependence expected for laminar flow until the Reynolds number is below ~100. Within the semicircular, zigzag channels of the PCHE, the turbulent flow regime extends considerably below that of straight, circular tubes. This has also been shown by Haynes and Johnston[16], who in addition demonstrated that increased tortuosity of the PCHE flow paths depresses the transition between turbulent and laminar flow to lower Reynolds numbers. Additional insight into the hydraulic behavior of the PCHE could be obtained through separate experiments in which local flow profiles are measured for a variety of zigzag channels.

Before the heat exchanger was tested under Brayton cycle conditions with CO_2, it was operated with water on both the hot and cold sides to measure the heat transfer coefficient with water. The data is later used in the calculation of the average heat transfer coefficient on the hot (CO_2) side for the cooler conditions. The heat exchanger was operated with cold side inlet and outlet

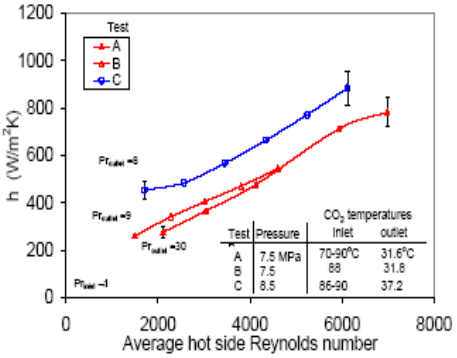

Fig. 8. Average hot side heat transfer coefficient for cooler conditions: water on the cold side and CO_2 on the hot side.

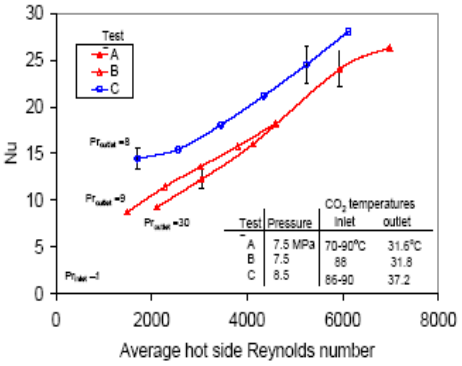

Fig. 9. Average hot side Nusselt number.

kW at the highest. The heat losses for these conditions are less than 100 W. The Prandtl number at the hot side inlet is ~1 for all three tests.

Figure 8 shows plots of the average heat transfer coefficient calculated from the three sets of test data and Eqns. 2-4. For the two 7.5 MPa tests, there appears to be no significant difference in the heat transfer coefficient. Of these two tests, Test A is the one with an outlet temperature closest to the pseudocritical point. This is seen from the outlet Prandtl number, which was determined using the NIST Standard Reference Database[17] with the measured outlet temperature and system pressure. The exit Prandtl number for Test A was about three times that of Test B. Such a large difference in Pr was expected to be reflected in the heat transfer coefficient. For example, the Nusselt number given by the Dittus-Boelter equation is proportional to $Pr^{0.4}$. Figure 9 shows the average hot side Nusselt number, which is seen to be similar for Tests A and B. Note that though the inlet Pr for both tests was ~1 so that fluid properties were similar along much of the channel length, the Prandtl number in Test A was between 10 and 30 along more than 20% of the channel length. This was thought to be sufficient to detect a significant difference in the overall heat transfer coefficient. Figures 8 and 9 show an increase in heat transfer coefficient and Nusselt number with pressure. This was also unexpected since any heat transfer enhancement that may occur in the pseudocritical region is expected to decrease with increasing pressure along with the peak value of the Prandtl number at the pseudocritical point.

Given that other studies have found substantial augmentation of the heat transfer coefficient within the pseudocritical region for minichannels, in many cases greater than a factor of two[11,12], we had expected to see significant differences between Tests A and B, which were at the same pressure and differed only in the proximity of the outlet temperature to the pseudocritical temperature. The same difference was expected for Tests A and C since previous studies have clearly shown that the particular influence of the pseudocritical region on heat transfer decreases with increasing pressure. One explanation for the similarity of Tests A and B may be that the heat transfer augmentation in the pseudocritical region observed for minitubes may, for the zigzag channels of the PCHE, be nonexistent or too weak to observe under the test conditions used in this study. Another explanation is pressure and temperature measurement uncertainty. The pseudocritical temperature varies with pressure so that uncertainty in the pressure introduces uncertainty in the state of the fluid near the outlet. This is particularly important near the critical point. The pressure transmitter is accurate to within ±0.2 bar, which, upon inspection of the thermophysical properties of CO_2, is seen to be significant at 7.5 MPa. For Test A, a pressure reduction of 0.2 bar (supposing the pressure sensor readings were too high) would reduce the Pr from ~30 to the range of 15-20. Uncertainty in the measured outlet temperature and the 0.1°C accuracy limit of the RTDs has approximately the same effect. Therefore it is possible that inaccuracies in the pressure and/or temperature measurements prevent us from determining that the exit Pr for Tests A and B were much closer than the factor of three shown. Note that such uncertainties in the exit Pr are strongly influenced by the actual temperature and pressure.

The reason for the apparent increase in Nusselt number with pressure remains unclear. The difference between the 7.5 MPa and 8.5 MPa data is, at the higher Reynolds numbers, within the given measurement uncertainty. However, this uncertainty is a conservative estimate based on the difference between measured electrical power used to heat the loop and actual HX heat load. The former was used for all calculations because it was the most consistent measurement, though the water/water heat transfer tests showed that it overestimates power to the HX by roughly 8%. Therefore a significant

portion of the uncertainty consists of a constant offset for all curves and so the observed pressure dependence of the Nusselt number, though small, is significant. This will be explored further in future tests by repeating the measurements at 8.5 MPa and conducting a third test near 9.5 MPa.

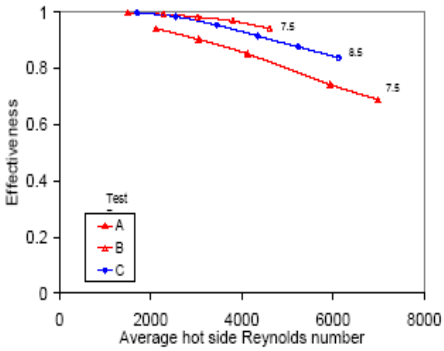

Fig. 10. Heat exchanger effectiveness.

The effectiveness of the heat exchanger is the ratio of the actual heat transfer rate to the maximum rate achieved if the hot side outlet was cooled to the temperature of the cold side inlet. The effectiveness is written as:

$$eff = \frac{i_{hin} - i_{hout}}{i_{hin} - i_{cin}} \quad (5)$$

Figure 10 provides the measured effectiveness for the test conditions shown in Fig. 8. The effectiveness at 7.5 MPa is about 0.95 at the lowest flow rate and drops to ~0.7 at the highest. Like the heat transfer coefficient, the effectiveness is slightly higher at 8.5 MPa. The preliminary design of the LFR secondary side calls for cooler effectiveness >90%. However, the Reynolds number range in which the heat exchanger would operate has not yet been determined. In addition, this PCHE has been optimized for CO_2/CO_2 heat exchange rather than CO_2/water and so the particular measured level of effectiveness under cooler conditions is not critical. Instead, the value of these tests lies in the data that can be used to validate models used to predict PCHE behavior under conditions approximating those of the LFR cooler.

IV. CONCLUSIONS

The hydraulic and heat transfer characteristics of a Heatric printed circuit heat exchanger have been tested for the conditions of the cooler in a LFR operating with a supercritical CO_2 Brayton cycle. The heat exchanger was operated with water at atmospheric pressure on the cold side and supercritical CO_2 on the hot side. Tests were conducted with the CO_2 at pressures of 7.5 and 8.5 MPa, mass flow rates in the range of 100 to 700 kg/h, and heat loads between 10 and 30 kW. The hot side inlet and outlet temperatures were near 85 and 31°C, respectively, to match the planned cooler conditions. The measured overall heat transfer coefficients for the tested Reynolds number range of 2000-6000 are between 200 and 700 W/m^{2}K. The accompanying water side heat transfer coefficient, measured in separate tests, was ~3500 W/m^{2}K and so the heat transfer rate for these cooler operating conditions is controlled by the CO_2 side. The heat transfer augmentation near the pseudocritical point found in other studies with minichannels was not observed with the PCHE. This may be due to the particular zigzag channel geometry of the PCHE or measurement uncertainty that results in uncertainty in state of the CO_2 at the HX outlet. This can be addressed in the future by performing several additional tests with slightly different pressures and temperatures near those of the completed 7.5 MPa tests. This study also found a weak, though significant increase in heat transfer coefficient with pressure, which was unexpected. The reason for this dependence is currently unclear. Current plans are to investigate this pressure dependence with additional tests at 8.5 MPa and higher pressures.

ACKNOWLEDGMENTS

Thanks to Anton Moisseytsev and Jim Siniecki, both at ANL, for their assistance and guidance. This work was supported in part by the U.S. Department of Energy, Nuclear Energy Research Initiative, Project number 05-146, Award Number DE-FC07-05ID14672, Heat Exchanger Studies for Supercritical CO_2 Power Conversion System.

NOMENCLATURE

A = heat transfer area
c_p = specific heat
D_h = hydraulic diameter
f = Fanning friction factor
h = heat transfer coefficient
i = enthalpy
k = thermal conductivity
L = length
Nu = Nusselt number = hD_h/k
Pr = Prandtl number = $c_p\mu/k$
ΔP = differential pressure
T = temperature
ΔT_{LM} = logarithmic mean temperature difference
U = overall heat transfer coefficient

v = velocity
ρ = density
μ = viscosity

Subscripts

cin = cold side inlet
cout = cold side outlet
hin = hot side inlet
hout = hot side outlet

REFERENCES

1. J. J. SIENICKI, A. V. MOISSEYTSEV, D. C. WADE, M. T. FARMER, C. P. TZANOS, J. A. STILLMAN, J. W. HOLLAND, P. V. PETKOV, I. U. THERIOS, R. F. KULAK, and Q. WU, "The STAR-LM Lead-Cooled Closed Fuel Cycle Fast Reactor Coupled to a Supercritical Carbon Dioxide Brayton Cycle Advanced Power Converter," *Proc. 2nd Int. Conf. on Heavy Liquid Metal Coolants in Nuclear Technologies* (HLMC-2003), Paper 2105, December 8-12, Obninsk, Russia (2003).
2. V. DOSTAL, P. HEJZLAR, N. TODREAS, and J. BUONGIORNO, "Medium-power lead-alloy fast reactor balance-of-plant options," *Nuclear Technology,* **147** 388 (2004).
3. A. MOISSEYTSEV, J. SIENICKI, and D. WADE, "Cycle Analysis of Supercritical Carbon Dioxide Gas Turbine Brayton Cycle Power Conversion System for Liquid Metal-Cooled Fast Reactors," *Proc. 11th Int. Conf. on Nuclear Engineering (ICONE11)*, April 20-23, Tokyo, Japan (2003).
4. P. F. PETERSON, "Multiple-Reheat Brayton Cycles for Nuclear Power Conversion with Molten Coolants," *Nuclear Technology*, **144** 279 (2003).
5. T. ISHIZUKA, Y. KATO, Y. MUTO, K. NIKITIN, N. TRI, and H. HASHIMOTO, "Thermal-hydraulic Characteristics of a Printed Circuit Heat Exchanger in a Supercritical CO2 Loop," *Proc. 11th Int. Topical Meeting on Nuclear Reactor Thermal-Hydraulics (NURETH-11)*, paper 218, October 2-6, Avignon, France (2005).
6. I. PIORO, H. KHARTABIL, and R. DUFFEY, "Heat Transfer to Supercritical Fluids Flowing in Channels-Empirical Correlations (Survey)," *Nuclear Engineering and Design*, **230** 69 (2004).
7. S. PITLA, D. ROBINSON, E. GROLL, and S. RAMADHYANI, "Heat Transfer from Supercritical Carbon Dioxide in Tube Flow: a Critical Review," *HVAC&R Research*, **4** *3* 281 (1998).
8. X PENG and G. PETERSON, "Convective Heat Transfer and Flow Friction for Water Flow in Microchannel Structures," *Int. J. Heat Mass Transfer,* **39** *12* 2599 (1996).
9. S. LIAO and T. ZHAO, "An Experimental Investigation of Convection Heat Transfer to Supercritical Carbon Dioxide in Miniature Tubes," *Int. J. Heat Mass Transfer*, **45** 5025 (2002).
10. S. LIAO and T. ZHAO, "Measurements of Heat Transfer Coefficients from Supercritical Carbon Dioxide Flowing in Horizontal Mini/Micro Channels," *Transactions of the ASME J. Heat Transfer*, **124** 413 (2002).
11. X HUAI, S. KOYAMA, and T. ZHAO, "An Experimental Study of Flow and Heat Transfer of Supercritical Carbon Dioxide in Multi-Port Mini Channels Under Cooling Conditions," *Chemical engineering Science* **60** 3337 (2005).
12. J. PETTERSEN, R. RIEBERER, A. LEISTER, "Heat Transfer and Pressure Drop Characteristics of Supercritical Carbon Dioxide in Microchannel Tubes under cooling," *Proc. 4th IIR-Gustav Lorentzen Conference on Natural Working Fluids*, pp. 315-22, Purdue University, USA (2000).
13. T. M. HARMS, M. A. JOG, and R. M. MANGLIK, "Effects of Temperature-Dependent Viscosity Variations and Boundary Conditions on Fully Developed Laminar Forced Convection in a Semicircular Duct, *Transactions of the ASME*, **120** 600 (1998).
14. S. LOMPERSKI, D. CHO, R. JAIN, and M.L. CORRADINI, "Stability of a Natural Circulation Loop with a Fluid Heated Through the Thermodynamic Pseudo-critical Point, *Proc. 2004 Int. Congress on Advances in Nuclear Power Plants (ICAPP 04),* paper 4268, June 13-17, Pittsburgh, PA, (2004).
15. R. BIRD, W. STEWART, E. LIGHTFOOT, *Transport Phenomena*, Chapter 6, John Wiley & Sons, Inc., New York (1960).
16. B. S. HAYNES AND A. M. JOHNSTON, High-Effectiveness Micro-Exchanger Performance, Unpublished, www.heatric.com (2002).
17. National Institute of Standards and Technology, Standard Reference Database Number 69 June 2005 release, http://webbook.nist.gov/chemistry/fluid/.

NTHAS5: Fifth Korea-Japan Symposium on Nuclear Thermal Hydraulics and Safety
Jeju, Korea, November 26- 29, 2006

NTHAS5-N002

Experimental Investigations of a Printed circuit heat exchanger for Supercritical CO_2 and Water Heat Exchange

H. Song[1], J. Van Meter[1], S. Lomperski[2], D. Cho[2], H. Y. Kim[3], and A. Tokuhiro[1]

[1]*Kansas State University*
3002 Rathbone hall, Manhattan, KS 66506-5205
hoseok@ksu.edu,jwv3333@ksu.edu, tokuhiro@ksu.edu

[2]*Argonne National Laboratory*
9700 S. Cass Avenue, Argonne, IL 60439
Tel:630-252-1144 , Fax: 630-252-6080,
lomperski@anl.gov, cho@anl.gov

[3]*Korea Atomic Energy Research Institute*
150 Deokjin-dong, Yusung-gu, Daejeon, S. Korea 305-353
hykim1@kaeri.re.kr

ABSTRACT

A printed circuit heat exchanger (PCHE) manufactured by Heatric has been tested for operating conditions of the cooler in the STAR-LM lead fast reactor (LFR) concept, which is designed with an indirect supercritical CO_2 Brayton cycle for power production. Also the heat exchanger was operated in the small temperature difference between inlet and outlet on the hot side. The heat exchanger was operated with water(H_2O) at atmospheric pressure on the cold side and supercritical CO_2 on the hot side. Tests were conducted with the CO_2 at pressures of 7.5 and 8.5 MPa. For the condition of the cooler, the measured overall heat transfer coefficients for Reynolds numbers between 2000 and 6000 are 200-700 W/m^2K. The accompanying H_2O side heat transfer coefficient, measured in separate tests, was ~3500 W/m^2K. For the condition of the small temperature difference, the average heat transfer coefficient on the hot side has the peak value at the pseudocritical point of 7.5 and 8.5MPa. The trend looks like the specific heat line whose values increase before, has the peak value at, and decrease after the pseudocritical point as the temperature of CO_2 increase.

1. INTRODUCTION

The Generation IV Advanced Reactor systems are expected to achieve significant reductions in capital and operating costs by taking advantage of the benefits of modular construction, up-to-date manufacturing practices, design simplifications, design innovations, and advanced technologies. Significant realistic reductions in plant costs, size, and complexity combined with a significant increase in plant efficiency may potentially be realized through the use of an advanced power conversion technology consisting of a gas turbine Brayton cycle utilizing supercritical CO_2 as the working fluid. Supercritical CO_2 has significantly higher density (relative to helium), which reduces the need for compressive work in the bottom part of Brayton cycle; thus increasing the overall cycle efficiency.

The supercritical CO_2 Brayton cycle has been considered as the power conversion system for the Secure Transportable Autonomous Reactor (STAR) project at Argonne National Laboratory. The STAR-LM (Liquid Metal) version is a high temperature, fast flux reactor driven by natural circulation. It employs molten lead (or lead-bismuth eutectic) as the primary coolant and uses an indirect Brayton cycle for the generation of electricity. The plant is designed to operate with a turbine inlet temperature of ~550°C and is expected to have a cycle efficiency of about 45 percent.

One of the key components for the S-CO_2 power system is the regenerative heat exchanger, known as the "recuperator". This is where heat exchange between two flowing streams of supercritical CO_2 takes place. While the benefits of the S-CO_2 Brayton cycle are attributed to the unique thermophysical properties of S-CO_2 (e.g. density and specific heat), these same

properties also present technical challenges to the recuperator design.

The high and low temperature recuperators, HTR and LTR, respectively, each operate with supercritical CO_2 on both sides of the heat exchanger. The precooler uses supercritical CO_2 on the hot side and H_2O from the ultimate heat sink on the cold side. In particular, cycle efficiency is sensitive to the effectiveness of both the recuperators and precooler. The hydraulic characteristics of the heat exchangers are also of interest because pressure drops must be considered in the task of detailed cycle optimization.

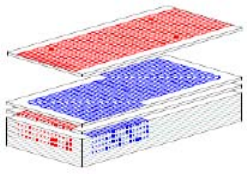

Fig. 1. Minichannel structure of printed circuit heat exchanger (courtesy of Heatric).

One kind of compact heat exchanger that is being considered for the recuperator and precooler is a PCHE. This is a heat exchanger manufactured by Heatric, a subsidiary of Meggitt (UK) Ltd. in the UK. A PCHE is constructed from a series of plates that have been chemically-etched and diffusion bonded. This is shown in Figure 1.

In fact, Moisseytsev et al. showed a comparison of 7 heat exchanger designs for the STAR-LM LFR concept. A heat exchanger design such as a PCHE was indeed much smaller than traditional configurations. However, basic heat transfer data to evaluate the PCHE's performance, under reactor-relevant conditions, are lacking. Further its performance level in an actual power plant is uncertain. In this paper, a printed heat exchanger will be studied under the condition for the precooler in the STAR-LM system and near the pseudocritical region of CO_2.

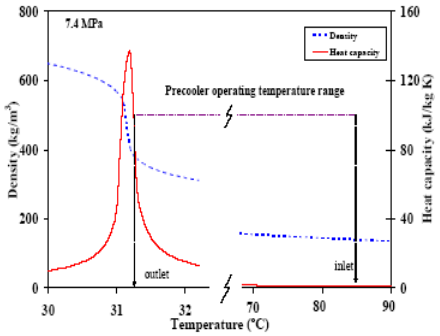

Fig. 2. CO_2 density and heat capacity at cooler operating pressure of 7.4 MPa; inlet 86°C, outlet 31.2°C; note discontinuous temperature scale.

Ishizuka et al. have conducted thermal hydraulic tests with a 3 kW PCHE using CO_2 on the hot and cold side, whose pressures ranged between 2-4 and 6-11 MPa respectively. The fluid temperatures ranged between 110 and 280°C. The effectiveness of the heat exchanger was found to be very high (~99%) for all test cases. Pressure loss and heat transfer coefficients correlated well with Reynolds number, and there were no notable differences between subcritical and supercritical conditions. Differently from Ishizuka's study, this paper presents the experimental result under the condition of the LFR cooler, which uses H_2O on the cold side and CO_2 on the hot side. Figure 2 shows the cooler operating range along with the specific heat and density of CO_2 at the operating pressure of 7.4 MPa. It can be seen that the outlet lies in a region of abruptly changing heat capacity and density. The outlet temperature was chosen to utilize the density increase near the critical point to reduce compressor work and increase cycle efficiency. This is a consequence of the elevated fluid heat capacity so that a larger fraction of the heat transfer takes place in the pseudocritical region. Therefore it is of interest to determine whether the fluid property variations within the pseudocritical region influence the performance of the PCHE.

There are few studies related with heat transfer of the CO_2 near the psedocritical region in minichannels. Liao et al. conducted a heat transfer experiment in ~1 mm-diameter tubes with the CO_2in horizontal, upflow, and downflow configurations at various bulk temperatures. Bulk temperature is defined as:

$$T_{bulk} = \frac{T_{in} + T_{out}}{2} \qquad (1)$$

In this experiment they found a heat transfer increase in the pseudocritical region for the horizontal and upflow configurations, but decrease of heat transfer for downflow configuration.

This paper shows the results of testing a PCHE under conditions that are close to those of the precooler in the LFR. It also presents how a small temperature difference between inlet and outlet on the hot side of the heat exchanger affects the device's heat transfer. This study has three purposes: to measure heat exchanger performance under precooler conditions, to determine whether it is influenced by proximity of the CO_2 outlet side to the pseudocritical region, and to discover how the heat transfer coefficient of the CO_2 side changes in relation to bulk temperature.

2. TEST APPARATUS

2.1. Printed circuit heat exchanger (PCHE)

A printed circuit heat exchanger (PCHE), whose heat load is 17kW, was operated under several experimental conditions. The heat exchanger tested for this study is rated for 200°C at hot and cold side pressures of 21.6 and 8.2MPa, respectively. The unit is constructed from 316 SS, has dimensions of 120 × 200 × 1200 mm, and weighs about 200 kg. Additional details of the design are provided in Table 1.

The etched plates shown in Figure 1 are stacked by high temperature diffusion bonding process to form a block that can

Table 1. Design specifications for PCHE.

	Hot side	Cold side
Design pressure (MPa)	21.6	8.3
Design temperature (°C)	200	200
Flow area (mm^2)	930	1047
Number of channels	1050	1176
Hydraulic diameter (mm)	0.92	0.92
Capacity (liters)	2	2
Total heat transfer area (m^2)	5.6	
Total mass (kg)	203	
Dimensions (mm)	120 x 200 x 1200	

Fig. 3. PCHE under test and outlet headers.

be welded to others to build up the desired flow area. The strength of the diffusion bond is equal to that of the base metal, making it possible to construct heat exchangers that are suitable for high temperatures and pressures. A photo of the heat exchanger showing connections to inlet and outlet manifolds is provided in Figure 3.

2.2. Test loop

The test apparatus consists of two forced circulation loops that link a heat source and heat sink to the heat exchanger under test. A closed loop is used for the supercritical CO_2 on the hot side and an open loop with lab H_2O on the cold side. A schematic of the test apparatus is shown in Figure 4.

The heated section, risers, and elbows are constructed from ½" schedule 80 pipe (i.d.=14 mm). All wetted components are made of type 316 stainless steel. Heating is provided within a 1 m-long horizontal section of the loop by passing a low voltage, AC current directly through the pipe. A magnetic drive gear pump (Micropump model 10k) circulates the CO_2 while flow rate is measured with a coriolis mass flow meter (Endress & Hauser Promass 80M). Absolute and differential pressures are measured with Rosemount model 2088 and 3051CD pressure transmitters, respectively.

Fluid temperatures near the inlets and outlets of the heat exchanger were measured with platinum RTDs having an accuracy of ±0.1°C. A pressurizer is connected to the main loop to accommodate the thermal expansion of the CO_2 as it is heated from the liquid state at room temperature to supercritical

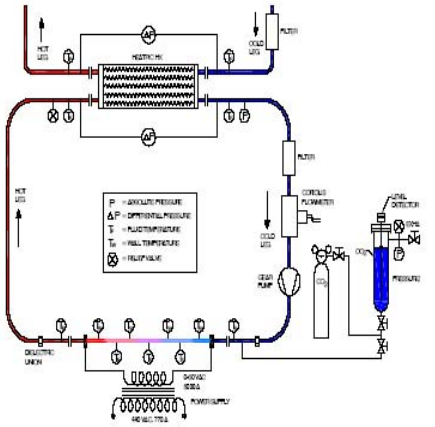

Fig. 4. Schematic of test loop.

conditions. Additional details regarding loop specifications and operating procedure can be found in reference.

3. TEST RESULTS

The pressure drop and flow rate in the heat exchanger were measured to investigate its hydraulic characteristics. Both the hot and cold sides were tested with ambient pressure H_2O at two different temperatures, 20 and 50°C. The measured data was used to calculate pressure loss coefficients for each side. The well-known relationship for the Fanning friction factor has been used:

$$C_f = \frac{1}{4}\frac{D_h}{L}\left(\frac{\Delta P}{\frac{1}{2}\rho v^2}\right) \qquad (2)$$

The pressure loss measurements with H_2O were made over the full available flow rate range. As seen in Figure 5, the Reynolds numbers for H_2O are rather low and well below the laminar-turbulent transition region of ~2000 for straight circular tubes. The measured friction factor does not exhibit the characteristic Re^{-1} dependence expected for laminar flow until the Reynolds number is below ~100. Within the semicircular, zigzag channels of the PCHE, the turbulent flow regime extends considerably below that of straight, circular tubes. This has also been shown by Haynes and Johnston, who in addition demonstrated that increased tortuosity of the PCHE flow paths depresses the transition between turbulent and laminar flow to lower Reynolds numbers.

Before the heat exchanger was tested under Brayton cycle conditions with CO_2, it was operated with H_2O on both the hot and cold sides to measure the heat transfer coefficient of the H_2O. The data is later used in the calculation of the average heat transfer coefficient on the cold (H_2O) side for the cooler conditions with the Reynolds number of H_2O. The heat exchanger was operated with cold side inlet and outlet

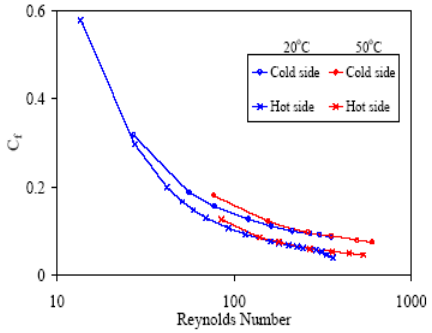

Fig. 5. Hot and cold side friction factors measured with H_2O and CO_2.

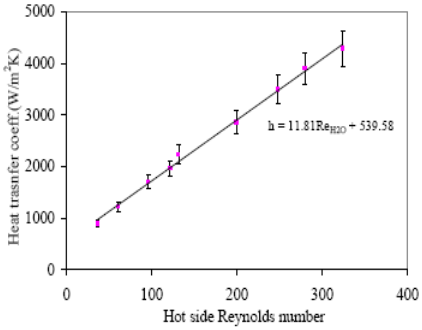

Fig. 6. Average heat transfer coefficient for H_2O.

temperatures of about 20 and 50°C, respectively, with similar temperatures on the hot side. The mass flow ranged 100 to 1000kg/hr and the heat load between 4 and 40kW.

The overall heat transfer coefficient U is calculated in terms of the heat load q and logarithmic mean temperature difference ΔT_{LM}:

$$q = AU\Delta T_{Lm} \tag{3}$$

The heat load was determined from an energy balance using the measured flow rate and inlet and outlet fluid temperatures. The logarithmic mean temperature difference is:

$$\Delta T_{LM} = \frac{\left(T_{H\_out} - T_{C\_in}\right) - \left(T_{H\_in} - T_{C\_out}\right)}{\ln\left[\left(T_{H\_out} - T_{C\_in}\right)/\left(T_{H\_in} - T_{C\_out}\right)\right]} \tag{4}$$

Equation 3 is based on the assumption of constant values of U and fluid heat capacity, which does not strictly apply to the CO_2 side of the cooler. However, the formula is adequate for identifying the trends of interest.

By back calculating the thickness of the metal wall between the hot and cold channels using the experimental data from Heatric, the thickness is about the 0.92 mm. The data from Heatric cannot be shown here because it is proprietary. However, the thermal resistance of the metal wall between the channels is small enough that it can be neglected in calculating the overall heat transfer coefficient. So the overall heat transfer coefficient can be written in terms of the hot and cold side heat transfer coefficients:

$$U^{-1} = \frac{1}{h_H} + \frac{1}{h_C} \tag{5}$$

If both the hot and cold sides are geometrically similar and heat transfer measurements are made with matched Reynolds numbers, the heat transfer coefficients can be determined by assuming that $h_H \approx h_C$ with the simplified overall heat transfer coefficient. The assumption of geometric similarity is supported by the heat exchanger specifications in Table 1 and the friction factor data in Fig 5, which differs by less than 50% at a given Reynolds number. For comparison, the Heatric PCHE tested by Ishizuka et al. had the identical diameter (1.88mm) hot and cold, zigzag angled (115 vs 100°) channels but observed a difference in measured friction factor ($C_{f\_C}/C_{f\_H} > 2$). Yet in their study with CO_2 they found that both the hot and cold side heat transfer coefficients were well proportional to the Reynolds number. It seems that the small zigzag angle difference does not affect the heat transfer coefficient. Although the zigzag angle of our PCHE is unknown, the heat transfer coefficient changes linearly with Reynolds number like Ishizuka et al. The present difference in Fanning friction factor is less than that of the PCHE tested by Ishizuka et al. So the influence of the zigzag angle is thought to be small when considering Ishizuka's result. With this in mind, the Reynolds numbers of hot and cold sides were matched for each measurement in order to make the heat transfer coefficients on both hot and cold side nearly equal. Equation 5 was then used to calculate the heat transfer coefficient for H_2O from the overall heat transfer coefficient. The result is shown in Fig. 6. The heat transfer coefficient of the cold side with H_2O as a working fluid is defined in terms of the Reynolds number of the H_2O as follows,

$$h_{H_2O} = 11.81 \times \mathrm{Re}_{H_2O} + 539.58\left[\frac{W}{m^2K}\right] \tag{6}$$

For the tests with precooler conditions, three sets of measurements were made. Tests were conducted with the CO_2 at pressures of 7.5 and 8.5MPa. The Reynolds numbers ranged between 2000 and 6000. For each measurement, the loop outlet temperature was set near the pseudocritical temperature. The inlet temperatures varied within the range about 87-89°C as shown in Figure 7. The H_2O flow rate was set to 12lpm for all tests, producing a H_2O side heat transfer coefficient of 3.5-4kW/m^{2}K. The heat load ranged from about 10 to 30 kW. Two data sets were measured for CO_2 at a pressure, 7.5MPa. The two sets differ in the proximity of the outlet temperature to the pseudocritical point. Figure 7 shows the fractional temperature points where data relative to that at the pseudocritical point was taken. This is where the peak value of specific heat is reached. As shown in the figure, it is clear that Test A is much closer to the pseudocritical point because the temperature fraction is almost 1 and the specific fraction is much bigger than for Test B. Recall too that the thermal properties of CO_2 near the

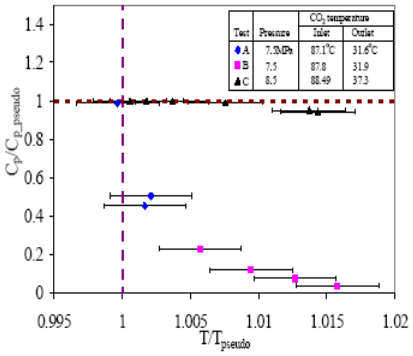

Fig. 7. The fraction of specific heat and temperature of the measurement points to the pseudocritical point.

pseudocritical point change rapidly. The third set of measurements was made at a pressure of 8.5 MPa which is called Test C. Comparing Test B versus C, we see that the fractional temperature span is similar but their specific heat fractions are very different, which means that the thermal properties near the critical point (at 30.98°C and 7.38MPa from the NIST database) changes sharply; that is, Test B is closer than Test C. In Figure 7, the error bar corresponds to the documented ±0.1°C accuracy noted fro the RTD temperature sensor.

Liao et al. showed augmentation on heat transfer near the pseudocritical point and the decrease in the heat transfer with increasing pressure near the pseudocritical point. Figure 8 shows the average heat transfer coefficient calculated from the three sets of test data and Eqns. 3-6. For the two 7.5MPa tests, there appears to be no significant difference in the heat transfer coefficient. Figure 8 also shows an increase in heat transfer coefficient with pressure. The trend per Liao et al. was not observed. One possible explanation for the unexpected heat transfer trend may be from the log mean temperature difference method. In order to use the LMTD, the thermal properties of fluid should be constant, but in our case, the supercritical CO_2 has variable properties. Especially near the pseudociritical point, the thermophysical properties change sharply. To account for variable properties, we have been working on calculation of the local heat transfer coefficient in the PCHE.

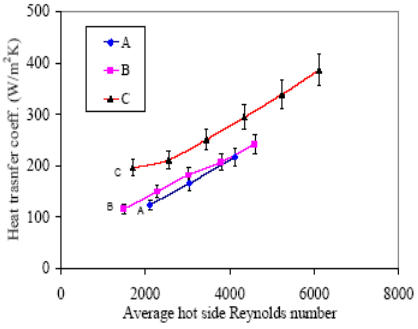

Fig. 8. Average hot side heat transfer coefficient for precooler conditions

To supplement the above test results, one more test was conducted while varying the bulk temperature. For this test, the outlet and inlet temperature difference of the hot (CO_2) side was set as small as possible. In this way, the thermal properties do not change much in the small temperature range compare to the above tests. This allowed us to use the LMTD. To take a closer look at the augmentation heat transfer coefficient within the pseudocritical region, two sets of data were measured at CO_2 pressures of 7.5 and 8.5MPa. The H_2O flow rate was 12 lpm. The CO_2 flow rate was 250kg/hr. The heat load was less than 2kW. The heat load was kept as small as possible in order to measure data with small temperature difference between the CO_2 inlet and outlet. Figure 9 shows the heat transfer

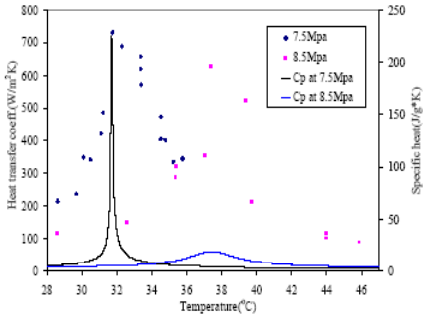

Fig. 9. Heat transfer coefficient along with the bulk temperature:
H_2O on the cold side and CO_2 on the hot side.

coefficients at 7.5 and 8.5MPa calculated from the test. The heat transfer coefficient increases, reaches a peak, and then decreases as the bulk temperature increases. This trend in heat transfer coefficient along with the bulk temperature has been observed by others. Huai et al. shows a similar result in a straight mini-channel. It is though that the heat transfer is affected by specific heat. As CO_2 has a high heat capacity at the pseudocritical point, it transports much thermal energy to the H_2O side. This can also be observed in the experimental data. The heat transfer rate in CO_2 was the largest near the pseudocritical point at both 7.5 and 8.5MPa. Again, this result shows the CO_2 can transfer more heat to H_2O as it gets closer to the pseudocritical point. Therefore, the heat transfer appears strongly correlated to specific heat in Figure 9.

4. Simple computational approach

For the precooler condition of the STAR-LM system, there is an analysis that shows results for the outlet and inlet temperature of hot and cold side. Also, it can show a rough temperature distribution inside the heat exchanger. This calculation is based on the LMTD method and the thermal properties data base from NIST web site. Considering rapid change in thermal properties of the CO_2 over a narrow temperature range, some modification

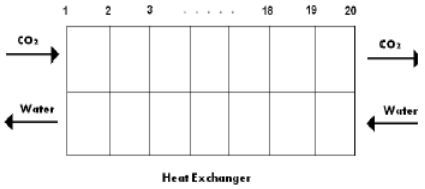

Fig. 10. The simplified drawing of the PCHE

of the LMTD method is needed in order to account for property changes. If we were to divide the heat exchanger into smaller sections like Figure 10, one can assume that the fluid properties remain quasi-constant over each subsection. With this approach, we might be able to use the LMTD method in the subsections. The heat exchanger was first divided into 19 pieces, that is, 20 nodes. Figure 10 shows a simplified drawing of the heat exchanger. The heat exchanger consists of the hot side, which uses CO_2 as the working fluid, and the cold side, which uses H_2O as the working fluid. The metal wall between channels is also neglected in this simple calculation as it was neglected above to process the experimental data.

The pressure drop on the CO_2 side in the heat exchanger is neglected in the calculation. This is a reasonable assumption since the measured pressure drop in the heat exchanger is very small relatively to the pressure at the inlet of the CO_2 side. This assumption makes the properties of the CO_2 a function of the temperature alone. In this way, we can easily make the correlation between the thermophysical properties of the CO_2 and temperature, even though the properties change dramatically near the pseudocritical region.

Figure 11 shows a single section of Figure 10. In Figure 11, "H_n" and "C_n" mean the n^{th} node on the hot side and the cold side. On the hot side (CO_2 side), the enthalpy of CO_2 is taken as a function of the temperature at the given CO_2 inlet pressure. The mass flow rates of the H_2O and CO_2 are taken from the experimental results. The energy transferred from the hot side in the section can be expressed as:

$$q_n = \dot{m}_H \cdot (i_{H_n} - i_{H_{n+1}}) \qquad (7)$$

where q_n is the heat transfer rate from the CO_2 to H_2O. The heat transfer rate to the cold side can be calculated using:

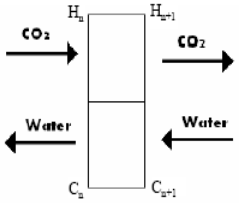

Fig. 11. A subsection of the drawing of the PCHE

$$q_n = \dot{m}_C \cdot c_{p\_C} \cdot (T_{C_n} - T_{C_{n+1}}) \qquad (8)$$

The LMTD method also applies to this region in Figure 11 as is seen in Equation 9 because the property in the small section is assumed to be constant. The overall heat transfer coefficient and mass flow rate of each side are taken from the experimental result. The heat transfer area, 5.6 m^2, provided from Heatric is used in this calculation. So,

$$q_n = U \cdot A \cdot \frac{(T_{H_n} - T_{C_n}) - (T_{H_{n+1}} - T_{C_{n+1}})}{\ln\left[\frac{T_{H_n} - T_{C_n}}{T_{H_{n+1}} - T_{C_{n+1}}}\right]} \qquad (9)$$

We now have three equations for one section of the heat exchanger. These equations can be related to each other through the following:

Hot side energy balance equation (Eqn.7)
= Cold side energy balance equation (Eqn.8)
= Energy calculated by LMTD method (Eqn.9)

We can use this method for the entire heat exchanger. Using this method with 19 individual heat exchanger sections lead to

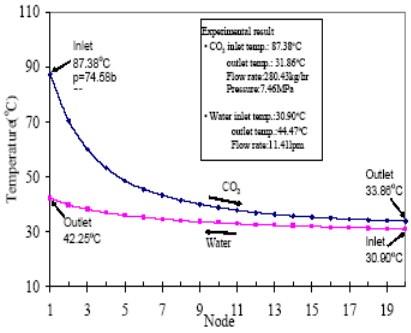

Fig. 12. The calculated temperature distribution

38 unknowns. There are also 38 equations generated. Since we have as many equations as unknowns, the temperature distribution inside the heat exchanger can be calculated using this method. The temperature distribution is shown in Figure 12. The hot side inlet temperature is 87.38°C, and the cold side inlet temperature is 30.90°C. The inlet pressure of the CO_2 side is 7.46MPa. These are the input values for the calculation. The outlet temperature on the hot side and the outlet temperature on the cold side were calculated via the above analytical method. These calculated temperatures can then be compared with the measured temperatures for these conditions. From the analytical results, the outlet temperature of the hot side is 33.86°C, and the outlet temperature of the cold side is 42.25°C. Comparing these

to the experimental result, the error is within ±6% on each side. This calculation shows the analytical results compare reasonably well to the experimental results. Figure 12 shows the general temperature trend in the PCHE.

5. CONCLUSIONS

The hydraulic and heat transfer characteristics of a Heatric PCHE have been tested for the conditions of the cooler in a LFR operating with a supercritical CO_2 Brayton cycle. The heat exchanger was operated with H_2O at atmospheric pressure on the cold side and supercritical CO_2 on the hot side. Tests were conducted with the CO_2 at pressures of 7.5 and 8.5MPa, mass flow rates in the range of 100 to 700kg/h, and heat loads between 10 and 30kW. The hot side inlet and outlet temperatures were near 85 and 31°C, respectively, to match the planned cooler conditions. The measured overall heat transfer coefficients for the tested Reynolds number range of 2000-6000 are between 200 and 700W/m^{2}K. The accompanying H_2O side heat transfer coefficient, measured in separate tests, was ~3500W/m^{2}K and so the heat transfer rate for these cooler operating conditions is controlled by the CO_2 side.

The test in terms of the bulk temperature clearly shows the same trends found in other studies. It can be concluded that the heat transfer in the PCHE is influenced by the specific heat and as such, the heat transfer coefficient follows the increase in specific heat line near pseudocritical point.

We also presented a discretize computational approach, where the traditional LMTD method was applied and shown as valid for small segments of the PCHE. In this work, 19 segments showed good comparison to experimental data. Finally, in order to consider flow channel designs, a Computational Fluid Dynamics (CFD) program model of a PCHE using the software program STAR-CD is under development. The STAR-CD modeling will be run under the same conditions as the experiment. Through the CFD program, we expect to see more accurate results of not only the temperature distribution, but also the pressure distribution inside the PCHE.

ACKNOWLEDGMENTS

The authors thank to Anton Moisseytsev and Jim Sienicki, both at ANL, for their assistance and guidance. This work was supported in part by the U.S. Department of Energy, Nuclear Energy Research Initiative, Project number 05-146, Award Number DE-FC07-05ID14672, Heat Exchanger Studies for Supercritical CO_2 Power Conversion System.

NOMENCLATURE

A	area of bubble surface	[m^2]
A	overall heat transfer area	[m^2]
c_p	specific heat	[kJ/kg·K]
D_h	hydraulic diameter	[m^2]
C_f	Fanning friction factor	
h	Convection heat transfer coefficient	[W/ m^2·K]
i	enthalpy	[kJ/kg]
K	thermal conductivity	[W/m·K]
L	length	[m]
ΔP	differential pressure	[pa]
T	temperature	[K]
ΔT_{LM}	logarithmic mean temperature difference	[K]
U	overall heat transfer coefficient	[W/ m^2·K]
V	velocity	[m/s]

Greek Letters

ρ	density	[kg/ m^3]
μ	viscosity	[kg/s·m]
q	heat transfer rate	[W]

Subscripts

C	cold side
H	hot side
h	hydarulic
H_2O	water
in	inlet
n	nth node
out	outlet
pseudo	pseudocritical point

REFERENCES

Huai, X. *et al*. (2005). "An Experimental Study of Flow and Heat Transfer of Supercritical Carbon Dioxide in Multi-Port Mini Channels Under Cooling Conditions", *Chemical engineering Science*, 60(12), pp. 3337-3345.

Ishizuka, T. *et al*. (2005). "Thermal-hydraulic Characteristics of a Printed circuit heat exchanger (PCHE) in a Supercritical CO_2 Loop", *'Proc. 11th Int. Topical Meeting on Nuclear Reactor Thermal-Hydraulics (NURETH-11)*, Avignon, France, October 2-6.

Liao, S. *et al*. (2002). "An Experimental Investigation of Convection Heat Transfer to Supercritical Carbon Dioxide in Miniature Tubes", *Int. J. Heat and Mass Transfer*, 45(25), pp. 5025-5034.

Liao, S. *et al*. (2002). "Measurements of Heat Transfer Coefficients from Supercritical Carbon Dioxide Flowing in Horizontal Mini/Micro Channels", *Transactions of the ASME J. Heat Transfer*, 124(3), pp. 413-420.

Lomperski, S. *et al*. (2004). "Stability of a Natural Circulation Loop with a Fluid Heated Through the Thermodynamic Pseudo-critical Point", *'Proc. 2004 Int. Congress on Advances in Nuclear Power Plants (ICAPP 04)*, Pittsburgh, PA, USA, June 13-17.

Lomperski, S. *et al*. (2006). "Testing of a Compact Heat Exchanger for Use as the Cooler in a Supercritical CO_2 Brayton Cycle", *'Proc. 2006 Int. Congress on Advances in Nuclear Power Plants (ICAPP 06)*, Reno, NV, USA, June 4-8.

Moisseytsev, A. *et al*. (2003). "Cycle Analysis of Supercritical Carbon Dioxide Gas Turbine Brayton Cycle Power Conversion System for Liquid Metal-Cooled Fast Reactors", *'Proc. 11th Int. Conf. on Nuclear Engineering (ICONE11)*, Tokyo, Japan, April 20-23.

Peterson, P. F. *et al*. (2003). "Multiple-Reheat Brayton Cycles for Nuclear Power Conversion with Molten Coolants", *Nuclear Technology*, 144(3), pp. 279-288.

Pettersen, J. *et al*. (2000). "Heat Transfer and Pressure Drop Characteristics of Supercritical Carbon Dioxide in Microchannel Tubes under cooling", *'Proc. 4th IIR-Gustav Lorentzen Conference on Natural Working Fluids*, Purdue University, USA.

SIENICKI, J. J. *et al*. (2003). "The STAR-LM Lead-Cooled Closed Fuel Cycle Fast Reactor Coupled to a Supercritical Carbon Dioxide Brayton Cycle Advanced Power Converter", *'Proc. 2nd International Conference on Heavy Liquid Metal Coolants in Nuclear Technologies (HLMC-2003)*, Obninsk, Russia, December 8-12.